Adaptive Imaging with a Cylindrical, Time-Encoded Imaging System

by

Niral P Shah

A dissertation submitted in partial fulfillment
of the requirements for the degree of
Doctor of Philosophy
(Nuclear Engineering and Radiological Sciences)
in The University of Michigan
2020

Doctoral Committee:

Professor David K. Wehe, Chair
Professor Jeffrey A. Fessler
Professor Igor Jovanovic
Dr. Peter Marleau, Sandia National Laboratories

Niral P Shah

nirpshah@umich.edu

ORCID iD: 0000-0002-7299-0774

To my family

ACKNOWLEDGEMENTS

I owe a debt of gratitude to the many people who supported and inspired me while earning this doctorate. First, I want to thank Professor David Wehe for being a fantastic advisor both academically and personally. From the very beginning, his sole focus has been on cultivating an environment with the opportunities and resources necessary for me to succeed. He never sparred any expense and I am very grateful for his time and effort. I am also indebted to Dr. Peter Marleau for his mentorship over the years. He consistently pushed this research in new directions and provided valuable feedback along the way. Professor Jeffery Fessler and Professor Igor Jovanovic are also great resources to learn from and emulate. In particular, I appreciate the many hours Professor Fessler spent teaching me the foundations of image reconstruction both in his classes and in one-on-one meetings. His expertise was instrumental in this dissertation.

I am privileged to have worked alongside so many wonderful people. I am glad I joined the NERS department with Daniel Shy (now Dr. Shy) and Charles Leak - they have been great friends and researchers to learn from. In particular, I am grateful for the countless hours Daniel and I spent discussing research ideas. He played an important role in shaping this work. I also want to thank Professor Zhong He and his entire research group for their hospitality. They graciously welcomed me into their group and taught me so much along the way.

Many researchers contributed to this work including James Berry, Jacob Van-

derZanden, Konrad Rauscher, Mackenzie Warwick, Joe Bath, and John (Jack) Kuchta. Without their assistance and expertise, I would have struggled to finish various projects in time - thank you. Also, thank you Dr. David Chichester, Jay Hix, Dr. Scott Thompson, and the team at Idaho National Laboratory for facilitating the measurements at the Zero Power Physics Reactor facility.

I would be remiss not to recognize the staff in the NERS department - they make the NERS department a friendly and welcoming place. In particular, Garnette Roberts has been a great advisor and friend. Thank you all.

Finally, not one piece of this dissertation would have been possible without the immense sacrifices made by my parents, Paresh and Shobhana Shah. Their tireless work to improve and enrich the lives of their children has allowed me the space to pursue this academic accomplishment. I am blessed and deeply grateful for them; I hope I am making them proud. In the same thread, I want to thank Deanna, my wife, for always supporting me and encouraging me. I am eternally grateful for having her in my life.

This research was performed under appointment to the Nuclear Nonproliferation International Safeguards Fellowship Program sponsored by the National Nuclear Security Administration's Office of International Nuclear Safeguards (NA-241).

The work was funded in-part by the Consortium for Verification Technology under Department of Energy National Nuclear Security Administration, USA award number DE-NA0002534.

The work was funded in-part by the Consortium for Monitoring, Technology and Verification under Department of Energy National Nuclear Security Administration, USA award number DE-NA0003920.

TABLE OF CONTENTS

LIST OF FIGURES

Figure

LIST OF TABLES

Table

LIST OF APPENDICES

Appendix

LIST OF ABBREVIATIONS

AUROC the area under the ROC curve

c-TEI cylindrical, time-encoded imaging

CLLBC $Cs_2LiLa(Br, Cl)_6$

CNR contrast-to-noise ratio

CRLB Cramér-Rao lower bound

FBP filtered back-projection

FIM Fisher information matrix

FOM figure-of-merit

FOV field-of-view

FWER family wise error rate

FWHM full width at half maximum

GLRT generalized likelihood ratio test

HDPE high-density polyethylene

INL Idaho National Laboratory

LMMSE linear minimum mean squared error

LRT likelihood ratio test

LSI linear shift-invariant

MAP maximum a posteriori estimator

MCMC Markov chain Monte Carlo

ML maximum likelihood

MLE maximum likelihood estimate

MLEM maximum likelihood expectation maximization

MOX mixed oxide

NRMSE normalized root mean squared error

OLS ordinary least squares

PDF probability density function

PMT photomultiplier tube

PSD pulse shape discrimination

PSF point spread function

ROC receiver operator characteristic

S:B source-to-background ratio

SBP simple back-projection

SCA spatial coded aperture

SI shift-invariant

SIQ singlet ionization quenching

SNR signal-to-noise ratio

SOE stochastic origin ensembles

TEI time-encoded imaging

TTA triplet-triplet annihilation

URA uniformly redundant array

ZPPR Zero Power Physics Reactor

ABSTRACT

Most imaging systems for terrestrial nuclear imaging are static in that the design of the system and the data acquisition protocol are defined prior to the experiment. Often, these systems are designed for general use and not optimized for any specific task. The core concept of adaptive imaging is to modify the imaging system during a measurement based on collected data. This enables scenario specific adaptation of the imaging system which leads to better performance for a given task. This dissertation presents the first adaptive, cylindrical, time-encoded imaging (c-TEI) system and evaluates its performance on tasks relevant to nuclear non-proliferation and international safeguards.

We explore two methods of adaptation of a c-TEI system, adaptive detector movements and adaptive mask movements, and apply these methods to three tasks, improving angular resolution, detecting a weak source in the vicinity of a strong source, and reconstructing complex source scenes. The results indicate that adaptive imaging significantly improves performance in each case.

For the MATADOR imager, we find that adaptive detector movements improve the angular resolution of a point source by 20% and improve the angular resolution of two point sources by up to 50%. For the problem of detecting a weak source in the vicinity of a strong source, we find that adaptive mask movements achieve the same detection performance as a similar, non-adaptive system in 20%-40% less time,

depending on the relative position of the weak source. Additionally, we developed an adaptive detection algorithm that doubles the probability of detection of the weak source at a 5% false-alarm rate.

Finally, we applied adaptive imaging concepts to reconstruct complex arrangements of special nuclear material at Idaho National Laboratory. We find that combining data from multiple detector positions improves image uniformity of extended sources by 38% and reduces the background noise by 50%. We also demonstrate 2D (azimuthal and radial) imaging in a crowded source scene. These promising experimental results highlight the potential for adaptive imaging using a c-TEI system and motivate further research toward specific, real-world applications.

CHAPTER I

Introduction

In the world of nuclear non-proliferation and international safeguards, passive radiation imaging is a valuable tool that can provide richer information to the end user compared to non-imaging, detection systems. For example, directing authorities to search for undeclared sources in a specific location can help reduce inspection times and increase confidence in the inspection results [1–3]. In a treaty verification setting, radiation imaging can be used to count the number of warheads on a missile [4, 5] or to monitor radioactive sources in storage [6–9]. In the nuclear power industry, imaging systems are used to monitor power plants for contamination and recently they have also been used during the decommissioning of reactors and in emergency response scenarios such as the Fukashima Daiichi disaster [10–12]. For all of these applications, users need simple, robust, and cost-effective imaging solutions that can be used in the field. Cylindrical, time-encoded imaging (c-TEI) may be ideal for these types of applications. In this dissertation, we design and build a 1D, dual-particle, c-TEI system for use in nuclear non-proliferation scenarios and explore the benefit of adaptive imaging in c-TEI systems when considering the important tasks of reconstructing high resolution images, detecting sources, and reconstructing complex source scenes.

1.1 Radiation Imaging

For all nuclear non-proliferation applications that require gamma-ray or neutron imaging, there are two general categories of imaging systems: scatter-based imaging systems and occlusion-based imaging systems.

As the name implies, scatter-based imaging systems, also called scatter cameras, rely on the physics of scatter to localize sources. For gamma rays, scatter cameras rely on Compton scattering and for fast neutrons, they rely on elastic scattering [13–16]. In either case, there is a direct relationship between the energy deposited in the detector during the scatter and the deflection angle of the particle. Thus, if one can measure the energy deposited and the post-scatter energy and direction of the particle, the incident direction of the particle can be restricted to a cone of possibilities (or in some cases, an arc [17]). By collecting many such cones, scatter cameras can localize the source(s) in the field-of-view (FOV). Fig. 1.1 is a depiction of a neutron scatter camera.

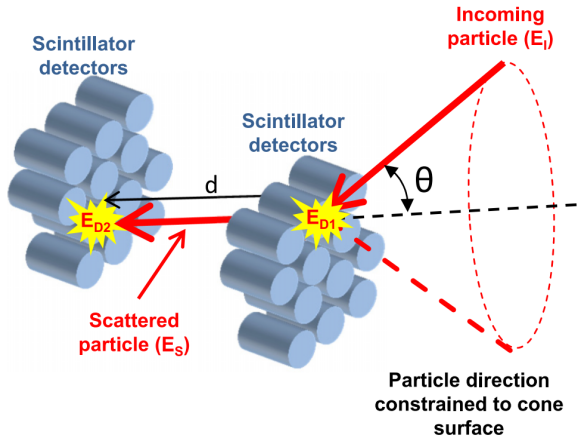

Figure 1.1: Depiction of a neutron scatter camera. Using the deposited energy, time, and position of interaction from two interactions, the incident direction of the particle is constrained to a cone. Reproduced from [18].

Although semiconductor-based gamma-ray scatter cameras are widely used in

the field and are commercially available [19,20], the neutron equivalent is still under development. Scatter cameras must record the position and energy deposited for multiple interactions that may occur less than a nanosecond apart. This leads to complex detector arrays with expensive readout systems and high channel count. Moreover, since they require multiple interactions from the same particle, their efficiency may be low.

On the other hand, occlusion-based imaging systems utilize an intervening material, often called a mask, to constrain the potential incident directions of a particle. A mask consists of open and closed elements where particles can pass through open elements but are attenuated by closed elements. Thus, as particles travel from the source to the detector, the particle flux is changed or modulated by the mask. The detector system records this modulated pattern and then that information along with knowledge of the mask pattern and orientation is used to create an image of the source scene. There are two ways to modulate the particle flux: spatially [21–25] or temporally [26–37]. We will refer to these methods respectively as spatial coded aperture (SCA) and time-encoded imaging (TEI).

As a concrete example, consider the pinhole camera in Fig. 1.2 which is an example of a SCA system with one open element. The only particles that can be detected by the detector array are the ones that travel through the pinhole. Thus, one can easily reconstruct the source scene by using the spatial distribution of counts on the detector array and the position of the pinhole.

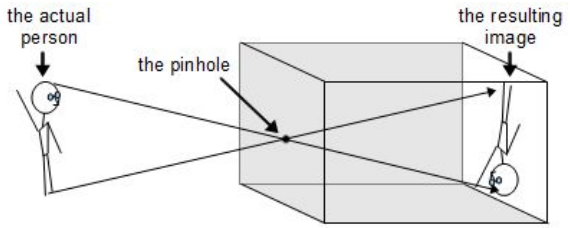

Figure 1.2: The basic pinhole camera. The detector array can only detect particles that travel through the pinhole. Original reference unknown.

Since SCA systems need to record the spatial distribution of particles, they require an array of detectors which invariably leads to expensive readout systems and high channel count. In contrast, TEI systems only require one detector and a moving mask to create an image[1]. Instead of spatially modulating the particle flux, in TEI, a moving mask temporally modulates the particle flux. Thus, the detector system does not need to be position-sensitive but instead needs to be time-sensitive as in the detector system must be capable of recording time dependent count rates. For most commercially available detector systems, this is an easy task.

1.2 Cylindrical, Time-Encoded Imaging

There are many types of TEI systems, but the focus of this work is on cylindrical, time-encoded imaging (c-TEI)[2]. In a c-TEI system, a detector is placed in the interior region of a cylindrical, rotating, coded mask. As the mask rotates, the count rate from the source changes based on if there is an open element or a closed element along the line-of-sight between the detector and the source. Fig. 1.3 is a simple 1D example of a c-TEI system with one open element, similar to the pinhole camera in Fig. 1.2.

[1]One can build a TEI system where the mask is stationary and the detector is moving, or where the mask and detector are stationary and the source is moving, although these is less common.

[2]For a review of TEI from a historical perspective, see [38].

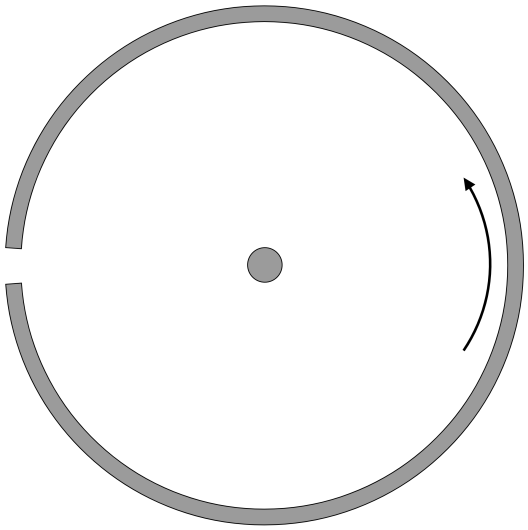

Figure 1.3: c-TEI version of a 1D pinhole camera.

Compared to scatter cameras or SCA systems, c-TEI systems have some key characteristics that may make them advantageous for nuclear non-proliferation applications; they are summarized in Table 1.1. Critically, the minimal requirements placed on the detector system mean that c-TEI systems are simple, robust, and cost-effective. Since only one detector is necessary, the detector system is easy to inspect and data can be collected using commercially available readout systems. Additionally, the imaging performance of c-TEI systems is only dependent on geometric factors such as the size of the detector and mask elements. In both scatter cameras and SCA systems, imaging performance is dependent on both geometric factors and detector performance. In scatter cameras, the angular resolution is dependent on the distance between interactions and on the position and energy resolution of the detector system. This makes optimization and characterization of scatter cameras a complex process. For SCA systems, each detector element must have the same sensitivity as the rest to achieve high signal-to-noise ratio (SNR) images. This means each detector element

must be carefully calibrated and gain matched to the other elements[3].

Table 1.1: Key characteristics of scatter cameras, SCA systems, and c-TEI systems.

Characteristics	Scatter Camera	SCA	c-TEI
Directionality	Scatter-based	Spatial encoding	Temporal encoding
Mask	N/A	Stationary	Moving
Detector Requirements	Position, energy, and timing (∼ns)	Position	Timing (∼ms)
Channel Count	High	High	Low
Resolution[4]	Strongly	Weakly	Weakly
Sensitivity[5]	Low	High	Moderate
Field of View	4π, non-uniform	limited, uniform	$> 2\pi$, uniform

In large part due to these advantages, there is growing interest in c-TEI systems. The resurgence of c-TEI started in 2010 when Marleau et al.'s proof-of-concept 1D c-TEI system showed promising results for fast neutron imaging [44]. That initial work lead to the development of a 2D, fast-neutron, c-TEI system composed of a single organic scintillator and a thick HDPE mask with a random coding pattern [37]. Since there is only one detector, random coding patterns might perform better than coding patterns based on cyclic difference sets since not every mask element is sampled[6] [45]. If one wants to use coding patterns based on cyclic difference sets, they can follow Liang et al.'s approach where they used a vertical array of detectors instead of a single detector to sample the entire coding pattern [46]. Additionally, Liang et al. utilized a self-supporting coding pattern which makes for simpler mask construction.

[3]Mask/antimask methods may also be used [39–43].

[4]This row is read as: "When considering angular resolution, in a $(\cdot)$ system, geometric factors and detector performance are $(\cdot)$ coupled."

[5]Sensitivity is the detection efficiency of the system. Since scatter cameras require multiple scatters from the same particle, its sensitivity is lower than SCA or c-TEI systems. Additionally, SCA systems typically utilize many detectors and thus have greater sensitivity. If a SCA and a c-TEI system used similar detector volumes, they would have similar sensitivities.

[6]Imagine the set of integers from 0 to n $(0, 1, 2, \ldots, n)$ - we call this set a group. A cyclic difference set is a subset of the group $(a_1 = 0, a_2, \ldots a_I)$ such that there are exactly λ ways any non-zero element of the group can be represented by a modular difference of two elements of the subset $(a_i - a_j \mod n)$. Cyclic difference sets form the basis of many coded aperture patterns.

One of the disadvantages of using a coding patterns based on cyclic difference sets is that the entire coding pattern must be sampled to reconstruct artifact-free images. In some cases, this can lead to long measurement times. As an alternative, Boardman et al. built a c-TEI system that reconstructs images using compressed sensing[7] [47]. Their system consists of two nested masks that rotate independently and create quasi-random mask patterns. Preliminary results indicate that using compressed sensing can reduce measurement times by 90%.

Although several c-TEI systems have been built, there exists relatively little work on which analytical models to use when designing a c-TEI system. Thus, in Chap. III, we discuss the design spaces where the conventional small detector assumption may be valid and where a more robust model, the large detector model, would be necessary to generate accurate responses. Additionally, Chap. III introduces the offset detector model for use when the detector is not at the center of the mask. For simplicity, all of the system response models used throughout the dissertation are presented in Chap. III.

Using the large detector model, Chap. IV evaluates different c-TEI designs and explores the tradeoffs between size, weight, angular resolution, and contrast-to-noise ratio (CNR). With these tradeoffs in mind, we design and construct a 1D, dual-particle c-TEI system called MATADOR[8] for use in nuclear non-proliferation scenarios. We hope that Chap. IV can provide a starting point for future researchers who are designing c-TEI systems, and in some cases, provide a design that meets their design criteria.

[7] In compressed sensing, one assumes that the reconstructed image has a sparse representation in some basis. By enforcing a sparsity constraint, compressed sensing methods can reconstruct images using significantly fewer measurements than their non-regularized counterparts, provided that the measurements are incoherent.

[8] MATADOR stands for mobile adaptive time-encoded asymmetric dual-particle one-dimensional rotating imager.

Next, Chap. V uses experimental data collected with the MATADOR system to verify the system response models introduced in Chap. III. We predominantly focus on verifying the offset detector model as it is the most general model considered here.

The simplicity of c-TEI systems enables the unique opportunity to implement adaptive imaging. In adaptive imaging, an imaging system or data acquisition protocol is modified during the measurement based on collected data. Due to this scenario specific adaptation, the system collects higher quality data which translates to producing higher quality images in the same measurement time or accomplishing a specified task in less time than the conventional (non-adaptive) alternative. As a real-world example, consider how optical cameras adaptively change the lens' focus to create sharper images. There are two ways a c-TEI system can be adapted: through adaptive detector movements and through adaptive mask movements. Implementing adaptive imaging on a c-TEI system and exploring the potential benefits are the core contributions of this dissertation.

1.3 Adaptive Imaging

Perhaps the oldest implementation of adaptive imaging is in astronomical imaging. Earth-based telescopes commonly suffer from turbulent atmospheric conditions that distort the light from stars or other bodies of interest resulting in blurry images[9]. In 1953, Babcock et al. suggested using wavefront sensors and adaptive optics such as deformable mirrors to detect the wavefront distortions and then correct the distortions on-the-fly to recover the original image [48]. Since the 1990s, the use of adaptive optics in astronomy has exploded and these methods have pushed the resolution of earth-based telescopes to the diffraction limit [49].

[9]This is why stars twinkle.

Adaptive imaging is also an active area of research for medical imaging systems such as ultrasound [50], CT [51], MRI [52], PET [53], and SPECT [54]. In particular, there has been growing interest in adaptive SPECT systems. Poopalasingam et al. are building an adaptive cardiac SPECT system where the slit-slat collimator can be modified to obtain higher resolution images of the heart without disturbing the patient [55]. Their adaptive scheme has two steps: first, a scout image with high sensitivity is collected to roughly localize the radiotracer followed by a high resolution collection with a smaller FOV focused on the heart. In this way, the cardiac SPECT system can be optimized for each patient and provide higher quality diagnostic data. Additionally, Chaix et al. are building a small animal adaptive SPECT system where the pinhole and mask-to-object distance can be adaptively controlled [56]. This gives the researchers control over magnification, resolution, and FOV.

In emergency response, adaptive imaging concepts aid in the search, localization, and mapping of potentially dangerous radioactive sources. Data from simple counting detectors can be utilized to plan sensor movement for tasks such as source search [57] or dose contour mapping [58, 59]. Route planning using imaging systems on autonomous drones has also been considered [60]. Kreucher et al. are investigating methods to coordinate multiple sensors where many parallel decisions are made for a group of sensors as opposed to a single decision [61]. In these large area search scenarios, leveraging collected data to inform where to collect new data is an indispensable technique which can reduce search times by orders of magnitude [62].

Comparatively, the use of adaptive imaging concepts in terrestrial nuclear imaging systems is relatively limited. Willcox et al. investigated the value of adaptively orienting a rotating modulation collimator to position a source in the highest resolution region of the FOV [63]. Their results show clear angular resolution benefits when

imaging a single point source. Fitzgerald et al. built a liquid SCA system where the mask pattern is created by automated plungers filled with liquid metal [64]. They found that reconstructions made using sequences of random masks have greater SNR than those made using conventional mask patterns. Fitzgerald et al. clearly show the potential for adaptive imaging in SCA although they did not incorporate collected data when choosing the next mask pattern.

Across these fields, the general goal has been the same: to leverage collected data and modify the data acquisition system to collect more valuable data. Most of these applications utilize some version of the flowchart shown in Fig. 1.4.

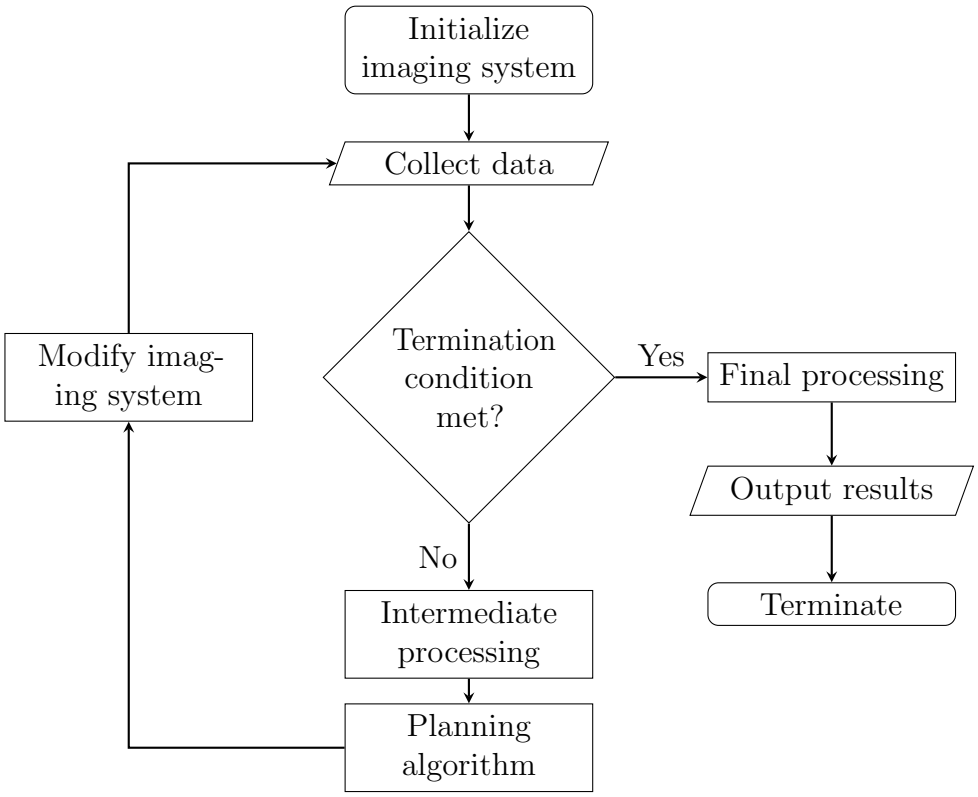

Figure 1.4: Adaptive imaging flowchart.

Given that the user has no prior information, the first step is to collect some preliminary data. That raw data is then processed and sent to a planning algorithm which

predicts the performance of the system for some or all of the possible adaptations[10]. Based on a predefined task, the planner then decides which system configuration or sequence of configurations will lead to the best performance. The decision is translated to the imaging system which adapts accordingly and collects more data. This process is repeated until the user intervenes or a termination condition, such as elapsed time or the completion of a predefined goal, ends the process. One can also envision the adaptive imaging process from a Bayesian point of view where the system is initialized based on some prior information and before each planning step, the algorithm updates the prior using the collected data.

In a c-TEI system, adaptive imaging concepts can be applied in two ways: adaptive detector movements and adaptive mask movements. In the MATADOR system, the detector is hanging from of an x-y linear actuator system such that the detector can move to any position inside the mask rather than being fixing at the center. As shown in Fig. 1.5, if one moves the detector from the center of the mask (D_0) to an offset position (D_1), along one axis, called the imaging axis, the mask-to-detector distance increases. This increase in distance means that the angular width of a mask element is smaller ($\theta_1 < \theta_0$) and thus the angular resolution of the system is improved along the imaging axis. Chap. VI presents an upper bound on the achievable gain in angular resolution from adaptive detector movements and verifies those results experimentally.

[10]For some tasks or algorithms, the raw data may be sent directly to the planning algorithm.

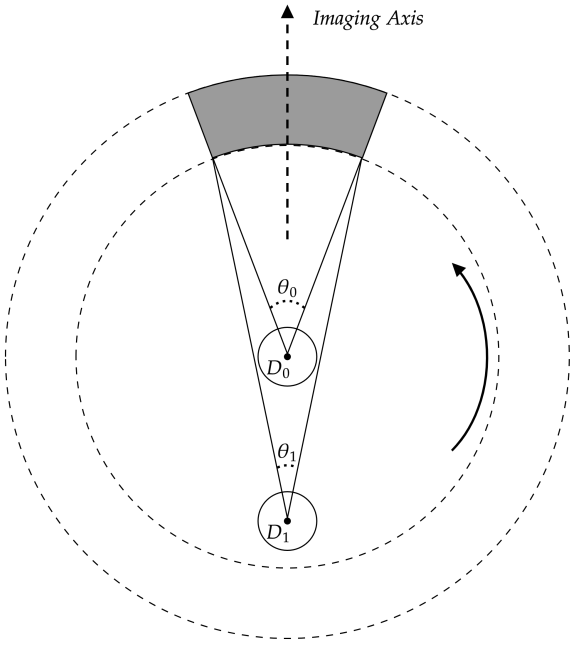

Figure 1.5: Schematic showing adaptive detector movements in a c-TEI system. If one moves the detector from the center of the mask (D_0) to an offset position (D_1), along one axis, called the imaging axis, the mask-to-detector distance increases and thus the angular resolution along the imaging axis improves.

Data collection in a c-TEI system can also be controlled through adaptive mask movements. The time spent at each mask rotation angle does not need to be constant and data collected at some mask orientations may be more valuable than other orientations. Chap. VII utilizes this concept to achieve greater detection performance for a weak source in the vicinity of a strong source. We also develop an adaptive detection algorithm to capture some of the predicted gain and experimentally show the benefit of adaptive mask movements.

Chap. VIII contains results from a measurement campaign at the Zero Power Physics Reactor (ZPPR) at Idaho National Laboratory (INL). This measurement campaign gave us the unique opportunity to measure special nuclear material in complex arrangements and apply adaptive imaging concepts to real-world scenarios. Chap. VIII shows how combining data from multiple detector positions leads to better

uniformity and lower background noise when reconstructing complex source scenes.

But first, Chap. II provides the foundations for c-TEI. The focus is on providing both the background to understand the research and broader context to critique the work.

CHAPTER II

Foundation for Cylindrical, Time-Encoded Imaging

This chapter provides an overview of cylindrical, time-encoded imaging (c-TEI) and introduces the tools used throughout the dissertation. The purpose is to provide both the background to understand the research and broader context to critique the work.

Sec. 2.1 covers how gamma rays and fast neutrons are detected in the MATADOR system starting from the signal generation process to pulse processing. We also discuss detector specific characterization, performance, and capabilities in terms of energy calibration, timing resolution, and pulse shape discrimination (PSD). The goal is to provide a detailed understanding of the pulse processing methods used in this dissertation as they are essential to generating high-quality images.

Sec. 2.2 provides a more detailed foundation for coded aperture imaging. Although much of the theory has its roots in spatial coded aperture (SCA), under a set of ideal coded aperture assumptions, the fundamentals also apply to c-TEI.

Next, Sec. 2.3 reviews the image reconstruction methods commonly used in the field. The section has two parts: analytical image reconstruction and statistical image reconstruction. For analytical image reconstruction techniques, we focus on simple

back-projection and filtered back-projection and for statistical image reconstruction techniques, we focus on maximum likelihood expectation maximization.

In Sec. 2.4, we introduce some specific analysis tools and concepts that are used throughout the dissertation including the Cramér-Rao lower bound, source detection using the generalized likelihood ratio test, and bootstrapping experimental data in a c-TEI system.

Finally, in Sec. 2.5, we distill and review some key takeaways from the chapter.

2.1 Particle Detection

There are a myriad of ways to detect neutrons [65–69] or gamma rays [70, 71], but few detectors exist that can detect both particles without some concessions. One of the simplest options is to use a PSD capable scintillator, such as stilbene, to detect both fast neutrons and gamma rays using the same detector. Recent developments in stilbene production have greatly improved its availability, cost, and properties [72]. Stilbene has excellent PSD and gamma-ray rejection rates [73] making it a good choice as a fast neutron detector. Unfortunately, stilbene, like all organic scintillators, has low density and low Z, and thus has poor efficiency, practically no full-energy deposition peak, and poor energy resolution for gamma rays. To compensate for these downsides, we will also be using an inorganic scintillator, $Cs_2LiLa(Br, Cl)_6$ (CLLBC) [74] to collect higher quality gamma-ray data.

Both stilbene and CLLBC are coupled to photomultiplier tubes (PMTs) to amplify the signal. PMTs convert the light emitted by the scintillator into electrons, and then use a series of dynodes to amplify the signal [71, 75]. After the PMT, the signal can be easily detected and recorded with commercially available readout devices such as an oscilloscope or a digitizer.

Sec. 2.1.1 provides an overview of the signal generation and collection process in scintillators coupled to PMTs, and Sec. 2.1.2 and 2.1.3 provide more detail for both stilbene and CLLBC respectively. Finally, Sec. 2.1.4 is an overview of pulse processing in the MATADOR system.

2.1.1 Signal Generation and Collection

Scintillation is a complex process - an interested reader may refer to foundational work by Birks [76] as a starting point. For our purposes, signal generation in a scintillator starts with the displacement of an electron by a gamma ray or the displacement of a nucleus by a neutron. In both cases, the particle is left with excess kinetic energy, and as it travels through the material, it displaces many other particles, primarily electrons, along its path. In organic scintillators such as stilbene, these electrons excite various molecular states, some of which emit visible light when they de-excite. In doped inorganic scintillators such as CLLBC, scintillation light is created when electron-hole pairs recombine at activation sites.

The emission rate from scintillators is not an instantaneous process. Each de-excitation pathway is governed by exponential decay:

$$I(t) = I_0 e^{-t/\tau} \tag{2.1}$$

where t is time, τ is the decay constant, I_0 is the initial emission intensity, and $I(t)$ is the emission intensity as a function of time t. Many crystals have more than one pathway and thus the resulting pulse is often a summation of exponential functions.

As depicted in Fig. 2.1, the emitted photons scatter, reflect, and stream through the crystal. Of those that reach the photocathode, $\sim$35% are converted into electrons [75]. At this point, the electrical signal from the photocathode is relatively small and so a strong electric field pulls the electrons towards a series of dynodes which amplifies

the signal by a factor of $10^6 - 10^7$. For every electron that impinges on a dynode, 2-3 secondary electrons are emitted; standard PMTs often have 10-12 dynodes in series. The amplified signal is then transmitted to a digitizer where the analog signal is converted into a digital signal. All of the experiments presented in this dissertation used a CAEN DT5730 digitizer [77] which has 8 channels, 14 bits of precision, and samples the waveform every 2 ns.

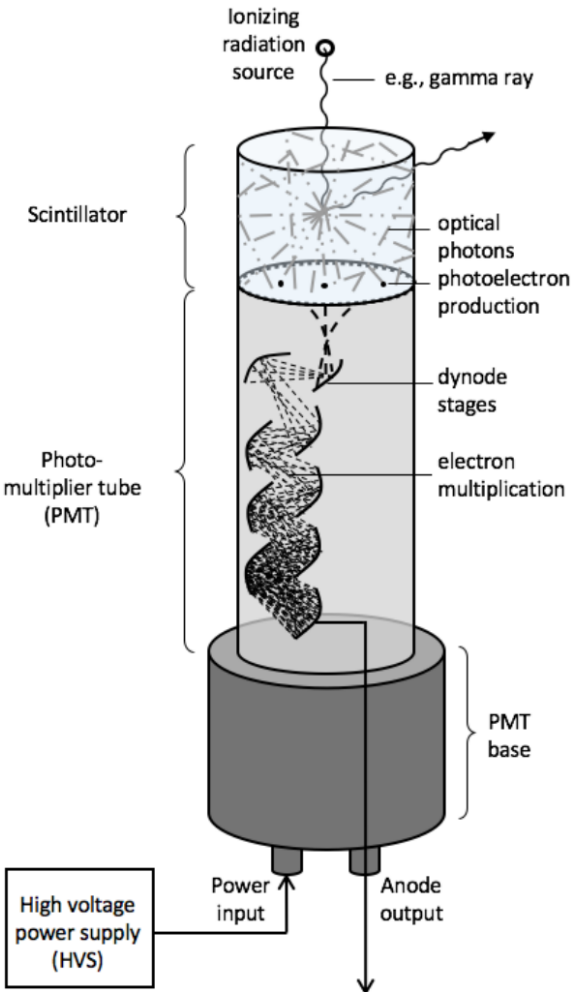

Figure 2.1: A schematic depicting the signal generation and collection process for a scintillator. Reproduced from [78].

2.1.2 Stilbene

Stilbene, also known as trans-stilbene or (E)-stilbene, is an organic scintillator with the chemical formula $C_{14}H_{12}$. The high H content makes it sensitive to fast neutrons and its PSD properties enable excellent gamma-ray rejection. We use a 2" stilbene crystal coupled to a R6231-100 PMT.

Scintillation Process

After an interaction with ionizing radiation, energetic electrons excite molecular states in stilbene, some of which produce light when they de-excite. In stilbene, the de-excitation of the π-molecular orbitals in the two benzene rings cause scintillation [76]. Fig. 2.2 is a Jablonski diagram showing emission from singlet and triplet states - a Jablonski diagram shows the electronic states of a molecule and the transitions between them [76]. When a singlet π-orbital is excited, it will jump to either an excited singlet state or an excited triplet state. The jump to the triplet state is less likely because of the spin transition, consequently fewer triplet states are created during an interaction. Excited singlet states may decay back down to the ground state through a process known as fluorescence (timescale: ns) or transition to a triplet state through a process called intersystem crossing. Similarly, triplet states may decay back down to the ground state through a process known as phosphorescence, but the decay is much slower on average due to the spin transition, on the order of μs-ms.

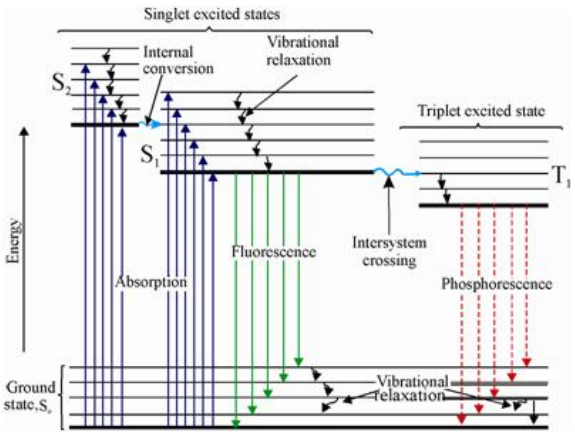

Figure 2.2: Jablonski diagram showing singlet and triplet excited states and some scintillation pathways. Original reference unknown.

If there is a high density of excited π-orbitals, then two excited states can interact with each other instead of independently de-exciting [79]. In singlet ionization quenching (SIQ), two excited singlet states interact to produce a ground singlet state and a singlet state at a higher excitation level:

$$S_1 + S_1 \rightarrow S_n^* + S_0 \tag{2.2}$$

where S stands for singlet and the subscripts indicate the excited state [79]. This process is referred to as quenching since the amount of scintillation produced is reduced.

In the triplet-triplet annihilation (TTA) process shown in Eq. 2.3, two triplet states interact and create a ground singlet state and an excited singlet state:

$$T_1 + T_1 \rightarrow S_1 + S_0 \tag{2.3}$$

where T stands for triplet. The amount of light produced through this process is also reduced. On average, both SIQ and TTA are slower than fluorescence.

The interplay between the creation, intersystem crossing, quenching, and annihilation of excited π-orbitals is what enables PSD. As discussed in [76, 79], the rate

of SIQ and TTA is dependent on the density of singlet and triplet excited states. Energy deposition per unit length, $\frac{dE}{dx}$, and consequently the density of excited states is dependent on the recoiling particle, its ionization, and kinetic energy. Thus, the proportion of SIQ and TTA is different for gamma rays and fast neutrons since gamma rays will liberate electrons and fast neutrons liberate nuclei. Since SIQ and TTA are slower than fluorescence, the pulse created from a neutron interaction has more light later in the pulse than a gamma-ray event. We exploit this difference to classify pulses as gamma-ray or fast neutron induced as described in Sec. 2.1.2. Before we discuss PSD, we must first cover energy calibration (Sec. 2.1.2) and timing (Sec. 2.1.2) which are used in PSD.

Energy Calibration

In the context of organic scintillators where photopeaks are extremely rare, energy calibration is often done using the Compton edge. Fig. 2.3 shows a pulse integral spectrum[1] of Cs-137 measured by the stilbene detector. We define the Compton edge at 85% of the peak value [80].

[1]We use a pulse integral spectrum instead of a pulse height spectrum since the total energy deposited in the interaction is spread out over the pulse. No shaper is used to accumulate the pulse before digitizing.

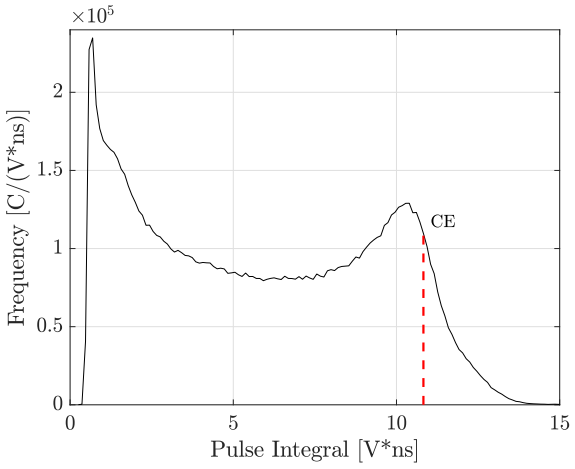

Figure 2.3: Pulse integral spectrum of Cs-137 on the stilbene detector. The red dashed line is the Compton edge defined at 85% of the peak value.

Fig. 2.4 shows a light output calibration curve for the stilbene detector. A linear calibration curve for gamma rays is appropriate, and thus light output in units of keVee is equivalent to energy deposited in units of keV for gamma rays, but for neutron interactions, the curve is expected to be non-linear. In this dissertation, we do not need fast-neutron energy calibrations since we never use the absolute energy of the neutron in image reconstruction.

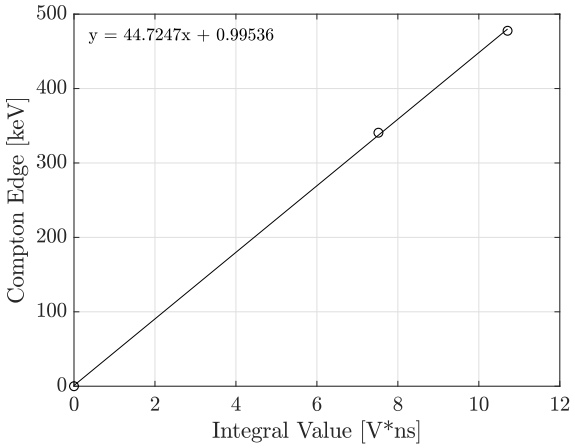

Figure 2.4: Stilbene calibration curve using the 662 keV line from Cs-137 and the 511 keV line from Na-22.

Timing Resolution and Dead Time

Although c-TEI depends on timing information to reconstruct images, the resolution needed is on the order of ms, whereas stilbene can have timing resolution better than 0.5 ns [81]. We use a constant fraction discrimination method with a threshold of 0.5 (arbitrarily selected) to find the start time of pulses [71]. Since stilbene is a fast scintillator, collecting overlapping pulses in the same acquisition window is generally not a concern until the count rate is above tens of thousands of counts per second. Throughout the experiments in this dissertation, the count rate in the stilbene detector never exceeded 5000 C/s. Given a window of 400ns, the probability of an overlapping pulse is 0.2%[2].

Pulse Shape Discrimination

The time-dependent difference in light emission between fast neutron and gamma-ray interactions can be used to classify pulses as neutron or gamma-ray induced. Below, we first introduce the tail-to-total charge comparison method to calculate the PSD parameter and then we detail how one can use that information is used to classify pulses.

For reference, Fig. 2.5 and 2.6 show expected pulses from fast neutrons and gamma rays for the same pulse height. Fast neutron pulses emit more of the light later in the pulse, often referred to as the tail, relative to the total light emitted.

[2]Given a detection has triggered data acquisition, the probability of there being more than one pulse in that acquisition window is one minus the probability of there being no pulses in the acquisition window. This analysis assumes each disintegration from the source only emits one particle.

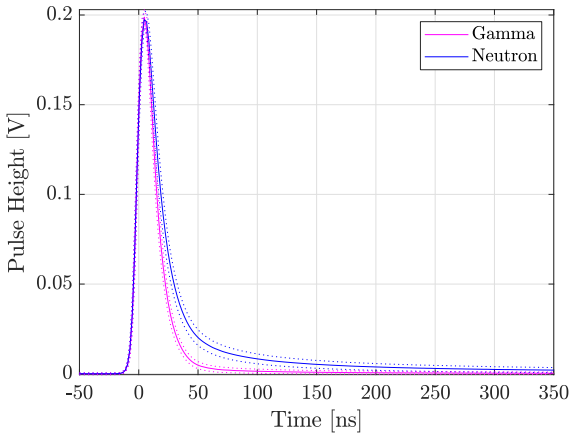

Figure 2.5: Expected pulse from a gamma-ray and neutron interaction. Dashed lines represent 68% of the data.

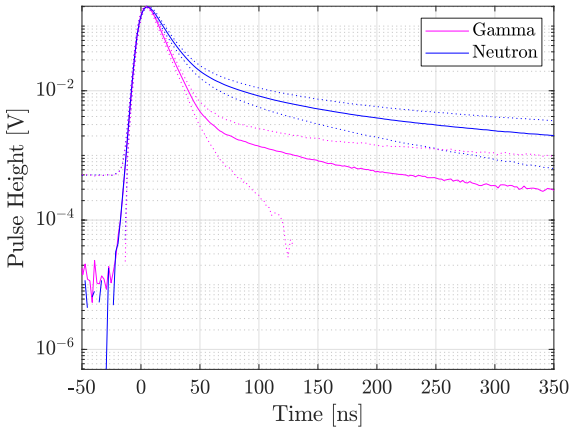

Figure 2.6: Expected pulse from a gamma-ray and neutron interaction. Dashed lines represent 68% of the data. Note the log scale.

There are many different PSD methods [82–87], we use tail-to-total charge comparison method. Eq. 2.4 defines the PSD parameter, s,

$$s = \frac{\sum_{i=i_{\text{tail,start}}}^{N} p[i]}{\sum_{i=i_{\text{total,start}}}^{N} p[i]} \tag{2.4}$$

where $i_{\text{tail,start}}$ is the start time of the tail integral, $i_{\text{total,start}}$ is the start time of the total integral, N is the total number of samples, and $p[i]$ is the pulse value at the ith sample. For simplicity, we use the same end times for both the tail and the total regions thus only the tail start time must be optimized for effective PSD. Fig. 2.7

shows a PSD plot for a Cf-252 source shielded by 5.08 cm of lead. The pulses with higher PSD parameters correspond to neutrons and the others to gamma rays.

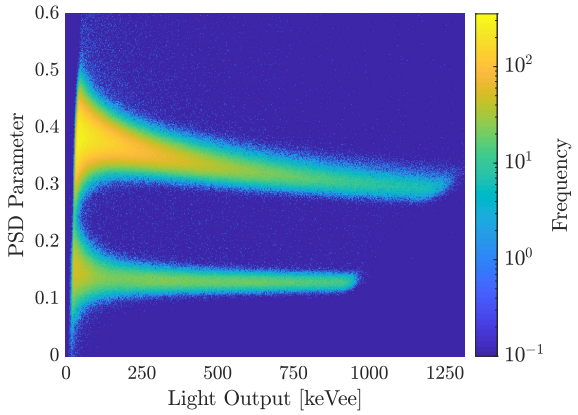

Figure 2.7: PSD plot of a Cf-252 source shielded by 5.08 cm of lead measured with stilbene. The total start time is 20 ns before the start time of the pulse and the tail start time is 30 ns after the start time. The tail and total end time was set at 350 ns after the start time.

Note that in Fig. 2.7, PSD is easier for higher energy pulses. Thus, it is best to optimize the tail start time to give good discrimination for low energy pulses. Fig. 2.8 shows a vertical slice of Fig. 2.7 at 40-45 keVee.

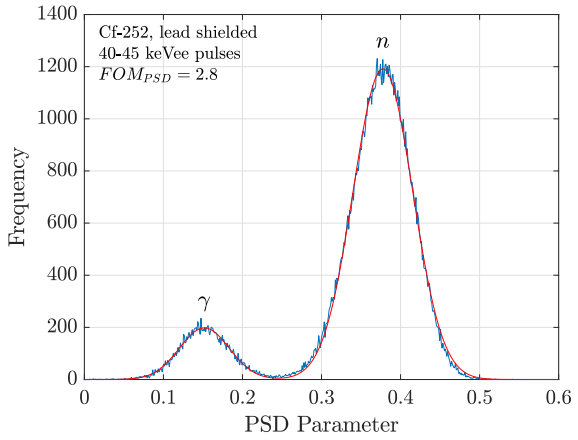

Figure 2.8: 40-45 keVee vertical slice from Fig. 2.7. Double Gaussian fits (Eq. 2.5) are shown in red.

At low pulse energies, the gamma-ray and neutron distributions overlap. We use a double Gaussian to fit Fig. 2.8 and then use the fitted parameters to calculate a

figure-of-merit (FOM) to quantify the level of overlap between the two distributions. The double Gaussian fit is defined as

$$
\begin{aligned}
f_{\gamma+n}(s) &= f_{\gamma}(s) + f_{n}(s) \\
f_{\gamma}(s) &= \frac{A_{\gamma}}{\sigma_{\gamma}\sqrt{2\pi}} \exp\left(-\frac{(s-\mu_{\gamma})^2}{2\sigma_{\gamma}^2}\right) \\
f_{n}(s) &= \frac{A_{n}}{\sigma_{n}\sqrt{2\pi}} \exp\left(-\frac{(s-\mu_{n})^2}{2\sigma_{n}^2}\right)
\end{aligned}
\tag{2.5}
$$

where $f_{\gamma+n}(s)$ is the double Gaussian distribution, the subscript γ stands for gamma ray, the subscript n stands for fast neutron, A is the amplitude, μ is the mean, and σ is the standard deviation. We define the FOM for PSD as

$$
\mathrm{FOM}_{\mathrm{PSD}} = \frac{\mu_n - \mu_{\gamma}}{\left(\mathrm{FWHM}_n + \mathrm{FWHM}_{\gamma}\right)/2} \tag{2.6}
$$

where $\mathrm{FOM}_{\mathrm{PSD}}$ is PSD figure-of-merit.

$\mathrm{FOM}_{\mathrm{PSD}}$ should be optimized to provide the largest value and therefore the least overlap. For this stilbene detector, the tail start time was set to 30 ns after the start time of the pulse and the total start time was set to 20 ns before the start time. The tail and total end time was set at 350 ns after the start time.

To classify pulses as fast neutron or gamma-ray induced, we use a Bayesian method [88]. The method has two stages. In stage one, high statistics data are used to characterize the distribution of fast neutron and gamma-ray PSD parameter values (s) as a function of energy. In stage two, those distributions are leveraged to estimate the probability of the pulse being a neutron or a gamma ray on a per pulse basis. The first stage is summarized below:

1. Collect pulses from a dual-particle source such as Cf-252.

2. Create a PSD plot similar to Fig. 2.7.

3. For each energy slice of the PSD plot, fit a double Gaussian to the joint neutron and gamma-ray distribution, similar to Fig. 2.8.

4. Save these Gaussian fits.

To estimate the posterior probability of each pulse being induced by a neutron or a gamma ray, the following two equations are used:

$$\begin{aligned} P(\gamma|s) &= \frac{f_\gamma(s)R_{\gamma/n}}{f_\gamma(s)R_{\gamma/n} + f_n(s)} \\ P(n|s) &= \frac{f_n(s)R_{\gamma/n}}{f_n(s)R_{\gamma/n} + f_n(s)} \end{aligned} \tag{2.7}$$

where $P(n|s)$ is the posterior probability of a pulse being caused by a fast neutron given the PSD parameter is s, $f_n(s)$ is the neutron Gaussian fit from stage one evaluated at s and $R_{\gamma/n}$ is the ratio of gamma-ray to neutrons for this light output bin. Since $R_{\gamma/n}$ is not known a priori, it must be iteratively estimated using the measurement as follows:

$$\begin{aligned} N_\gamma &= \sum_{s\in E_i} P(\gamma|s) \\ N_n &= \sum_{s\in E_i} P(n|s) \\ R_{\gamma/n} &= \frac{N_\gamma}{N_n} \end{aligned} \tag{2.8}$$

$R_{\gamma/n}$ is initialized as 1 and Eq. 2.7 and 2.8 are evaluated iteratively. Once the relative change of $R_{\gamma/n}$ from one iteration to the next falls below 1%, the process is terminated. Fig. 2.9 shows a cleaned PSD plot (see Sec. 2.1.4) with only 99.9999% probable neutron or gamma-ray pulses.

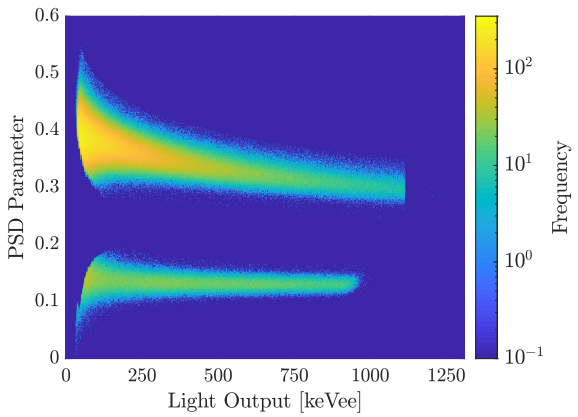

Figure 2.9: Cleaned PSD plot of a lead shielded Cf-252 source from stilbene. Only 99.9999% probable neutrons or gamma rays shown.

Anisotropy

Stilbene's performance in terms of light output, PSD, and timing are dependent on the trajectory of the charged particle with respect to the crystal planes. Recent measurements by Schuster et al. [89] and Weldon et al. [90] show that the light output can vary by up to 30%[3].

With respect to a stationary c-TEI system imaging a stationary source, the anisotropic response of stilbene would have practically no impact on the performance of the imaging system in terms of angular resolution, but the anisotropic response does result in a nonuniform sensitivity.

Nonetheless, all of the work here assumes that the anisotropy of stilbene is negligible.

2.1.3 CLLBC

$Cs_2LiLa(Br, Cl)_6$ (CLLBC) is an inorganic scintillator from the elpasolite family which has attracted attention due to its high light output, good energy resolution as a scintillator, and multi-particle detection capability [74, 92, 93]. CLLBC can detect

[3]This anisotropic response has also been used to create an imaging system [91].

gamma-rays and both thermal and fast neutrons via $^{6}\mathrm{Li}(n,\alpha)^{3}\mathrm{T}$ and $^{35}\mathrm{Cl}(n,p)^{35}\mathrm{S}$ reactions respectively. Unlike stilbene, CLLBC is slow and high energy pulses will last multiple μs.

We use a 1 inch CLLBC crystal coupled to a R14095-100 SEL PMT.

Energy Calibration

Fig. 2.10 shows a typical pulse integral spectrum of Cs-137 on the CLLBC detector and Fig. 2.11 shows the energy calibration. We use the integral of the pulse rather than its amplitude to measure energy since the pulse is not shaped. At 662 keV, the energy resolution is 3.7%. as opposed to the 3.3% reported by the manufacturer[4]. This difference may be the result of our shorter collection time and the lack of pulse shaping with a shaping amplifier.

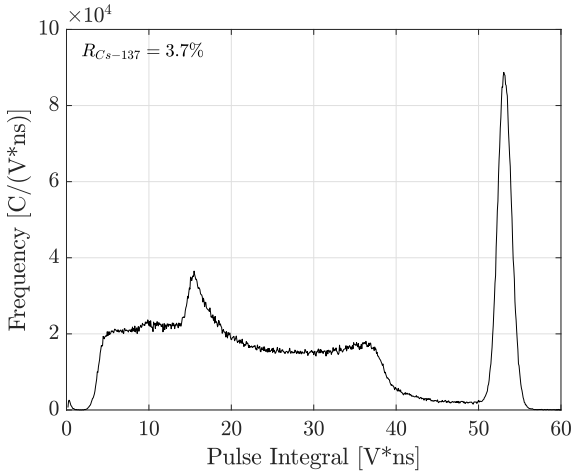

Figure 2.10: Pulse integral spectrum of Cs-137 on the CLLBC detector.

[4]CLLBC can achieve energy resolution down to 2.9% [74], but for this crystal the manufacturer reported 3.3%.

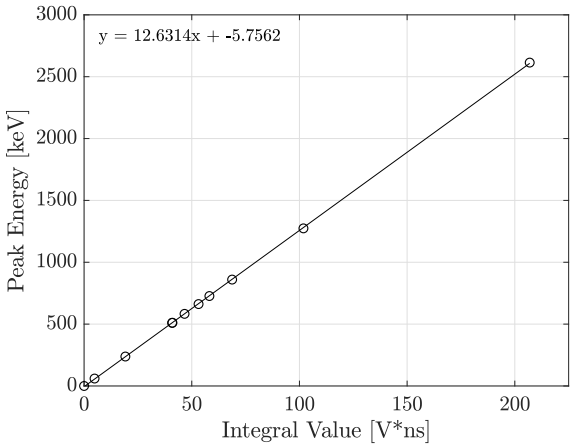

Figure 2.11: CLLBC linear calibration curve.

Timing Resolution and Dead Time

The timing resolution of CLLBC is much better than necessary for c-TEI. Even though CLLBC pulses are much longer than stilbene pulses, overlapping pulses are still not a concern unless the count rate is well above thousands of counts per second. Throughout the experiments in this dissertation, the count rate in the CLLBC detector never exceeded 2500 C/s. Given a window of 3200ns, the probability of an overlapping pulse is 0.8%[5].

Pulse Shape Discrimination

Discrimination between neutron and gamma-ray interactions is also possible in CLLBC. The $^{6}\mathrm{Li}(n,\alpha)^{3}\mathrm{T}$ reaction deposits 4.78 MeV in the crystal resulting in a $\sim$3.1 MeVee pulse. By pulse height alone, one can implement effective PSD, but the shape of the pulse also changes. Similar to Sec. 2.1.2, we use the tail-to-total method to create a PSD plot and separate thermal neutron interactions. The tail start time was set to 300 ns after the start of the pulse and the total start time was set to 20

[5]Given a detection has triggered data acquisition, the probability of there being more than one pulse in that acquisition window is one minus the probability of there being no pulses in the acquisition window. This analysis assumes each disintegration from the source only emits one particle.

ns before the start of the pulse. The tail and total end time was 3000 ns after the start time of the pulse. A Bayesian method was not implemented to classify CLLBC pulses. Fig. 2.12 and 2.13 show expected neutron pulses and gamma-ray pulses of the same magnitude and Fig. 2.14 is the PSD plot from a Cf-252 source shielded by 5.08 cm of lead. The island of counts at ∼3 MeV are thermal neutrons. The pulses with greater light output but a similar PSD parameter may be fast neutrons although we have not confirmed this for CLLBC [94].

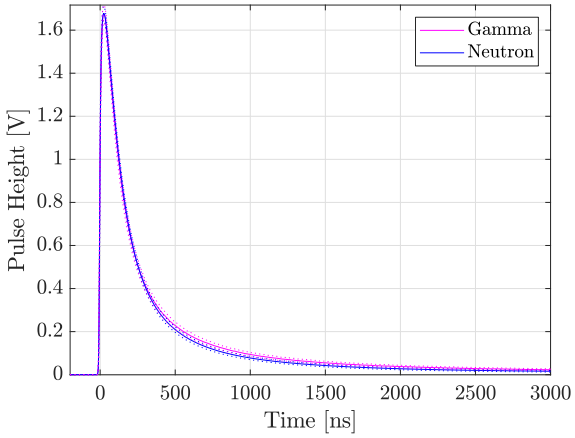

Figure 2.12: Expected pulse from a gamma-ray and neutron interaction. Dashed lines represent 68% of the data.

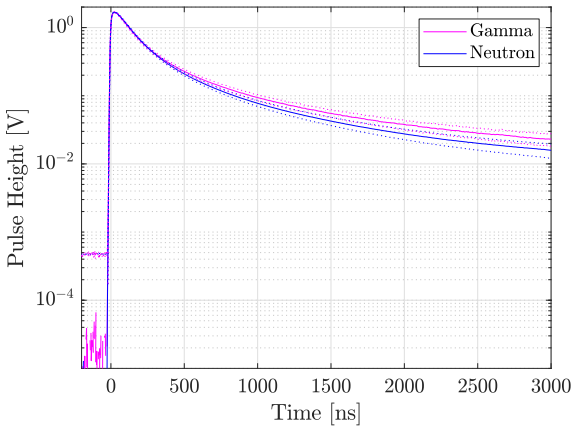

Figure 2.13: Expected pulse from a gamma-ray and neutron interaction. Dashed lines represent 68% of the data.

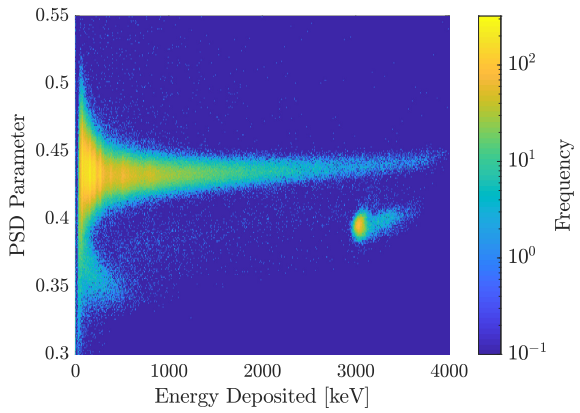

Figure 2.14: PSD plot of a Cf0-252 source shielded by 5.08 cm of lead. The island of counts at ∼3 MeV are thermal neutrons undergoing $^6\mathrm{Li}(n,\alpha)^3\mathrm{T}$ reaction.

2.1.4 Overview of Pulse Processing

The steps below outline the pulse processing procedure:

1. Baseline correction: For each pulse, the baseline is estimated using the first 32 samples. Then the pulse is baseline corrected and inverted.

2. Find start time: The start time for each pulse is found using the constant fraction discrimination technique with the cutoff set at 0.5 of the pulse height.

3. Units conversion: Using the calibrations in Fig. 2.4 and Fig. 2.11 for stilbene and CLLBC respectively, the pulse is converted from V·ns to keVee.

4. Find PSD parameter: The PSD parameter value is calculated for each pulse using the tail-to-total charge comparison method (refer to Sec. 2.1.2 and Sec. 2.1.3). For stilbene, the total start time is 20 ns before the pulse start time, the tail start time is 30 ns after the pulse start time, and the tail and total end time is 350 ns after the start of the pulse. For CLLBC, the total start time is 20 ns before the start time, the tail start time is 300 ns after the start time, and the tail and total end time is 3000 ns after the start time.

5. Classify pulses: For stilbene, we use the Bayesian method described in Sec. 2.1.2 to give each pulse a probability of being a fast neutron or a gamma-ray. Pulses with >99.9999% probability of being a neutron are classified as such, and the same for gamma-rays. For CLLBC, any pulses above 2.9 MeV with a PSD parameter below 0.42 are classified as thermal neutrons.

Pulses are cleaned at various times in the procedure detailed above. To summarize, we remove any pulses that have

- a maximum above the dynamic range of the digitizer,
- a maximum below zero,
- an integral below zero,
- a baseline that is 6 sigma outside of the mean baseline,
- a start time that is 6 sigma outside of the mean start time,
- a PSD parameter value below 0 or greater than 1, or
- a PSD parameter value that is 3 sigma outside of the mean for either neutrons and gamma-rays at that energy.

2.2 Coded Aperture Imaging

Occlusion-based imaging methods block incoming radiation from parts of the field-of-view (FOV) and record the resulting distribution of counts using some detector system. If the object used to block the incoming radiation, commonly called a mask, is appropriately designed, the radiation shadow it creates will be different for each possible source position. Thus, we can locate a source by utilizing the

recorded distribution of counts and the expected distribution of counts. The simplest occlusion-based system is the pinhole camera shown in Fig. 2.15.

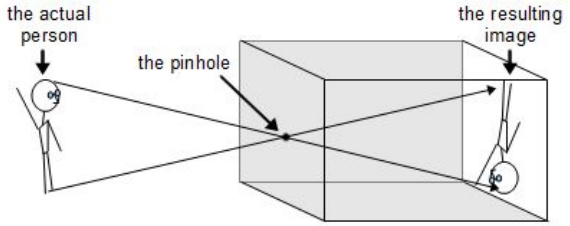

Figure 2.15: The basic pinhole camera. The detector array can only detect particles that travel through the pinhole.

In an ideal pinhole camera, the mask is entirely opaque to radiation and any particles that reach the detector must travel through a small pinhole such that if the detector observes a detection, the particle must have come from a restricted region in the source space. Traditionally, the pinhole camera is made using a position-sensitive detector, but one can also use a non-position-sensitive detector and a moving pinhole to create an image. For example, Fig. 2.16 shows a c-TEI version of a 1D pinhole camera. The count rate in the detector increases when the pinhole is on the line-of-sight between the detector and the source.

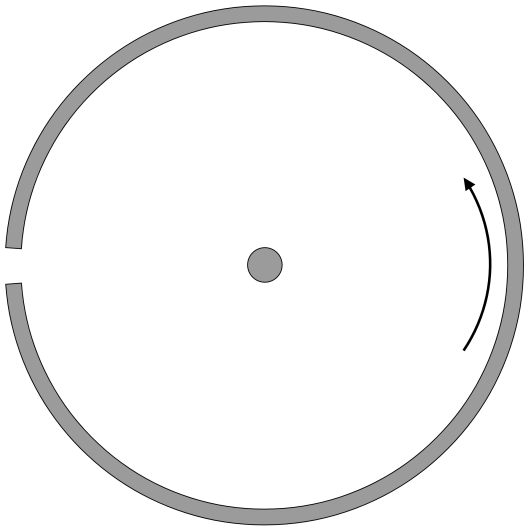

Figure 2.16: c-TEI version of the 1D pinhole. Original reference unknown.

In both case, because the pinhole has finite size, the object is blurred, as shown in Fig. 2.17. Making the pinhole smaller reduces the blur but also reduces the flux of particles. Thus, there is a trade-off between angular resolution and sensitivity.

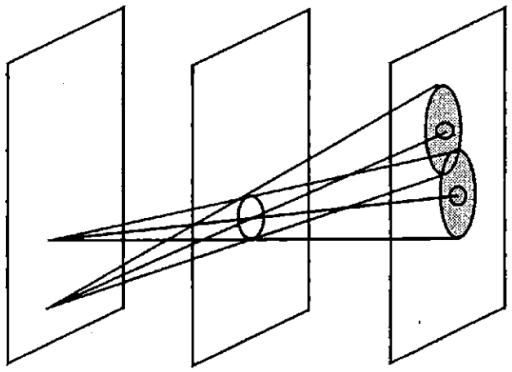

Figure 2.17: Diagram showing the blur resulting from the large pinhole. [41]

One way to recover some of the lost sensitivity is to introduce multiple pinholes in the mask. This will lead to an overlapping pattern in the detection space which destroys the approximate one-to-one relationship of a pinhole camera and reduces the selectivity[6] of the imaging system. In exchange, multiple pinholes increase the number of counts observed, thereby improving the signal-to-noise ratio (SNR). A mask with multiple pinholes is known as a coded aperture.

For a SCA system, a stationary mask spatially encodes the source distribution onto a position-sensitive detector whereas in c-TEI, a moving mask temporally encodes the source distribution onto a detector which may be non-position sensitive. As discussed in [38], under a set of ideal coded aperture assumptions, the two are methods are equivalent.

[6]Selectivity is the ability to distinguish and accurately reconstruct many sources in the field of view [30]

2.2.1 Ideal Coded Aperture

Fig. 2.18 is a classic schematic of image reconstruction with a SCA system.

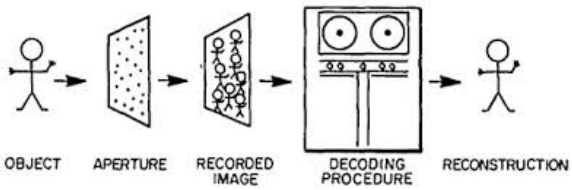

Figure 2.18: A graphical depiction of the coded aperture image reconstruction process.[7] Reproduced from [95]

To enable imaging, the mask must be designed such that each source pixel in the image space creates a unique shadow on the detector. For example, consider the mask in Fig. 2.19. Each open mask element is 90° apart and thus the observed responses of any sources that are 90° apart, or a multiple thereof, are the same. Thus, the mask in Fig. 2.19 would be a poor choice for imaging applications that require the full FOV.

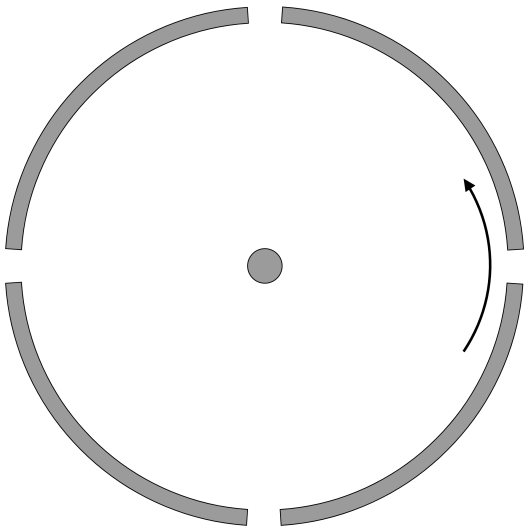

Figure 2.19: Example of a poor mask design.

One can verify that a mask is good for imaging by ensuring that the periodic

[7]Note that each projection of the object onto the recorded image should be flipped over both axes in Fig. 2.18.

auto-correlation of the mask is the Kronecker delta function (δ) riding on a baseline. There are a number of different mask patterns that meet or approximately meet this requirement. In general, one can use cyclic difference sets[8] to make such patterns; in this dissertation, we use uniformly redundant arrays (URAs) [45]. URAs are convenient as they have flat sidelobes (i.e. autocorrelation is approximately a delta function), have 50% open fraction, and are easy to construct [95]. Refer to [41, 45] for a deeper discussion on coded aperture families.

In coded aperture, the observed response in the detector space can be described as linear shift-invariant (LSI). Linear means that the response for any source distribution can be modelled as the superposition of point responses and shift-invariant (SI) means the point response does not change from one source pixel to the next besides a phase shift in the response. We use convolutions to describe a LSI system:

$$\boldsymbol{y} = \boldsymbol{x} \circledast \boldsymbol{m}_b \tag{2.9}$$

where $\boldsymbol{y}$ is the expected observation vector, $\boldsymbol{x}$ is the source distribution, and $\boldsymbol{m}_b$ is the binary mask. The symbol $\circledast$ is the periodic convolution defined as:

$$c[n] = a[n] \circledast b[n] = \sum_{n'=1}^{N} b[n']a[n - n'] \tag{2.10}$$

Herein, Eq. 2.9 is referred to as the "ideal coded aperture model". The ideal coded aperture model is accurate for both SCA and c-TEI if the following assumptions are true:

[8] Imagine the set of integers from 0 to n $(0, 1, 2, \ldots, n)$ - we call this set a group. A cyclic difference set is a subset of the group $(a_1 = 0, a_2, \ldots a_I)$ such that there are exactly λ ways any non-zero element of the group can be represented by a modular difference of two elements of the subset $(a_i - a_j \mod n)$.

Table 2.1: Assumptions for the ideal coded aperture model.

	Ideal Coded Aperture
System	The system is LSI.
Sampling	All sources are at the center of their respective pixels.
	The mask pattern is sampled only once per element.
Source	All sources are in the far field such that magnification is negligible. A near field coded aperture model can be found in [42].
	All sources are in the fully-coded FOV.
	For c-TEI, all sources have long half-lives relative to the measurement time.
Mask	The mask is infinitely thin.
	The mask is perfectly opaque and absorbing - scatter from the mask is negligible.
	For SCA, the mask is mosaicked.
Detector	For SCA, the detector system is spatially uniform.
	For c-TEI, the detector performance is temporally constant.
	The detector is only absorbing meaning that particles can not scatter to other detector elements.
Background	There is no background.
Environment	Scatter from the environment is negligible.

In Eq. 2.9, the periodic convolution is used instead of a linear convolution because for a SCA, the mask is often mosaicked[9] allowing it to capture the entire mask pattern without using a larger detector array as shown in Fig. 2.20. In c-TEI, we use

[9]By mosaicked, we mean that the pattern is repeated in both dimensions.

cylindrical coordinates so the convolution is periodic.

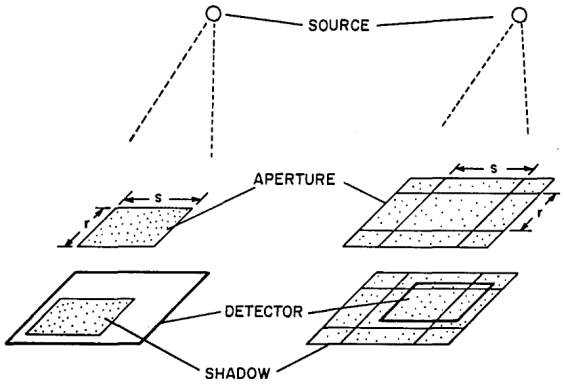

Figure 2.20: A comparison between a non-mosaicked and mosaicked mask for SCA. Note that the detector is smaller in the mosaicked case at the expense of a larger mask. Reproduced from [96].

In ideal coded aperture, reconstruction of $\boldsymbol{x}$ is done using an inverse filter, also known as the decoding array $\boldsymbol{g}$:.

$$\begin{aligned} \hat{\boldsymbol{x}}_g &= \boldsymbol{y} \otimes \boldsymbol{g} \\ &= (\boldsymbol{x} \circledast \boldsymbol{m}_b) \otimes \boldsymbol{g} \\ &= \boldsymbol{x} \circledast (\boldsymbol{m}_b \otimes \boldsymbol{g}) \\ &= \boldsymbol{x} \circledast \boldsymbol{p} \end{aligned} \tag{2.11}$$

where $\hat{\boldsymbol{x}}_g$ is the estimated source using the decoding array (g), $\boldsymbol{p}$ is the shift-invariant point spread function (PSF), and $\otimes$ is the periodic correlation operator. Thus, the reconstructed image $\hat{\boldsymbol{x}}_g$ is a convolution of the true image with the PSF. If one is using a URA pattern, the PSF is a delta function and thus the image is reconstructed exactly. If the PSF is not a delta function, then $\hat{\boldsymbol{x}}_g$ will be a superposition of each non-zero source pixel blurred by the PSF. For a URA, the inverse filter is very closely related to the mask itself [95].

In practice, the assumptions required for the ideal coded aperture model are not

true and alternative models are required[10]. As we relax assumptions, models for SCA and c-TEI begin to differ, although there are still many similarities. In Chap. III, we will introduce three other system response models and discuss the conditions under which they should be used.

Unfortunately, for the models in Chap. III, there rarely exist decoding arrays, such as $\boldsymbol{g}$, that will reconstruct the image exactly (PSF is not a delta function). Instead, we will have to use alternative methods to reconstruct the image. The reconstruction methods commonly used in the field are discussed in the following section.

2.3 Image Reconstruction

Once we have selected an imaging model, we can use the model to reconstruct an image. Many imaging models can be described as

$$\boldsymbol{y} = A\boldsymbol{x} \tag{2.12}$$

where A is the system response. The process of taking the source image, $\boldsymbol{x}$, and generating the expected observations, $\boldsymbol{y}$, is commonly called forward projection.

Although not the only definition, in this dissertation, each element $A[i, j]$ is proportional to the probability of detecting an event in observation bin i given there was an emission from source bin j. Notice that Eq. 2.12 allows for shift-variant PSF. If the response of each column was merely a circularly shifted version of the first column, SI, then $A\boldsymbol{x}$ could be written as $\boldsymbol{a} \circledast \boldsymbol{x}$ where $\boldsymbol{a}$ is the first column of A.

Ideally, one can find $\boldsymbol{x}$ via the inverse filter, such as the decoding array ($\boldsymbol{g}$) from Eq. 2.11, or inverting A, but more often than not, A is not invertible. Even if it is invertible, A^{-1} is often ill-posed meaning that small changes in $\boldsymbol{y}$ can lead to large

[10]For more on coded aperture and other occlusion based imaging methods, see [5, 21–25, 28, 32, 36–38, 42–45, 63, 64, 96–109].

changes in $\boldsymbol{x}$. Fig. 2.21 shows a graphical depiction of ill-posedness.

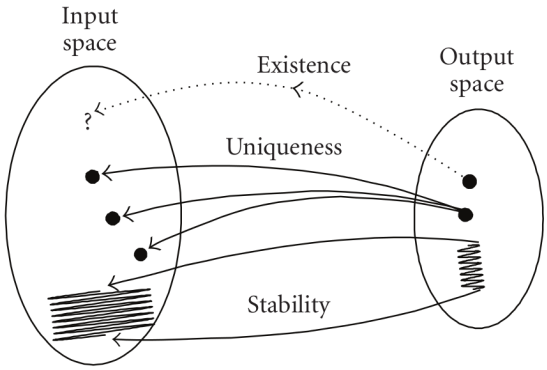

Figure 2.21: Graphical depiction of ill-posedness. Looking at "stability", small changes in the output space result in large differences in the input space. This makes parameter estimation more challenging particularly in the presence of noise. Reproduced from [110].

There are many different methods to reconstruct $\boldsymbol{x}$ without A^{-1}. In Sec. 2.3.1 and 2.3.2, we discuss two commonly used analytical reconstruction methods: simple back-projection and filtered back-projection. Intrinsically, these methods do not consider the statistical nature of the measurements and thus in low count scenarios, the reconstructions are often noisy and biased. This motivates Sec. 2.3.3 where we discuss statistical image reconstruction and specifically focus on maximum likelihood expectation maximization which is widely used in both medical imaging and nuclear engineering.[11] In the sections below, we will show sample images reconstructed using each method. We use the offset detector model (Sec. 3.3) as the system response and experimental data from a Cf-252 source at $(90\text{ cm}, 178°)$. Data was collected using the MATADOR system with the detector at the center of the mask.

2.3.1 Simple Back Projection

Simple back-projection (SBP) is one of the simplest and fastest methods to

[11]Note that statistical image reconstruction or iterative methods in general are much slower than analytical methods.

reconstruct an image but it often suffers from a low contrast-to-noise ratio (CNR) and a blurred reconstruction. For the noiseless case:

$$\hat{\boldsymbol{x}}_{\text{SBP}} = A^T \boldsymbol{y} = A^T A \boldsymbol{x} = P \boldsymbol{x}. \tag{2.13}$$

where $\hat{\boldsymbol{x}}_{\text{SBP}}$ is the SBP estimate of $\boldsymbol{x}$ and P is the PSF in matrix form. If there are sensitivity differences in the system response[12], one may want to normalize the system response by the sensitivity for each source and then find the SBP image - we refer to this as the sensitivity-normalized SBP.

One can think of SBP as taking the measured counts in an observation bin i, scaling by the probability of detecting those counts if they were emitted from source bin j, and accumulating over all measurement bins. $A^T \boldsymbol{y}$ is usually referred to as back-projection. Fig. 2.23 is a SBP image of the experimental data shown in Fig. 2.22.

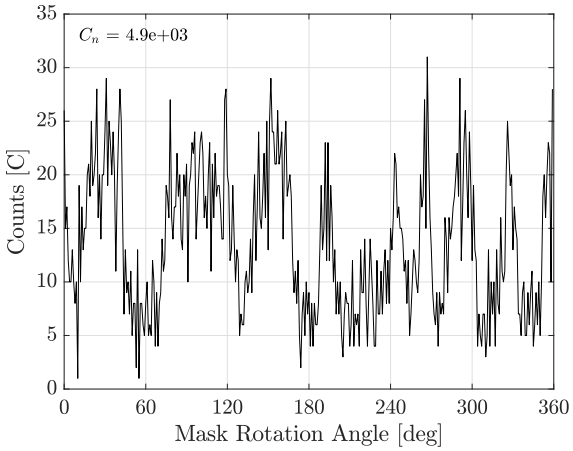

Figure 2.22: Experimental data from a neutron point source at $(90\text{ cm}, 178°)$.

[12]For example, if one is creating a system response with source bins at different radial distances from the detector, then there will be large sensitivity differences in the system response due to the inverse square law. In the definition of A used in this dissertation, each column of A is not normalized thus there are large sensitivity differences.

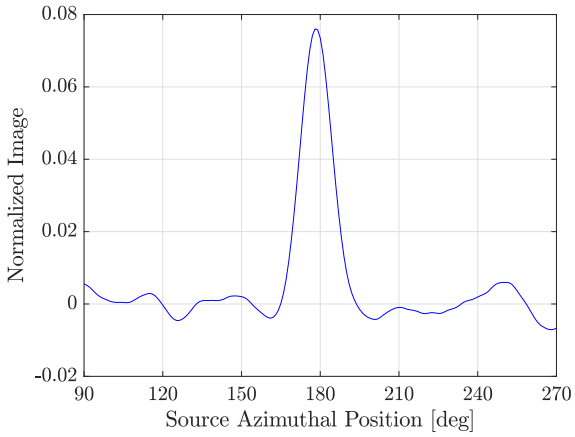

Figure 2.23: SBP reconstruction of Fig. 2.22. The image is background subtracted and normalized by the sum. Background is defined as the average intensity of image pixels that are at least 30° away from the max image pixel.

2.3.2 Filtered Back Projection

In SBP, the reconstructed image is the true source blurred by P. Filtered back-projection (FBP), attempts to remove the blur by inverting P. For the noiseless case:

$$\hat{\boldsymbol{x}}_{\text{FBP}} = P^{-1}\hat{\boldsymbol{x}}_{\text{SBP}} = \left(A^T A\right)^{-1} A^T \boldsymbol{y} = \left(A^T A\right)^{-1} A^T A\boldsymbol{x} = P^{-1}P\boldsymbol{x} = \boldsymbol{x} \tag{2.14}$$

where $\hat{\boldsymbol{x}}_{\text{FBP}}$ is the FBP estimate of $\boldsymbol{x}$. Thus, FBP can exactly recover $\boldsymbol{x}$ if there is no noise. One might recognize Eq. 2.14 as the ordinary least squares (OLS) solution to the problem:

$$\hat{\boldsymbol{x}}_{\text{OLS}} = \arg\min_{x} \ \|\boldsymbol{y} - A\boldsymbol{x}\|_2^2 \tag{2.15}$$

While Eq. 2.14 is applicable for any system described by Eq. 2.12, if the system is SI, one can use Fourier transforms to evaluate $\hat{\boldsymbol{x}}_{\text{FBP}}$. Understanding FBP in the Fourier space can provide some insight into why reconstructions suffer from high-frequency noise.

Convolution in Cartesian space is equivalent to multiplication in the Fourier domain. In Eq. 2.16 and 2.17, we describe SBP and FBP using this property for the

noiseless case and in Eq. 2.18 we consider the effect of additive noise. Starting with SBP:

$$\hat{\boldsymbol{x}}_{\text{SBP}} = P\boldsymbol{x} = \boldsymbol{p} \circledast \boldsymbol{x} = \mathcal{F}^{-1}\left(\mathbf{P} \odot \mathbf{X}\right) \tag{2.16}$$

where $\boldsymbol{p}$ is the first column of P, the non-italicized capital letters are in frequency space, and $\odot$ is the element-wise multiplication operator. Next, for FBP:

$$\begin{aligned}\hat{\boldsymbol{x}}_{\text{FBP}} =& P^{-1}\hat{\boldsymbol{x}}_{\text{SBP}} = \boldsymbol{p}_{\text{inv}} \circledast \hat{\boldsymbol{x}}_{\text{SBP}} = \mathcal{F}^{-1}\left(\mathbf{P}_{\text{inv}} \odot \hat{\mathbf{X}}_{\text{SBP}}\right) = \\ & \mathcal{F}^{-1}\left(\mathbf{P}_{\text{inv}} \odot \mathbf{P} \odot \mathbf{X}\right) = \mathcal{F}^{-1}\left(\frac{1}{\mathbf{P}} \odot \mathbf{P} \odot \mathbf{X}\right) = \mathcal{F}^{-1}\left(\mathbf{X}\right) = \boldsymbol{x}\end{aligned} \tag{2.17}$$

where the divisions are element-wise. Thus, we can see that the inverse filter, $\boldsymbol{p}_{\text{inv}}$, is simply the inverse Fourier transform of the element-wise reciprocal of the PSF ($\mathcal{F}^{-1}\left(1/\mathbf{P}\right)$).

If A is ill-posed and the measurements are noisy, FBP often results in images dominated by high-frequency noise. Assume the system is LSI and that the SBP image is corrupted by additive noise, then the FBP image is

$$\hat{\boldsymbol{x}}_{\text{FBP}} = \boldsymbol{p}_{\text{inv}} \circledast \left(\hat{\boldsymbol{x}}_{\text{SBP}} + \boldsymbol{n}\right) = \mathcal{F}^{-1}\left(\frac{1}{\mathbf{P}} \odot \left(\hat{\mathbf{X}}_{\text{SBP}} + \mathbf{N}\right)\right) = \mathcal{F}^{-1}\left(\mathbf{X} + \frac{\mathbf{N}}{\mathbf{P}}\right) \tag{2.18}$$

In frequency space, $\mathbf{P}$ often has very small values at high frequencies while white Gaussian noise, for example, has a constant response in frequency space. Thus when we divide (element-wise) $\mathbf{N}$ by $\mathbf{P}$, the high frequency components of the noise are greatly amplified. If we were to apply FBP to the experimental data in Fig. 2.22, the reconstruction would be entirely dominated by noise and no source would be discernible.

One way to combat this problem is through the use of the Wiener filter which is the linear minimum mean squared error (LMMSE) estimator. As opposed to the

FBP or OLS estimator which attempt to find a set of parameters that minimize the least squared error for a given sample of data, the Wiener filter attempts to find the parameters that minimize the expected squared error considering the probabilistic nature of the signal and noise. For use with the Wiener filter, we define $\mathbf{SNR}_{\text{Wiener}}$ as

$$\mathbf{SNR}_{\text{Wiener}} = \frac{\mathbb{E}\left[\|\mathbf{X}\|^2\right]}{\mathbb{E}\left[\|\mathbf{N}\|^2\right]} \tag{2.19}$$

where $\mathbb{E}\left[\|\mathbf{X}\|^2\right]$ and $\mathbb{E}\left[\|\mathbf{N}\|^2\right]$ are the expected power spectral densities of the true signal, $\boldsymbol{x}$, and the noise, $\boldsymbol{n}$, respectively. The Wiener filter is defined as

$$\mathbf{H}_{\text{W}} = \frac{\mathbf{B}^*}{\|\mathbf{B}\|^2 + \dfrac{1}{\mathbf{SNR}_{\text{Wiener}}}} \tag{2.20}$$

where $\mathbf{H}_{\text{W}}$ is the Wiener filter, $\mathbf{B}$ is the blurring filter[13], and * is the complex conjugate operator. Thus, the Wiener filtered image is

$$\hat{\boldsymbol{x}}_{\text{Wiener}} = \mathcal{F}^{-1}\left(\mathbf{H}_{\text{W}} \cdot \left(\hat{\mathbf{X}}_{\text{SBP}} + \mathbf{N}\right)\right) \tag{2.21}$$

where $\hat{\boldsymbol{x}}_{\text{Wiener}}$ is the Wiener filtered estimate of $\boldsymbol{x}$.

As shown in Eq. 2.20, the Wiener filter prevents small values of $\|\mathbf{B}\|^2$ from amplifying the noise by the addition of a $1/\mathbf{SNR}_{\text{Wiener}}$ term, often called a regularizer. One can apply the Wiener filter in the image space or the measurement space - for SCA or c-TEI the noise properties in the measurement space are better known thus we apply the Wiener filter directly to the noisy measurements. While the Wiener filter significantly improves images, it can only be applied to LSI systems.

Fig. 2.24 is a comparison between SBP and Wiener filter reconstruction of the noisy observation in Fig. 2.22. Notice that the Wiener filtered image has a narrower

[13]If one is applying the Wiener filter in the image space, then $\mathbf{B} = \mathbf{P}$ whereas if one is applying the Wiener filter in the measurement space, $\mathbf{B} = \mathbf{A} = \mathcal{F}(\boldsymbol{a})$, where $\boldsymbol{a}$ is the LSI system response.

peak but greater noise amplification. These two observations are inherently tied together. A narrow reconstruction requires high frequency components, but at high frequencies, the relative power spectral density of the noise with respect to the filter is larger than at low frequencies. Thus, noise is amplified.[14]

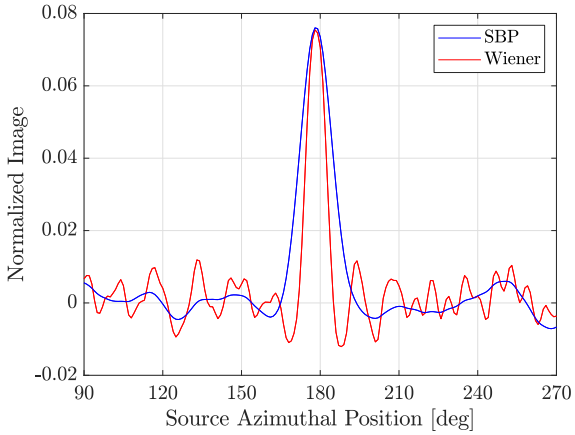

Figure 2.24: Reconstructions from SBP and the Wiener filter applied in the observation space. Normalized by sum. For the Wiener filter, the noise is assumed to be Gaussian with $\sigma^2 = \max(\boldsymbol{y})$.

The Wiener filter assumes that the signal is corrupted by additive noise and that the noise is independent from the signal. Although this assumption is not true for c-TEI systems or radiation imaging systems in general, the Wiener filter is often used in practice because it is fast, simple to implement, and can generate higher resolution images when compared to SBP. Below, we will consider other statistical reconstruction methods that take into account the Poissonian nature of c-TEI systems. These methods tend to produce images with greater SNR and angular resolution.

2.3.3 Statistical Image Reconstruction

This section provides an overview of statistical image reconstruction methods starting with Bayes' theorem and then describes maximum likelihood expectation

[14]This discussion on high-frequency noise in FBP will help us understand why maximum likelihood expectation maximization suffers from high frequency noise at high iterations.

maximization which is the reconstruction method used throughout the dissertation.

Bayes' theorem [111,112] describes the probability of an image given some measured data ($\boldsymbol{y}$):

$$p(\boldsymbol{x} \mid \boldsymbol{y}) = \frac{p(\boldsymbol{y} \mid \boldsymbol{x})p(\boldsymbol{x})}{p(\boldsymbol{y})} \tag{2.22}$$

where $p(\boldsymbol{x} \mid \boldsymbol{y})$ is the posterior distribution of $\boldsymbol{x}$ given $\boldsymbol{y}$, $p(\boldsymbol{y} \mid \boldsymbol{x})$ is the likelihood of $\boldsymbol{y}$ given $\boldsymbol{x}$, $p(\boldsymbol{x})$ is the prior distribution of $\boldsymbol{x}$, and $p(\boldsymbol{y})$ is the marginal distribution $\boldsymbol{y}$. $p(\boldsymbol{y})$ is constant as a function of $\boldsymbol{x}$ so it is typically ignored when estimating $\boldsymbol{x}$.

Conceptually, one starts with knowledge or prior information on how $\boldsymbol{x}$ is distributed and then updates that prior through Eq. 2.22 after making a measurement. In this way, the posterior takes into account both the user's prior knowledge on $\boldsymbol{x}$ through $p(\boldsymbol{x})$ and the probability of $\boldsymbol{x}$ generating the measured data through $p(\boldsymbol{y} \mid \boldsymbol{x})$. In practice, there are a number of challenges to overcome:

1. $\boldsymbol{x}$ usually has many parameters thus $p(\boldsymbol{x} \mid \boldsymbol{y})$ must be compressed through some metric, or in another sense, one still needs to estimate $\boldsymbol{x}$ from $p(\boldsymbol{x} \mid \boldsymbol{y})$.

2. Analytical solutions to Eq. 2.22 often do not exist, thus one must use numerical methods.

3. The user must make decisions on $p(\boldsymbol{x})$ which, if incorrect, can significantly bias the resulting distribution.

Two estimators are most often used to estimate $\boldsymbol{x}$ from $p(\boldsymbol{x} \mid \boldsymbol{y})$. One is the posterior mean (Eq. 2.23) which finds the average $\boldsymbol{x}$ and consequently minimizes the mean squared error:

$$\hat{\boldsymbol{x}}_{E[\boldsymbol{x}|\boldsymbol{y}]} = \int \boldsymbol{x} p(\boldsymbol{x} \mid \boldsymbol{y}) d\boldsymbol{x} \tag{2.23}$$

Solving Eq. 2.23 requires the evaluation of a multidimensional integral which can be very time consuming when $\boldsymbol{x}$ is large. One option is to use Markov chain Monte Carlo [113] to sample the the posterior distribution and estimate $\hat{\boldsymbol{x}}_{E[\boldsymbol{x}|\boldsymbol{y}]}$. Stochastic origin ensembles is an implementation that has been used for scatter cameras [114, 115].

The second estimator is the maximum a posteriori estimator (MAP) which finds the image with the greatest posterior probability:

$$\begin{aligned}\hat{\boldsymbol{x}}_{\text{MAP}} &= \arg\max_{\boldsymbol{x}} p(\boldsymbol{x} \mid \boldsymbol{y}) \\ &= \arg\max_{\boldsymbol{x}} \ell(\boldsymbol{y} \mid \boldsymbol{x}) + \ell(\boldsymbol{x}) \\ &= \arg\max_{\boldsymbol{x}} \ell(\boldsymbol{y} \mid \boldsymbol{x}) - \beta R(\boldsymbol{x})\end{aligned} \tag{2.24}$$

where $\ell(\boldsymbol{x}) = \ln(p(\boldsymbol{x}))$. In the literature, $\ell(\boldsymbol{y} \mid \boldsymbol{x})$ is often called the data-fit term, $R(\boldsymbol{x})$ (which replaces $\ln(p(\boldsymbol{x}))$) is called the regularizer, and β is a hyperparameter that controls the relative weight of the regularizer.

If one does not have any prior information for $\boldsymbol{x}$, one can set $\beta = 0$ or pick a uniform prior, $R(\boldsymbol{x}) = k$. In this case, the MAP solution collapses into the maximum likelihood (ML) solution. The ML solution only considers how well the forward projection of the image matches the measurements given some statistical model for $\boldsymbol{y}$. In a sense, the ML solution allows the data to dictate the solution without applying additional constraints on $\boldsymbol{x}$ besides those imposed by $\ell(\boldsymbol{y} \mid \boldsymbol{x})$.

To understand the value and risk of regularization, consider the example in Fig. 2.25. Since the system response is usually ill-posed, there are many potential images that fit the measurements well and thus the ML solution for noisy measurements of a scene may differ. Regularization can help reduce the difference between the two reconstructions. For example, notice in Fig. 2.25, that measurements 2 and 3

are only slightly different but their ML reconstructions lead to D and E which are very different in the image domain. On the other hand, if some prior knowledge is incorporated in the reconstruction, 2 and 3 reconstruct to F and G which are more similar reconstructions and are closer to the true image (T2).

In some cases, A may be under-determined in which case the solution is not unique. In this case, regularization can help constrain the set of solutions to those which are physically possible or to solutions that the user deems more likely to occur. For example, notice in Fig. 2.25 how measurement 1 can be created by both image A or B. In the ML case, there is no way to tell if 1 was caused by A or B, but in the regularized case, the reconstruction uniquely maps to C.

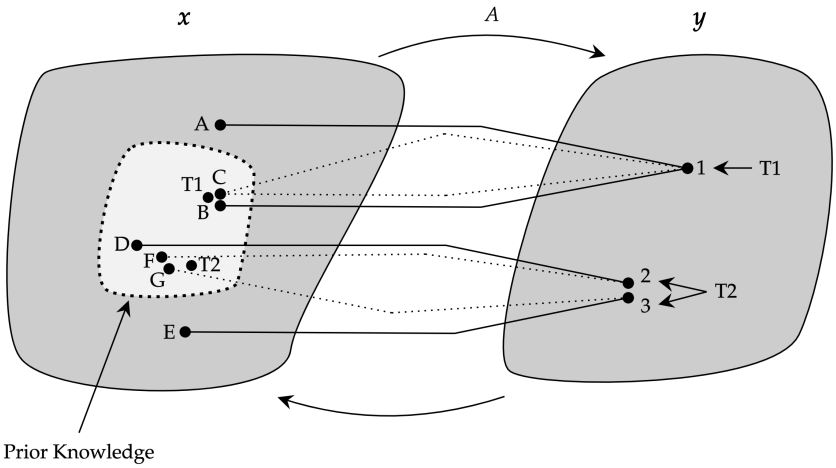

Figure 2.25: A graphical depiction of regularization. The solid lines represent the ML (non-regularized) reconstruction and the dotted lines represent a MAP (regularized) reconstruction.

There is a large and rapidly growing body of work on regularization and algorithms to efficiently reach the MAP solution. See [116, 117] for an overview and [118–120] for some implementations. For example, in source search problems, regularizers that enforce sparsity in the image are often appropriate since many tasks involve reconstructing point-like sources [121]. Sparsity-based regularizers place a higher

weight on $\boldsymbol{x}$ that only have a few non-zero elements and thus force the image to be sparse.

Although regularization is a powerful technique, it has some downsides. For example, if one is using a sparsity-based regularizer and the true image has many sources or an extended source, then the regularized reconstructed image may not reflect reality. Moreover, the optimal weighting of β is scenario and imaging-system specific which adds another layer of complexity [122, 123]. Thus in this dissertation, we do not use regularization and instead focus on ML. Nonetheless, it is important to understand regularization as an alternative to ML as it is often used in nuclear engineering and medical imaging.

For Poisson distributed data, the log-likelihood function is as follows

$$\begin{aligned} p(\boldsymbol{y} \mid \boldsymbol{x}) &= \prod_{i=1}^{I} \frac{\overline{y}_i^{y_i} e^{-\overline{y}_i}}{y_i!} \\ \ell(\boldsymbol{y} \mid \boldsymbol{x}) &= \sum_{i=1}^{I} \left(y_i \ln\left(\overline{y}_i\right) - \overline{y}_i - \ln\left(y_i!\right) \right) \\ \ell(\boldsymbol{y} \mid \boldsymbol{x}) &= \sum_{i=1}^{I} \left(y_i \ln\left(A\boldsymbol{x}\right) - A\boldsymbol{x} - \ln\left(y_i!\right) \right) \end{aligned} \tag{2.25}$$

where $\overline{\boldsymbol{y}}$ is the expected measurement, $\boldsymbol{y}$ is the experimental measurement, and the ML solution is

$$\begin{aligned} \hat{\boldsymbol{x}}_{\mathrm{ML}} &= \arg\min_{\boldsymbol{x}} \; -\ell(\boldsymbol{y} \mid \boldsymbol{x}) \\ &= \arg\min_{\boldsymbol{x}} \; \sum_{i=1}^{I} \left(-y_i \ln\left(A\boldsymbol{x}\right) + A\boldsymbol{x} + \ln\left(y_i!\right) \right) \\ &= \arg\min_{\boldsymbol{x}} \; \sum_{i=1}^{I} \left(-y_i \ln\left(A\boldsymbol{x}\right) + A\boldsymbol{x} \right) \end{aligned} \tag{2.26}$$

where the problem is usually cast as a minimization problem[15].

[15] We take the logarithm of $p(\boldsymbol{y} \mid \boldsymbol{x})$ so that the product of probabilities simplifies to a summation and the optimization problem becomes convex.

Usually, there is no closed analytical solution for $\hat{\boldsymbol{x}}_{\mathrm{ML}}$ and instead one must use an iterative algorithm. For small scale problems (<10 unknowns), we will use the fmincon function in Matlab to reach the ML solution. For large scale problems, we use maximum likelihood expectation maximization (MLEM) algorithm.

Maximum Likelihood Expectation Maximization

Maximum likelihood expectation maximization (MLEM) [16] is an iterative algorithm that finds the ML solution for a Poisson distributed process [132–134]. It is commonly used in both nuclear engineering and medical imaging because it is straight forward to implement, monotonically approaches the ML solution, and the resulting solution is non-negative. Unfortunately there are some disadvantages to using MLEM such as slow convergence and poor image quality at high iterations. Consequently, MLEM is often not run to convergence which results in reconstructions that are biased by the initial guess. Below we discuss each of these topics.

The MLEM update equation is

$$\hat{x}^{n+1}[j] = \frac{\hat{x}^{n}[j]}{s[j]} \sum_{i=1}^{I} A[i,j] \frac{y_i}{\sum_{j=1}^{J} A[i,j] x^{n}[j]} \tag{2.27}$$

where n indicates the nth iteration and $s[j] = \sum_{i=1}^{I} A[i,j]$ is known as the sensitivity of the system to a source at pixel j. It is important to note that $A[i,j]$ is proportional to the probability of detecting an event in observation bin i given there was an emission from source bin j.

Notice that the MLEM algorithm updates each element of $\hat{\boldsymbol{x}}^{n}$ independently. Thus, Eq. 2.27 can be recast in matrix form:

$$\hat{\boldsymbol{x}}^{n+1} = \frac{\hat{\boldsymbol{x}}^{n}}{\boldsymbol{s}} \odot A^{T} \frac{\boldsymbol{y}}{A\hat{\boldsymbol{x}}^{n}} \tag{2.28}$$

[16] There are many methods to derive the MLEM algorithm. The majorize-minimize based derivations seem to be the most clear. See [124–126] or [127–131].

where $\odot$ is element wise multiplication, the divisions are element wise, and $\boldsymbol{s}$ is the sensitivity vector where $s[j] = \sum_{i=1}^{I} A[i,j]$ for the jth source bin.

Since the ML solution does not depend on the choice of $\hat{\boldsymbol{x}}^0$, any non-negative initialization will work if MLEM is run to convergence. In practice, as the number of iterations increases, the image quality degrades as shown in Fig. 2.26. Thus, the user must decide how many iterations to run and how to choose $\hat{\boldsymbol{x}}^0$. Recall from the discussion in Sec. 2.20 that high frequency noise amplification is directly linked to higher resolution reconstructions[17]. As the number of iterations increases, the energy in the high frequency components increases. This leads to narrower reconstructions and noise amplification in the image.

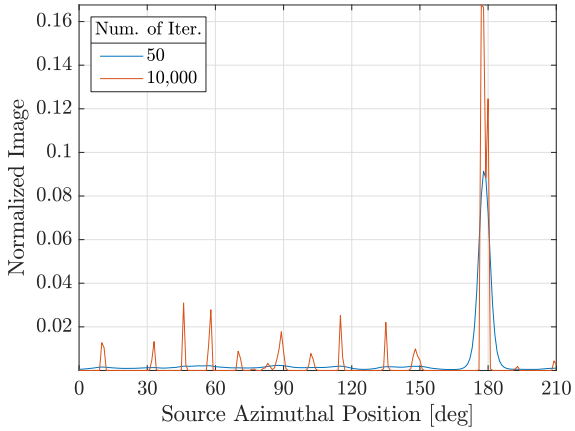

Figure 2.26: MLEM reconstructions for 50 and 10,000 iterations of Fig. 2.22.

There are a number of ways to combat this problem including heuristic stopping rules [135, 136], statistical stopping rules [137, 138], cross validation [139–141], sieves [142–144]; our preferred solution is to under-iterate as it is fastest and simplest. A rigorous stopping rule was not used but in general, MLEM is terminated when the normalized root mean squared error (NRMSE) of the observation vector relative to

[17] One can also think of this high frequency noise as a result of overfitting to noisy observations with an ill-posed system response. Model mismatch may also play a role.

the forward projection is nearly constant. NRMSE is defined as

$$\text{NRMSE} = \sqrt{\frac{\|\boldsymbol{y} - \overline{\boldsymbol{y}}\|_2^2}{\|\overline{\boldsymbol{y}}\|_2^2}} \tag{2.29}$$

where $\overline{\boldsymbol{y}}$ is the forward projection of the assumed image. In this context, $\overline{\boldsymbol{y}}$ would be the forward projection of the MLEM reconstruction at the current iteration. Fig. 2.27 shows the NRMSE as function of MLEM iteration. The star is the point where we determined the NRMSE was nearly constant.

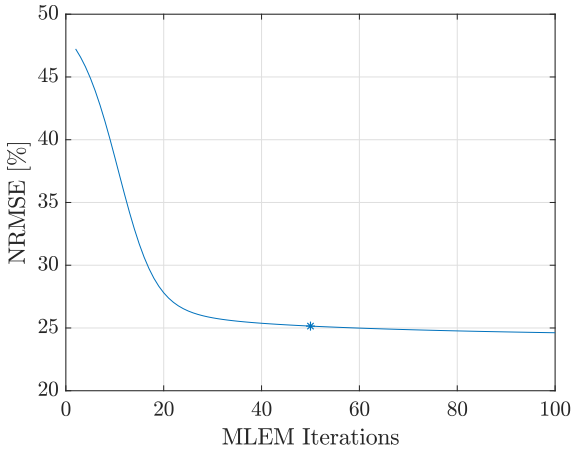

Figure 2.27: NRMSE of the observation vector as a function of MLEM iteration. Reconstruction of data in Fig. 2.22.

Generally speaking, there are some disadvantages with early termination:

1. Under-iterated images are biased by $\hat{\boldsymbol{x}}^0$.

2. Different system responses converge at different rates thus holding the number of iterations constant and comparing between MLEM reconstructions of two different systems is not a direct comparison.

3. Different parts of the image converge at different rates [145].

4. High frequency components in the image converge slower than low frequency components [146].

5. Convergence rates are source scene dependent thus termination criteria rarely work for all source scenes, count rates, and source-to-background ratio (S:B) ratios [147, 148].

6. Quantification is less accurate for under-iterated images.

Since the images in this dissertation are under-iterated, the solution will be biased by the initialization of $\hat{\boldsymbol{x}}$. All MLEM images in this dissertation are initialized as

$$\hat{\boldsymbol{x}}^0 = \frac{1}{\boldsymbol{s}} \tag{2.30}$$

where $\boldsymbol{s}$ is the sensitivity vector where $s[j] = \sum_{i=1}^{I} A[i,j]$ for the jth source bin.

Thus, each element of $\hat{\boldsymbol{x}}$ contributes the same number counts in the forward projection at the first iteration[18].

In spite of these challenges, under-iterated MLEM is widely used for image reconstruction because of its simplicity and performance relative to SBP. The alternative of running MLEM until convergence is not reasonable due to the computation time required, and, as we discussed earlier, regularization based methods have their own set of challenges including parameter optimization and complexity depending on the selected method. Thus, we will be using under-iterated MLEM reconstructions to evaluate the performance of MATADOR.

Below is an MLEM reconstruction after 50 iterations. Notice how both the Wiener filter and the MLEM reconstructions for the point sources are much narrower than the SBP reconstruction. Additionally, the noise suppression in the MLEM reconstruction is much better than the Wiener filter.

[18] One may also use a constant image or the SBP image is used as $\hat{\boldsymbol{x}}^0$.

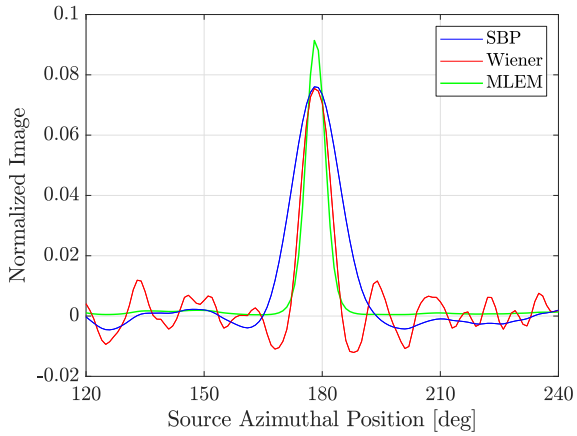

Figure 2.28: Reconstructions from SBP, Wiener filter, and MLEM terminated at 50 iterations, normalized by sum. For the Wiener filter, the noise is assumed to be Gaussian with $\sigma^2 = \max(\boldsymbol{y})$. For MLEM, the NRMSE of the observation vector is shown in Fig. 2.29.

2.4 Applied Analysis Methods and Metrics

The following sections describe analysis tools that are used throughout the dissertation.

2.4.1 Cramér-Rao Lower Bound

Cramér-Rao lower bound (CRLB) is the lower bound on the variance for all unbiased estimators of a deterministic parameter [149]. For example, say we are interested in estimating the background count rate. In this case, one may use some unbiased estimator such as the mean counts measured in a time interval. The variance in this estimator must be greater than or equal to the CRLB. In the context of source localization, the CRLB is the lowest variance on the source position when using any unbiased estimator. Before we introduce the CRLB, we first introduce some relevant variables and notation.

Let $\boldsymbol{\theta}$ be a vector of the parameters of interest. For example, if there is only one point source in the field, then there are four parameters of interest that must be

estimated: source intensity (α), source azimuthal position (ϕ), source radial position (r), and unmodulated intensity (b)[19]. Thus, $\boldsymbol{\theta} = [\alpha\ \phi\ r\ b]^T$ [20]. Additionally, let the gradient, $\nabla_{\boldsymbol{\theta}} f(\boldsymbol{\theta})$, and the Hessian matrix, $\nabla_{\boldsymbol{\theta}} \nabla_{\boldsymbol{\theta}}^T f(\boldsymbol{\theta})$, be

$$\begin{aligned}
\nabla_{\boldsymbol{\theta}} f(\boldsymbol{\theta}) &= \begin{bmatrix} \dfrac{\partial f}{\partial \theta_1} \cdots \dfrac{\partial f}{\partial \theta_N} \end{bmatrix} \\
\nabla_{\boldsymbol{\theta}} \nabla_{\boldsymbol{\theta}}^T f(\boldsymbol{\theta}) &= \begin{bmatrix} \dfrac{\partial^2 f}{\partial \theta_1^2} & \dfrac{\partial^2 f}{\partial \theta_1 \partial \theta_2} & \cdots & \dfrac{\partial^2 f}{\partial \theta_1 \partial \theta_N} \\ \dfrac{\partial^2 f}{\partial \theta_2 \partial \theta_1} & \dfrac{\partial^2 f}{\partial \theta_2^2} & & \dfrac{\partial^2 f}{\partial \theta_2 \partial \theta_N} \\ \vdots & & \ddots & \vdots \\ \dfrac{\partial^2 f}{\partial \theta_N \partial \theta_1} & \dfrac{\partial^2 f}{\partial \theta_N \partial \theta_2} & \cdots & \dfrac{\partial^2 f}{\partial \theta_N^2} \end{bmatrix}
\end{aligned} \tag{2.31}$$

where $\dfrac{\partial f}{\partial \theta_i}$ is the partial derivative of f with respect to θ_i.

Given these definitions, we introduce the Fisher information matrix (FIM):

$$I(\boldsymbol{\theta}) = -\mathbb{E}\left[\left(\nabla_{\boldsymbol{\theta}} \ln\left(p(\boldsymbol{y} \mid \boldsymbol{\theta}) \right) \right) \left(\nabla_{\boldsymbol{\theta}} \ln\left(p(\boldsymbol{y} \mid \boldsymbol{\theta}) \right) \right)^T \right] \tag{2.32}$$

where $I(\boldsymbol{\theta})$ is the FIM and the expectation is over $\boldsymbol{y}$. Through integration by parts, Eq. 2.32 can be rewritten as

$$I(\boldsymbol{\theta}) = -\mathbb{E}\left[\nabla_{\boldsymbol{\theta}} \nabla_{\boldsymbol{\theta}}^T \ln\left(p(\boldsymbol{y} \mid \boldsymbol{\theta}) \right) \right] \tag{2.33}$$

Finally, the CRLB is found by inverting the FIM:

$$\text{CRLB}(\boldsymbol{\theta}) = I(\boldsymbol{\theta})^{-1} \tag{2.34}$$

[19]Unmodulated intensity consists of natural background and source scatter from the mask, environment, and detector.

[20]To be clear, in the general image reconstruction problem, we are attempting to estimate the intensity of each source pixel in $\boldsymbol{x}$. For example, in the 1D reconstruction problem in this dissertation, there are 100s of source pixels or unknowns to estimate. For such inverse problems, we use methods such as SBP, FBP, or MLEM. When using the CRLB, we are usually trying to find a bound on a few parameters and thus $\boldsymbol{\theta}$ contains many fewer elements.

where $\boldsymbol{\theta}$ are the known or estimated values of the parameters of interest.

To gain some insight into the FIM and the CRLB, consider the two 1D Gaussian log-likelihood functions in Fig. 2.29. Since the blue log-likelihood function is sharper than the red one, it is easier to estimate the parameter value that maximizes the likelihood, $\hat{\mu}_{\mathrm{ML}}$, for the blue curve. From Eq. 2.33, the CRLB of $\hat{\boldsymbol{\theta}}_{\mathrm{ML}}$ is dependent on the second derivative of the log-likelihood - we can think of the second derivative as a measure of sharpness or curvature. The greater the second derivative, the easier it is to estimate the parameters of interest.

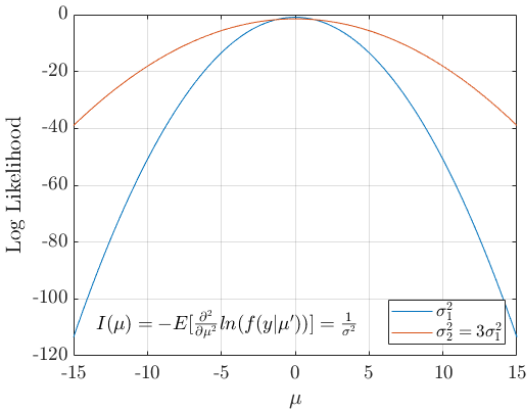

Figure 2.29: Log-likelihood functions of two Gaussian distributions with known variances.

Note that the maximum likelihood estimator is asymptotically unbiased and asymptotically efficient meaning that as the number of counts goes to infinity, the ML estimate of the parameters reaches the true values ($\hat{\boldsymbol{\theta}}_{\mathrm{ML}} \rightarrow \boldsymbol{\theta}$) and the covariance of the parameter vector reaches the CRLB ($\mathrm{cov}(\hat{\boldsymbol{\theta}}_{\mathrm{ML}}) \rightarrow I(\boldsymbol{\theta})^{-1}$). If $\boldsymbol{\theta}$ is unknown, we will use $\hat{\boldsymbol{\theta}}_{\mathrm{ML}}$ in Eq. 2.33.

We use the CRLB and the FIM for both Chap. VI and VII. In Chap. VI, we use the CRLB has a proxy for the angular resolution of an imaging system and in Chap. VII, we use the FIM to predict which potential system configurations of the

MATADOR system will lead to good detection performance.

2.4.2 Source Detection

This section provides a brief overview of source detection. For background, we first discuss the likelihood ratio test (LRT) and then discuss the generalized likelihood ratio test (GLRT). We use the GLRT extensively in Chap. VII.

The detection problem is often addressed using hypothesis testing where the user defines a set of hypotheses before collecting data and then utilizes a test statistic and corresponding thresholds for detection. In the binary case, the two hypotheses are referred to as the null ($\mathcal{H}_N$) and the alternative hypothesis ($\mathcal{H}_A$). Ideally, one would know the probability density functions (PDFs) for the measurements under each hypothesis and would use that information to design the test, but often this information is not known. For simple[21] hypothesis tests where the PDFs are entirely known, the LRT maximizes the probability of detection for a given probability of false alarm. The LRT is simply the likelihood of the measurements under the alternative hypothesis divided by the likelihood of the measurements under the null hypothesis. Here is an example:

$$\begin{aligned} \mathcal{H}_N &: \boldsymbol{\theta} = \boldsymbol{\theta}_N \\ \mathcal{H}_A &: \boldsymbol{\theta} = \boldsymbol{\theta}_A \end{aligned} \tag{2.35}$$

where $\boldsymbol{\theta}_N$ and $\boldsymbol{\theta}_A$ are the known parameters under the null and alternative hypotheses respectively.

The LRT is

$$\Lambda_{\text{LRT}} = \frac{p(\boldsymbol{y}|\mathcal{H}_A)}{p(\boldsymbol{y}|\mathcal{H}_N)} \underset{H_N}{\overset{H_A}{\gtrless}} \gamma_{\text{crit}} \tag{2.36}$$

[21]Here, simple refers to the fact that the PDFs under each hypothesis are known, as opposed to composite hypothesis testing where some unknown parameters must be estimated. In a simple hypothesis test, both the probability distribution and the underlying parameters are exactly known.

where Λ_{LRT} is the test statistic under the LRT and γ_{crit} is the threshold for detection. If Λ_{LRT} is less than γ_{crit}, then the test fails to reject the null hypothesis and if Λ_{LRT} is greater than γ_{crit}, then the test rejects the null hypothesis.

Let $\mathcal{T}$ be the test statistic, such as Λ_{LRT}. Then, as depicted in Fig. 2.30, we define the probability of detection (P_D) as

$$P_D = \int_{\gamma_{\text{crit}}}^{\infty} f(\mathcal{T}(\boldsymbol{y}), \mathcal{H}_A) d\mathcal{T} \tag{2.37}$$

where $f(\mathcal{T}(\boldsymbol{y}), \mathcal{H}_A)$ is the distribution of the test statistic under the alternative hypothesis. We define the probability of false alarm (P_{FA}) as

$$P_{FA} = \int_{\gamma_{\text{crit}}}^{\infty} f(\mathcal{T}(\boldsymbol{y}), \mathcal{H}_N) d\mathcal{T} \tag{2.38}$$

where $f(\mathcal{T}(\boldsymbol{y}), \mathcal{H}_N)$ is the distribution of the test statistic under the null hypothesis.

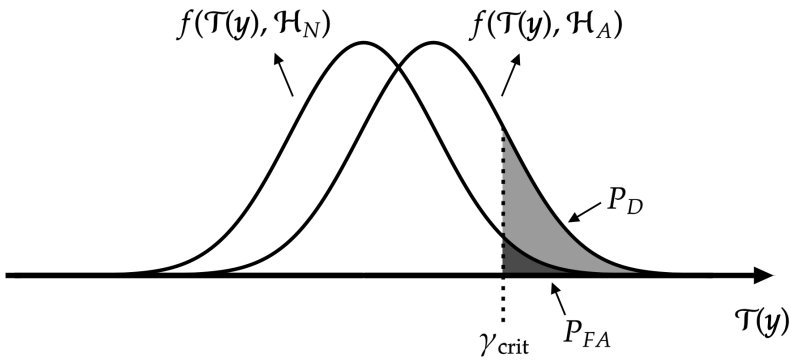

Figure 2.30: Graphical description of probability of detection and probability of false alarm.

The critical value to decide between the null or alternative hypothesis is found by fixing the false-alarm rate at a user defined significance level, α_{FA}, and then solving Eq. 2.38 for γ_{crit}. It is common to use 0.05 as the significance level - this controls the probability of false alarm below 5%.

More often than not, the underlying PDFs of the null and alternative hypotheses are not known exactly due to unknown parameters. In general, there is no optimal test for this scenario but often the GLRT is used. The GLRT is similar to the LRT except the maximum likelihood estimates of the unknown parameters are used instead of the known or assumed values. The composite hypothesis is

$$\begin{aligned} \mathcal{H}_N &: \boldsymbol{\theta} \in \boldsymbol{\Theta}_N \\ \mathcal{H}_A &: \boldsymbol{\theta} \in \boldsymbol{\Theta}_A \end{aligned} \tag{2.39}$$

where $\boldsymbol{\Theta}_N$ and $\boldsymbol{\Theta}_A$ are parameter spaces under the null and alternative hypotheses respectively. $\boldsymbol{\theta}$ may consist of parameters that are relevant to the test and nuisance parameters that are not relevant to the test but are still unknown and thus must be estimated. Let $\boldsymbol{\theta} = [\boldsymbol{\theta}_r^T \ \boldsymbol{\theta}_n^T]^T$ where $\boldsymbol{\theta}_r$ (size: $r \times 1$) are the parameters relevant to the test and $\boldsymbol{\theta}_n$ (size: $n \times 1$) are the nuisance parameters.

The corresponding GLRT is

$$\Lambda_{\text{GLRT}} = \frac{p(\boldsymbol{y} \mid \hat{\boldsymbol{\theta}}_{\text{MLE},H_A})}{p(\boldsymbol{y} \mid \hat{\boldsymbol{\theta}}_{\text{MLE},H_N})} \underset{H_N}{\overset{H_A}{\gtrless}} \gamma_{\text{crit}} \tag{2.40}$$

where $\hat{\boldsymbol{\theta}}_{\text{MLE},H_{N/A}}$ is the maximum likelihood estimate (MLE) of the unknown parameters under the specified hypothesis.

The GLRT has some useful asymptotic properties if:

1. The parameter space of the null hypothesis is a subset of the parameter space of the alternative hypothesis: $\Theta_N \in \Theta_A$

2. The optimization of $\boldsymbol{\theta}$ under the alternative hypothesis is unrestricted.

3. Nuisance parameters are the same under both the null and alternative hypotheses.

4. The number of counts must be large such that $\hat{\boldsymbol{\theta}}_{\mathrm{MLE}}$ reaches the CRLB.

If the above conditions are met, then

$$\Lambda'_{\mathrm{GLRT}} = 2\ln(\Lambda_{\mathrm{GLRT}}) \sim \begin{cases} \chi^2_r(0), & \mathcal{H}_N \\ \chi^2_r(\lambda), & \mathcal{H}_A \end{cases} \tag{2.41}$$

where $\chi^2_r(\lambda)$ is the non-central chi-squared distribution with r degrees of freedom and non-centrality parameter λ (see Appendix 6C of [149] for more details). For the null hypothesis, $\lambda = 0$, thus $\chi^2_r(0)$ is simply a chi-squared distribution with r degrees of freedom. For the alternative hypothesis, λ is

$$\lambda = \left(\boldsymbol{\theta}_{r,A} - \boldsymbol{\theta}_{r,N}\right)^T \left[I_{\boldsymbol{\theta}_r\boldsymbol{\theta}_r}\left(\boldsymbol{\theta}_{r,A}, \boldsymbol{\theta}_n\right) - I_{\boldsymbol{\theta}_r\boldsymbol{\theta}_n}\left(\boldsymbol{\theta}_{r,A}, \boldsymbol{\theta}_n\right) I^{-1}_{\boldsymbol{\theta}_n\boldsymbol{\theta}_n}\left(\boldsymbol{\theta}_{r,A}, \boldsymbol{\theta}_n\right) I_{\boldsymbol{\theta}_n\boldsymbol{\theta}_r}\left(\boldsymbol{\theta}_{r,A}, \boldsymbol{\theta}_n\right) \right] \left(\boldsymbol{\theta}_{r,A} - \boldsymbol{\theta}_{r,N}\right) \tag{2.42}$$

where $\boldsymbol{\theta}_{r,A}$ and $\boldsymbol{\theta}_{r,N}$ are the true values of the test-relevant parameters under the alternative and null hypotheses and $\boldsymbol{\theta}_n$ are the true values of the nuisance parameters. The matrices $I_{\boldsymbol{\theta}_r\boldsymbol{\theta}_r}$, $I_{\boldsymbol{\theta}_r\boldsymbol{\theta}_n}$, $I_{\boldsymbol{\theta}_n\boldsymbol{\theta}_n}$, and $I_{\boldsymbol{\theta}_n\boldsymbol{\theta}_r}$ are partitions of the FIM:

$$I\left(\boldsymbol{\theta}_{r,A}, \boldsymbol{\theta}_n\right) = \begin{bmatrix} I_{\boldsymbol{\theta}_r\boldsymbol{\theta}_r}\left(\boldsymbol{\theta}_{r,A}, \boldsymbol{\theta}_n\right) & I_{\boldsymbol{\theta}_r\boldsymbol{\theta}_n}\left(\boldsymbol{\theta}_{r,A}, \boldsymbol{\theta}_n\right) \\ I_{\boldsymbol{\theta}_n\boldsymbol{\theta}_r}\left(\boldsymbol{\theta}_{r,A}, \boldsymbol{\theta}_n\right) & I_{\boldsymbol{\theta}_n\boldsymbol{\theta}_n}\left(\boldsymbol{\theta}_{r,A}, \boldsymbol{\theta}_n\right) \end{bmatrix}$$

2.4.3 Bootstrapping

Bootstrapping is a method to find the uncertainty of an estimate using experimental data [150]. Assuming one has a representative sample from the population and the sample data are independent and identically distributed, bootstrapping treats the sample as the population. As shown in Fig. 2.31, if many samples from the population are not available, one can create replicates from the experimental data by

sampling with replacement and processing those replicates to get a distribution of sample estimates.

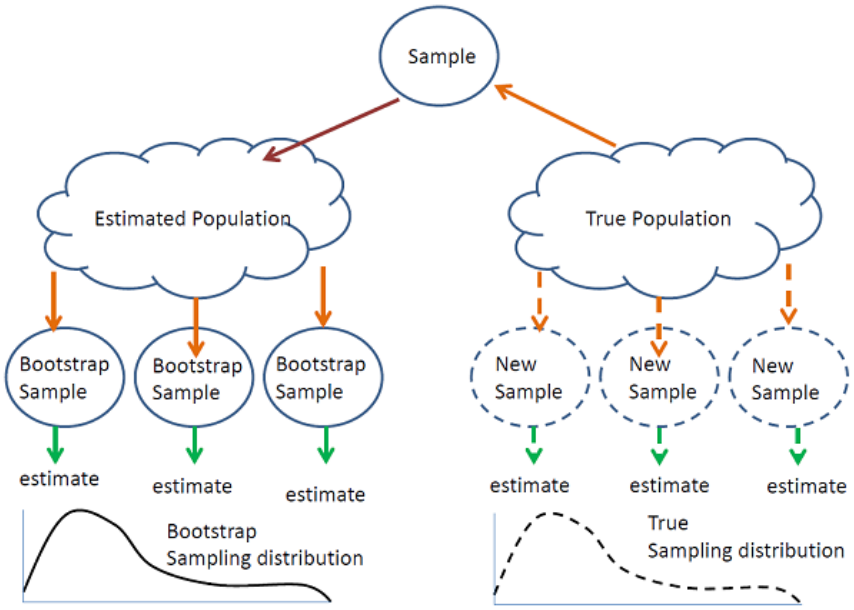

Figure 2.31: Concept behind of bootstrapping. Adapted from [151].

For c-TEI data, we use a block-based bootstrapping approach. Imagine a stream of pulses being detected by the detector as the mask continuously rotates. In Fig. 2.32, the start of each pulse is indicated by a dot. From this list mode data, we can create the observation vector $\boldsymbol{y}$ by binning the data into N_O bins. We refer to this as coarse binning[22]. For example, a full mask revolution collected over 90 seconds with one bin per degree has a coarse bin width of 0.25s.

To create a replicate of the observation vector, we will create a new stream of data for each coarse bin. We do this by binning the list mode data from each coarse bin into a fine bin structure, in our case $10\mu s$ bins, and then randomly pulling N_{FS} samples with replacement. The number of fine bin samples, N_{FS}, can be controlled to reduce the expected counts. Fig. 2.32 is a graphical depiction of this process.

[22]Typically, $N_O = 360$.

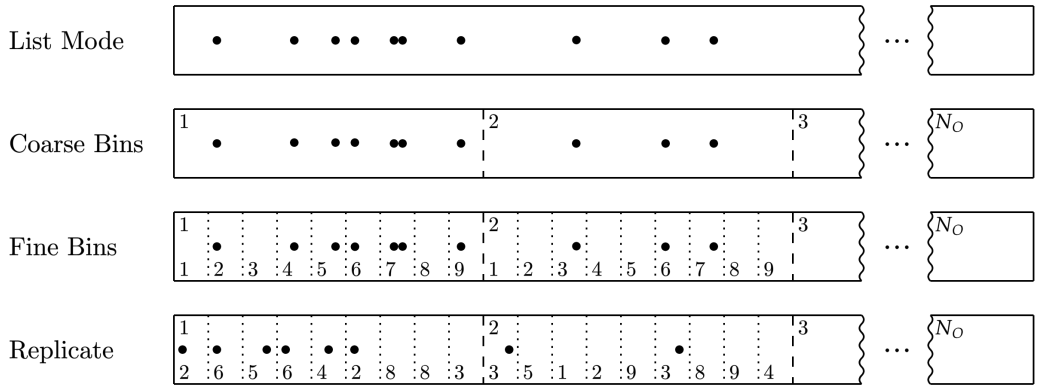

Figure 2.32: Bootstrapping using list mode data in a TEI system. The block dots represent the start times of pulses. Within each coarse bin, the fine bins are sampled with replacement to create each replicate.

When experimental data is not available, we will create replicates by assuming the samples come from a Poisson distribution with an estimated mean. For example, we will assume that the expected counts for a specific mask rotation angle is the ML forward projection and then pull Poisson random samples from that distribution.

2.5 Key Takeaways

Here are some key takeaways from each section.

Particle detection:

- Gamma ray and neutron interactions have different pulse shapes in stilbene and CLLBC. This effect can be exploited to classify pulses as gamma-ray induced or neutron induced.
- We use a Bayesian method to classify pulses as gamma-ray induced or fast-neutron induced in the stilbene detector. Throughout the dissertation, pulses are only classified as gamma rays or fast neutrons if they are 99.9999% probable in their respective groups.

Coded aperture imaging:

- Unique source localization is dependent on the mask design. We use URAs.
- The ideal coded aperture model requires many assumptions that cannot be met in the real-world. As we relax those assumptions, the point spread function is no longer a delta function and we need other methods to reconstruct images.

Image reconstruction:

- The system response, $A[i, j]$, is proportional to the probability of detecting an event in observation bin i **given** the particle was emitted in source bin j.
- The system response is often ill-posed. This means creating high resolution images results in noise amplification.
- We use under-iterated MLEM to reconstruct images. The image is initialized proportional to the inverse sensitivity of the system response. MLEM is user terminated when the NRMSE between the experimental data and the forward projection is nearly constant.

Applied analysis methods and metrics:

- The CRLB is the lower bound on the variance for all unbiased estimators of a deterministic parameter.
- The FIM depends on the second derivative of the log-likelihood function with respect to the parameters of interest.
- The MLE is asymptotically unbiased and asymptotically efficient.
- Under some conditions, Λ'_{GLRT} is distributed as a non-central chi-squared distribution.

- The asymptotic detection performance using the GLRT of a system is a function of the FIM.

- We use a block-based bootstrapping approach. For each observation bin, we sample with replacement from a fine-binned set of data.

CHAPTER III

System Response Models

A critical component for high-quality image reconstruction is an accurate model for the observed data. Eq. 2.9 described the ideal coded aperture model which is the basis of both spatial coded aperture (SCA) and cylindrical, time-encoded imaging (c-TEI). Unfortunately, in most real-world scenarios, the assumptions required for the ideal coded aperture model are not true. This chapter describes three system response models for c-TEI systems with more realistic assumptions or conditions under which they should be used[1].

Sec. 3.1 describes the small detector model which is a simple extension of the ideal coded aperture model. In particular, the small detector model relaxes the no-background and no-scatter assumptions, models exponential attenuation through the mask, and allows each mask element to be sampled more than once.

A key limiting assumption of the small detector model is the requirement that the detector be small relative to the mask radius. For some c-TEI systems, such as handheld systems, this assumption may not true. Thus, Sec. 3.2 introduces the large detector model which addresses this limitation by splitting the detector into many elements and finding the expected response for each piece. We use this model in

[1]Parts of this chapter are adapted from [152].

Chap. IV to design the MATADOR system.

Both the small and large detector models are only applicable for c-TEI systems where the detector is at the center of the mask. To address this limitation, Sec. 3.3 describes a slightly modified version of the large detector model that can be applied to off-center detectors - we refer to this model as the offset detector model. Chaps. VI - VIII use the offset detector model to investigate the potential of adaptive detector movements and adaptive mask movements.

All three of these models assume that scatter from the mask and environment is constant as a function of mask rotation angle. As we will see when verifying these models against experimental data (Chap. V), this assumption may not be true. Although in our experience, this model mismatch does not significantly impact imaging performance with respect to angular resolution, for applications that are sensitive to the log-likelihood, such as source detection, the model mismatch leads to inaccurate results. Thus, in Sec. 3.4, we use experimental data to create a system response which is only used in Chap. VII for source detection.

For convenience, all system responses used in this dissertation are collected and presented in this chapter.

3.1 Small Detector Model

For many real-world c-TEI systems, the ideal coded aperture model is not accurate enough to match measured data. For example, the gamma rays and fast neutrons relevant to nuclear non-proliferation are highly penetrating, thus the mask is not perfectly opaque. Additionally, the ideal aperture model only allows the mask to be sampled once per mask element. This restriction leads to worse imaging performance in terms of both angular resolution and signal-to-noise ratio (SNR) [97]. Fortunately,

many of the ideal coded aperture assumptions can be relaxed while retaining the linear shift-invariant (LSI) properties of the model.

The critical assumption in the small detector model is that the detector is small relative to the mask radius. We start with the extreme case where the detector is a point at the center of the mask. In this case, from the perspective of the point detector, the mask is translating horizontally in front of any source. Thus, we can treat the mask as flat instead of cylindrical as shown in Fig. 3.1. If the detector is finite but small relative to the mask radius, then the small detector model is approximately accurate. This follows from the small angle approximation where $\sin(\theta) \approx \theta$ for small θ. In Sec. 3.2.1, we will map out when this assumption is viable for thick masks and larger detectors.

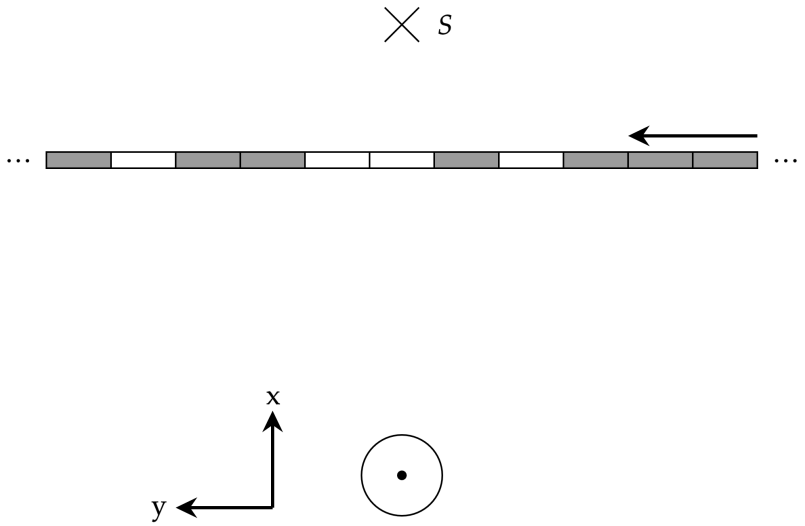

Figure 3.1: From the perspective of a point detector, the mask is translating horizontally in front of any source. Thus, for a c-TEI system, if the detector is small relative to the mask, then we can treat the mask as flat instead of cylindrical. The shaded grey mask elements represent closed elements.

Since a c-TEI system with the detector at the center is LSI, we only consider the case of a point source at $+\infty$ on the x-axis. Thus, all source particles are travelling

in the -x direction.

To describe the expected measurement vector, we must first define two other variables: the mask transmission vector and the detector response. Since high energy gamma-rays and fast neutrons are highly penetrating, we must account for the attenuation of the mask as shown in Eq. 3.1.

$$\boldsymbol{m} = \exp\left(-\lambda_M t_M \odot (1 - m_b(\boldsymbol{y}_m))\right) \tag{3.1}$$

where $m_b(\boldsymbol{y}_m)$ is a function that returns the value of the binary mask at mask position vector $\boldsymbol{y}_m$ (1 is an open element and 0 is a closed element in $m_b(\cdot)$), t_M is the thickness of the mask, and λ_M is the attenuation coefficient of the mask. λ_M is a function of the particle type and energy; for brevity we omit those subscripts. The mask transmission vector can be evaluated at any mask position thus the mask may be sampled more than once per element.

The detector response for a cylindrical detector can be modeled as:

$$d(y) = 1 - \exp\left(-\lambda_D \cdot 2\sqrt{r_D^2 - y^2}\right) \tag{3.2}$$

where λ_D is the detector attenuation coefficient and r_D is the radius of the detector.

The mean detector attenuation coefficients for gamma-rays and fast neutrons were found via MCNPX-PoliMi simulations for each energy group. The energy deposited from each collision was converted to light output using the Voltz approximation [153]. Fig. 3.2 shows the detection probability, $d(y)$, of 1-2 MeV neutrons on a 5.08 cm stilbene detector as a function of position alongside the fit of Eq. 3.2 to find λ_D.

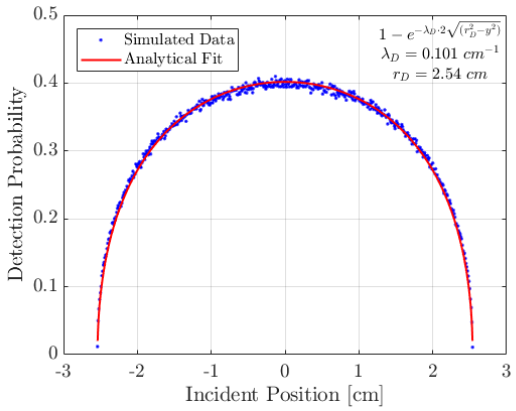

Figure 3.2: Detector response of a 5.08 cm cylindrical stilbene crystal from 1-2 MeV neutrons as a function of incident position found via MCNPX-PoliMi simulations. The simulated data was fit with Eq. 3.2 to find λ_D.

Finally, the expected measurement vector is

$$\boldsymbol{y} = (\boldsymbol{x} \circledast \boldsymbol{m} \circledast \boldsymbol{d} + b) \odot \boldsymbol{t} \tag{3.3}$$

where $\boldsymbol{m}$ is the mask transmission vector (Eq. 3.1), $\boldsymbol{d}$ is the detector response (Eq. 3.2), $\boldsymbol{t}$ is the measurement time per bin, and b is the unmodulated intensity from natural background and source scatter from the mask, environment, and detector. Herein, we refer to Eq. 3.3 as the "small detector model". Table 3.1 shows the corresponding assumptions.

Table 3.1: Assumptions for the small detector model.

	Small Detector
System	The system is LSI.
Sampling	All sources are at the center of their respective pixels. The mask pattern may be sampled multiple times per mask element.

Continued on next page

Table 3.1 – *Continued from previous page*

	Small Detector Model
Source	All sources are in the far field such that magnification is negligible. A near field coded aperture model can be found in [42].
	All sources are in the fully coded field-of-view.
	All sources have long half-lives relative to the measurement time.
Mask	Scatter from the mask is a constant additive factor for all mask rotation angles.
Detector	Detector performance is temporally constant.
	Scatter from the detector is a constant additive factor for all mask rotation angles.
	The detector is small relative to the mask radius such that the small angle approximation is accurate.
Background	Background is a constant additive factor for all mask rotation angles.
Environment	Scatter from the environment is a constant additive factor for all mask rotation angles.

For some c-TEI systems, such as handheld systems, the small detector assumption may not true. The large detector model address this limitation by splitting the detector into many elements and finding the expected response for each piece.

3.2 Large Detector Model

First, we introduce the large detector model and then compare its response to the small detector model in Sec. 3.2.1. The goal is to provide guidelines as to when the small detector model is accurate enough to use and when one should use the large

detector model instead.

When the detector is large relative to the mask radius, the edge of the detector observes a significantly different mask transmission vector than the center of the detector, and the prediction from the small detector model degrades. To predict an accurate observation vector, the large detector model segments the monolithic detector into smaller detector elements and calculates the mask transmission vector for each detector element. Then, it scales the response from each segment by the probability of detection and sums over all segments.

Because a c-TEI system with the detector at the center is LSI, we assume that the source is located at $+\infty$ on the x-axis. Thus, all source particles are travelling in the -x direction. The mask rotation angle is zero and, as usual, θ is defined counter-clockwise from the x-axis.

Consider the difference between Ray 0 and Ray 1 in Fig. 3.3. Although both Ray 0 and Ray 1 are travelling along the same direction, because Ray 1 is not travelling to the center of the mask, it must travel through a different mask thickness than Ray 0. The mask thickness that a ray offset by y from the mask center must traverse is

$$\begin{aligned} t'_M(y) = x_o - x_i &= \sqrt{r_o^2 - y^2} - \sqrt{r_i^2 - y^2} \\ &= \sqrt{r_i^2 + 2r_i t_M + t_M^2 - y^2} - \sqrt{r_i^2 - y^2} \end{aligned} \tag{3.4}$$

where the subscript o stands for outer, the subscript i stands for inner, x_o is the x coordinate of the position at which the offset ray intersects the outer radius of the mask, r_o, and t_M is the radial thickness of the mask.

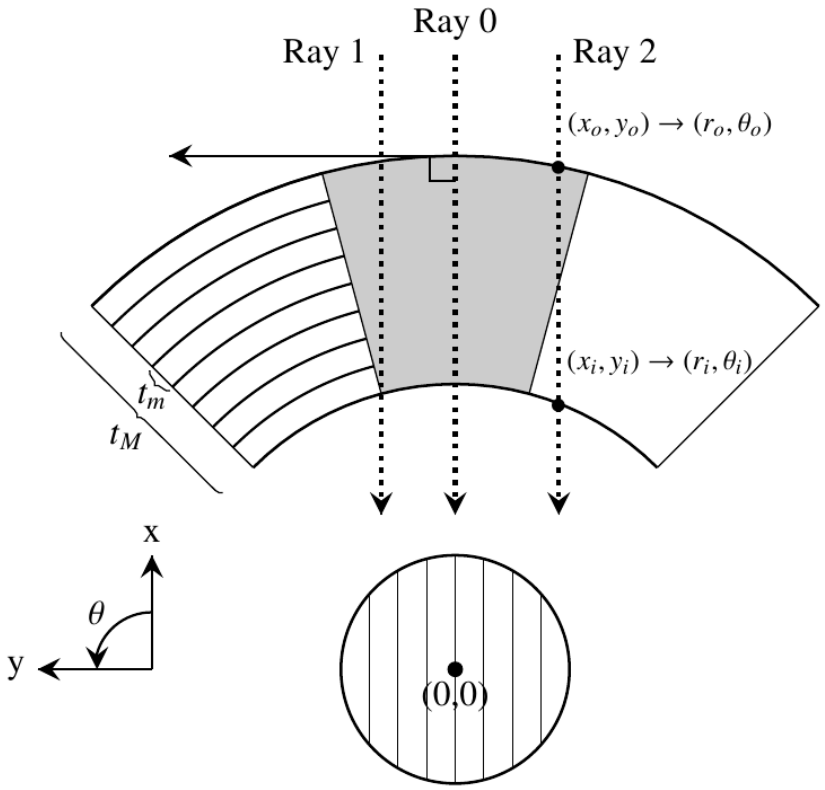

Figure 3.3: Detailed schematic of a c-TEI system. The detector is centered at (0,0) and the mask rotates counter-clockwise around the detector. The shaded grey mask elements represent closed elements. The parallel rays are potential paths for a far-field source at $+\infty$ on the x-axis.

Besides traversing different mask thicknesses, offset rays may also pass through multiple mask elements, such as Ray 2 in Fig. 3.3. Ray 2 enters the mask at $(x_o, y_o) \rightarrow (r_o, \theta_o)$ which is a closed mask element and leaves the mask at $(x_i, y_i) \rightarrow (r_i, \theta_i)$ which is an open mask element. We address this problem by segmenting the thick mask into many thin mask slices and assuming that any ray that enters a mask slice at a particular mask element will also exit that mask slice at the same mask element. Then, the mask thickness traversed by each ray becomes a summation:

$$t'_M(y) = \sum_{m=0}^{N_M-1} \left(\sqrt{r_{i,m}^2 + 2r_{i,m}t_m + t_m^2 - y^2} - \sqrt{r_{i,m}^2 - y^2} \right) \cdot m_b(\theta_m(y)) \qquad (3.5)$$

where the thick mask is segmented into N_M slices, t_m is the thickness of the mth

mask slice, and $m_b(\theta_m(y))$ is the binary mask pattern evaluated at the angular offset the ray will enter the mask slice. For a source at $+\infty$ on the x-axis, $\theta_m(y)$ can be calculated as:

$$\theta_m(y) = \sin^{-1}\left(\frac{y}{r_m}\right) \tag{3.6}$$

Eq. 3.5 can be simplified by assuming that the mask slices are thin such that they are essentially planes from the perspective of the ray. Also, instead of treating $m_b(\theta)$ as a function that must be evaluated for each mask rotation angle and angular offset, we can treat it as a vector that must be circularly shifted by the angular offset for each slice:

$$\boldsymbol{t}'_M(y) = \sum_{m=0}^{N_M-1} \frac{t_m \ \mathrm{circ}(1-\boldsymbol{m}_b, \theta_m(y))}{\cos(\theta_m(y))} \tag{3.7}$$

Finally, the observed response vector can be calculated as

$$\boldsymbol{y} = (\boldsymbol{a} \circledast \boldsymbol{x} + b) \odot \boldsymbol{t} \tag{3.8}$$

where

$$\boldsymbol{a} = \sum_{i=0}^{N_D-1} d(y[i]) \cdot \exp\left(-\lambda_M \boldsymbol{t}'_M\left(y[i]\right)\right) \tag{3.9}$$

and $\boldsymbol{t}$ is the measurement time per bin, $d(y[i])$ is the detector response evaluated at position $y[i]$ for the ith detector element, and λ_M is the mask attenuation coefficient, and b is the unmodulated intensity from natural background and source scatter from the mask, environment, and detector. Eq. 3.8 can be applied to irregular or multiple masks and expanded to include particle and energy dependence. Herein, Eq. 3.8 is referred to as the "large detector model".

3.2.1 Small and Large Detector Model Predictions

Fig. 3.4 maps out the normalized root mean squared error (NRMSE) between the small and large detector model as a function of detector diameter, outer mask

radius, and mask thickness for a high-density polyethylene (HDPE) mask arranged in a URA-35 pattern [95]. For most system designs with $r_D \ll r_M$, the small detector model is sufficient to predict the system response accurately[2], however when the mask is quite close to the detector, as may be the case in a handheld system, the large detector model is more accurate.

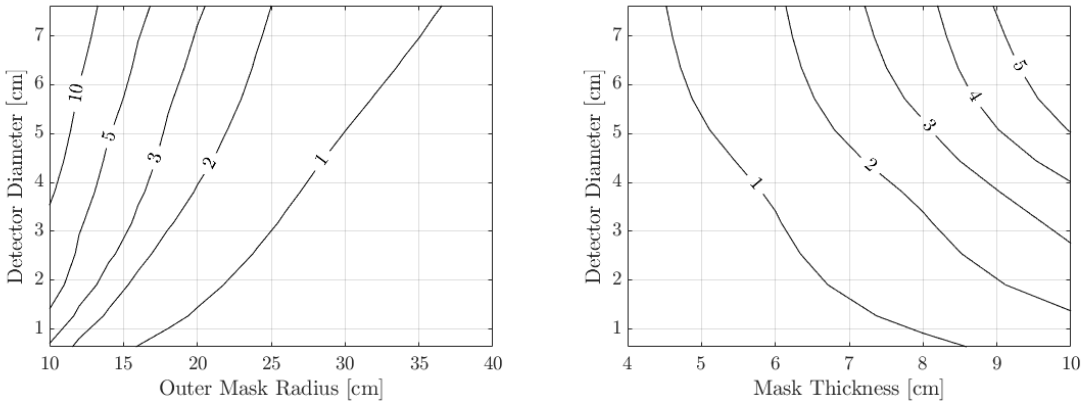

(a) Fixed mass thickness of 6 cm.

(b) Fixed outer mask radius of 26 cm.

Figure 3.4: NRMSE contours between the small detector and large detector model predictions for Cf-252 neutrons in units of percent. The HDPE mask pattern is in a URA-35.

Fig. 3.5 shows the system response from the small and large detector models for the hypothetical handheld system described in Table 3.2.

Table 3.2: Handheld c-TEI system design parameters

Detector Diameter	5.08 cm stilbene crystal
Mask pattern	URA-35
Inner mask radius	4.0 cm
HDPE thickness	6.0 cm
Pixel pitch	10.28°

The small detector model overpredicts the overall count rate by 12.7% and has a NRMSE of 14.5%. Using the small detector model for such a system would likely result in lower contrast, increased noise, and artifacts in the reconstructed image.

[2]Within a NRMSE of 1%.

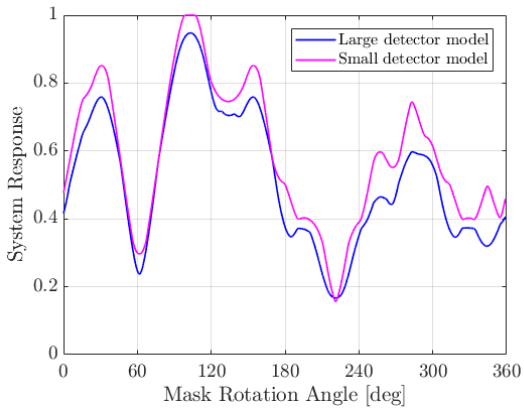

Figure 3.5: System response from a handheld c-TEI system to Cf-252 neutrons. The small detector model overpredicts the overall count rate by 12.7% and has a NRMSE of 14.5%.

3.3 Offset Detector Model

The small and large detector models can only be used when the detector is at the center of the mask. When the detector is not at the center of the mask, the system is no longer shift-invariant (SI) and we must use a different model. In this case, we will use the offset detector model which is a simple extension from the large detector model. Note that for any scenario that calls for the small or large detector model, one can instead use the offset detector model, but we do not recommend this due to the increased computational burden. Below, we briefly outline the offset detector model without going into detail since the model is based on ray-tracing.

Both the small and the large detector model assume that the imaging system is SI meaning that the response from a source at 0° is the same as the response from a source at 90° after a 90° phase shift. Thus, they both use convolutions in the imaging model, but when the detector is not at the center, the imaging system is no longer SI. Fig. 3.6 is a schematic showing how the expected response changes as a function of source and detector position. With respect to D_0, notice how the open element

is fully open for the source at S_0 and S_1. In contrast, with respect to D_1, the open mask element is significantly distorted by the nearby closed elements for a source at S_1 compared to a source at S_0.

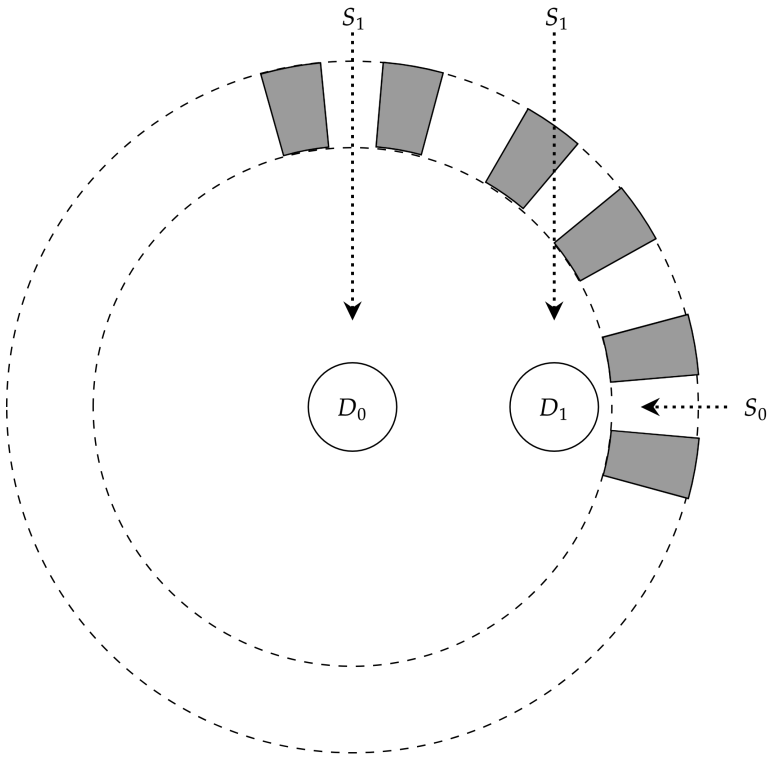

Figure 3.6: Schematic of a c-TEI system with an offset detector.

Fortunately, this problem is easily solved by replacing Eq. 3.6 with ray tracing and calculating the system response for every source position instead of just one. Also, as the detector moves, the detection efficiency will change with the inverse square law, thus the model must be near-field. We assume that the unmodulated intensity is constant with mask rotation angle but may change with detector position. Thus,

$$\boldsymbol{y} = (A\boldsymbol{x} + \boldsymbol{b}_D) \odot \boldsymbol{t} \tag{3.10}$$

where A is a slightly modified version of the large detector model and $\boldsymbol{b}_D$ is the unmodulated intensity from natural background and source scatter from the mask,

environment, and detector. The subscript D is meant to emphasize that the unmodulated intensity changes as a function of detector position.

We can rewrite Eq. 3.10 in the usual $\boldsymbol{y} = A\boldsymbol{x}$ form by treating the unmodulated intensity as another source whose response is constant as a function of mask position (but not as a function of detector position) and then scaling each column of A by $\boldsymbol{t}$:

$$\begin{aligned} \boldsymbol{y} &= (A\boldsymbol{x} + \boldsymbol{b}_D) \odot \boldsymbol{t} \\ &= A_b\boldsymbol{x} \odot \boldsymbol{t} \\ &= A_{b,t}\boldsymbol{x} \end{aligned} \tag{3.11}$$

A_b is a block matrix:

$$\left[\begin{array}{c|c|c|c|c} \begin{bmatrix} & A_0 & \end{bmatrix} & \begin{bmatrix} b_D[0] \\ \vdots \\ b_D[0] \end{bmatrix} & \begin{bmatrix} 0 \\ \vdots \\ 0 \end{bmatrix} & & \begin{bmatrix} 0 \\ \vdots \\ 0 \end{bmatrix} \\ \hline \begin{bmatrix} & A_1 & \end{bmatrix} & \begin{bmatrix} 0 \\ \vdots \\ 0 \end{bmatrix} & \begin{bmatrix} b_D[1] \\ \vdots \\ b_D[1] \end{bmatrix} & & \begin{bmatrix} 0 \\ \vdots \\ 0 \end{bmatrix} \\ \hline \vdots & & & \ddots & \\ \hline \begin{bmatrix} & A_D & \end{bmatrix} & \begin{bmatrix} 0 \\ \vdots \\ 0 \end{bmatrix} & \begin{bmatrix} 0 \\ \vdots \\ 0 \end{bmatrix} & & \begin{bmatrix} b_D[D] \\ \vdots \\ b_D[D] \end{bmatrix} \end{array}\right]$$

where the subscripts on A represent the dth detector position and $b_D[d]$ is the unmodulated count rate at the dth detector position. Herein, Eq. 3.11 is known as "offset detector model".

In the offset detector model, for both neutrons and gamma rays, we use 24 non-uniformly spaced energy bins to calculate the system response for a Cf-252 source and the detection threshold is 40 keVee. The Cf-252 Watt spectrum [154] and binned spectrum are shown in Fig. 3.7.

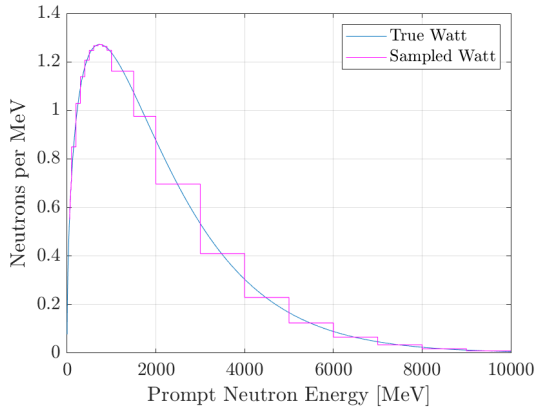

Figure 3.7: Cf-252 Watt spectrum and binned Watt spectrum using 24 non-uniform bins.

3.4 Experimental System Response

All three of these models only account for particles that are travelling directly from the source to the detector and thus do not account for particle scatter on the mask or the environment. We will see in Chap. V that this simplification leads to mismatch between the expected response and the experimental data. For applications that are sensitive to the log-likelihood, such as source detection using the generalized likelihood ratio test (GLRT), this model mismatch may lead to inaccurate results. Thus for Chap. VII which focuses on source detection, we will use a system response made using experimental data. The experimental system response is only for the case where the source is 90 cm from the detector and the detector at the center of the mask.

A 1.85 mCi Cf-252 source was placed at (90 cm, 175°) and data was collected

with the detector at the center for 64.5 min. Fig. 3.8 is the experimental data with 1° bins. To find the system response in units of counts per emission, we divide the experimental counts by the source strength and measurement time.

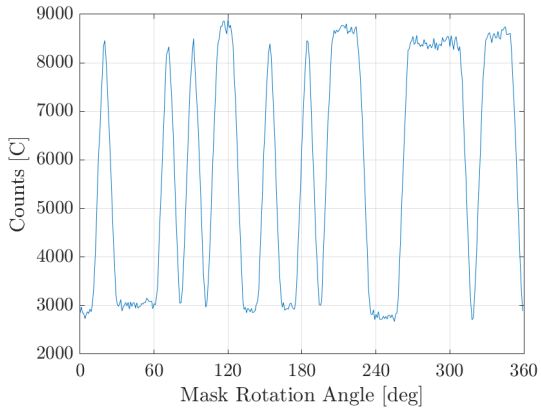

Figure 3.8: Experimental data from a 1.85 mCi Cf-252 point source placed at (90 cm, 175°). Measurement time is 64.5 min.

We assume the imaging system is LSI when the detector is in the center, and thus we can circularly shift the experiment system response at 175° to find the response at other source positions. Fig. 3.9 is the experimental system response.

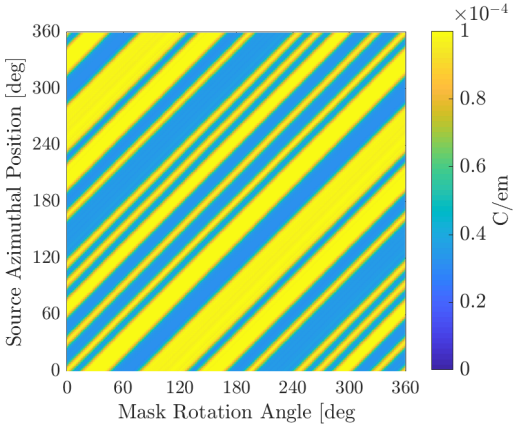

Figure 3.9: Experimental system response generated from the measured data in Fig. 3.8.

3.5 Conclusion

Previous work on the system response models for c-TEI systems is limited, including the design space where these models are accurate. With respect to the small and large detector models, we explored the design space and mapped out regions where the small detector assumption may be sufficient and regions where a more robust model, the large detector model, would be necessary to generate accurate responses. For example, in a handheld system, where the mask is close to the detector, the small detector model is inaccurate as it overpredicts the overall count rate by 12.7% and the NRMSE between the small and large detector models is 14.5%. Using the small detector model for such a system would likely result in lower contrast and artifacts in the reconstructed image.

For use in cases where the detector is not at the center of the mask, we developed the offset detector model. The offset detector model is a simple extension of the large detector model where the angular offset with which a ray enters a mask slice is calculated using ray tracing instead of Eq. 3.6. Finally, we described an experimental system response model which may be used in applications that are sensitive to model mismatch.

Before we verify the large and offset detector models in Chap. V, we will first describe the design and construction of the MATADOR system. Experimental data from the MATADOR system will be used to verify the models.

CHAPTER IV

Design and Construction of MATADOR

Compared to spatial coded aperture (SCA), there exists little work on the factors to consider when designing a cylindrical, time-encoded imaging (c-TEI) system. This chapter uses the large detector model to calculate the system response of different c-TEI designs and grapples with the tradeoffs between size, weight, angular resolution, and contrast-to-noise ratio (CNR). Throughout the design process, we only consider the imaging performance when the detector is at the center of the mask. Sec. 4.1 contains those results.

Sec. 4.2 describes the construction of the MATADOR system alongside updates that were made to the system years after the initial construction. As an imaging demonstration, Sec. 4.3 contains neutron and gamma reconstructions of a Cf-252 source[1].

4.1 Design Process

MATADOR[2] is a 1-D, dual particle, c-TEI system consisting of a 2" stilbene detector inside a dual layer mask. The outer layer of the mask is made of high-density polyethylene (HDPE) for its high mass attenuation coefficient for fast neutrons and

[1]Parts of this chapter are adapted from [152].

[2]MATADOR stands for mobile adaptive time-encoded asymmetric dual-particle one-dimensional rotating imager.

the inner layer of the mask is made of tungsten. While tungsten's mass attenuation coefficient for Cf-252 gamma rays is 6.5% less than that of lead, its mass attenuation coefficient for Cf-252 neutrons is 23% greater, thus tungsten was the preferred choice. The following design space was considered:

1. Mask radius: The inner mask radii simulated ranged from 4 cm to 50 cm.

2. Mask thickness: The HDPE layer was varied from 1-10 cm and the tungsten layer was varied from 1/4 - 2 cm.

3. Mask pattern: Because of their optimality properties, the mask patterns explored were limited to uniformly redundant arrays [95]. Uniformly redundant arrays (URAs) with 35 and 143 elements were simulated.

4. Detector diameter: Each detector is a right circular cylinder with its height equal to its diameter. The detector diameter was varied from 0.635 - 7.62 cm.

The requirements for the c-TEI system include:

1. Constrain the system size to 60 cm wide such that the system can pass through doorways.

2. Achieve better than 20° full width at half maximum (FWHM) when reconstructing fast neutron or gamma-ray point sources with simple back-projection (SBP).

3. Limit the mass of the dual-particle mask to 23 kg.

The results below are found using the large detector model with 10 uniformly spaced energy groups from 0-10 MeV and a 70 keVee light output threshold.

4.1.1 Quantitative Metrics for Comparing c-TEI Designs

As with other coded aperture imaging systems, in c-TEI, there exists the classic trade-off between angular resolution and sensitivity. In this chapter, we define angular resolution as the FWHM of the point spread function (PSF) reconstructed using SBP in units of degrees.[3] More advanced reconstruction methods, such as filtered back projection or maximum likelihood expectation maximization (MLEM), were not implemented as they would require additional optimization that would vary from one system design to the next.

Sensitivity is measured via the CNR. The CNR was found via resampling the expected response from an assumed source. For these simulations, the source was defined as a 1 mCi Cf-252 point source placed 9 m from the detector and measured for 10 minutes with no background. Assuming the detection process is Poisson in nature, ten thousand realizations of the expected response were generated for each system design and then reconstructed using SBP. From these realizations, the mean value and the standard deviation of each image pixel was calculated. The CNR is defined using those values as:

$$\mathrm{CNR} = \frac{\bar{\hat{x}}_{\max} - \bar{\hat{x}}_{\min}}{\sigma_{\hat{x}_{\max}}} \tag{4.1}$$

where $\bar{\hat{x}}_{\max}$ is the maximum value in the mean reconstructed image, $\bar{\hat{x}}_{\min}$ is the minimum value of the mean reconstructed image, and $\sigma_{\hat{x}_{\max}}$ is the standard deviation of the maximum image pixel.

4.1.2 Choice of Detector Diameter, Mask Radius, and Coding Pattern

For a given mask pattern, the best angular resolution is possible only for a point detector. As the detector diameter increases, the sharp mask transitions begin to

[3] FWHM was found via linear interpolation.

blur and the angular resolution degrades. Fig. 4.1a depicts this effect for an infinitely thin, opaque mask arranged in a URA-35 pattern. For a mask radius of 15 cm and a point detector, the angular resolution is 10.28° which is the angular width of a mask element. As the detector diameter increases, the angular resolution degrades at an increasing rate (non-linear).

For a fixed mask radius, as the detector diameter increases, the CNR improves, although not as the square root of counts. For a large mask radius of 50 cm, the CNR approximately doubles when increasing the detector diameter from 2.54 cm to 5.08 cm. That is expected since the count rate has quadrupled and to the first order CNR is dependent on the square root of the counts. But for cases where the detector is large relative to the mask radius, increasing the detector diameter does not improve the CNR in the same way. For example, at a mask radius of 15 cm, doubling the detector diameter from 2.54 cm to 5.08 cm only results in a CNR increase of 54%. For these large detector cases, although increasing the size of the detector leads to more particles being detected, the resulting blur in the PSF leads to a weaker peak signal. For an extreme example, consider how the CNR is essentially constant for a detector diameter around 7 cm and a mask radius of 10 cm in Fig. 4.1a.

Fig. 4.1b is similar to Fig. 4.1a except the mask pattern is a URA-143 instead of a URA-35. While the trends described for the URA-35 case apply for the URA-143 case, the values are quite different. For mask radii less than 25 cm and detector diameters greater than 2.54 cm, the system designs using a URA-143 pattern perform similarly to the designs using the URA-35 pattern in terms of angular resolution, but the CNR is markedly worse. This is because the detector is much larger than a single mask element and the detector is sampling multiple mask elements at the same time. Because of the URA-143 lower CNRs for systems meeting the constraints described

in Sec. 4.1, the URA-35 pattern was chosen. The detector diameter was set to 5.08 cm as there are ample system designs that meet our requirements.

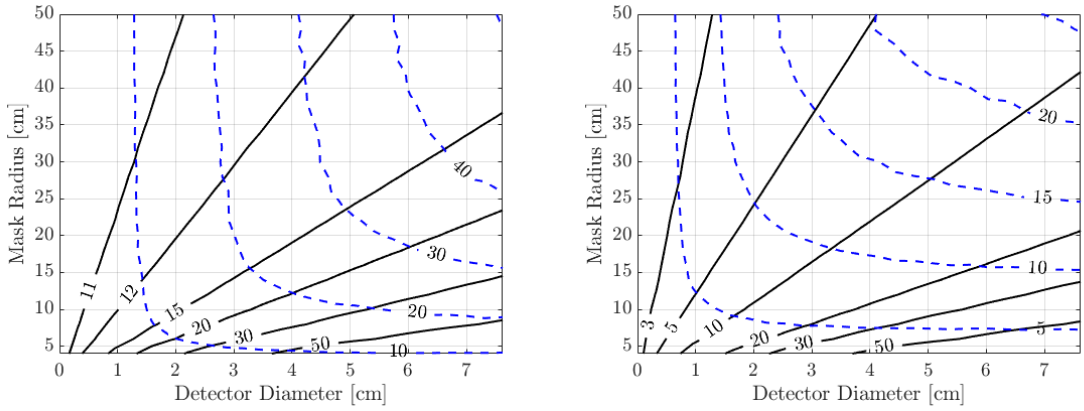

(a) URA-35 (b) URA-143

Figure 4.1: The tradeoff between angular resolution [deg] (solid black) and CNR (dashed blue) as a function of mask radius and detector diameter.

4.1.3 Mask Thickness

Transmission through the mask significantly degrades the CNR for any coded aperture system. Weight constraints prevent completely attenuating high energy gamma rays since multiple centimeters of tungsten would make for a heavy mask. Fully blocking fast neutrons would require 10+ centimeters of HDPE, which would increase the system size. Thus, there is an important trade-off between imaging performance and physical constraints. Fig. 4.2a and 4.2b illustrate this trade-off for gamma-ray and neutron imaging respectively. For both contour plots, the mask pattern is fixed as a URA-35 and the detector diameter is fixed at 5.08 cm. Fig. 4.2a shows the performance when imaging Cf-252 gamma rays with a fixed HDPE thickness of 6 cm and variable tungsten thickness and Fig. 4.2b is the equivalent for Cf-252 neutrons with a fixed tungsten thickness of 0.5 cm and variable HDPE thickness. Areas that are not physically possible are left blank.

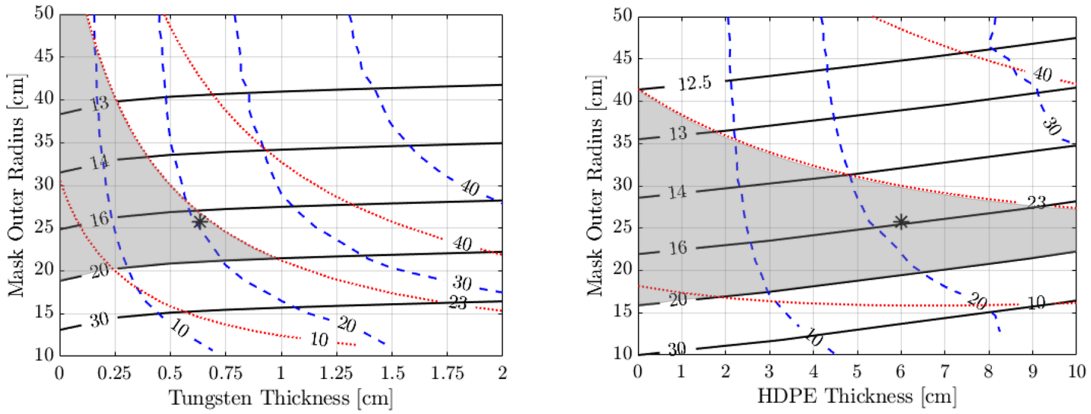

(a) For Cf-252 gamma rays where the HDPE thickness is fixed at 6 cm.

(b) For Cf-252 neutrons where the tungsten thickness is fixed at 0.5 cm.

Figure 4.2: The tradeoff between angular resolution [deg] (solid black), CNR (dashed blue), and mask mass [kg] (dotted red) for a URA-35 pattern and a 5.08 cm stilbene detector. The grey shaded area represents the set of possible system designs constrained by the requirements set out in Sec. 4.1. The black asterisk represents the final design selected.

Notice in both Fig. 4.2a and 4.2b, for a fixed outer mask radius, as the mask thickness increases, the angular resolution degrades. This is because the average mask radius is decreasing. At the same time, the mask is becoming more opaque and CNR is improving. Note that the improvement in CNR from increasing the mask thickness depends on the outer mask radius. CNR is a function the number of particles detected, mask transmission, and angular resolution which makes it difficult to predict.

The shaded region in Fig. 4.2a and 4.2b highlights all of the possible system designs that meet the requirements set in Sec. 4.1. Thus the best design, that is the design that maximizes CNR, is at the rightmost edge of the shaded region. Because both Fig. 4.2a and 4.2b are for fixed tungsten or HDPE thicknesses, finding the optimal design that meets all of the requirements in Sec. 4.1 involves an iterative process.

For research and flexibility reasons, we selected a non-optimal design for MATADOR which is shown as the black asterisk in Fig. 4.2a and 4.2b and described in Table 4.1.

Table 4.1: Final design parameters of MATADOR

Detector Diameter	5.08 cm stilbene crystal
Mask pattern	URA-35
Inner mask radius	17.5 cm
Tungsten thickness	0.635 cm
Tungsten width	3.04 cm
Inner mask radius	19.7 cm
HDPE thickness	6.0 cm
Pixel pitch	10.28°
Mask height	20 cm
Total mask weight	23 kg
Max extent	60 cm x 60 cm

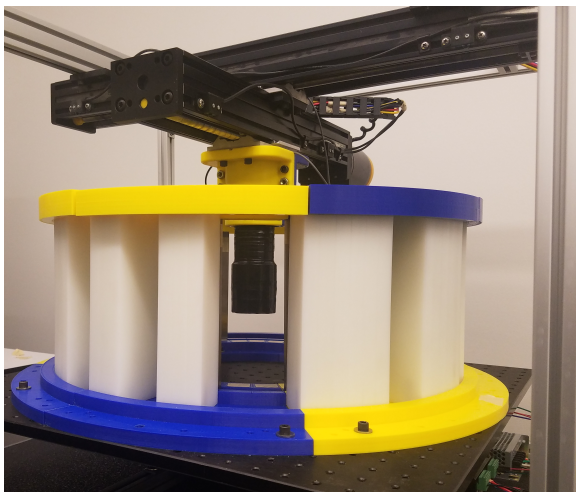

Figure 4.3: Picture of MATADOR. The central detector is a 5.08 cm stilbene crystal and the cylindrical mask consists of two layers. The outer layer is 6 cm of HDPE and the inner is 0.635 cm of tungsten. The mask is arranged in a URA-35 pattern and is held in place by a 3D printed frame. The mask frame is affixed to an optics breadboard that sits atop of a 360° rotary table.

4.2 Construction

The outer layer of the mask is composed of HDPE annular sectors with a radial thickness of 6 cm and an angular width of 10.28°. The inner layer of the mask is a

35-gon of tungsten bars; each bar is 0.635 cm thick and 3.04 cm wide. The mask elements are held in place by a 3D printed frame which sits on a 360° rotary table.

4.2.1 Updates

Since [152] was published, MATADOR has been updated. Now, there are two detectors, a 5.08 cm stilbene detector and a 2.54 cm $Cs_2LiLa(Br, Cl)_6$ (CLLBC) detector, hanging from an x-y linear stage. To make more vertical space, the mask was moved up using threaded standoffs. Fig. 4.4 is a picture of the updated MATADOR system. The updates do not significantly change the imaging performance of the system.

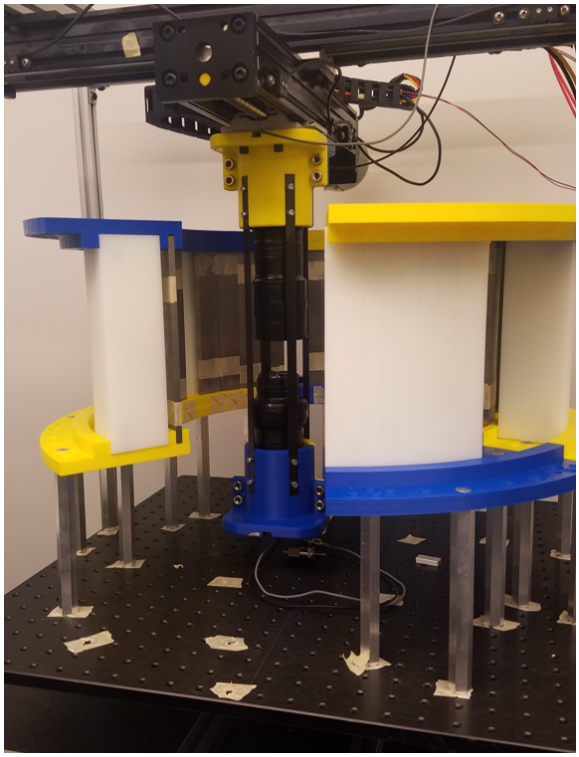

Figure 4.4: Updated picture of MATADOR. There are two detectors, a 5.08 cm stilbene detector and a 2.54 cm CLLBC detector, hanging from an x-y linear stage.

4.2.2 Electronics and Communication

The rotary table, x-linear actuator, and y-linear actuator are all driven by stepper motors. Each motor is controlled by a M542T microstep driver which is connected to a Arduino Uno for movement commands. The rotary table is zeroed using a magnet and a Hall effect sensor. The motors are connected to a relay to provide a software based power control switch and there are physical disconnect switches as a precautionary measure.

4.2.3 Limitations

The rotary table has a gear ratio of 180:1 and the stepper motor takes 200 steps/revolution, thus it takes 36,000 steps of the stepper motor to rotate the table once. Although theoretically the angular resolution of the rotary table is 0.01°, the mask's large inertia cause some skipped steps. To mitigate this problem, the mask is accelerated and decelerated over 10 steps which results in 3 lost steps per start and stop. Thus even when the rotary table is fully weighted down by the mask, the angular position uncertainty is <0.03° if re-zeroed after every revolution. The rotary table can make a full rotation in 90 seconds.

Theoretically, the x-y linear stage can take steps that are 5μm each but the accuracy of the system has only been measured up to 100μm.

4.3 Experimental Results

A 2.4 mCi Cf-252 point source was placed 3 m from the detector and imaged for 30 minutes at 12°/min. Fig. 4.5a and 4.5b show SBP and MLEM reconstructed images of gamma rays and neutrons respectively. The angular resolution from the SBP reconstruction for the gamma rays and fast neutrons is 17.3° and 16.2° respectively,

which agrees well with the large detector model prediction from Fig. 4.2a and 4.2b. The MLEM algorithm was terminated when the normalized root mean squared error (NRMSE) of the observation vector plateaued as shown in the figure inset. The MLEM reconstructed image of this point source had a FWHM of 7.7° for both gamma rays and fast neutron.

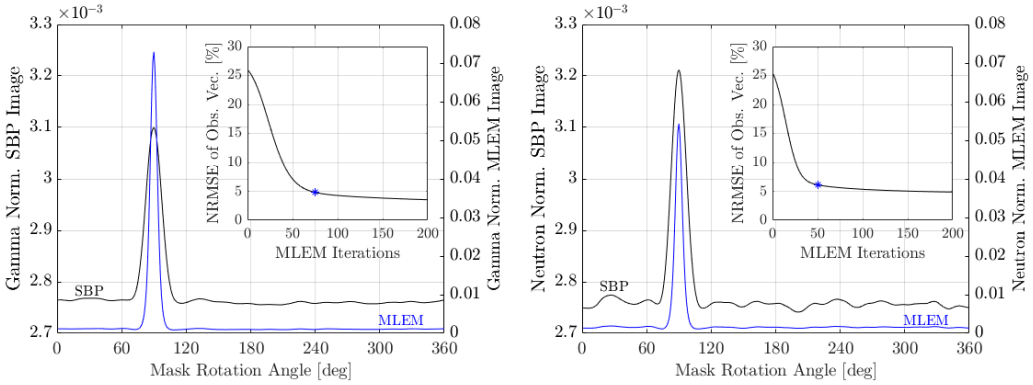

(a) Reconstructed image from gamma rays. The SBP FWHM is 17.3° while the MLEM FWHM is 7.7°. The MLEM algorithm was terminated at 75 iterations.

(b) Reconstructed image from fast neutrons. The SBP FWHM is 16.2° while the MLEM FWHM is 7.7°. The MLEM algorithm was terminated at 50 iterations.

Figure 4.5: A 2.4 mCi Cf-252 point source was placed 3 meters from the detector. Measurement time was 30 minutes. One degree bins were used. The MLEM algorithm was terminated when the NRMSE of the observation vector plateaued as shown in the insets.

After MLEM reconstructions using both the small and large detector models on the bare Cf-252 point source data, we find that using the small detector model degrades the angular resolution by 0.8% and increases the NRMSE of the observations by 1.3%. Thus, for this c-TEI design, using the large detector model instead of the small detector model does not lead to appreciable improvement in the reconstructed images.

4.4 Conclusion

Previous work on the design process of c-TEI systems is limited, thus this chapter explores the tradeoffs between size, weight, angular resolution, and CNR. Based on those simulations, we built a 1D, dual-particle, c-TEI system called MATADOR. We also showed that when the NRMSE between the small and large detector models is small ($\sim$ 1.4% for MATADOR), the benefit of using the large detector model as opposed to the small detector model is minimal. For MATADOR, the angular resolution is only 0.8% better. Although the benefit from using the large detector model is not appreciable for this c-TEI system, it is easy to imagine smaller mask geometries where it would provide greater improvement on performance, such as for a handheld system.

In the following chapters, we use the MATADOR system to verify the system responses described in Chap. III and then explore and implement adaptive imaging concepts.

CHAPTER V

Verifying the System Response Models

This chapter presents experimental validation of the large and offset detector models (Sec. 5.1 and 5.2 respectively) using data collected with the MATADOR system[1].

5.1 Verifying the Large Detector Model

To verify the large detector model, we use a shadow bar measurement. A 2.4 mCi Cf-252 point source was placed 3m from the MATADOR system[2] and imaged for 30 min at 12°/min. Next, as shown in Fig. 5.1, a 7.62 cm × 10.16 cm × 30 cm high-density polyethylene (HDPE) block was placed directly between the Cf-252 source and the detector such that no source neutrons would interact with the detector without first scattering off the mask or the surrounding environment. The shadow bar neutron count rate as a function of mask rotation angle was then subtracted from the bare source neutron count rate, thus removing all source scatter from the mask, source scatter from the surrounding environment, and natural background. This yields the modulation of the source by the mask. Fig. 5.2 shows the experimental data alongside the predictions from both the small detector and the large detector

[1]Parts of this chapter are adapted from [152].
[2]For details on the MATADOR system, see Chap. IV.

models. Qualitatively, the experimental data and the expected response match.

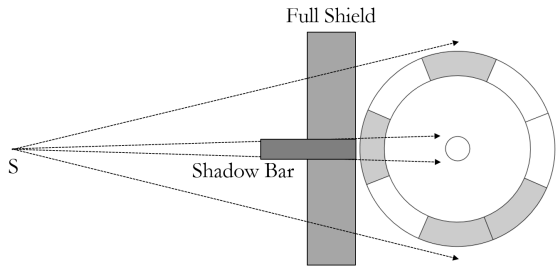

Figure 5.1: Experimental set-up for two separate measurements. The 2.4 mCi Cf-252 point source is 3 meters from the detector. In the first measurement, a shadow bar blocks all neutrons from directly interacting with the detector. In the second measurement, a HDPE shield blocks all neutrons from directly interacting with the detector and the mask. Not to scale.

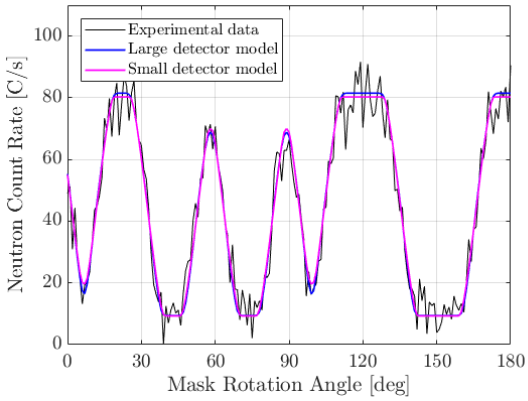

Figure 5.2: Neutron count rate versus mask rotation angle found from subtracting the shadow bar measurement from the bare source measurement. For this c-TEI design, both the small and large detector models show good agreement with the measured data.

5.1.1 Regarding the Assumption of Uniform Mask Scatter

The large detector model assumes that source scatter from the mask is constant as a function of mask rotation angle. To test this assumption, we isolate the mask scatter component and conduct a chi-square goodness-of-fit test. As shown in Fig. 5.1, a 15 cm thick HDPE shield was placed between the source and the entire imaging system such that no source particles would interact with the detector or the mask

without first scattering off the surrounding environment. Recall that the shadow bar measurement blocked only the direct path between the source and detector. By subtracting the shadow bar measurement from this full shield measurement, for each mask orientation, we can isolate the contribution from the source scatter off the mask. A chi-square test was conducted with the null hypothesis that the source scatter off the mask was sampled from a Skellam distribution[3]. Using the typical significance level 0.05 and a sample size of 360, we failed to reject the null hypothesis, $\chi^2(df = 22, N = 360) = 28.4, p = 0.164$[4]. That is to say, we failed to reject the assumption that the scatter from the mask is uniform as a function of mask rotation angle.

5.2 Verifying the Offset Detector Model

The offset detector model must be verified for two different tasks. First, given some measured data, the offset detector model must be able to accurately and precisely estimate the underlying source parameters (e.g. source position and source strength) that generated the measured data. To do this, we collect data from a known source, in this case a Cf-252 point source, and see how well the offset detector model can estimate the source parameters as a function of detector position. If the imaging model is accurate and precise, then the source position and intensity estimates will match the expected values and the estimates will be the same for all detector positions. To estimate the unknown parameters, we use maximum likelihood (ML) (Eq. 2.26).

Second, the offset detector model must predict the expected observation vector for any MATADOR configuration using data from a different configuration. As we will

[3]The difference of two Poisson distribution is a Skellam distribution with the mean equal to the difference of the means and variance equal to the sum of the two means.

[4]*df* stands for degrees of freedom.

see, the source position and source intensity estimates do not vary significantly with detector position, but the unmodulated intensity[5] does vary significantly with detector position. Scatter from the environment and scatter from the mask are difficult to predict since the scattered energy plays a large role in the detection efficiency for fast neutrons. It is possible to take these effects into account using MCNP, but this approach was avoided here because of the large computational burden - scatter from the environment would need to be recalculated for every environment since factors such as the vertical position of the source can drastically change the environmental scatter contribution.

Although in the MATADOR system, the detector can move to any position inside the mask (+/- 100 μm), for computational reasons, we only verify the offset detector model for 145 detector positions as shown in Fig. 5.3. Detector positions are sampled in concentric rings, each ring being 2 cm larger in radius than the previous. Within each ring, each detector position is <2 cm away from the next nearest detector position. Detector position indices are arbitrarily assigned from the outer most ring starting at $(12\text{ cm}, 0^\circ)$ and moving in the $+\theta$ direction. Once all detector positions in one ring have been assigned an index, indexing moves one ring inwards. Since all detector positions are placed 2 cm apart, the number of detector positions decreases from the outer most ring to the center. There are 145 different detector positions with the 145th representing the center.

[5]Recall that the unmodulated intensity consists of natural background and source scatter from the mask, environment, and detector.

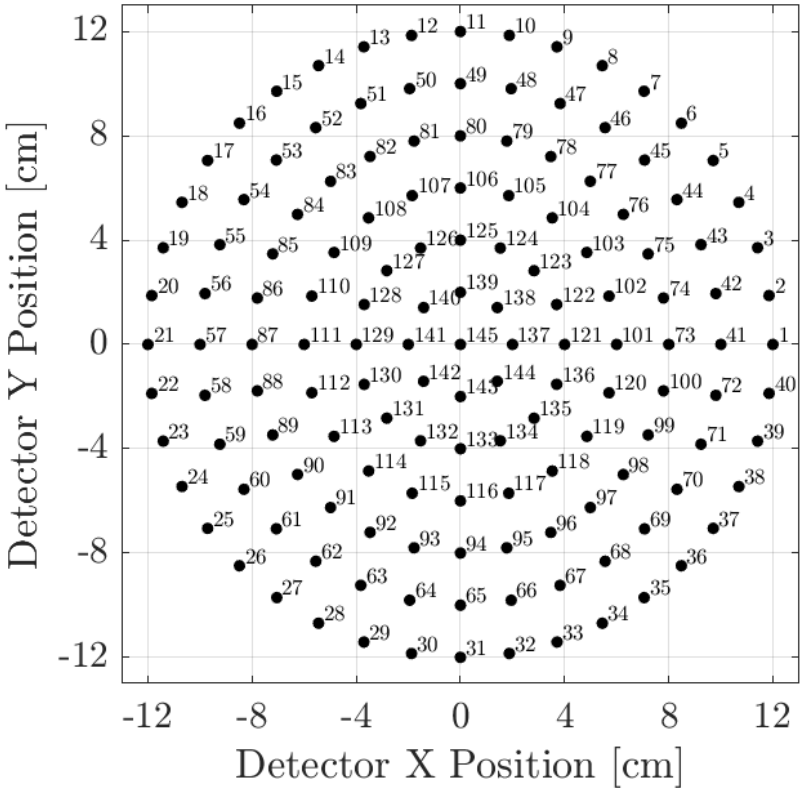

Figure 5.3: Index map for detector positions.

5.2.1 Experimental Setup

A 1.85 mCi Cf-252 source was placed at (90 cm, 178°) and data was collected at each detector position for 90s. When the detector is at the center, data was collected for 70.5 minutes.

The known sources of scatter from the environment are the concrete floor ∼1.25 m from the center of the system and a concrete wall ∼2 m in the +y direction from the system. All of the data was collected sequentially on the same day in approximately 5 hours. The source was not moved during the duration of this measurement and the rotary table was re-zeroed every 10 revolutions and likely has an error <0.30°.

5.2.2 Analysis

For each detector position, there are three unknowns for the point source: the source position (ϕ), the source intensity (α), and the unmodulated intensity (b_d) - we assume the radial position of the source (r) is known and fixed at 90 cm. To find the maximum likelihood estimate (MLE), for each source position, we created a new system response matrix that contained only the system response for that source position and the system response for the unmodulated intensity and then found the ML solution for that source position and recorded the negative log-likelihood. The source position with the minimum negative log-likelihood is the ML source position alongside the ML intensity estimates for that position. Since scatter is a key process that is not modelled in Eq. 3.11, this process was repeated for different light output ranges to get an idea of how scatter impacts the MLEs.

Light output ranges considered:

- $>$ 40 keVee
- 50-150 keVee, 150-250 keVee, ... 950-1050 keVee.

For each of the unknown parameters, we will create a plot of the MLEs as a function of detector position. If the offset detector model is accurate and precise, the estimates will not change as a function of detector position. In order to see if the estimates do change as a function of detector position, we will look at the average value for source-side and non-source-side detector positions. Since the source is at $\sim$180°, any detector position with an x-position less than 0 is considered source-side and any detector position with an x-position greater than 0 is considered non-source-side.

Additionally:

- The number of detections at each light output ranges was not held constant; the measurement time was held constant.

- For this analysis, we only utilize pulses with 99.9999% probability of being a fast neutron thus misclassification of gamma rays as fast neutrons is likely not a factor in model mismatch. These results are for stilbene only.

- The system response map was not changed for different light output ranges. The system response has 0.2° bins.

- For almost all detector positions, only 90s of data is available. When the detector is at the center, 70.5 minutes of data is available. Most of the results in Sec. 5.2.3 only use 90s of data when the detector is at the center of the mask. Only Fig. 5.11 uses all of the data.

5.2.3 Results

The 1.85 mCi Cf-252 source is at (90 cm, 178°) as shown in Fig. 5.4.

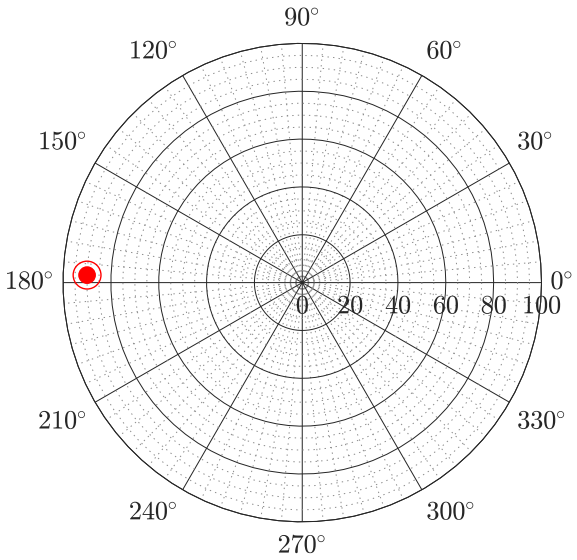

Figure 5.4: A 1.85 mCi Cf-252 source placed at (90 cm, 178°). For reference, in MATADOR, the outer radius of the mask is 25.7 cm and the detector radius is 5.08 cm.

Fig. 5.5 shows the source position MLEs plotted for each detector position for fast neutrons depositing more than 40 keVee. Although the source never moved throughout the experiment, the source position estimates range from 178°-181°. Note that most of the estimates are within 1°. There are a finite number of counts at each detector position, see Fig. 5.6, thus some of the variance may be due to counting statistics.

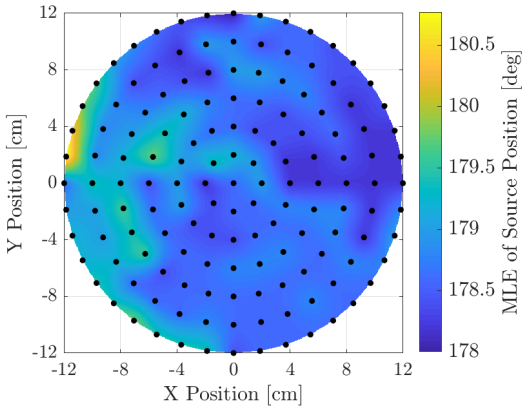

Figure 5.5: Source position MLE for fast neutrons deposition > 40 keVee. The black dots are all of the detector positions that were considered. Space between detector positions has been interpolated.

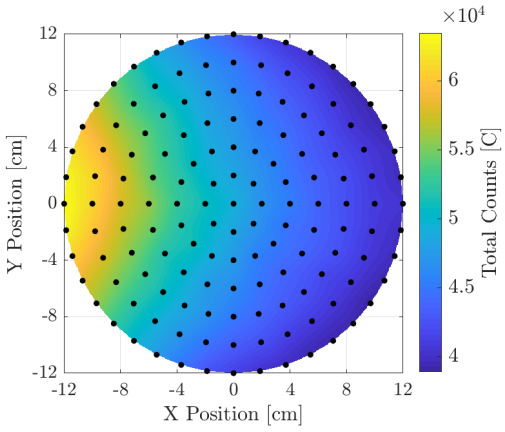

Figure 5.6: Neutron counts with > 40 keVee as a function of detector position. Since the source is in the near field, the count rate is strongly dependent on the source-to-detector distance.

In Fig. 5.5, there appears to be a systematic difference in source position MLEs

from detector positions that are closer to the source (source-side, x < 0) compared to those that are further away (non-source-side, x > 0). Fig. 5.7 plots the average source position MLE from the source-side detector positions and non-source-side detector positions as a function of light output[6]. Regardless of energy deposited, there appears to be a 0.5° difference between the source-side and non-source-side estimates.

Thus, we conclude that offset detector model suffers from model mismatch < 1°. This model mismatch is not dependent on the light output range implying that it is not due to scatter but instead may be caused by loss of alignment of the rotary table during measurement or imperfect manufacturing and alignment of the mask and linear actuators. There also appears to be a bias of ∼1° in the source position MLEs since the true source is at 178°. This bias and uncertainty is small since the angular width of a mask element is ∼10.3°.

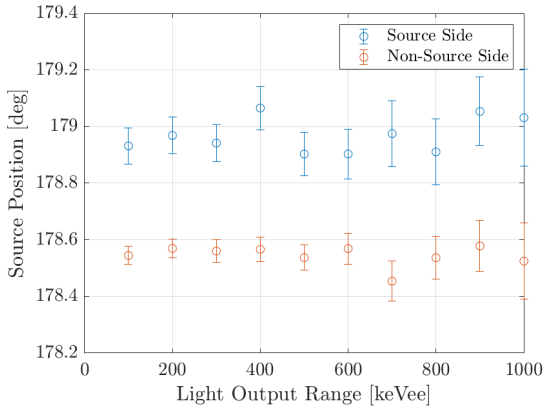

Figure 5.7: Average source position MLE from source-side (x < 0) and non-source-side (x > 0) detector positions as function of light output. Error bars represent one standard error of the mean.

Fig. 5.8 shows the source intensity MLEs plotted as a function of detector position. A 1.85 mCi Cf-252 source emits 7.97×10^6 n/s thus the offset detector model over predicts the source intensity by 7-17% of the true emission rate. Also, in Fig. 5.8,

[6]The source position MLE maps for different light output ranges are in Appendix A.

we see a clear systematic bias in the source intensity MLEs. Compared to the mean, the estimated source intensities are up to 5% lower when the detector is closer to the source and up to 5% greater when the detector is further away from the source. This systematic bias may be due to scatter from the environment or the mask. Note that scatter from the environment or mask must be modulated in a similar manner to the point source for the source intensities to change. Also, because the detector is moving with respect to the mask, the fully coded field-of-view (FOV) in the z direction[7] is changing which will affect the probability of environmental scatter being modulated by the mask.

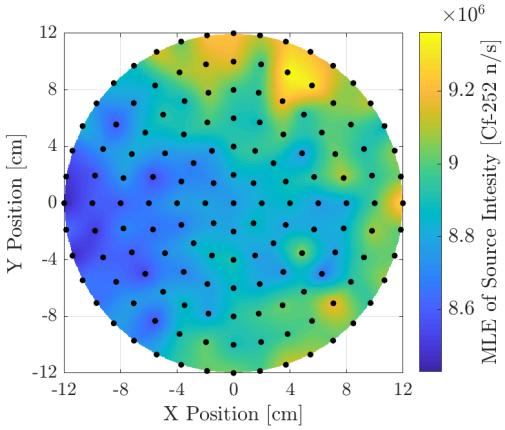

Figure 5.8: Source intensity MLE from fast neutrons depositing > 40 keVee. Space between detector positions has been interpolated.

If scatter from the environment or mask are dominant causes for the model mismatch, then increasing the light output range should reduce scatter related bias. Fig. 5.9 shows the average source intensity MLEs from source-side detector positions and non-source-side detector positions as a function of light output[8]. Fig. 5.10 shows the corresponding percent difference plot.

[7]The z direction is defined as the cross product of the x and y axes.
[8]The source intensity MLE maps for different light output ranges are in Appendix A

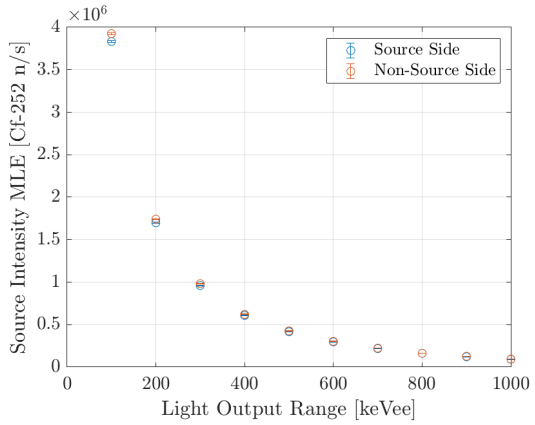

Figure 5.9: Average source intensity MLEs from source-side (x < 0) and non-source-side (x > 0) detector positions as function of light output. Error bars represent one standard error of the mean.

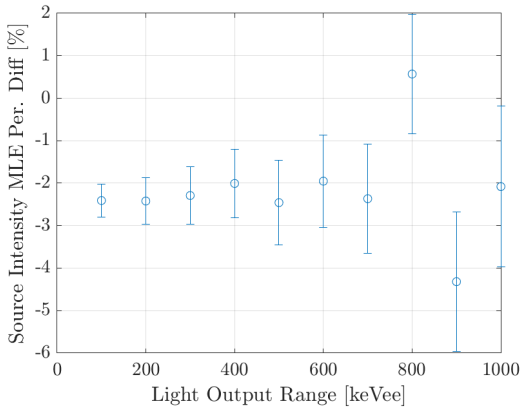

Figure 5.10: Percent difference between source-side (x < 0) and non-source-side (x > 0) average source intensity MLE as function of light output. Error bars are propagated from Fig. 5.9.

For most light output ranges, there is a consistent, systematic bias of 2-3% between the source-side and non-source-side intensity estimates. This implies that the difference in source intensity MLEs made with data collected closer to the source or further away from the source is not dependent on scatter. Instead such a difference might occur if the source was positioned a few centimeters further away from the detector than the response map expected. Thus, we attribute the systematic bias between the source-side and non-source-side intensity estimates to an imperfect

experimental setup.

To see if the offset detector model can fit the observed data, we will compare the experimental data collected when the detector is centered to the point source ML forward projection. The two responses should match closely. As a quantitative way to gauge the fit from the offset detector model, we will compare the measured normalized root mean squared error (NRMSE) between the experimental data and the ML forward projection to the expected NRMSE if the ML forward projection was only corrupted by Poisson noise.

Fig. 5.11 shows the experimental data and the ML forward projection when the detector is at the center[9]. For a light output threshold of 40 keVee, the NRMSE is 3.3% - from Poisson noise, one would expect a NRMSE of 2.6%[10]. This implies that the offset detector model does not perfectly fit the experimental data. We can observe this effect in Fig. 5.11. For example, at a mask rotation angle of $\sim 50^\circ$, the large detector model is under predicting the count rate and at $\sim 240^\circ$, the large detector model is over predicting the count rate. At both positions, the source is fully blocked by a closed mask region. Similarly, $\sim 210^\circ$ and $\sim 280^\circ$ are under and over predictions in the expected counts when the source is in a fully open region of the mask. This mismatch may be caused by non-uniform background or non-uniform scatter from the environment or mask.

[9]Note that all 70.5 minutes of data was used to make Fig. 5.11 instead of 90s.

[10]The expected NRMSE was found by creating 1,000 Poisson replicates the ML forward projection of the experimental data, finding the ML forward projection for each replicate, and then calculating the NRMSE for each replicate and averaging.

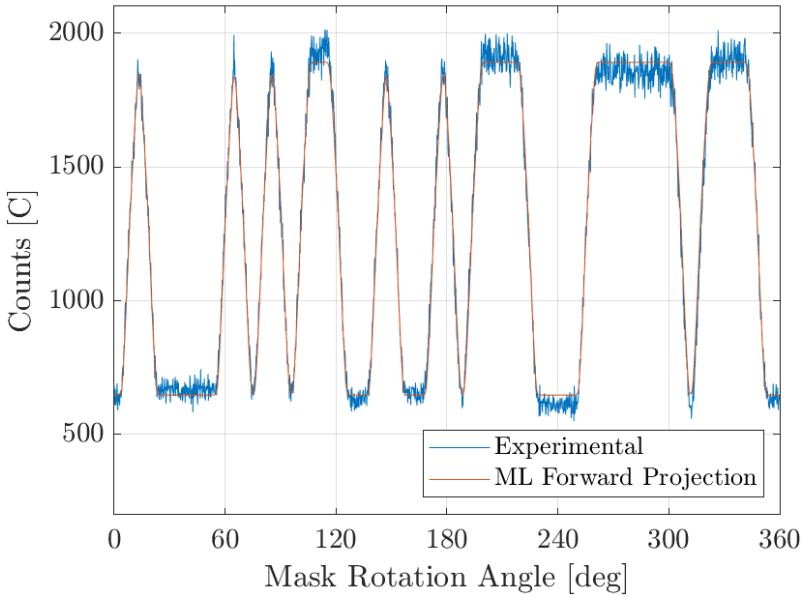

Figure 5.11: Measured counts and point source ML forward projection from the large detector model as a function of mask rotation angle. Notice that the large detector model may under or over predict the expected count rate.

If this model mismatch is caused by scatter, then the experimental NRMSE should match the expected as the light output threshold increases. As shown in Fig. 5.12, as the light output range increases, the NRMSE approaches the expected NRMSE, implying that the mismatch is related to scatter from the environment or the mask. In Sec. 5.1.1, we verified the assumption that scatter from the mask is constant for all mask rotation angles when the detector is at the center of the mask. Thus, either the chi-squared goodness-of-fit test in Sec. 5.1.1 did not have the power to detect the non-uniform scatter from the mask or scatter from the environment was not uniform for this experiment. This can happen if there is a source of scatter in the environment such as a concrete pillar or a wall. At this point, we cannot attribute the non-uniform scatter to any specific cause.

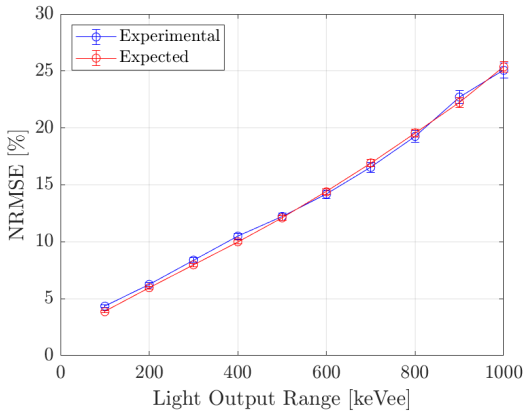

Figure 5.12: NRMSE between the measured data and the point source ML forward projection from the large detector model as a function of light output range. As the light output range increases, the model mismatch decreases.

Based on Fig. 5.12, one method to reduce the model mismatch is to raise the detection threshold to ∼600 keVee. Unfortunately, this solution is not reasonable since the majority of pulses have low light output. Raising the detection threshold to 600 keVee would reduce the count rate by 90% relative to the count rate for a threshold of 40 keVee. For general image reconstruction applications, we find that this model mismatch does not cause significant artifacts in the image. For applications that are sensitive to model mismatch, one may need a more accurate system response such as one made from experimental data (see Sec. 3.4).

For the second task of predicting, the source position and source intensity estimates from one detector position can be readily used to predict the response at any other detector position evidenced by the low variability in these estimates with detector position. But, the unmodulated intensity is not constant with detector position which poses a challenge.

As shown in Fig. 5.13, unmodulated intensity has a strong dependence on source-to-detector distance. Although room return does not fall with the inverse square law, since scatter off the floor is a large component in room return, it is not surprising

to see a strong dependence on source-to-detector distance. We can roughly account for this effect through the source-to-background ratio (S:B) as shown in Fig. 5.14. Here, S:B is defined as the expected count rate from a fully open region of the mask[11] divided by the unmodulated intensity. In this case, the S:B ratio is mostly constant as a function of detector position - the values range from ± 5% from the average.

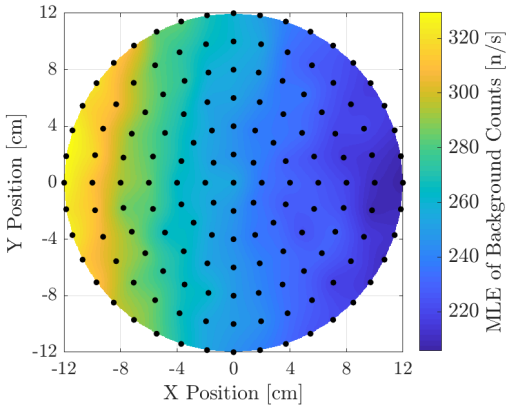

Figure 5.13: Unmodulated intensity MLEs as a function of detector position.

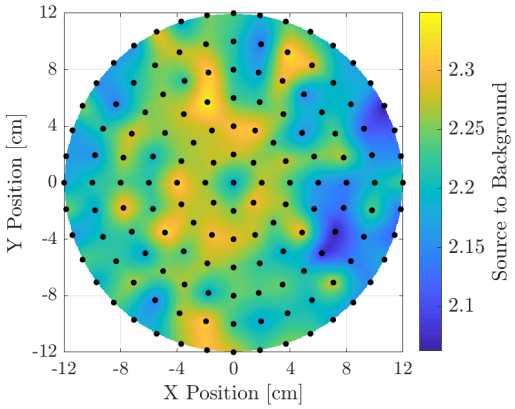

Figure 5.14: S:B ratio as a function of detector position.

Thus, for the prediction task, we will assume that the S:B ratio is constant at 2.2:1 for all detector and source positions. Note that scatter from the environment is highly dependent on many experiment specific factors including distance to the

[11]By fully open, we mean that no part of the detector is blocked by the mask.

source and height of the source relative to the ground. Thus, assuming the S:B ratio is the same for all experiments will have limited validity.

Overall, based on these findings, we can conclude that the offset detector model can be used to generate precise estimates of source position and source intensity from data collected from the MATADOR imaging system. For this well-controlled scenario, the source position uncertainty is $< 1^\circ$ and the source intensity uncertainty is $< 5\%$. In terms of accuracy, the source position estimates were within 1° of the true source location and the source intensity estimates were within 10%. Finally, the offset detector model can also be used to predict the expected observation vector for any detector position since the S:B ratio is mostly constant at 2.2:1 for all detector positions.

5.3 Conclusion

We used experimental data collected with the MATADOR system to verify the large and offset detector models. Based on the shadowbar results, the large detector model fits the measured data well. Additionally, we failed to reject the assumption that scatter from the mask is constant as a function of mask rotation angle when the detector is at the center of the MATADOR system.

With respect to the offset detector model, we find that it can be used to generate precise estimates of source position and source intensity for the MATADOR system. The source position uncertainty is $< 1^\circ$ and the source intensity uncertainty is $< 5\%$. In terms of accuracy, the source position estimates were within 1° of the true source location and the source intensity estimates were within 10%. Additionally, we find that although the unmodulated intensity changes as the detector moves inside the

mask, the S:B[12], is relatively constant. This enables one to use the source position, source intensity, and unmodualted intensity estimates from one system configuration to predict the response expected in a different system configuration. The ability to predict the expected response is essential to adaptive imaging.

[12]S:B is defined as the count rate from a fully open region of the mask divided by the unmodulated intensity

CHAPTER VI

Improving Angular Resolution Using Adaptive Detector Movements

High resolution imaging is an important task in nuclear non-proliferation. For example, one may need high resolution to separate multiple sources that are close together such as warheads on an inter-continental ballistic missile. From a technical perspective, often the angular resolution of a system is used as a metric to compare different imaging systems. Thus, this chapter investigates the benefit of adaptive imaging on improving angular resolution in a cylindrical, time-encoded imaging (c-TEI) system. For simplicity, we focus on achieving greater angular resolution with only adaptive detector movements and no adaptive mask movements. For each detector position, a full mask rotation of data was collected at a constant rotation speed. Also, we treat the radial position of a source, r_j, as an known - all sources are at 90 cm and only the system response for sources at 90 cm is used.

The goal for this chapter is to set an upper bound on the achievable gain in angular resolution using adaptive detector movements. We assume that the number and positions of all sources are known before hand, thus there is no added uncertainty from source detection or parameter estimation processes. In this sense, we are considering clairvoyant detector movements. We consider the following source scenarios:

1. One point source

2. Two point sources

    A Equal intensity sources that are close together

    B Different intensity sources at various separations

For each case, we find the detector position that achieves the best angular resolution and compare that to the detector-centered, conventional c-TEI case. We also consider what benefit collecting data at multiple detector positions may have. Most of the analysis is done using simulations, but we will use experimental data to spot check the results. Only fast neutron results are shown.

Sec. 6.1 develops some first-order intuition for this problem to help understand results later in the Chapter. As a proxy for angular resolution, we use the square root of the Cramér-Rao lower bound (CRLB) of the source position, which is discussed in more detail in Sec. 6.2. Sec. 6.3 provides an overview of the simulations. Sec. 6.4 includes results for a point source and Sec. 6.5 includes results for two point sources.

6.1 First-Order Intuition

In spatial coded aperture (SCA) systems, to the first order, the angular resolution is proportional to the angular width of a mask element - we use the same intuition here. As shown in Fig. 6.1, when one moves the detector from the center of the mask (D_0) to an offset position (D_1), along one axis, called the imaging axis, the mask-to-detector distance increases. This increase in mask-to-detector distance means that the angular width of a mask element decreases ($\theta_1 < \theta_0$) and thus the angular resolution of the system is better along the imaging axis. The imaging axis is an extension of vector pointing from the center of the detector to the center of the mask.

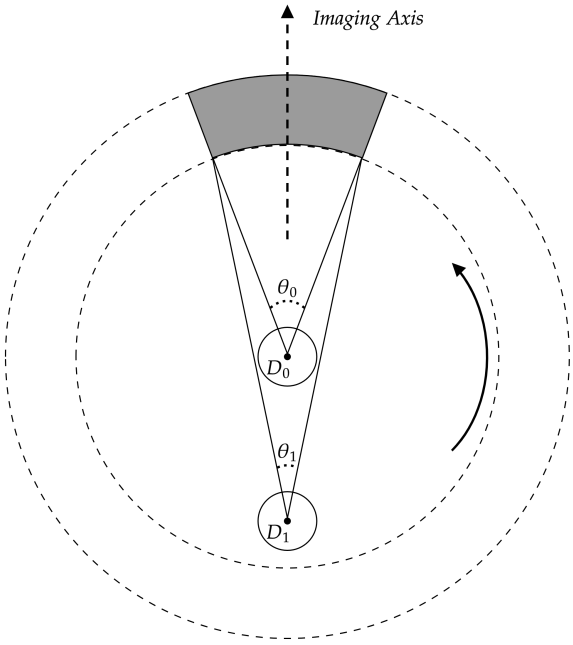

Figure 6.1: Schematic showing an example of adaptive imaging. If one moves the detector from the center of the mask (D_0) to an offset position (D_1), along one axis, called the imaging axis, the mask-to-detector distance increases and thus the angular resolution along the imaging axis improves.

While moving the detector can provide better angular resolution along the imaging axis, along other directions, the angular resolution may be worse if the mask-to-detector distance has decreased or the open-to-closed mask element transitions are obscured and blurred by the thick mask elements. To help understand this concept, imagine another axis, called the source axis, that is an extension of the vector from the center of the mask to the source as shown in Fig. 6.2. When the imaging axis and the source axis are closely aligned, the system will achieve better angular resolution, but when the imaging axis and the source axis are not aligned, the system will have worse angular resolution. This is clear when looking at the sensitivity-normalized point spread functions (PSFs) shown in Fig. 6.3. Since the detector is at (12,0) cm, sources near 180° will be reconstructed with higher resolution than those near 0°. Fig. 6.4 is a plot of some horizontal slices of Fig. 6.3. Notice that as the source axis

and the imaging axis move further apart, the PSF broadens and the sidelobes change.

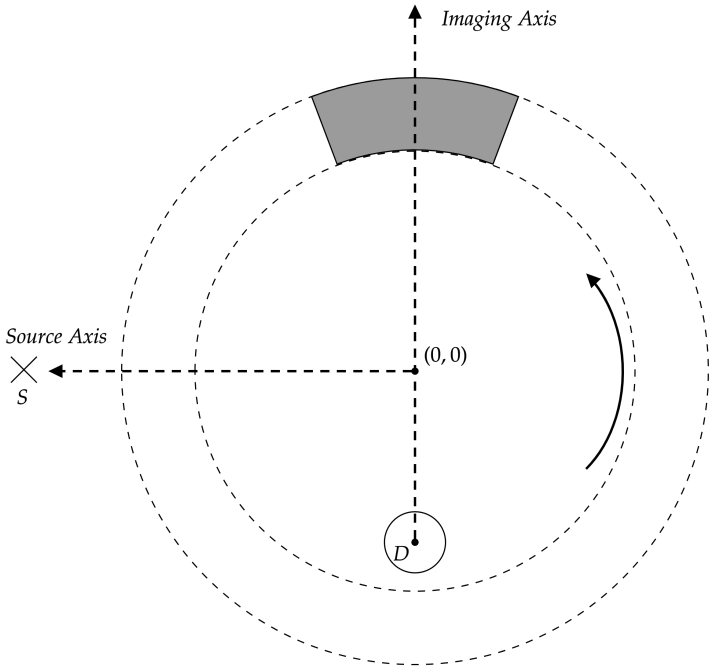

Figure 6.2: Schematic showing both the imaging axis and the source axis. The imaging axis points from the center of the detector to the center of the mask. The source axis points from the center of the mask to the source.

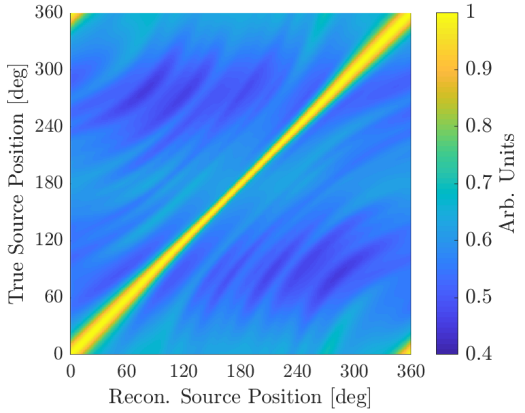

Figure 6.3: Sensitivity-normalized PSFs for a detector at D(12,0) cm. The PSF changes with true source position because the system is not LSI. Sources are 90 cm from the center of the mask.

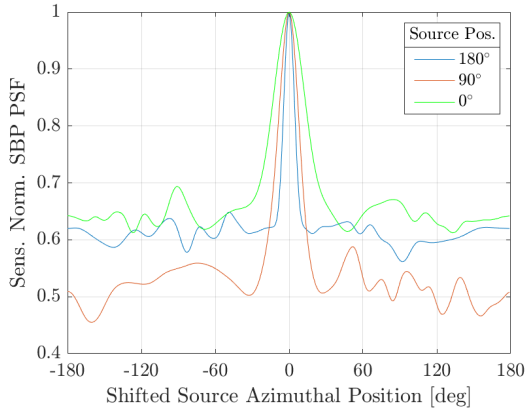

Figure 6.4: Sensitivity-normalized PSF for sources at 180°, 90°, and 0°. The detector is at D(12,0) cm thus 180° has the best resolution since it is directly in line with the imaging axis. Notice that the PSF broadens as the sources move off axis from the imaging axis and the sidelobes change.

We can confirm this intuition with some experimental reconstructions. Fig. 6.5 is a plot of fast-neutron maximum likelihood expectation maximization (MLEM) reconstructions of a 1.85 mCi Cf-252 point source at (90 cm,178°). Reconstructions were made using data from detectors at (12,0) cm, (0,12) cm, and (-12,0) cm - the detector at (12,0) cm has the best angular resolution since the source axis and imaging axis closely aligned. As the source axis and the imaging axis move apart, the angular resolution for the source is worse.

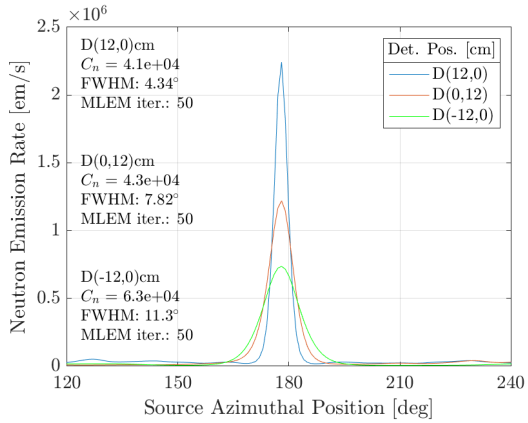

Figure 6.5: MLEM reconstructions using data from detectors at (12,0) cm, (0,12) cm, and (-12,0) cm. The source is at (90 cm,178°).

Thus, we expect that maximizing the detector-to-mask distance along the source axis will lead to higher angular resolution reconstructions. Although this intuition is helpful in understanding angular resolution in c-TEI systems, it is only applicable when there is one source in the field-of-view (FOV). When there are multiple sources spread out in the FOV with different intensities, using our intuition to guide detector movements may not achieve the best results. Instead, we use a definition of angular resolution based on the CRLB which incorporates the effect of other sources and counting statistics into the calculation for angular resolution.

6.2 Cramér-Rao Lower Bound

First, this section introduces a definition for angular resolution based on the CRLB and then calculates the Fisher information matrix (FIM) and the CRLB for the offset detector model. To gain some insight into this measure of angular resolution, we consider a simple case where there is one source in the field and no background.

As discussed in Sec. 2.4.1, the CRLB is the lower bound on the variance for all unbiased estimators of a deterministic parameter [149]. As a measure for angular resolution, both the CRLB of the source position and the CRLB of the distance between two sources have been used [155, 156]. Here, we define angular resolution for a source as the square root of the CRLB of the source position:

$$\sigma_{\phi_j}(\boldsymbol{\theta}, A) = \sqrt{\text{CRLB}(\boldsymbol{\theta}, A)[I_{\phi_j}, I_{\phi_j}]} \tag{6.1}$$

where σ_{ϕ_j} is the angular resolution, $\boldsymbol{\theta}$ are the parameters of interest, and $[I_{\phi_j}, I_{\phi_j}]$ are the indexes of the jth source position ϕ_j. To simplify notation, we will simply use $[\phi_j, \phi_j]$ instead of $[I_{\phi_j}, I_{\phi_j}]$. For the clairvoyant analysis in this chapter, we assume that $\boldsymbol{\theta}$ is known. Recall that the CRLB is found by inverting the FIM - see Sec. 2.4.1.

To find the CRLB matrix for the offset detector model, assume there are S sources in the field of view and the imaging system has collected data at D detector positions.

For each source, there are two unknown parameters $\boldsymbol{\theta}_j = [\alpha_j \ \phi_j]^T$ where

- $\boldsymbol{\theta}_j$ is the parameter vector for the jth source,
- α_j is the intensity of the jth source, and
- ϕ_j is the azimuthal position of the jth source.

Let

- $\boldsymbol{\theta}_S = \left[\boldsymbol{\theta}_1^T \cdots \boldsymbol{\theta}_j^T\right]^T$ be a vertically concatenated parameter vector,
- $\boldsymbol{\alpha} = [\alpha_1 \cdots \alpha_j]^T$ be the vector of source intensities, and
- $\boldsymbol{\phi} = [\phi_1 \cdots \phi_j]^T$ be the vector of azimuthal source source positions.

Since data was collected at D detector positions, let $\boldsymbol{b}_D$ be a vector of unmodulated intensities and $\boldsymbol{\theta} = \left[\boldsymbol{\theta}_S^T \ \boldsymbol{b}_D^T\right]^T$. Thus, there are $(2S + D)$ unknowns. For clarity, we redefine the offset detector model using summations instead of matrix notation:

$$\overline{y}_i = \left(\sum_{j=1}^{S} \left(\alpha_j A\left[i, j'(\phi_j)\right] \right) + b_D[i] \right) t[i] \tag{6.2}$$

where i is the measurement index that spans all mask rotation angles and detector positions measured, and j' is a function that transforms the source position into index space. We use the overline symbol, $\overline{(\cdot)}$, to differentiate between expected measurement and noisy measurement. Thus, $\overline{y}_i$ is the expected measurement for the ith measurement.

Recall from Sec. 2.4.1 that the FIM is

$$I(\boldsymbol{\theta}) = -\mathbb{E}\left[\nabla_{\boldsymbol{\theta}} \nabla_{\boldsymbol{\theta}}^T \ \ell(\boldsymbol{y} \mid \boldsymbol{\theta})\right] \tag{6.3}$$

and the log-likelihood ($\ell(\boldsymbol{y} \mid \boldsymbol{\theta})$) is

$$\ell(\boldsymbol{y} \mid \boldsymbol{\theta}) = \sum_{i=1}^{N_O} \left(y_i \ln\left(\overline{y}_i\right) - \overline{y}_i - \ln\left(y_i!\right) \right) \tag{6.4}$$

where N_O is the number of observations. Plugging Eq. 6.4 into Eq. 6.3, we find[1]

$$I(\boldsymbol{\theta}) = \sum_{i=1}^{N_O} \left(\frac{\nabla_{\boldsymbol{\theta}}\ \overline{y}_i \nabla_{\boldsymbol{\theta}}^T\ \overline{y}_i}{\overline{y}_i} \right) \tag{6.5}$$

where $\nabla_{\boldsymbol{\theta}}\ \overline{y}_i$ is a vector of the partial derivatives of $\overline{y}_i$ with respect to each unknown parameter. For the jth source:

$$\begin{aligned} \frac{\partial \overline{y}_i}{\partial \alpha_j} &= A[i, j'(\phi_j)] t[i] \\ \frac{\partial \overline{y}_i}{\partial \phi_j} &= \alpha_j t[i] \frac{\partial A[i, j'(\phi_j)]}{\partial \phi_j} \\ \frac{\partial \overline{y}_i}{\partial b_d} &= t[i] \end{aligned} \tag{6.6}$$

We use a numerical approach to find the derivative of the system response matrix with respect to the jth source position:

$$\frac{\partial A[i, j'(\phi_j)]}{\partial \phi_j} = \frac{A[i, j'(\phi_j + \Delta\phi)] - A[i, j'(\phi_j - \Delta\phi)]}{2\Delta\phi}. \tag{6.7}$$

For the MATADOR system, we find that $\Delta\phi$ can be as large as 1° without any loss of accuracy in calculating $\dfrac{\partial A[i, j'(\phi_j)]}{\partial \phi_j}$.

Thus, plugging in Eq. 6.7 and 6.6 into Eq. 6.5, we can find the FIM - the diagonal

[1]For more details, see Appendix B

elements are

$$
\begin{aligned}
I(\boldsymbol{\theta})[\alpha_j, \alpha_j] &= \sum_{i=1}^{N_O} \frac{\left(A\left[i, j'(\phi_j)\right]\right)^2 t[i]}{\sum_{j=1}^{S}\left(\alpha_j A\left[i, j'(\phi_j)\right]\right) + b[i]} \\
I(\boldsymbol{\theta})[\phi_j, \phi_j] &= \sum_{i=1}^{N_O} \frac{\left(\alpha_j \dfrac{\partial A[i, j'(\phi_j)]}{\partial \phi_j}\right)^2 t[i]}{\sum_{j=1}^{S}\left(\alpha_j A\left[i, j'(\phi_j)\right]\right) + b[i]} \\
I(\boldsymbol{\theta})[b_d, b_d] &= \sum_{i=1}^{N_O} \frac{t[i]}{\sum_{j=1}^{S}\left(\alpha_j A\left[i, j'(\phi_j)\right]\right) + b[i]}
\end{aligned}
\tag{6.8}
$$

We can use Eq. 6.8 to gain some insight into σ_{ϕ_j}. Assume that there is no background, $S = 1$, and the covariance between α_1 and ϕ_1 is small such that the CRLB ($I(\boldsymbol{\theta})^{-1}$) can be approximated as the reciprocal of the diagonal elements. In this case, σ_{ϕ_1} is minimized (thus best angular resolution) when $I(\boldsymbol{\theta})[\phi_1, \phi_1]$ is maximized:

$$
I(\boldsymbol{\theta})[\phi_1, \phi_1] = \sum_{i=1}^{N_O} \overline{y}_i \left(\frac{\dfrac{\partial A[i, j'(\phi_j)]}{\partial \phi_j}}{A[i, j'(\phi_j)]} \right)^2 . \tag{6.9}
$$

From Eq. 6.9, notice that the angular resolution improves both as the number of counts increases and as the relative difference of the system response between the estimated source position and its neighbors increases. This aligns with prior intuition: greater counts result in less measurement uncertainty and the greater the measurement difference between neighboring source pixels, the easier it is to estimate the source position.

As noted in Sec. 6.1, as the imaging axis and the source axis move apart, the angular resolution of the system degrades. Fig. 6.6 is the angular resolution predicted

by the CRLB as a function of source position for both the conventional, detector-centered case and for the detector at D(12,0) cm in the MATADOR system. There is only one source in the FOV ($S = 1$) and the S:B ratio is 2.2:1; $\boldsymbol{\theta} = [\alpha_1\ \phi_1\ b_1]^T$.

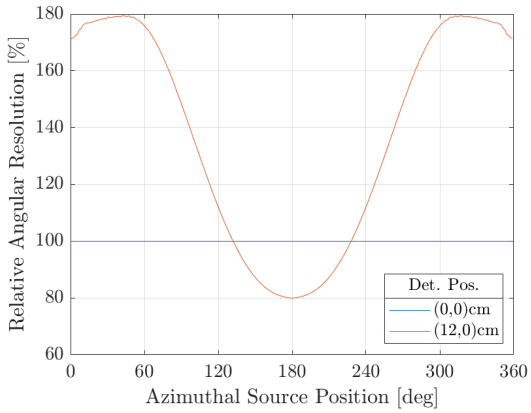

Figure 6.6: Relative change in angular resolution as a function of source position for the detector centered and detector at (12,0) cm. If the source axis is within ±50° of the imaging axis, the angular resolution improves, otherwise the performance for that source is worse than the conventional, detector-centered case.

When the source axis is within ±50° of the imaging axis, angular resolution of the offset detector is better than that of the centered detector, but if the source axis and imaging axis are more than ±50° apart, then the angular resolution is worse. Note that the source is in the near-field thus the number of counts is not constant.

Using the CRLB as a proxy for the angular resolution accounts for

- the covariances between unknowns such as the effect on estimating the position of a source given there is another source close by,
- the system response, thus any physics that are modelled in the system response are reflected in the CRLB, and
- the measured counts

but does not account for

- model mismatch between the imaging model and the experimental data and
- incorrect assumptions.

6.3 Overview of Simulations

We use a clairvoyant analysis to set an upper bound on the achievable gain in angular resolution from adaptive detector movements. By clairvoyant,we mean that the number and positions of all sources are known before hand so that there is no added uncertainty from the parameter estimation process. This section provides an overview of the simulations and the task-dependent objection function (ψ) that will be used to decide which detector position or positions provide the best performance.

All sources will be 90 cm from the center of the mask and the S:B ratio is assumed to be 2.2:1 for all detector positions. If there is one point source in the FOV, ψ is defined as

$$\psi(\boldsymbol{\theta}, A) = \left(1 - \frac{\sigma_\phi(\boldsymbol{\theta}, A)}{\sigma_\phi(\boldsymbol{\theta}, A_{D(0,0)})} \right) \tag{6.10}$$

where ψ is dependent on the parameters of interest ($\boldsymbol{\theta}$) and the system response (A). σ_ϕ is the angular resolution found using Eq. 6.1 and $A_{D(0,0)}$ is the system response for the conventional, detector-centered c-TEI system. We refer to Eq. 6.10 as the angular resolution gain. Since we are only considering adaptive detector movements, the optimization problem is

$$A_{\max} = \arg \max_{A \in \mathbb{A}} \psi(\boldsymbol{\theta}, A) \tag{6.11}$$

where $\mathbb{A}$ contains the system responses from each candidate detector position. Although in the MATADOR system, the detector can move to any position inside the mask (+/- 100 μm), for computational reasons, $\mathbb{A}$ only contains the system responses

from 145 detector positions which are shown in Fig. 6.7[2]. Thus for the analysis in this chapter, the optimal detector position must be one of the 145 detector positions in Fig. 6.7.

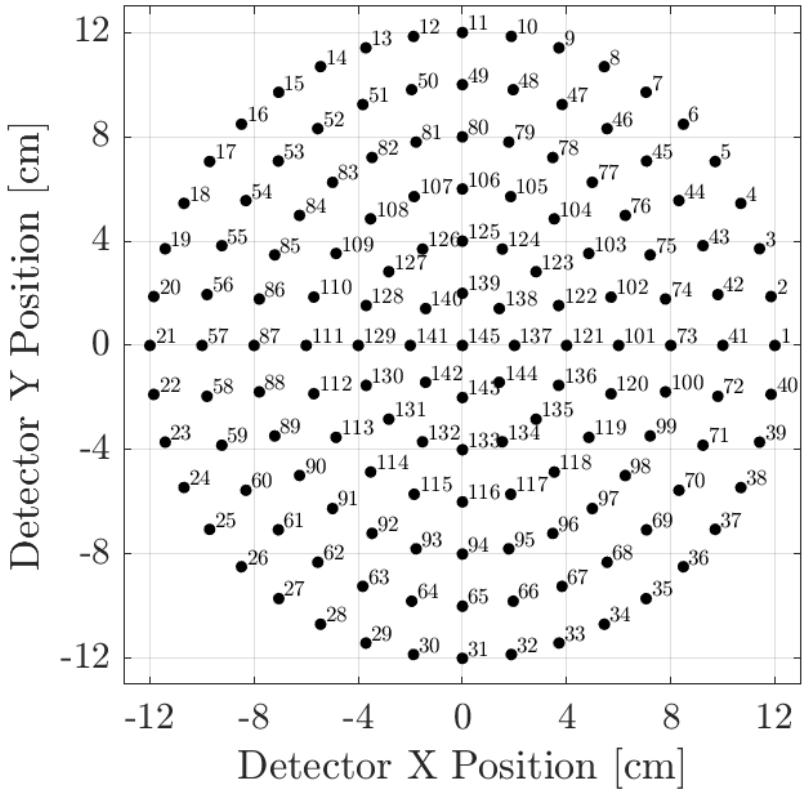

Figure 6.7: Index map for detector positions.

If there are multiple sources of interest, ψ is defined as

$$\psi(\boldsymbol{\theta}, A) = \left(1 - \frac{U\left(\boldsymbol{\sigma}_{\boldsymbol{\phi}}(\boldsymbol{\theta}, A)\right)}{U\left(\boldsymbol{\sigma}_{\boldsymbol{\phi}}(\boldsymbol{\theta}, A_{D(0,0)})\right)} \right) \tag{6.12}$$

[2]Recall that detector positions were sampled in concentric rings, each ring being 2 cm larger in radius than the previous. Within each ring, each detector position is < 2 cm away from the next nearest detector position. Detector indices are assigned from the outer most ring starting at $(12\text{ cm}, 0°)$ and moving in the $+\theta$ direction. Once all detector positions in one ring have been assigned an index, indexing moves one ring inwards. Since all detector positions are placed 2 cm apart, the number of detector positions decreases from the outer most ring to the center. There are 145 different detector positions with the 145th representing the center.

where $U\left(\boldsymbol{\sigma}_{\boldsymbol{\phi}}(\boldsymbol{\theta}, A)\right)$ is simply the quadrature-sum of the angular resolution for each source of interest:

$$U\left(\boldsymbol{\sigma}_{\boldsymbol{\phi}}(\boldsymbol{\theta}, A)\right) = \sqrt{\sum_{j=1}^{S} \sigma_{\phi_j}^2(\boldsymbol{\theta}, A)} \tag{6.13}$$

We will refer to Eq. 6.12 as the quadrature-sum angular resolution gain.

Sometimes we may want to find $A_{\max}$ that maximizes the angular resolution of a specific source when there are multiple sources in the FOV. In this case, we use Eq. 6.10 over Eq. 6.12. We refer to this as the individual angular resolution gain as opposed to the quadrature-sum angular resolution gain.

Finally, we also investigate the potential benefit of collecting data at two detector positions instead of just one. In this case, we must optimize over all combinations of detector positions and the relative time spent at each position. Let $\mathbb{A}^2$ be the set of system responses from 2 detector positions. Since Eq. 6.8 is order independent, there are $\binom{145+2-1}{2} = 10,585$ position combinations. Let $\mathbb{T}$ be the set that contains the time spent measuring at the first detector position relative to the total measurement time. We will constrain $\mathbb{T}$ to only vary from 10% to 90% every 10%. For the two detector optimization problem, we define A as

$$A = [A_{D_1} \cdot \tau; A_{D_2} \cdot (1 - \tau)] \tag{6.14}$$

where $A \in \mathbb{A}^2$, $\tau \in \mathbb{T}$, A_{D_1} is the system response at the first detector position, A_{D_2} is the system response at the second detector position, and the semicolon indicates vertical concatenation. Thus, the two detector optimization problem is

$$A_{\max}, \tau_{\max} = \underset{A \in \mathbb{A}^2, \tau \in \mathbb{T}}{\arg\max}\, \psi(\boldsymbol{\theta}, A) \tag{6.15}$$

Together, $A_{\max}$ and $\tau_{\max}$ describe the system response that maximizes ψ. All optimizations are done via brute force.

6.4 One Point Source Results

We start with the simplest case of one point source in the field. The source is positioned at 0° as shown in Fig. 6.8.

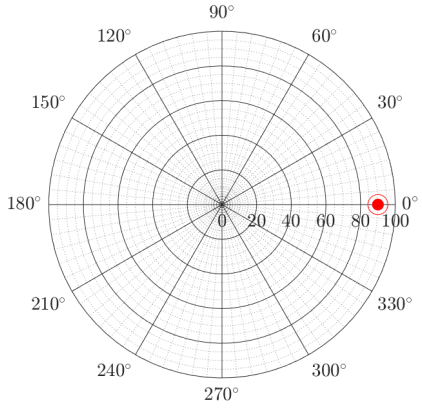

Figure 6.8: Point source at $(90\text{ cm}, 0°)$.

6.4.1 Best Detector Position

Fig. 6.9 shows the gain in angular resolution (Eq. 6.10) as a function of detector position - we call this a gain map. The black dots are all of the detector positions that were considered and the red dot represents the detector position with the greatest gain. The contour lines have the same values as the tick marks in the color bar. The space between detectors positions has been interpolated.

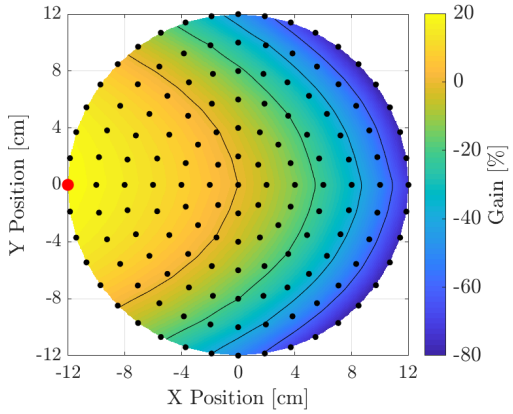

Figure 6.9: Gain in angular resolution as a function of detector position for a point source at $(90\text{ cm}, 0°)$. The black dots are all of the detector positions that were considered and the red dot represents the detector position with the greatest gain. The contour lines have the same values as the tick marks in the color bar. Space between detector positions has been interpolated.

As one would expect, the gain is greatest at $(-12, 0)$ cm which is the detector position that maximizes the detector-to-mask distance along the source axis. For a single point source, the CRLB predicts that adaptive detector movements can provide 20% better angular resolution compared to the conventional case, but if the detector position is incorrectly chosen, the loss in angular resolution can be up to 80%.

Experimental Validation

We experimentally validate the results using both MLEM reconstructions and ML estimation of the source position. For both analyses, we use data from a 1.85 mCi Cf-252 source at $(90\text{ cm}, 178°)$ measured for 90 s. For the conventional case, we use data collected when the detector is at the center of the mask and for the adaptive case, we use data collected when the detector is at $(-12, 0)$ cm.

Fig. 6.10 shows the MLEM reconstruction from both the conventional and adaptive data collections. Relative to the conventional reconstruction, the full width at half maximum (FWHM) of the adaptive reconstruction is 25.1% smaller.

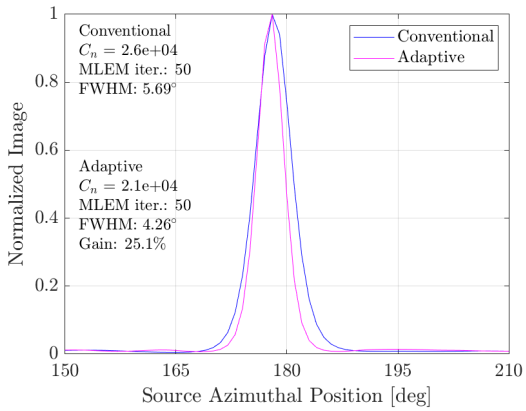

Figure 6.10: MLEM reconstructions for both the conventional, detector-centered case and the adaptive case. The source is at $(90\text{ cm}, 178°)$ and the adaptive case uses data collected at $(-12, 0)$ cm - the optimal clairvoyant detector position from Eq. 6.11.

Another method to validate the CRLB predictions is by comparing the distributions of source position maximum likelihood estimates (MLEs) ($\hat{\phi}_{\text{ML}}$) from both the conventional and adaptive cases. Using the experimental data described above, we created 10,000 replicates of data as if the source was 1% the original source strength and estimated $\hat{\phi}_{\text{ML}}$ for each replicate. Histograms of $\hat{\phi}_{\text{ML}}$ from both the conventional and adaptive case are shown in Fig. 6.11. Based on Gaussian fits, the histogram from the adaptive case is 17.7% narrower than the conventional case which is in line with the CRLB prediction.

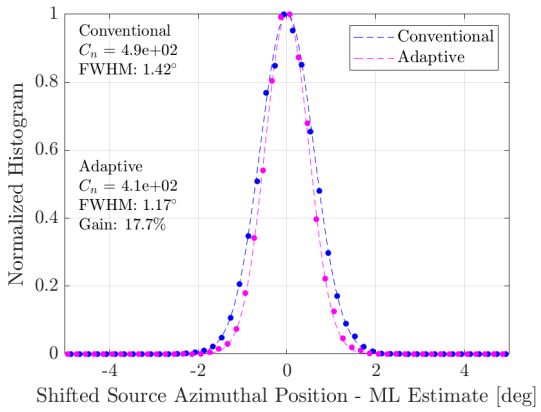

Figure 6.11: Normalized and shifted histograms of $\hat{\phi}_{\text{ML}}$ created from 10,000 replicates of experimental data. The source is at $(90\text{ cm}, 178°)$ and the adaptive case uses data collected at $(-12, 0)$ cm - the optimal clairvoyant detector position from Eq. 6.11. The dashed lines represent a Gaussian fit and the dots are points on the histogram.

These experimental validations provide us with confidence that the predictions made by the CRLB are experimentally achievable. Adaptive detector movements can improve angular resolution by approximately 20% for a fast neutron point sources in the MATADOR system.

6.4.2 Multiple Detector Positions

It may be possible to achieve better angular resolution by combining data from multiple detector positions instead of just one. We explore this idea by comparing the CRLB predictions from A_{max} in Eq. 6.11 and 6.15.

In Fig. 6.9, we plotted the gain in angular resolution as a function of detector position in (x, y) coordinates. In this section, we plot angular resolution gain as a function of detector position in index space[3]. Recall from Fig. 6.7 that each candidate detector position was assigned an index.

Since there are multiple detector positions under consideration, we optimize over

[3]One would need 6 dimensions to show objective function for all variables: 4 for the (x, y) coordinates of both detectors, the fifth for the relative measurement time, and the sixth for angular resolution gain. That seems challenging.

the time spent at the first detector position relative to the total measurement time (τ, see Eq. 6.15). Fig. 6.12 shows the gain as a function of the first and second detector positions - τ was optimized and only the gain from the optimal is shown. The red dot represents the pair of detectors that lead to the greatest gain in angular resolution. The conventional case is the top right corner at index $(145, 145)$. Any point along the diagonal from the bottom left to the top right is equivalent to collecting data at one detector position for the total time. If one were to extract the diagonal elements and plot them by their x, y detector positions, one would get Fig. 6.9.

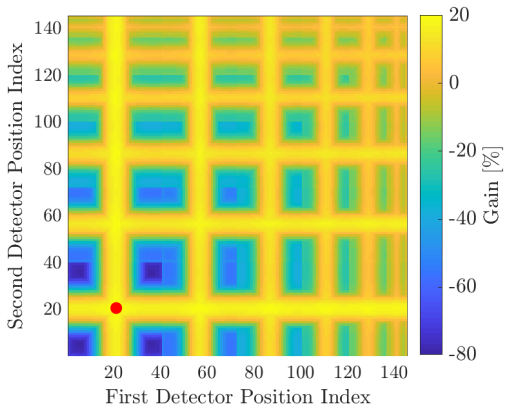

Figure 6.12: Angular resolution gain for two detector positions for a point source at $(90\text{ cm}, 0°)$. The relative time between the detector positions has been coarsely optimized.

Recall from Fig. 6.9 that for a point source at $(90\text{ cm}, 0°)$, the best detector position is $(-12, 0)$ cm. $(-12, 0)$ cm corresponds to index 21 in Fig. 6.7. As shown in Fig. 6.12, the best two detector positions to collect at are indices $(21, 21)$ - collecting data at the best detector position twice. Thus, there is no added benefit to collecting data at two detector positions. This is reasonable because the covariances between α_1, ϕ_1, and b_1 are relatively small for a point source and thus achieving the best angular resolution is mostly focused on maximizing the fisher information for the source position (for a simple example, see Eq. 6.9). Thus, spending valuable measurement

time at a detector position that does not maximize the fisher information leads to worse angular resolution.

Since there is no benefit in terms of angular resolution to collecting data at two detector positions compared to one, we conclude that collecting data at multiple detector positions is not valuable for point sources with respect to improving angular resolution[4].

6.5 Two Point Source Results

This section investigates the gain in angular resolution using adaptive detector movements when there are multiple sources in the FOV. We consider the performance of each source individually using Eq. 6.10 and collectively using Eq. 6.12. Note that even when we use Eq. 6.10, the CRLB calculation still includes the unknown parameters from both sources. We refer to the two sources as S_1 and S_2.

Sec. 6.5.1 summarizes the CRLB prediction for two equal intensity point sources that are close together and shows experimental results validating those predictions. Sec. 6.5.2 considers the performance improvement as a function of source separation and as a function of relative source intensity. Finally, Sec. 6.5.3 explores if collecting data at multiple detector positions provides significant benefit over collecting data at one detector position.

6.5.1 Best Detector Position for Equal Intensity Sources Close Together

There are two equal intensity sources in the field at $(90\text{ cm}, 5°)$ and $(90\text{ cm}, 355°)$ as shown in Fig. 6.13. Fig. 6.14 shows the quadrature-sum gain (Eq. 6.12) as a function of detector position.

[4]Note that in this analysis, the radial position of the source was not treated as an unknown.

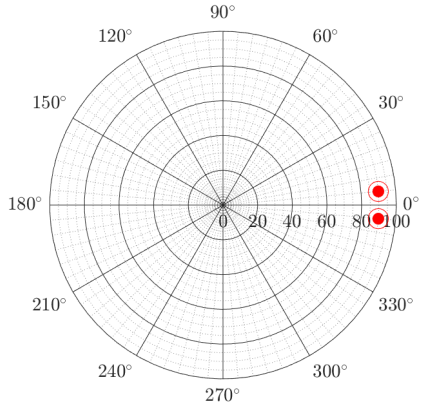

Figure 6.13: Two equal intensity point sources at $(90\text{ cm}, 5°)$ and $(90\text{ cm}, 355°)$.

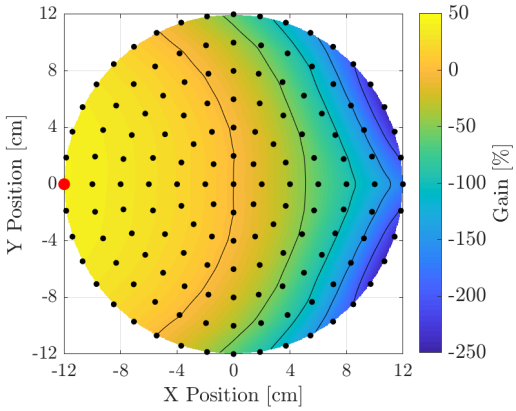

Figure 6.14: Quadrature-sum gain map for two equal intensity point sources at $(90\text{ cm}, 5°)$ and $(90\text{ cm}, 355°)$. The black dots are all of the detector positions that were considered and the red dot represents the detector position with the greatest gain. The contour lines have the same values as the tick marks in the color bar. Space between detector positions has been interpolated.

In line with intuition, the angular resolution gain increases as the mask-to-detector distance along the source axis increases. There are two main observations here:

1. The maximum gain is $\sim$50% which is significantly larger than the $\sim$20% gain in the single point source case.

2. The gain map is not symmetric with respect to the x-axis (y = 0).

Observation 1: the maximum gain is ∼50% which is significantly larger than in the ∼20% gain in the point source case. This is because the loss in angular resolution of a source (S_1) by the addition of another source (S_2) is highly dependent on both the relative positions of the sources and the angular resolution of the imaging system. Fig. 6.15 shows the percent change in angular resolution of S_1 when S_2 is introduced into the FOV as a function of the position of S_2. Fig. 6.16 is a magnified version of Fig. 6.15 at low source separations.

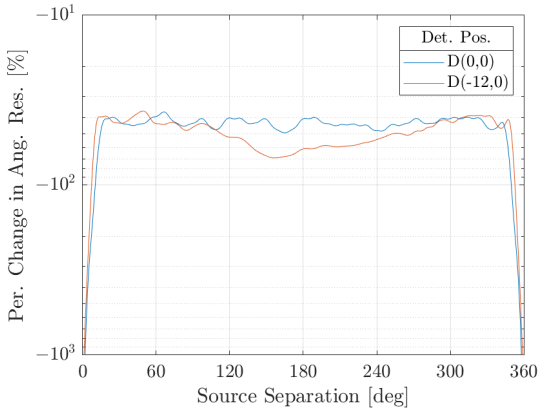

Figure 6.15: Percent change in angular resolution of a source when a second source is introduced in the FOV. The blue curve is for the detector centered case and the red for a detector at $(-12, 0)$ cm. The graph is relative to the single source case. The two sources are of equal strength. The source in consideration is at $(90\text{ cm}, 0°)$.

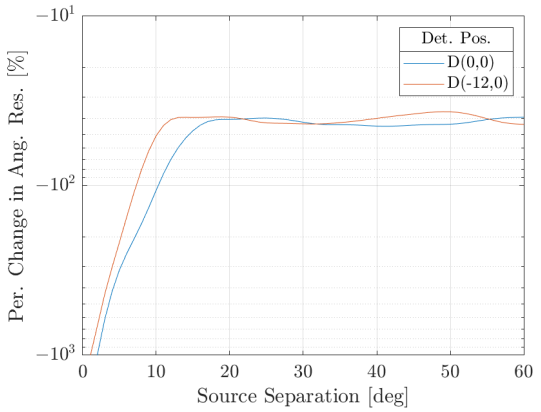

Figure 6.16: Magnified version of Fig. 6.15.

Focusing on the detector-centered case (blue line) in Fig. 6.15 and 6.16, if S_2 is introduced close to S_1, within 20°, the angular resolution of S_1 degrades by many factors. This is because the observed responses for the two sources are quite similar which leads to a high degree of covariance between ϕ_1 and ϕ_2. Even when the sources are far apart, S_2 degrades the angular resolution of S_1 by 40-50%[5]. At large separations, the resolution loss is not constant but depends on the exact location of the second source. Part of this variation is because mask elements are $360°/35 \approx 10.28°$ wide so when the detector is centered, any sources that are an integer multiple of 10.28° apart are more likely to experience mask element transitions at the same mask rotation angle.[6] These correlations make source localization more difficult. From the perspective of Eq. 6.8, for some source separations, $\partial A/\partial\phi$ for ϕ_1 and ϕ_2 are more closely correlated which results in larger values in the off-diagonal elements related to ϕ_1 and ϕ_2 in the FIM.

For the offset detector case in Fig. 6.15 and 6.16, for small source separations, the angular resolution loss is smaller. This is because the intrinsic resolution of the system is greater. Since the PSF is shift-variant and the detection efficiency is changing as the second source moves, the offset detector performs worse than the centered detector when the source separation is large. Notice that the curves in Fig. 6.15 are not reflected at 180° - the angular resolution loss is different if a source is introduced $+20°$ or $-20°$ from the source of interest.

Observation 2: the gain map is not symmetric with respect to the x-axis (y = 0). The effect is more obvious when the two sources are closer together - see Fig. 6.17 where the two sources at 6° apart. In Fig. 6.17, the best detector position is not the position that maximizes the detector-to-mask distance along the source axis,

[5]If $\alpha_2 << \alpha_1$, then there would be no degradation in angular resolution of the first source.
[6]The response is also blurred by the large detector and the thick mask elements.

$(-12, 0)$ cm, but instead the best position is $(-11.85, 1.88)$ cm which is slightly off from the centerline between the two sources. This effect is caused by the lack of symmetry in Fig. 6.15. In any case, the difference in gain between $(-11.85, 1.88)$ cm and $(-12, 0)$ cm is negligible but points to the interconnected nature of estimating a parameter in the presence of other unknowns.

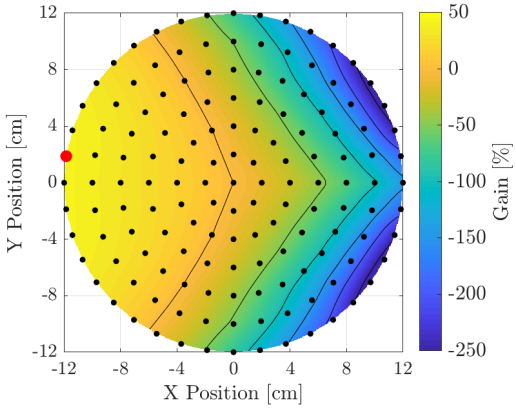

Figure 6.17: Quadrature-sum gain map for two equal intensity point sources at $(90 \text{ cm}, 3°)$ and $(90 \text{ cm}, 357°)$. The black dots are all of the detector positions that were considered and the red dot represents the detector position with the greatest gain. The contour lines have the same values as the tick marks in the color bar. Space between detector positions has been interpolated.

Experimental Validation

Similar to the one point source case, we experimentally validate these results with MLEM images and MLEs of the source positions. A 1.85 mCi source was placed at both $(90 \text{ cm}, 175°)$ and $(90 \text{ cm}, 185°)$ and data was collected for 90 s with the detector at the center and the detector at the position that provided the greatest quadrature-sum angular resolution gain - $(-12, 0)$ cm. In the conventional case, the two sources cannot be separated in the MLEM image while in the adaptive case, the two sources are clearly separated.

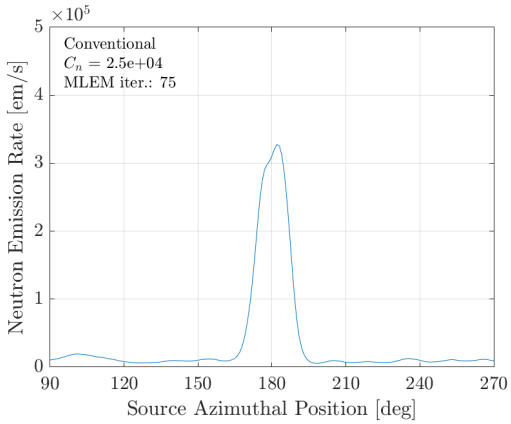

Figure 6.18: MLEM reconstruction for the conventional, detector-centered case. The sources are at (90 cm, 175°) and (90 cm, 185°).

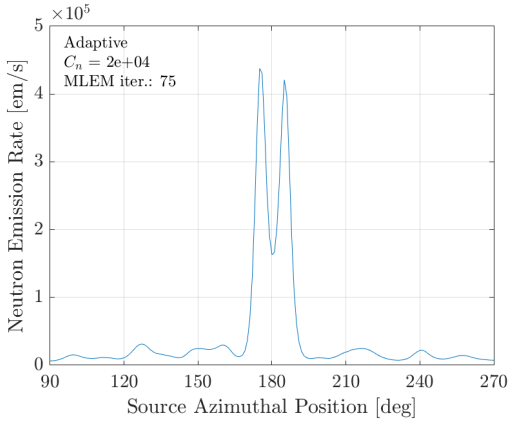

Figure 6.19: MLEM reconstruction for the adaptive case. The sources are at (90 $textcm$, 175°) and (90 cm, 185°). The detector is at (11.85, −1.88) cm.

For the same experimental setup, we created 1,000 replicates as if the sources were 1% of their original strengths and found the ML source positions for both sources. Below is the distribution of MLEs for both the conventional and adaptive case. Using the quadrature-sum of the standard deviations of the Gaussian fits, the gain is calculated as 41.6%, in line with the CRLB prediction.

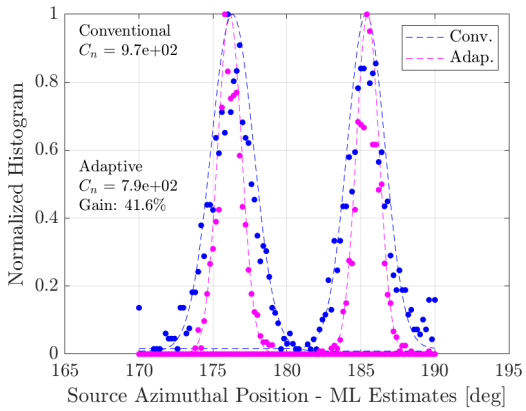

Figure 6.20: Histograms of MLE of the source position from both the conventional, detector-centered case and the adaptive case. The source is at $(90\text{ cm}, 175°)$ and $(90\text{ cm}, 185°)$ and the adaptive case uses data collected at $(-12, 0)$ cm. The dashed lines represent Gaussian fits and the dots are points on the histogram.

These validations provide confidence that the angular resolution gain predicted by the CRLB can be experimentally realized and that the gain is significant.

6.5.2 Best Detector Position for any Two Point Sources

When two equal intensity point sources are close together, adaptive detector movements can significantly improve angular resolution - up to 50% better. How does the performance change as a function of the azimuthal separation between sources or their relative intensities? To answer this question, we varied the source separation from 2° to 180° every 2° and varied the relative strength of the second source from 10% to 90% every 10%. For each case, we calculated the quadrature-sum angular resolution gain for each detector position and recorded the maximum quadrature-sum gain; Fig. 6.21 shows the corresponding plot as a function of source separation and relative source strength.

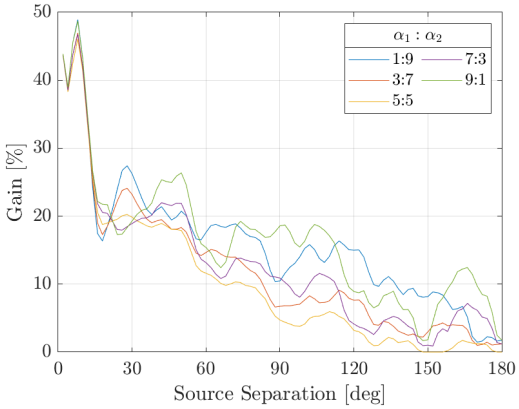

Figure 6.21: Maximum quadrature-sum gain for two point sources as a function of source separation and relative strength.

We make four observations from Fig. 6.21:

1. As the source separation increases, the quadrature-sum angular resolution gain decreases.

2. As the relative difference in soure intensity increases, the quadrature-sum angular resolution gain increases.

3. As a function of source separation, the quadrature-sum angular resolution gain is not smooth.

4. When sources are less than 20° apart, regardless of the relative source strengths, the quadrature-sum angular resolution gain is large.

Below, we discuss each observation. To aid in this process, we will use Fig. 6.22 and 6.23 which show individual and quadrature-sum gain maps for two sources that are close together and far apart for two relative intensities.

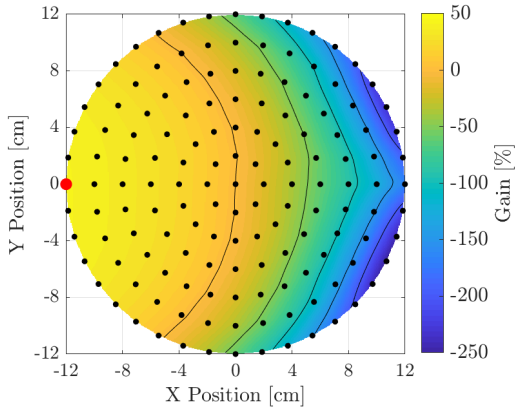

(a) For source at 5°. Equal intensity sources.

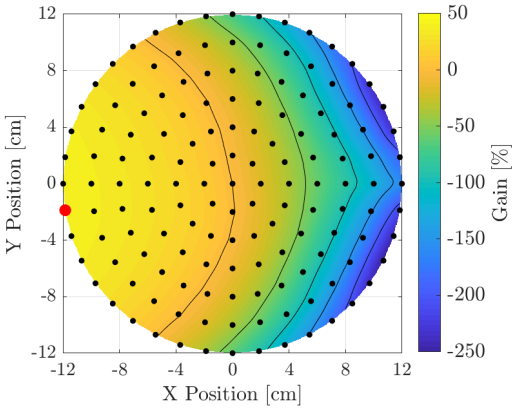

(b) For source at 5°. 9:1 intensity sources.

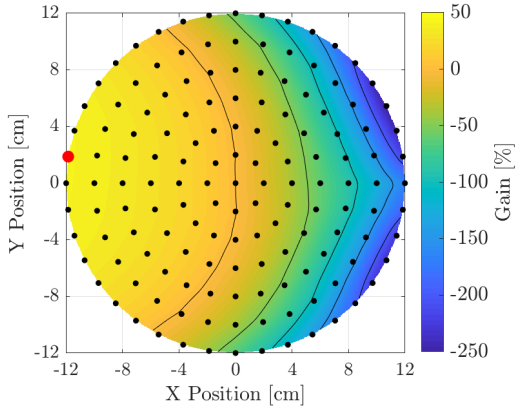

(c) For source at 355°. Equal intensity sources.

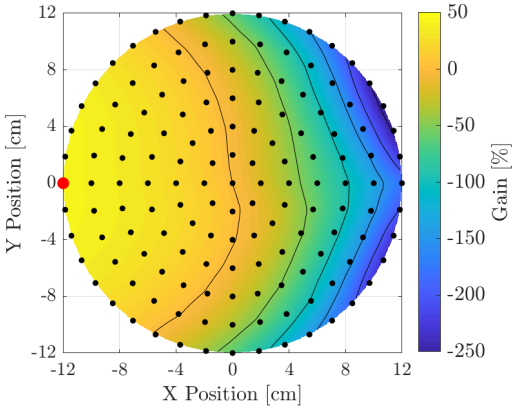

(d) For source at 355°. 9:1 intensity sources.

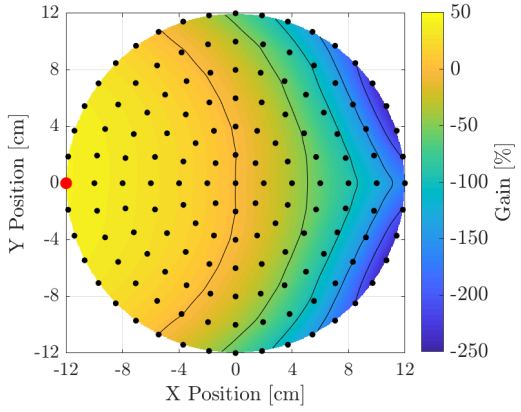

(e) quadrature-sum. Equal intensity sources.

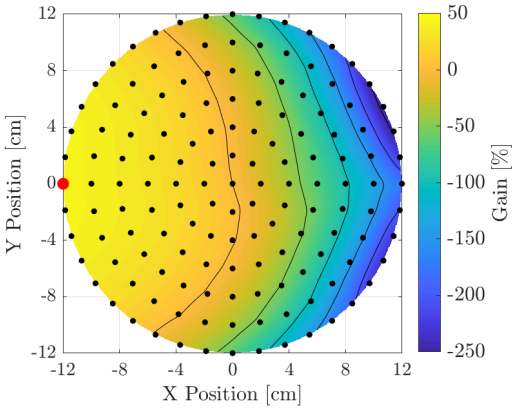

(f) quadrature-sum. 9:1 intensity sources.

Figure 6.22: Gain maps for two point sources at (90 cm, 5°) and (90 cm, 355°). Left column is equal intensity, the right is 9:1 intensity.

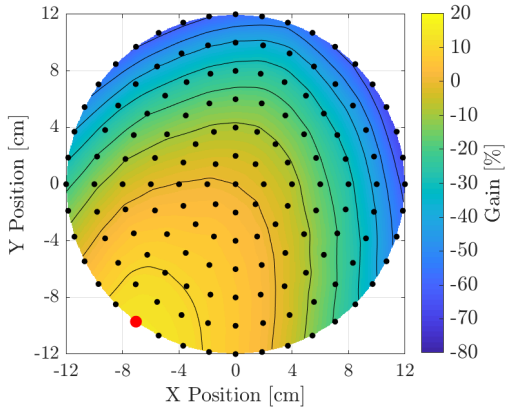

(a) For source at 72°. Equal intensity sources.

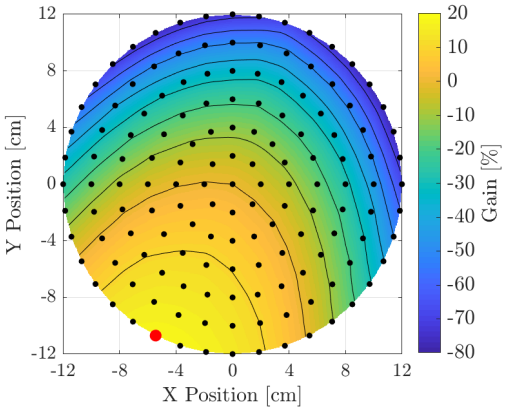

(b) For source at 72°. 9:1 intensity sources.

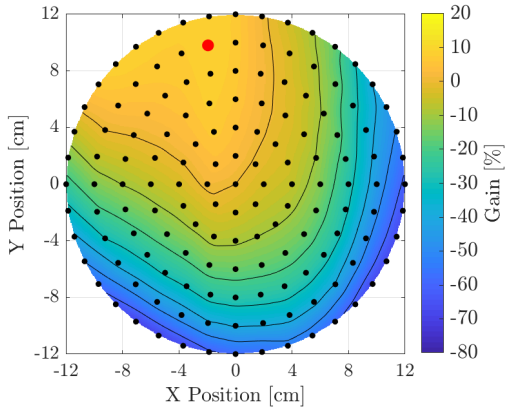

(c) For source at 288°. Equal intensity sources.

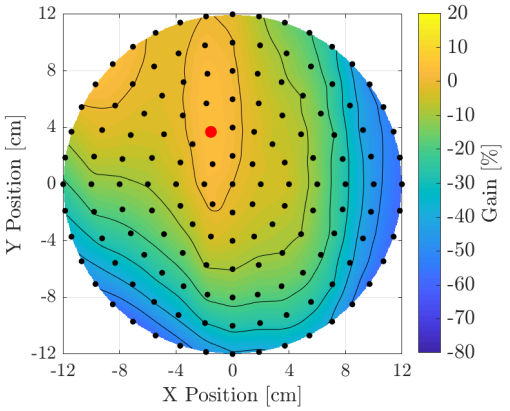

(d) For source at 288°. 9:1 intensity sources.

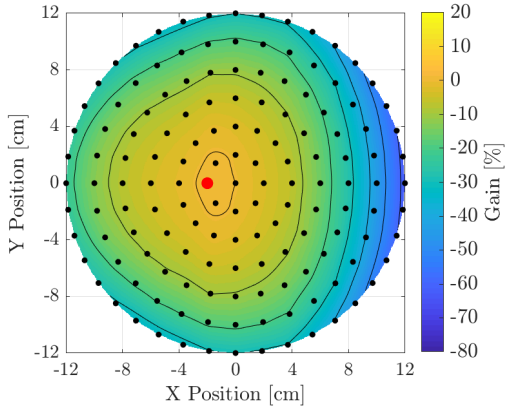

(e) quadrature-sum. Equal intensity sources.

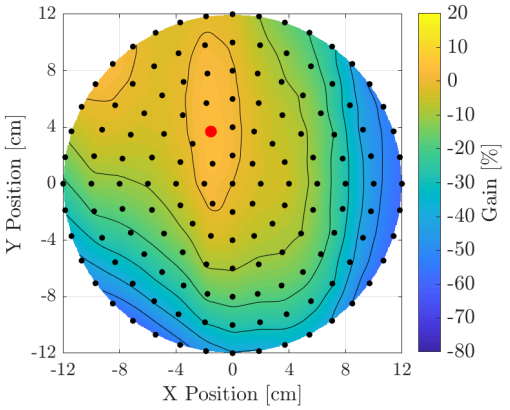

(f) quadrature-sum. 9:1 intensity sources.

Figure 6.23: Gain maps for two point sources at $(90\text{ cm}, 72°)$ and $(90\text{ cm}, 288°)$. Left column is equal intensity, the right is 9:1 intensity.

Observation 1: As the source separation increases, the quadrature-sum angular resolution gain decreases. Consider the equal intensity case (5:5) in Fig. 6.21. Once the sources are separated by 80°, the gain falls to below 10%. This is because the detector positions that provide high angular resolution gain for one source result in poor gain for the other. Recall from Fig. 6.6 that offsetting the detector only provides better angular resolution within -50° or +50° of the imaging axis. Sources outside that range are reconstructed with worse resolution as compared to keeping the detector in the center. This effect is also true for sources with large intensity differences. In addition, the sources in these simulations are 90 cm from the system, thus if the sources have large separations, moving away from a weak source means acquiring more counts, and more Poisson noise, from the strong source.

Since Fig. 6.21 uses the quadrature-sum gain, the angular resolution of both sources is important. Fig. 6.23a and 6.23c are the gain maps for each source individually for two equal intensity sources. For the source at $(90\text{ cm}, 72°)$, the best detector position is $(-7.05, -9.71)$ cm which provides 14% gain. The same detector position would result in a -68% gain, a loss, for the other source. Thus, it is better to move to a compromise position, $(-2, 0)$cm, that provides a small amount of gain overall.

Observation 2: As the relative difference in soure intensity increases, the quadrature-sum angular resolution gain increases. If there is a large intensity difference between two sources, the quadrature-sum gain will be dominated by the gain of the weaker source. This is because the lower count rate from the weak source makes it harder to estimate its position. Thus, maximizing the quadrature-sum gain means achieving better resolution for the weak source at the expense of the strong source. In the extreme case, the detector will move to the detector position that maximizes the individual angular resolution gain for the weak source without compromising for the

performance with respect to the strong source. For example, the detector position that maximizes the quadrature-sum angular resolution gain in Fig. 6.23f results in -12% individual gain for the strong source (Fig. 6.23b).

Observation 3: As a function of source separation, the quadrature-sum angular resolution gain is not smooth. This point was addressed in more detail in Sec. 6.5.1. Essentially, when sources are separated by integer multiples of the width of a mask element, mask transitions occur at the same mask rotation angle for both sources. This makes localization more difficult. This effect is muddled by the large detector response and thick mask elements.

Observation 4: When sources are less than 20° apart, regardless of the relative source strengths, the quadrature-sum angular resolution gain is large. For equal-intensity sources, the gain is large because the detector positions that achieve high gain for one source also lead to high gain for the second source. The same effect occurs when the relative difference in intensity is large. In contrast, as explained in the discussion on Observation 1, when the sources are far apart, the detector position that leads to high gain for one source will lead to poor gain for the second source.

6.5.3 Multiple Detector Positions

Naturally, one would be interested in knowing the gain when combining data from multiple detector positions instead of just one detector position. For example, perhaps collecting data at the individual best positions for both sources is better than collecting data at the quadrature-sum, compromise position. Similar to the one point source case, we answer this question though brute force. We calculate the quadrature-sum angular resolution gain for every pair of detector positions. Since there are two detector positions, we vary the relative time spent at the first detector

position from 10% to 90% every 10%. Fig. 6.25 plots of the maximum quadrature-sum angular resolution gain from two detector positions as a function of source separation and relative source strength. The plot for the one detector position is repeated for reference in Fig. 6.24. Fig. 6.26 shows the difference in gain between the two.

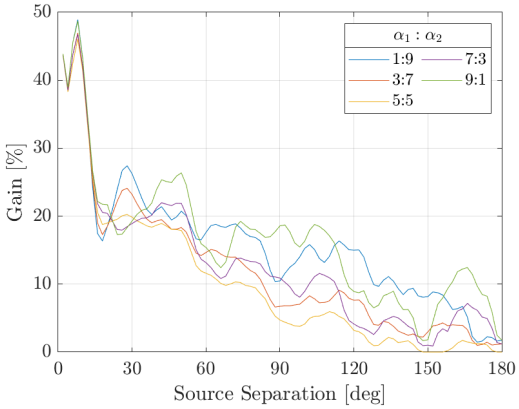

Figure 6.24: Quadrature-sum gain for two point sources as a function of source separation and relative strength. One detector position.

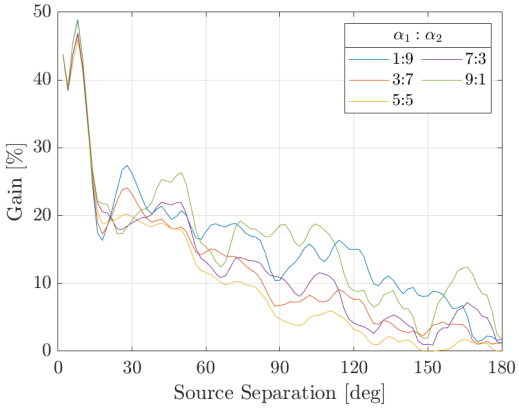

Figure 6.25: Quadrature-sum gain for two point sources as a function of source separation and relative strength. Two detector positions.

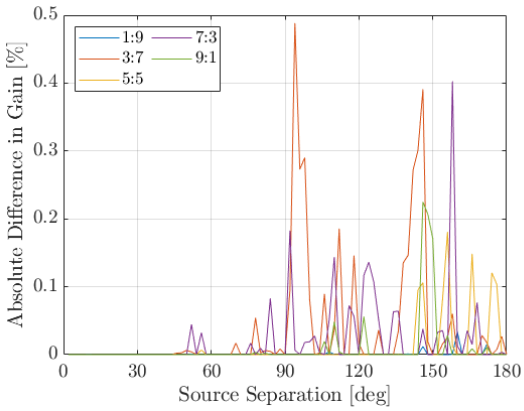

Figure 6.26: Absolute difference in gain between two detector positions and one as a function of source separation and relative strength.

Looking at Fig. 6.26, there is no benefit from collecting data at multiple detector positions for many of the scenarios considered here. In select cases, there is some benefit, but it is small and not worth the cost of moving the detector. We attribute these results to the observation that collecting higher quality data for one source often means collecting much lower quality data for the other source, thus it is almost always better to spend the entire measurement time at a compromise position.

6.6 Conclusions

We find that adaptive detector movements can provide significant angular resolution gain in the following cases:

1. Up to 20% better angular resolution for point sources,

2. Up to 50% better angular resolution for two point sources that are close together regardless of relative source strength,

3. Between 10%-30% better angular resolution if sources are far apart with large intensity differences.

The benefit from adaptive detector movements is minimal in the following cases:

1. <10% better angular resolution for equal intensity sources that are more than 80° apart.

2. <10% better angular resolution for sources that are more than 160° apart regardless of relative source strength.

We also find that collecting and combining data from multiple detector positions does not provide appreciable benefit above collecting data at one detector position for point sources or two point sources. This finding holds true for a range of different source separations and relative intensities.

These results have been experimentally spot checked by ML estimation of the source position and MLEM reconstructions. For one point source, the variance of the MLE of the source position reduced by ∼17.7% as predicted by the CRLB simulations and the FWHM of the MLEM reconstruction is ∼25.1% smaller. For two equal intensity point sources separated by 10°, the simulations predicted ∼50% quadrature-sum angular resolution gain and the experimental ML estimates showed ∼42% gain. The MLEM images for two equal intensity sources also showed significant resolution improvement. In the conventional case, two equal intensity sources that are 10° apart cannot be separated while in the adaptive case, the two sources are clearly resolved.

The results from this clairvoyant analysis clearly show the potential of adaptive detector movements in improving angular resolution. Thus far we have assumed that the unknown parameters are known, but this is unlikely to be the case in real-world scenarios. In order to make an adaptive imaging algorithm that generates higher resolution images when the unknown parameters are not know apriori, we must

address the detection problem of determining the number of sources in the field. As a starting point, in the next chapter, we explore how adaptive mask movements can improve detection of a weak source in the vicinity of a strong source.

CHAPTER VII

Improving Detection Using Adaptive Mask Movements

Searching for undeclared sources is an important task for nuclear non-proliferation and international safeguards. Although most source search tasks are focused on finding one point source in the presence of natural background, this chapter focuses on searching for a weak source in the presence of a strong source. This is a challenging scenario as the noise from the strong source obscures the signal from the weak source. We show that adaptive imaging can be used to improve the detection performance of a cylindrical, time-encoded imaging (c-TEI) system by reducing the particle flux from the strong source while modulating the weak source. In this way, the signal and noise from the strong source is reduced and detection performance with respect to the weak source improves.

This chapter uses adaptive mask movements instead of adaptive detector movements. For the conventional and adaptive data collections, the detector is always in the center but in the adaptive case, the measurement time is not uniformly spread out over the entire revolution. As we will see, some regions of the mask are better at detection than other regions of the mask. Thus, this chapter focuses on how to which regions of the mask to measure at. Additionally, we develop an adaptive detection

algorithm that improves detection performance.

Sec. 7.1 and 7.2 cover some necessary setup for the adaptive detection problem. Sec. 7.3 contains results for the clairvoyant case where we know the positions of the sources. Next, Sec. 7.4 presents an adaptive detection algorithm when the source positions are not known and applies the algorithm to experimental data. Finally, Sec. 7.5 discusses the performance differences between using the experimental system response and the offset detector model.

7.1 Overview of the Weak Source, Strong Source Problem

In the weak source, strong source problem, there are two sources in the field-of-view (FOV): a strong source which is easy to detect and a weak source that is difficult to detect. The weak source may be difficult to detect because of high natural background or because noise from the strong source is obscuring the weak source. As we will shortly discuss, for the experimental data we are using, fast-neutron natural background is essentially negligible thus in this work the weak source is only difficult to detect because of the presence of a strong source.

For the simulations used in the clairvoyant analysis in Sec. 7.3, the strong source is a $\sim 21\mu$Ci ($\sim 9\times 10^4$ n/s) Cf-252 point source at $(90\text{ cm}, 178^\circ)$ and the weak source is a $\sim 2.1\mu$Ci ($\sim 9\times 10^3$ n/s) Cf-252 point source at $(90\text{ cm}, 88^\circ)$[1]. The total measurement time is 900s and we use the offset detector model to create the observation vector ($\boldsymbol{y}$) with a S:B ratio is 2.2:1. Note that there is no additional natural background. Based on these parameters, in the conventional case, the expected number of counts from the strong source is 5,000 counts and the expected counts from the weak source is

[1]Both the strong and weak source at always at 90cm, and the strong source is always at 178°. Usually, the weak source is at 88°, but in a few cases it is not. We will be very clear to note the location of the weak source when it is not at 88°.

500 counts.

For the experiments, we use data collected from a 1.85 mCi Cf-252 point source at $(90\text{ cm}, 178^\circ)$. Data was collected for a total of 47, 90s revolutions. We randomly divided 46 of the 47 revolutions into 2 groups. To make experimental data for the strong source, we bootstrap (see Sec. 2.4.3) the data from group 1 and for the weak source, we bootstrap the data from group 2. The count rates from the experimental sources have been artificially reduced to match the expected counts from the clairvoyant analysis. Since the 1.85 mCi Cf-252 source in the experiment is quite strong, the natural fast neutron background is negligible. Calculation of the likelihood ratio in the generalized likelihood ratio test (GLRT) for experimental data is done using the experimental system response instead of the offset detector model. As discussed in Sec. 5.2, environmental scatter causes model mismatch between the experimental data and the offset detector model. Since the GLRT is sensitive to such model mismatch, the offset detector model cannot be reliably used for detection. Sec. 7.5 discusses this in more detail.

7.1.1 Hypotheses

For the weak source, strong source problem, we use the following hypotheses:

$$\begin{aligned} \mathcal{H}_N &: \alpha_2 = 0; \\ \mathcal{H}_A &: \alpha_2 \neq 0; \end{aligned} \tag{7.1}$$

We use the GLRT as the hypothesis test. Recall from Sec. 2.4.2 that under some conditions, the likelihood ratio from the GLRT is distributed as a non-central chi-squared distribution:

$$\Lambda'_{\text{GLRT}} = 2ln(\Lambda_{\text{GLRT}}) \sim \begin{cases} \chi^2_r(0), & \mathcal{H}_N \\ \chi^2_r(\lambda), & \mathcal{H}_A \end{cases} \tag{7.2}$$

where $\chi^2_r(\lambda)$ is the non-central chi-squared distribution with r degrees of freedom and non-centrality parameter λ (see Appendix 6C of [149] for more details). For the null hypothesis, $\lambda = 0$, thus $\chi^2_r(0)$ is simply a chi-squared distribution with r degrees of freedom. For the alternative hypothesis, λ is

$$\lambda = (\boldsymbol{\theta}_{r,A} - \boldsymbol{\theta}_{r,N})^T \left[I_{\boldsymbol{\theta}_r\boldsymbol{\theta}_r}(\boldsymbol{\theta}_{r,A}, \boldsymbol{\theta}_n) - I_{\boldsymbol{\theta}_r\boldsymbol{\theta}_n}(\boldsymbol{\theta}_{r,A}, \boldsymbol{\theta}_n) I^{-1}_{\boldsymbol{\theta}_n\boldsymbol{\theta}_n}(\boldsymbol{\theta}_{r,A}, \boldsymbol{\theta}_n) I_{\boldsymbol{\theta}_n\boldsymbol{\theta}_r}(\boldsymbol{\theta}_{r,A}, \boldsymbol{\theta}_n) \right] (\boldsymbol{\theta}_{r,A} - \boldsymbol{\theta}_{r,N}) \tag{7.3}$$

where $\boldsymbol{\theta}_{r,A}$ and $\boldsymbol{\theta}_{r,N}$ are the true values of the test-relevant parameters under the alternative and null hypotheses and $\boldsymbol{\theta}_n$ are the true values of the nuisance parameters.

In the hypotheses from 7.1, there is only one test relevant parameter, $\theta_r = [\alpha_2]$, and four nuisance parameters, $\boldsymbol{\theta}_n = [\alpha_1 \ \phi_1 \ \phi_2 \ b]^T$. Thus, there is only one degree of freedom ($r = 1$).

The Λ'_{GLRT} for a Poisson process is[2]

$$\Lambda'_{\text{GLRT}} = 2 \sum_{i=1}^{N_O} \left(y_i \ln \left(\frac{\overline{y}_{i,A}}{\overline{y}_{i,N}} \right) \right) - \sum_{i=1}^{N_O} \left(\overline{y}_{i,A} - \overline{y}_{i,N} \right) \underset{\mathcal{H}_N}{\overset{\mathcal{H}_A}{\gtrless}} \eta_{\text{crit}} \tag{7.4}$$

where $\hat{\boldsymbol{\theta}}_{\text{ML},N/A}$ is the maximum likelihood estimate (MLE) of $\boldsymbol{\theta}$ under the null or alternative hypothesis, $\overline{\boldsymbol{y}}_{\mathcal{H}_{N/A}}$ is the associated forward projection, and η_{crit} is the critical threshold between the null and alternative hypothesis. η_{crit} is usually set based on a desired false alarm rate (Eq. 2.38).

7.1.2 Metrics to Assess Detection

To assess and compare the performance of different system configurations, we use receiver operator characteristic (ROC) curves and some metrics derived from it. As shown in Fig. 7.1, a ROC curve plots the probability of detection as a function of

[2] See Appendix C.

the probability of false alarm. Notice in Fig. 7.1 that ROC curve 2 has a greater probability of detection for any probability of false alarm thus system configuration 2 is better at detection than system configuration 1.

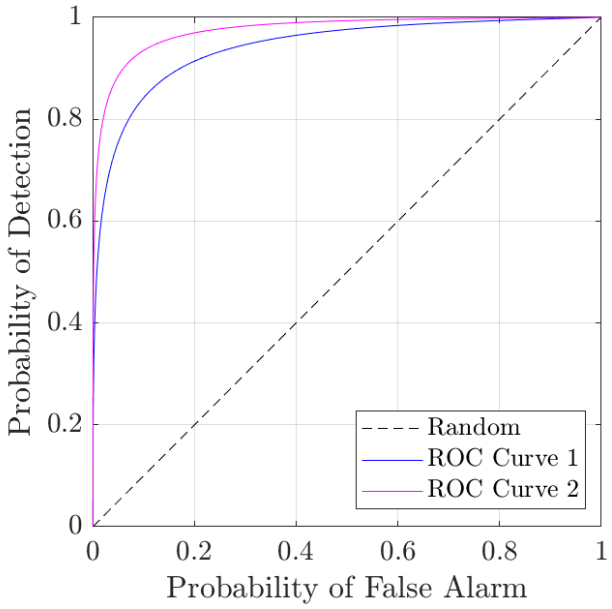

Figure 7.1: ROC curves plot the probability of detection as a function of probability of false alarm. ROC curve 1 is from a hypothetical system configuration 1 and ROC curve 2 is from a hypothetical system configuration 2.

To create an ROC curve, one needs to know the distribution of the test statistic ($\mathcal{T}$) under the null and alternative hypothesis. Since we are using the GLRT, we refer to these distributions as $f(\Lambda'_{\text{GLRT}}, \mathcal{H}_N)$ and $f(\Lambda'_{\text{GLRT}}, \mathcal{H}_A)$ respectively. One can find $f(\Lambda'_{\text{GLRT}}, \mathcal{H}_N)$ and $f(\Lambda'_{\text{GLRT}}, \mathcal{H}_A)$ through simulations or experiments. Additionally, one can also use Eq. 7.2 and 7.3 to find the asymptotic GLRT ROC curve. Given $f(\Lambda'_{\text{GLRT}}, \mathcal{H}_N)$ and $f(\Lambda'_{\text{GLRT}}, \mathcal{H}_A)$, one can create an ROC curve by evaluating Eq. 2.37 and 2.38 for a range of η_{crit} values.

To compare two ROC curves, we use the following metrics:

1. AUROC: area under the ROC curve

2. $P_{D,5\%} = P_D(P_{FA} = 0.05)$: the probability of detection when the probability of false alarm is 5%

3. $\tau_{2\to1}$: the relative change in time for ROC curve 2 to match ROC curve 1.

Given an experimental ROC curve, calculating the AUROC and $P_{D,5\%}$ is straight forward. For the AUROC, we use a trapezoidal sum and for $P_{D,5\%}$, we interpolate the ROC curve. On the other hand, experimentally calculating $\tau_{2\to1}$ by changing the measurement time is computationally expensive. Thus, we only use $\tau_{2\to1}$ to assess the asymptotic GLRT ROC curves and not experimental ROC curves. In the asymptotic case, $f(\Lambda'_{\text{GLRT}}, \mathcal{H}_N)$ is constant for all system configurations[3], thus $\tau_{2\to1}$ is equivalent to the relative change in time for $f_2(\Lambda'_{\text{GLRT}}, \mathcal{H}_A)$ to match $f_1(\Lambda'_{\text{GLRT}}, \mathcal{H}_A)$[4]. Since the non-centrality parameter, λ scales linearly with total measurement time (see Appendix D), $\tau_{2\to1}$ is

$$\tau_{2\to1} = \frac{\lambda_1}{\lambda_2} - 1 \tag{7.5}$$

where λ_1 is the non-centrality parameter of system configuration 1 and λ_2 is the non-centrality parameter of system configuration 2. If λ_2 is greater than λ_1, $\tau_{2\to1}$ is negative meaning system 2 can achieve similar performance to system 1 in less time.

As an example, Tab. 7.1 summarizes the relevant metrics for the hypothetical ROC curves in Fig. 7.1. ROC curve 2 has a greater AUROC and $P_{D,5\%}$ relative to ROC curve 1, and $\tau_{2\to1}$ is negative indicating that system configuration 2 can achieve the same performance as system configuration 1 in less time. In fact, system configuration 2 is significantly better than system configuration 1 given that it can achieve the same performance in 30% less time. Note that although the difference

[3] $f(\Lambda'_{\text{GLRT}}, \mathcal{H}_N)$ is only dependent on the degrees of freedom which is a property of the hypothesis test, not the imaging system.

[4] The subscripts 1 and 2 indicate which system configuration these distributions are from.

between AUROCs from system configuration 2 and system configuration 1 may seem small, the impact in terms of measurement time may still be large.

Table 7.1: Detection metrics for the ROC curves in Fig 7.1

	ROC Curve 1	ROC Curve 2
AUROC	0.941	0.975
$P_{D,5\%}$	0.755	0.885
$\tau_{1\to2}$	42.2%	-
$\tau_{2\to1}$	-	-29.7%

Although $\tau_{2\to1}$ is a relevant metric for real-world applications, for the low count experiments considered here, the GLRT has not converged to its asymptotic distribution thus we cannot use Eq. 7.5 to calculate $\tau_{2\to1}$ for experimental ROC curves. We only use AUROC and $P_{D,5\%}$ to assess the performance of experimental ROC curves. Fig. 7.2 shows experimental $f(\Lambda'_{\text{GLRT}}, \mathcal{H}_A)$ and $f(\Lambda'_{\text{GLRT}}, \mathcal{H}_N)$ for the weak source using a conventional c-TEI setup. Notice how the experimental distributions have not converged onto the asymptotic distributions.

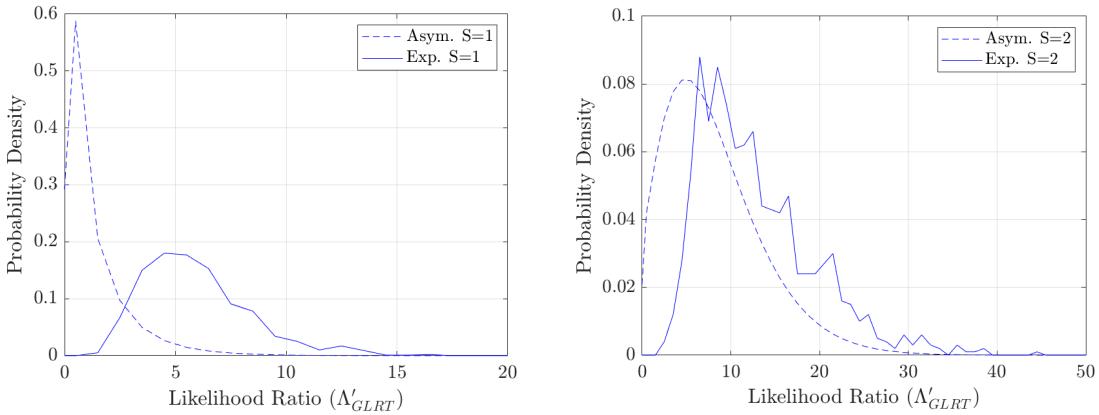

(a) Weak source not present ($\mathcal{H}_N$). (b) Weak source present ($\mathcal{H}_A$).

Figure 7.2: Asymptotic and experimental likelihood ratios. At low counts, the experimental distribution has not converged to the asymptotic GLRT predictions. These plots are for a the conventional c-TEI setup.

7.2 Overview of the Adaptive Detection Problem

Inherently, the adaptive detection problem is an optimization problem: which system configurations provide the greatest detection performance. To address this problem, we need to define an objective function, ψ, that predicts the detection performance for a system response and define the set of system responses that we will optimize over. For simplicity we use brute force for optimization.

7.2.1 Objective Function for Weak Source Detection

To predict the detection performance of a system, we use the asymptotic GLRT. Under the low count experiments considered here, the experimental $f(\Lambda'_{\mathrm{GLRT}}, \mathcal{H}_A)$ has not converged to its asymptotic distribution (see Fig. 7.2). Thus, we make the following simplifying assumption: we assume that the system configurations that maximize experimental detection performance at high counts are the same system configurations that maximize experimental detection performance at low counts. Since at high counts the experimental $f(\Lambda'_{\mathrm{GLRT}}, \mathcal{H}_A)$ converges to the asymptotic $f(\Lambda'_{\mathrm{GLRT}}, \mathcal{H}_A)$ and the asymptotic $f(\Lambda'_{\mathrm{GLRT}}, \mathcal{H}_A)$ is only dependent on the non-centrality parameter, we define ψ as

$$\psi = \lambda(\boldsymbol{\theta}_N, \boldsymbol{\theta}_A, A, T) \tag{7.6}$$

where λ is the non-centrality parameter, $\boldsymbol{\theta}_{N/A}$ are the true parameters under the null and alternative hypotheses, A is a candidate system response, and T is the allotted time for the measurement. If $\boldsymbol{\theta}_{N/A}$ are not know, we use $\boldsymbol{\theta}_{\mathrm{MLE},N/A}$. For simplicity, the measurement time is spread out evenly over all of the measurements. For example, if there are N_O observations in A, then the measurement time per bin is $\frac{T}{N_O}$.

7.2.2 Domain of System Response

In the adaptive case, the most general data collection would be to rotate the mask to any measurement bin and collect data for any amount of time. Although this is the most flexible approach and would lead to the greatest detection performance, it is not reasonable since the set of potential system responses is enormous. For example, if there are 30 unique measurements ($N_O = 30$) and the system response uses 1° bins for mask rotation, there are $\binom{360}{30} \approx 5 \times 10^{43}$ potential system responses to optimize over. To simplify the problem, instead of searching for N_O observations that maximize detection, we search for c regions of the mask (or patches of the mask) that maximize detection.

As shown in Fig. 7.3, we split a full mask revolution into patches where the width of each patch is P_w and the distance between the start of each patch, known as the stride, is P_s. If the stride is smaller than the width, then the patches are overlapping. For example, one might create patches with $P_w = 25$ and $P_s = 20$. In this case, there are 18 overlapping patches. The first patch always starts at a mask rotation angle of 0°.

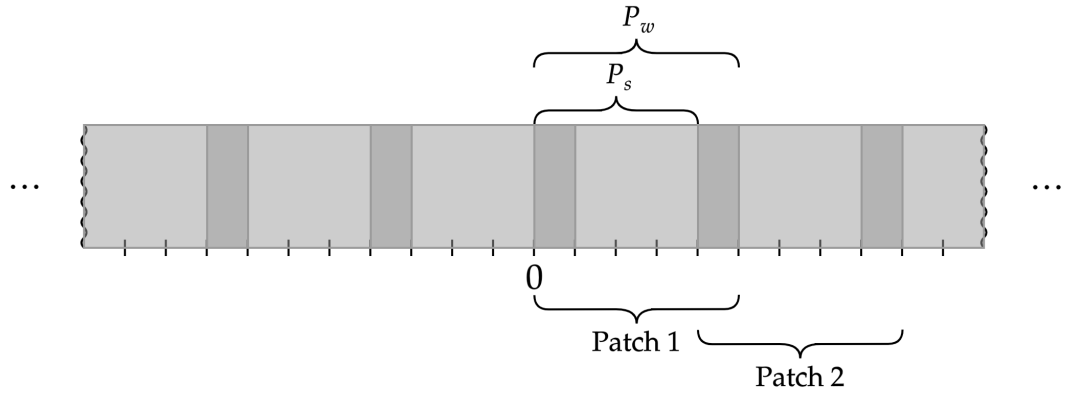

Figure 7.3: A full mask rotation is split into patches with a stride of P_s and a width of P_w.

Thus, the adaptive detection optimization problem has been simplified from finding N_O mask rotation angles into finding c patches that maximize detection:

$$A_{\max} = \arg\max_{A \in \mathbb{A}^c} \psi(\boldsymbol{\theta}_N, \boldsymbol{\theta}_A, A, T) \tag{7.7}$$

where $A_{\max}$ is the system configuration that maximizes detection and $\mathbb{A}^c$ is the set of system responses with c patches in each candidate system response. Also, let $\psi_{\max} = \psi(\boldsymbol{\theta}_N, \boldsymbol{\theta}_A, A_{\max}, T)$.

The number of system configurations in $\mathbb{A}^c$ is dependent on P_s and c. Since ψ is not order dependent, the number of candidate system configurations is

$$N_{\text{sys}} = \binom{\left\lfloor \frac{360}{P_s} \right\rfloor + c - 1}{c} \tag{7.8}$$

where N_{sys} is the number of candidate system configurations in $\mathbb{A}^c$ and $\lfloor \cdot \rfloor$ is the floor operator.

For an example, consider Fig. 7.4 which plots ψ as a function of patch center where $\mathbb{A}^c$ is created with $c = 1$, $P_w = 75$, and $P_s = 1$. Notice that detection performance is maximized when the patch is centered at 158° - i.e. mask rotation angles from 121° to 195° (inclusive).

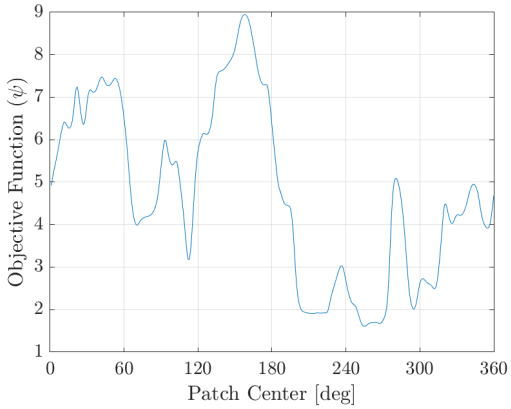

Figure 7.4: ψ as a function of patch center for $c = 1$, $P_w = 75$, and $P_s = 1$.

To get a sense as to why mask rotation angles from 121° to 195° offer better detection than other mask regions, see the expected measurements in Fig. 7.5. From 121° to 195°, there are two instances where the weak source is modulated by the mask while the strong source is fully blocked by closed mask elements. The lower signal and consequently lower noise from the strong source make it easier to detect the modulation of the weak source. Moreover, there are multiple instances where the strong source is modulated by the mask while the expected count rate from the weak source is constant. The lack of overlapping mask transitions makes estimation of the unknown parameters easier.

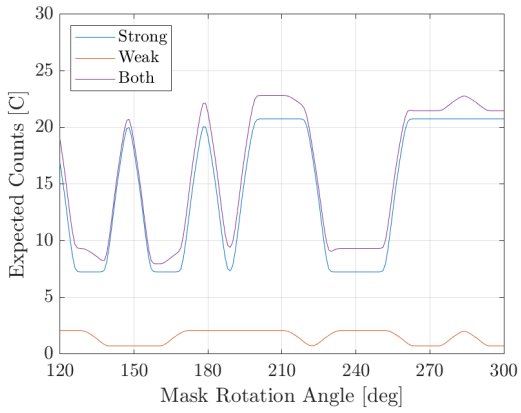

Figure 7.5: Expected counts vs mask rotation angle.

In contrast, the patch centered at 255° is a poor choice to detect the weak source. As shown in Fig. 7.5, during the mask rotation angles from 218° to 292°, both the weak and the strong source are modulated at the same time which makes the weak source more difficult to detect. The weak source modulation at 285° is during an open element for the strong source and thus suffers from greater noise from the strong source than if a closed mask element was blocking the strong source. Thus, detection performance is worse.

Now that we have an objective function and a method to create a set of candidate

system responses, we can explore the potential of adaptive mask movements for improving detection performance.

7.3 Clairvoyant Analysis Results

This section uses a clairvoyant analysis to explore the potential benefit adaptive mask movements can provide in terms of weak source detection. Sec. 7.3.1 investigates the effect of patch width, patch stride, and number of patches on detection performance. The goal is to find a combination of P_w, P_s, and c that leads to reasonable improvement in detection performance while enabling real-time optimization of Eq. 7.7. Once we have selected those parameters, we spot check the clairvoyant predictions with experimental results. Next, Sec. 7.3.2 investigates the detection performance as a function of weak source position relative to the strong source.

7.3.1 Detection Performance for Different Patches

The number of patches, patch width, and patch stride has a dramatic effect on detection performance. Fig. 7.6 - 7.8 show $\psi_{\max}$ and $\tau_{A\to C}$ for different combinations of P_w, P_s, and c. One can interpret $\tau_{A\to C}$ as the relative change in time for the adaptive ROC curve to match the conventional ROC curve. For example, if $\tau_{A\to C} = -20\%$ then the adaptive case can achieve the same performance as the conventional case in 20% less time. When the patch width is 360°, the detection performance is the same as the conventional case.

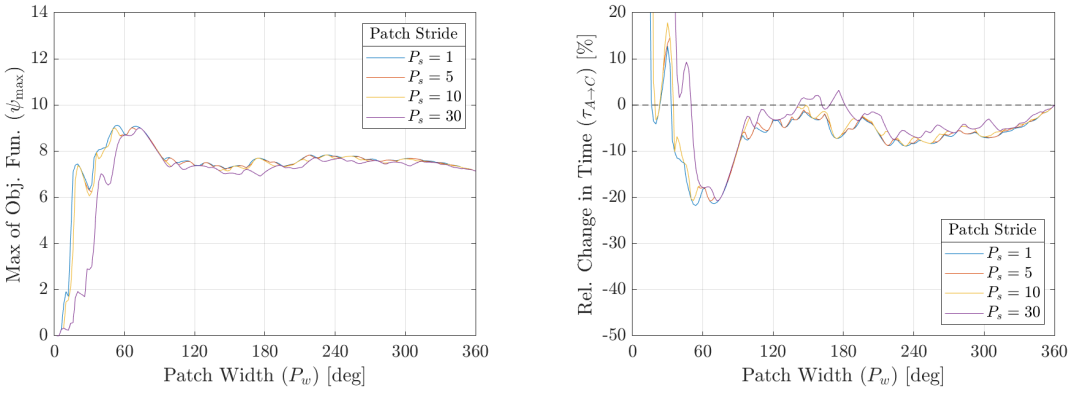

(a) Maximized objective function ($\psi_{\max}$). (b) Relative change in time ($\tau_{A\to C}$).

Figure 7.6: $\psi_{\max}$ and $\tau_{A\to C}$ as a function of patch width and patch stride. $c = 1$.

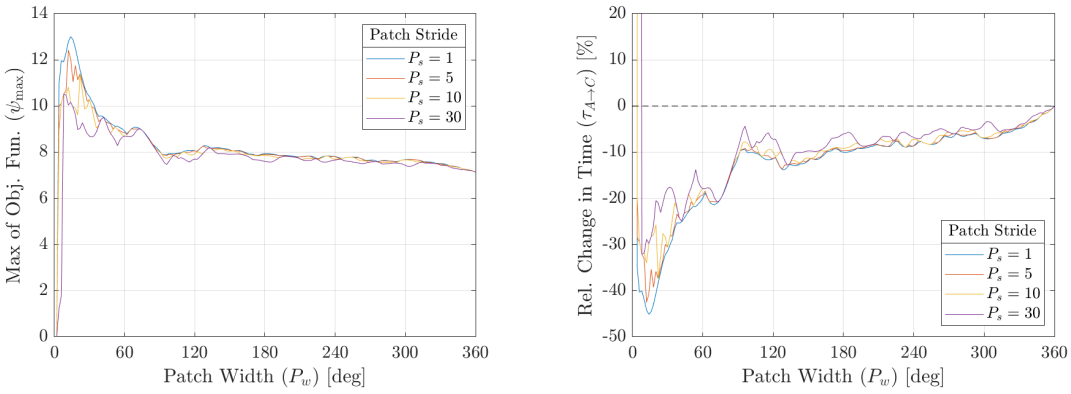

(a) Maximized objective function ($\psi_{\max}$). (b) Relative change in time ($\tau_{A\to C}$).

Figure 7.7: $\psi_{\max}$ and $\tau_{A\to C}$ as a function of patch width and patch stride. $c = 2$.

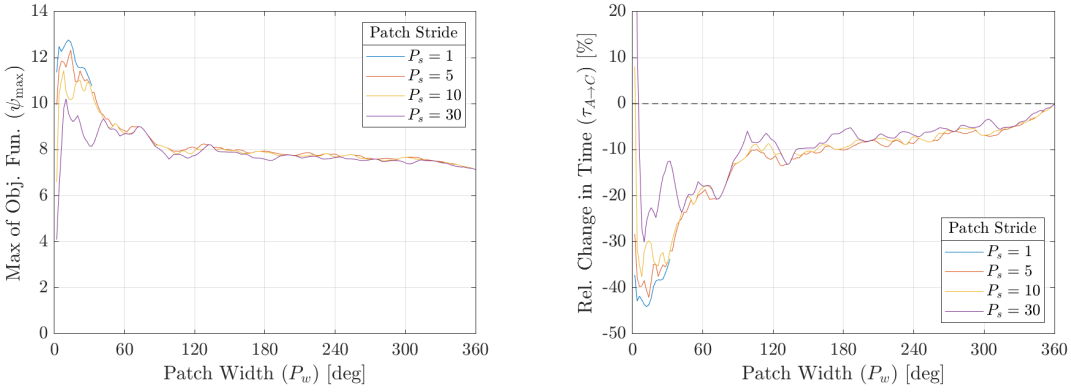

(a) Maximized objective function ($\psi_{\max}$). (b) Relative change in time ($\tau_{A\to C}$).

Figure 7.8: $\psi_{\max}$ and $\tau_{A\to C}$ as a function of patch width and stride. Due to the large computation cost, only some of the patch widths were evaluated for $c = 3$.

We make 5 observations from Fig. 7.6 - 7.8:

1. In general, reducing the patch width improves detection performance when the patch width is large.

2. If the number of patches is small and the patch width is small, detection performance is poor. In some cases, adaptive mask movements perform much worse than the conventional system.

3. Decreasing the patch stride improves detection regardless of patch widths or number of patches.

4. There are diminishing returns when decreasing the patch stride.

5. There are diminishing returns when increasing the number of patches.

Observation 1: In general, reducing the patch width improves detection performance when the patch width is large. As the patch width reduces, measurement time is reallocated to regions of the mask that are better at detection. Although this effect is overall true, locally a small reduction in patch width may result in worse performance.

Observation 2: If the number of patches is small and the patch width is small, detection performance is poor. In some cases, adaptive mask movements perform much worse than the conventional system. This is directly a consequence of not having enough information to make precise estimates of the unknown parameters. Imagine an extreme case where $P_w = 2$ and $c = 1$. In this case, regardless of which patch maximizes ψ, there is very little difference in the two measurements and thus noise will prevent effective detection.

Observation 3: Decreasing the patch stride improves detection for all patch widths or number of patches. A small patch stride means Eq. 7.7 has been optimized among many patches where as if the the patch stride is large, $\mathbb{A}^c$ may not contain the system response that is best for detection.

Observation 4: There are diminishing returns when decreasing the the patch stride. Notice in both Fig. 7.6 - 7.8 that $P_s = 5$ often has the same detection performance as $P_s = 1$. The performance difference between $P_s = 1$ and $P_s = 5$ is highly dependent on the patch width and the number of patches. For example, if the patch width is large, then a small change in the patch stride will not change the optimal patch(es) significantly, in which case decreasing the stride has little benefit. Considering the increased computational cost of $P_s = 1$ vs $P_s = 5$, $P_s = 5$ may be a good compromise for real-time optimization of Eq. 7.7. For example, for $P_s = 5$ and $c = 2$, there are 2628 patch combinations whereas for $P_s = 1$ and $c = 2$ there are 64980 - a 25 fold increase in computational cost for a marginal improvement in detection for most patch widths.

Observation 5: There are diminishing returns when increasing the number of patches. For a comparison of detection performance with respect to the number of patches, see Fig. 7.9.

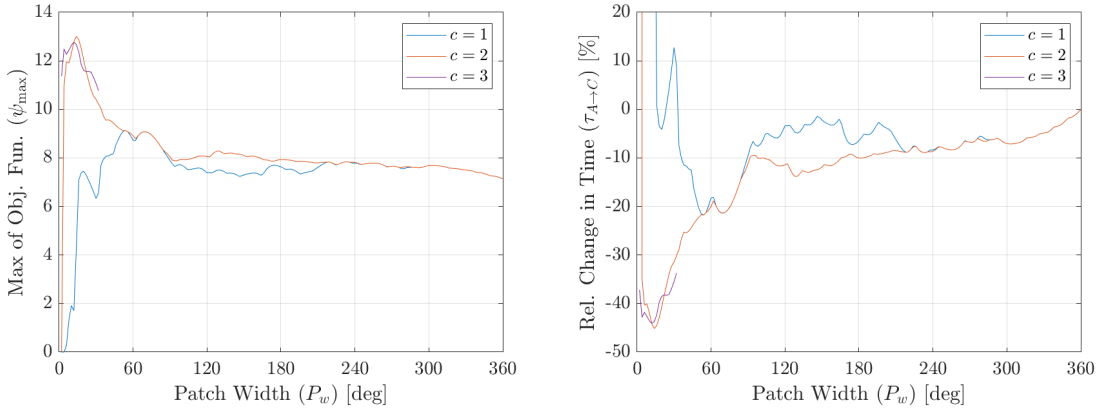

(a) Maximized objective function ($\psi_{\max}$). (b) Relative change in time ($\tau_{A\to C}$).

Figure 7.9: $\psi_{\max}$ and $\tau_{A\to C}$ as a function of the number of patches and patch width. $P_s = 1$. Due to the large computation cost, only some of the patch widths were evaluated for $c = 3$.

When increasing the number of patches from $c = 1$ to $c = 2$, for many patch widths, detection performance improves. Especially for small patch widths, optimizing Eq. 7.7 using $c = 2$ leads to significantly better detection performance compared to $c = 1$. This is because valuable measurements are not always close together in mask rotation space and allowing measurements from different parts of mask gives more flexibility when when optimizing Eq. 7.7.

As the number of patches increases from $c = 2$ to $c = 3$, for most patch widths, detection performance does not change significantly. In fact, for patch widths around 20°, increasing c from 2 to 3 degrades performance! This is because optimization of Eq. 7.7 is constrained - the measurement time must be uniformly distributed to all measurements.

Let $P_{1,c=2}$ and $P_{2,c=2}$ be the two patches that maximize detection when $P_w = 20$ and $c = 2$, and let $P_{1,c=3}$, $P_{2,c=3}$, and $P_{3,c=3}$ be the three patches that maximize detection when $P_w = 20$ and $c = 3$. We find that often two of the patches from the $c = 3$ case are sampling the same mask rotation angles as one of the patches in the

$c = 2$ case. For example, $P_{1,c=3}$, $P_{2,c=3}$ are sampling the same mask rotation angles as $P_{1,c=2}$ and $P_{3,c=3}$ is sampling the same mask rotation angles as $P_{2,c=2}$. Thus increasing c from 2 to 3 does not add unique measurements but instead changes the relative time spent at each patch. Since the measurement time is arbitrarily constrained to be be uniformly spread out to all patches, the relative time spent at each mask rotation angle may not be optimal. Thus there can be small reductions in detection performance when increasing c.

In terms of computational cost, $P_s = 5$, $c = 2$ is 25 times less expensive than $P_s = 5$, $c = 3$ and $P_s = 1$, $c = 2$ is 125 times less expensive than $P_s = 1$, $c = 3$. Given the significant increase in computational cost and the relatively small, if any, improvement in detection, we use $c = 2$ instead of $c = 3$.

These results indicate that adaptive mask movements significantly improve detection performance in the weak source, strong source problem. Given the diminishing gains with respect to patch stride and number of patches, we believe that $P_s = 5$ and $c = 2$ is a good compromise between detection performance and computational cost for real-time optimization of Eq. 7.7. For P_w, we selected 30°.

Experimental Results

Fig. 7.10 shows the experimental ROC curves from the adaptive and conventional cases (see Sec. 7.1 for more details on the experimental setup). For the adaptive case, $\mathbb{A}^c$ was generated with $c = 2$, $P_w = 30$, and $P_s = 5$ and $A_{\max}$ was found using the true values of $\boldsymbol{\theta}$. Note that when evaluating the performance of $A_{\max}$ (calculating Λ_{GLRT}, we used $\hat{\boldsymbol{\theta}}_{\text{ML}}$ instead of the true values. Table 7.2 contains the relevant detection metrics.

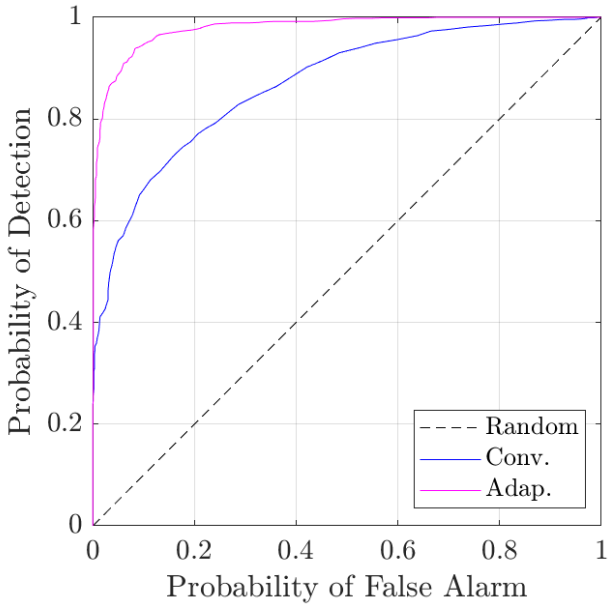

Figure 7.10: Experimental ROC curves from the adaptive and conventional cases. For the adaptive case, $\mathbb{A}^c$ was generated with $c = 2$, $P_w = 30$, and $P_s = 5$.

Table 7.2: Detection metrics for the ROC curves in Fig 7.10

	Conventional	Adaptive
AUROC	0.87	0.98
$P_{D,5\%}$	0.56	0.89

From Fig. 7.10 and Tab. 7.2, we see that utilizing adaptive mask movements leads to a considerable improvement in detection. It is important to note that since data was only collected for a fraction of mask rotation angles, the source cannot be uniquely localized. Fig. 7.11 is a histogram of maximum likelihood (ML) source position estimates ($\hat{\phi}_{\text{ML}}$) of the weak source. In reality, the weak source is at 88°, but often $\hat{\phi}_{\text{ML}}$ is estimated at other locations. In contrast, the conventional data collection almost always estimates the weak source in the correct location, but it is less powerful at detection. Thus, adaptive mask movements improve detection at the expense of unique localization. It is up to the user to decide what is more valuable.

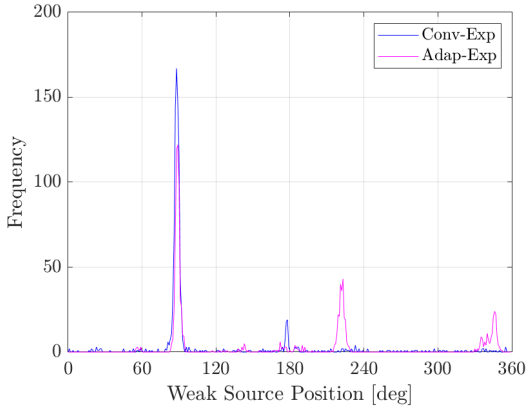

Figure 7.11: Experimental ML source positions for the weak source for the adaptive and conventional cases. The true position of the weak source is 88°. $c = 2$, $P_w = 30$, and $P_s = 5$.

7.3.2 Performance for Different Weak Source Positions

Thus far, we have only considered the case where the weak source is -90° from the strong source, but the relative position of the weak source with respect to the strong source can have an effect on detection performance. Fig. 7.12 plots $\psi_{\max}$ and $\tau_{A\to C}$ for the adaptive ($c = 2$, $P_w = 30$, $P_s = 1$) and the conventional cases as a function of the position of the weak source relative to the strong source.

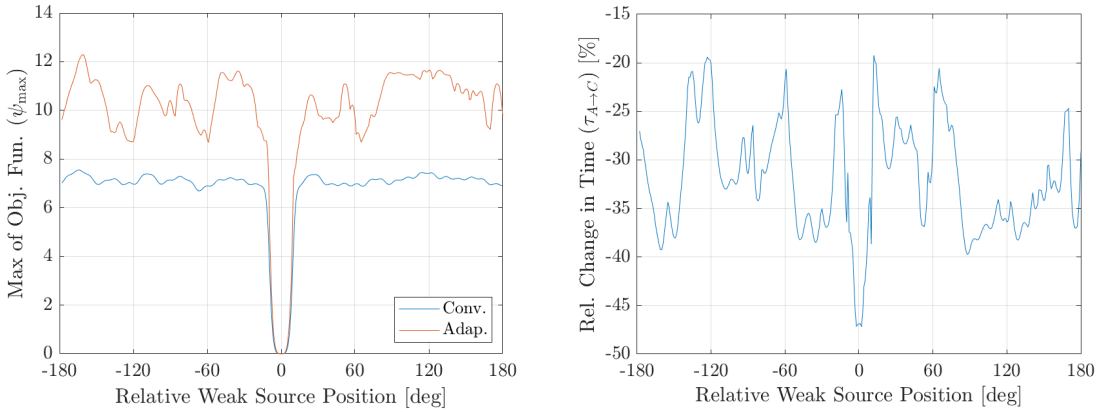

(a) Maximized objective function ($\psi_{\max}$). (b) Relative change in time ($\tau_{A\to C}$).

Figure 7.12: $\psi_{\max}$ and $\tau_{A\to C}$ as a function of weak source position. For the adaptive case, $\mathbb{A}^c$ was generated with $c = 2, P_w = 20, P_s = 1$. The conventional case represents data from a full revolution. The point at a relative position of 0° is omitted.

As one might expect, detection performance is not constant as a function of weak source position for either the conventional or adaptive cases. For some weak source positions such as when the weak source is +90° from the strong source, adaptive imaging can reduce measurement times by ∼40%. In contrast, if the weak source is -120° from the strong source, then measurement time is reduced by ∼20%. In any case, regardless of the true position of the weak source, adaptive mask movements can reduce measurement times by 20-40%. In the difficult case when the two sources are close together, the reduction in time is up to 45%.

7.4 Adaptive Detection Algorithm

The results from the clairvoyant analysis indicate that adaptive mask movements can significantly improve detection in the weak source, strong source problem. In this section, we present an adaptive detection algorithm that can achieve some of the gain predicted by the clairvoyant analysis. Thus far, when optimizing Eq. 7.7, we assumed the positions and intensities of the sources were known. In this section, all parameters are unknown and must be estimated from the measurements.

We separate the full measurement time into 10 cycles of equal measurement time. In each cycle, we determine the number of sources in the field, estimate the unknown parameters, and find the next set of system configurations at which to measure. For the first adaptive cycle when we have no information as to where the weak or strong source may be, we will collect a full revolution of data - i.e. conventional c-TEI imaging.

We redefine the optimization problem as

$$A^{k+1} = \underset{A^{k+1} \in \mathbb{A}^c}{\arg\max}\, \psi(\hat{\boldsymbol{\theta}}_{\mathrm{ML},N}, \hat{\boldsymbol{\theta}}_{\mathrm{ML},A}, A^{0-k}, \boldsymbol{t}^{0-k}, A^{k+1}, T^{k+1}) \tag{7.9}$$

where A^{k+1} is the system response that maximizes detection ability for the $k+1$

adaptive cycle, $\hat{\boldsymbol{\theta}}_{\mathrm{ML},N/A}$ are the MLE of the unknown parameters under the null and alternative hypotheses, A^{0-k} are the system responses where data has already been collected, $\boldsymbol{t}^{0-k}$ is the associated measurement time per bin, and T^{k+1} is the total measurement time allotted for the $k+1$ adaptive cycle. Given that there are 10 cycles, the measurement time per cycle is 90s. $\mathbb{A}$ is created using $c = 2$, $P_w = 30°$, $P_s = 5°$. All optimizations are done by a brute force search.

Sec. 7.4.1 presents a multiple source detection algorithm and Sec. 7.4.2 presents results from the adaptive detection algorithm. Below is an overview of the adaptive detection algorithm.

Algorithm 1: Adaptive Detection Algorithm

```
Let A^0 be a full revolution and T^0 = 90s
for k = 0 k < 10; k = k + 1 do
    Collect data at A^k
    Determine number of sources using Alg. 2
    Estimate θ̂_{ML,N} and θ̂_{ML,A}
    Solve for A^{k+1} in Eq. 7.9. Let T^{k+1} = 90s, c = 2, P_w = 30°, P_s = 5°
    Prepare imaging system for the k + 1 adaptive cycle
end
```

7.4.1 Multiple Source Detection

To detect multiple sources, we will be using a sequential binary testing strategy. We start with the null hypothesis as no sources present ($\mathcal{H}_N = \mathcal{H}_0$) and the alternative hypothesis as one source present ($\mathcal{H}_A = \mathcal{H}_1$)[5]. If the test rejects the null hypothesis, then the algorithm continues to the next binary test where the null hypothesis is one source present ($\mathcal{H}_N = \mathcal{H}_1$) and the alternative is two sources present ($\mathcal{H}_A = \mathcal{H}_2$). This process is continued until either the test fails to reject the null hypothesis or until the algorithm declares the maximum number of sources allowed by the user.

[5]The numbered subscripts on $\mathcal{H}$ indicate the number of sources under that hypothesis.

Each binary hypothesis test will be a modified GLRT. The parameter space for optimization increases exponentially with the the number of sources and thus the computational time necessary to optimize over the entire parameter space is not reasonable for real-time use. To alleviate some of the computational burden, we restrict the search space. Let h be the current hypothesis test where $\mathcal{H}_N = \mathcal{H}_{h-1}$ and $\mathcal{H}_A = \mathcal{H}_h$. We assume

$$\begin{aligned} \hat{\boldsymbol{\phi}}_{A,h} &= [\hat{\boldsymbol{\phi}}_{N,h}^T \ \hat{\phi}_h]^T \\ \hat{\boldsymbol{\theta}}_{N,h} &= \hat{\boldsymbol{\theta}}_{A,h-1} \end{aligned} \tag{7.10}$$

where h is the current test for h sources and goes from 1 to the maximum number of sources allowed by the user (N_S), $\hat{\boldsymbol{\phi}}_{A,h}$ are the estimated source positions under the alternative hypothesis for test h, $\hat{\boldsymbol{\phi}}_{N,h}$ are the estimated source positions under the null hypothesis for test h, $\hat{\phi}_h$ is the estimated source position for the hth source, $\hat{\boldsymbol{\theta}}_{N,h}$ is the null hypothesis parameter vector for test h, and $\hat{\boldsymbol{\theta}}_{A,h-1}$ is the alternative hypothesis parameter vector for test $h-1$.

In this way, for each modified GLRT, we only need to optimize the source position for one source ($\hat{\phi}_h$). The other unknown parameters such as source intensities and unmodulated intensity are re-optimized for each hypothesis. It is much faster to find $\hat{\boldsymbol{\alpha}}_{\mathrm{ML}}$ and $\hat{\boldsymbol{b}}_{d,\mathrm{ML}}$ than $\hat{\phi}_{\mathrm{ML}}$.

Since we are testing multiple hypotheses with the same data, it is important to control not just the false alarm rate for each hypothesis test, but also the family wise error rate (FWER) considering all of the tests. We use the Bonferroni method to control the FWER where the desired FWER, α_{FWER}, is divided by the total number of tests to find the significance level for each test [157, 158].

$$\alpha'_{\mathrm{FA}} = \frac{\alpha_{\mathrm{FWER}}}{N_S} \tag{7.11}$$

where α'_{FA} is the new significance level for each hypothesis test in the sequence.

To control the probability of false alarm below α'_{FA}, for each hypothesis test, we must find the distribution of the likelihood ratio under the null hypothesis ($f(\Lambda'_{\text{modGLRT}}, \mathcal{H}_N)$). Since we are using a modified GLRT with low counts, we cannot assume that $f(\Lambda'_{\text{modGLRT}}, \mathcal{H}_N)$ is distributed as a chi-squared distribution under the null hypothesis. Other simplifications such as approximating the Poisson distribution as a Gaussian distribution are also not justified because of the low counts. Instead, we use a Monte Carlo approach.

For each test, we forward project $\hat{\boldsymbol{\theta}}_{N,h}$ to find the expected measurement under the null hypothesis ($\overline{\boldsymbol{y}}_{\mathcal{H}_N}$) and then generate N_r Poisson replicates of $\overline{\boldsymbol{y}}_{\mathcal{H}_N}$. For each replicate, we calculate the modified GLRT and histogram the $\Lambda'_{\text{modGLRT}}$ values to find $f(\Lambda'_{\text{modGLRT}}, \mathcal{H}_N)$. Then, the corresponding critical threshold, $\Lambda'_{\text{modGLRT,crit}}$, is found by controlling the false alarm rate to the requisite level (Eq. 2.38). Alg. 2 is a

summary the multiple source detection algorithm.

Algorithm 2: Multiple Source Detection Algorithm

Solve $\hat{\theta}_{N,0} = \arg\max_{\theta \in \mathcal{H}_0} p(y;\theta)$
for $h = 1, \mathcal{H}_N = \mathcal{H}_{h-1}, \mathcal{H}_A = \mathcal{H}_h;\ h \leq N_S;\ h = h+1$ **do**
  Solve $\hat{\boldsymbol{\theta}}_{A,h} = \arg\max_{\boldsymbol{\theta} \in \mathcal{H}_A} p(\boldsymbol{y};\boldsymbol{\theta})$
  Find $\Lambda'_{\text{modGLRT,cand}}$
  Forward project $\hat{\boldsymbol{\theta}}_{N,h}$ to find $\overline{\boldsymbol{y}}_{\mathcal{H}_N}$
  Assuming Poisson statistics, create N_r replicates of $\overline{\boldsymbol{y}}_{\mathcal{H}_N}$
  for $r = 0;\ r < N_r;\ r = r+1$ **do**
    Find $\hat{\boldsymbol{\theta}}_{N,h,r} = \arg\max_{\boldsymbol{\theta} \in \mathcal{H}_N} p(\boldsymbol{y}_{\mathcal{H}_N,r};\boldsymbol{\theta})$
    Find $\hat{\boldsymbol{\theta}}_{A,h,r} = \arg\max_{\boldsymbol{\theta} \in \mathcal{H}_A} p(\boldsymbol{y}_{\mathcal{H}_N,r};\boldsymbol{\theta})$
    Calculate the likelihoods to find $\Lambda'_{\text{modGLRT},r}$
  end
  Histogram $\Lambda'_{\text{modGLRT},r}$ for all r to find $f(\Lambda'_{\text{modGLRT}}, \mathcal{H}_N)$
  Find $\Lambda'_{\text{modGLRT,crit}}$ using Eq. 2.38
  if $\Lambda'_{\text{modGLRT,cand}} > \Lambda'_{\text{modGLRT,crit}}$ **then**
    $\hat{\boldsymbol{\theta}}_{N,h+1} = \hat{\boldsymbol{\theta}}_{A,h}$
  else
    break
  end
end

where $\Lambda'_{\text{modGLRT,cand}}$ is the modified GLRT likelihood ratio of the experimental data (i.e. the candidate likelihood ratio), $\hat{\boldsymbol{\theta}}_{N/A,h,r}$ is the MLE parameter vector for Poisson replicate r, and $\Lambda'_{\text{modGLRT},r}$ is the corresponding modified GLRT likelihood ratio. Note that the parameter space for optimizing $\hat{\theta}_{N,h}$ and $\hat{\theta}_{A,h}$ is constrained according to Eq. 7.10 and the parameter space is unbounded meaning source and background intensity estimates can be negative.

For the weak source, strong source problem, $N_S = 2$ and we set $N_r = 20$. We will test four α_{FWER} values to see which works best: 2, 1.5, 1, or 0.5. These correspond to an false alarm rate per test (α'_{FA}) of 1, 0.75, 0.5, or 0.25 respectively. Changing

the α_{FWER} controls how aggressive or conservative the multiple source detection algorithm is when detecting sources. The number of sources declared by the multiple source detection algorithm affects the optimal system response ($A_{\max}$) for the next adaptive cycle.

For example, assuming the weak source exists but we do not have enough information to make a precise estimate of its position, setting α_{FWER} to a large value may result in non-optimal system configurations for the next adaptive cycle on account of the poor estimation of the weak source position. This may make it tougher to find the weak source if measurement time is spent collecting data at mask rotation angles that are poor at detection. On the other hand, a large α_{FWER} value also leads to the greatest probability of detection of the weak source by the multiple source detection algorithm and thus the largest potential benefit from adaptive mask movements. The sooner the weak source is detected, the more time can be spent at system configurations optimized for the weak source.

7.4.2 Results

Fig. 7.13 shows the experimental ROC curves using the adaptive detection algorithm (see Sec. 7.1) for more details on the experimental setup) and Table 7.3 are the corresponding detection metrics. $\mathbb{A}^c$ is created with $c = 2$, $P_w = 30°$, $P_s = 5°$. Each ROC curve is made with 1,000 replicates of experimental data. For each replicate, we used the same full-revolution, conventional data to initialize the adaptive detection algorithm for all values of α'_{FA}.

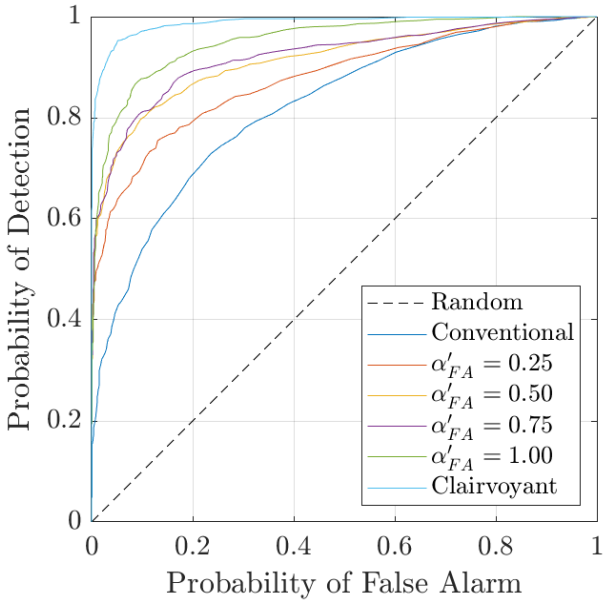

Figure 7.13: Experimental ROC curves using the adaptive detection algorithm outlined in Alg. 1 for different per test false alarm rates in Alg. 2.[6] The weak source is at 88°.

Table 7.3: Detection metrics for the ROC curves in Fig 7.13

	AUROC	$P_{D,5\%}$
Conventional	0.82	0.42
$\alpha'_{\text{FA}} = 0.25$	0.88	0.63
$\alpha'_{\text{FA}} = 0.50$	0.91	0.73
$\alpha'_{\text{FA}} = 0.75$	0.92	0.73
$\alpha'_{\text{FA}} = 1.00$	0.95	0.80
Clairvoyant	0.99	0.95

As α'_{FA} is allowed to increase, the benefit from adaptive imaging increases as well. The higher the α'_{FA}, the higher the the probability of detection for the weak source by the multiple source detection algorithm. Thus, more measurement time can be spent collecting data at mask rotation angles that provide greater detection ability. The adaptive detection algorithm with $\alpha'_{\text{FA}} = 1.00$ has double the detection ability

[6]To be clear, α'_{FA} refers to the per test false alarm rate set in the multiple source detection algorithm whereas the x-axis refers to the probability of false alarm using the adaptive detection algorithm.

for the weak source when the false alarm rate from the adaptive detection algorithm is 5%. This is significant improvement over the conventional system.

As another example, Fig. 7.14 shows experimental ROC curves using the adaptive detection algorithm for a weak source at 56° (-122° from the strong source). Table 7.4 are the corresponding detection metrics.

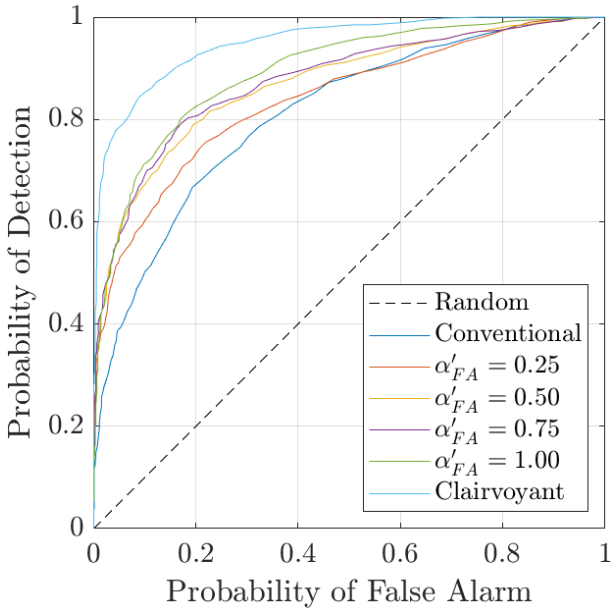

Figure 7.14: Experimental ROC curves using the adaptive detection algorithm outlined in Alg. 1 for different per test false alarm rates in Alg. 2. The weak source is at 56°.

Table 7.4: Detection metrics for the ROC curves in Fig 7.14

	AUROC	$P_{D,5\%}$
Conventional	0.81	0.39
$\alpha'_{\text{FA}} = 0.25$	0.84	0.53
$\alpha'_{\text{FA}} = 0.50$	0.87	0.58
$\alpha'_{\text{FA}} = 0.75$	0.88	0.57
$\alpha'_{\text{FA}} = 1.00$	0.89	0.57
Clairvoyant	0.95	0.78

The adaptive detection algorithm with $\alpha'_{\text{FA}} = 1.00$ has 50% greater probability of detection for the weak source when the false alarm rate from the adaptive detection

algorithm is 5%. Again, adaptive mask movements provide a significant improvement in detection.

7.5 Experimental vs Offset Detector System Response

Throughout this chapter, we used an experimental system response when estimating parameters instead of the offset detector model. As discussed in Sec. 5.2, because of environmental scatter, there is model mismatch between the experimental data and the offset detector model. Since the GLRT is sensitive to such model mismatch, the offset detector model cannot reliably be used for detection. Fig. 7.15 and 7.16 show simulated and experimental ROC curves made using the offset detector model and the experimental system response respectively. Due to model mismatch, the experimental results using the offset detector model do not match the simulated results. Moreover, this performance degradation seems to impact the adaptive case more than the conventional. On the other hand, the simulated and experimental results match when using the experimental system response. Because the experiments do not match the simulated results when using the offset detector model, we opted to use an experimental system response instead.

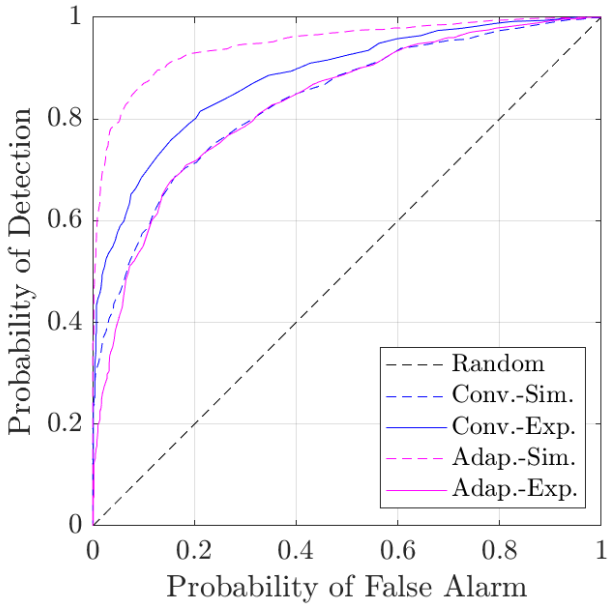

Figure 7.15: ROC curve using the offset detector model. $\mathbb{A}^c$ is created with $c = 2$, $P_w = 30°$, $P_s = 5°$.

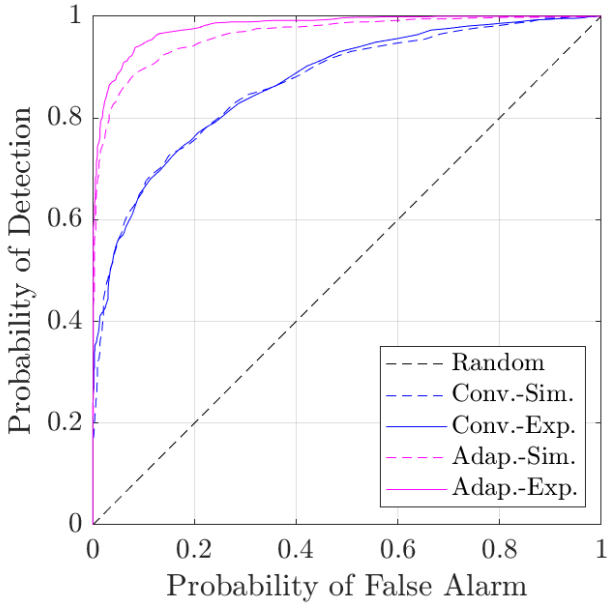

Figure 7.16: ROC curve using the experimental system response. $\mathbb{A}^c$ is created with $c = 2$, $P_w = 30°$, $P_s = 5°$.

7.6 Conclusions

We have shown through a clairvoyant analysis and through experiments that adaptive mask movements significantly improve the detection of a weak source in the vicinity of a strong source. Depending on the position of the weak source relative to the strong source, adaptive imaging can achieve the same performance as the conventional setup in 20% - 40% less time. Although detection performance improves, since the adaptive setup only collects measurements at a few mask rotation angles, the system cannot uniquely identify the location of the weak source.

We also present an adaptive detection algorithm that achieves some of the gain predicted by the clairvoyant analysis. In particular, we experimentally showed that the probability of detection for a false alarm rate of 5% doubles under the adaptive detection algorithm relative to the conventional when the weak source is -90° from the strong source.

There is an important caveat to note. When reconstructing experimental data, we used an experimental system response instead of the offset detector model. The experimental system response was generated from a very similar experiment as the one used in this chapter and thus has similar environmental scatter. To make adaptive detection applicable in the real-world, one needs to find a way to reduce the model mismatch between the offset detector model (or some other computationally inexpensive model) and experimental data. In any case, the results presented here demonstrate the potential for adaptive mask movements when considering the weak source, strong source problem.

CHAPTER VIII

Demonstrations using Special Nuclear Material

This chapter presents reconstructions from three experiments conducted at the Zero Power Physics Reactor (ZPPR) facility at Idaho National Laboratory (INL). The goal of these experiments is to demonstrate the benefit of combining data from multiple detector positions when reconstructing complex source scenes with special nuclear material.

We refer to these experiments as:

- Sec. 8.1: Line Source
- Sec. 8.2: Split Line Source
- Sec. 8.3: Multiple Sources

All of the experiments will use one or both of the following items:

1. High burn-up Pu-240 plates. Each plate is $0.32 \times 5.08 \times 7.62$ cm and contains $\sim$23.9 g of Pu-240 [159].
2. Mixed oxide (MOX) fuel pins (MOX pin ID 129). Each fuel pin is 15.24 cm in length by 0.95 cm in diameter. The pins contain $\sim$3.6 g of Pu-240 [160].

Although both fast-neutron and gamma-ray data was collected using the stilbene detector and the $Cs_2LiLa(Br, Cl)_6$ (CLLBC) detector, this chapter only presents the gamma-ray reconstructions from the CLLBC detector. The fast-neutron reconstructions are in Appendix E. The gamma-ray reconstructions only use pulses that deposited between 275-425 keV. To reduce the thermal neutron flux, a 0.58 mm, 90% enriched, cadmium sheet was wrapped around the CLLBC detector.

All conventional, cylindrical, time-encoded imaging (c-TEI) reconstructions are made using full revolutions of data with the detector at the center for the entire measurement time. All adaptive, c-TEI reconstructions are made using full revolutions of data with the 10% of the time spent with the detector at the center and the remaining 90% of time spent at other detector positions. The measurement time for the conventional and adaptive cases is the same.

For each experiment, data was collected at 145 detector positions. In post-processing, we select the detector positions to use in the reconstruction. In most cases, we do not have enough data at one off-center detector position to adequately reconstruct the images, thus we must combine data from multiple detector positions. For these demonstrations, we use our intuition to decide which detector positions to use for the adaptive reconstructions. Where applicable, we will explain our thought process.

8.1 Line Source

The line source is composed of 6 stacks of 3 Pu-240 plates. To make each stack, the Pu-240 were placed one on top of the other with the 5.08 $\times$ 7.62 cm planes in contact. The 5.08 $\times$ 0.96 cm plane of each stack is in contact with the stacks next to it. Thus, the line source is 45.72 $\times$ 5.08 $\times$ 0.96 cm. From the perspective of

MATADOR, the line source is 28.5° wide.[1] Fig. 8.1 is a picture of the setup. The line source is centered at (90cm,180°).

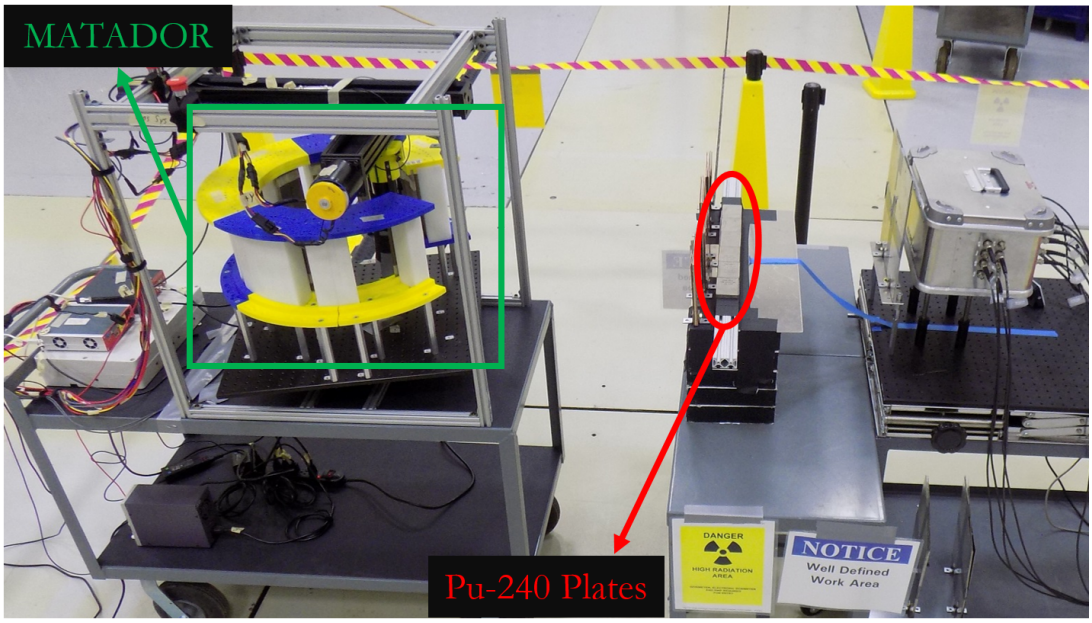

Figure 8.1: Picture of a line source measurement at the ZPPR facility at INL.

All of the reconstructions are made using maximum likelihood expectation maximization (MLEM) and the offset detector model. MLEM is terminated when the normalized root mean squared error (NRMSE) between the observation vector and the forward projection plateau (see Sec. 2.27). Additionally, we also show MLEM reconstructions at 1,000 iterations. Often, extended sources reconstruct as a group of point sources instead of a smooth, uniform extended source. This effect worsens as the number of iterations increases. We refer to the MLEM reconstruction that was terminated based on the NRMSE as the low-iteration MLEM reconstruction and we refer to the MLEM reconstruction made with 1,000 iterations as the high-iteration MLEM reconstruction.

We assess the reconstructions in terms of the full width at half maximum (FWHM)

[1] In reality, the Pu metal in the Pu-240 plates is smaller than the outer dimensions of the cladding so the true width of the source is smaller than 28.5°.

of the line source, uniformity of the source, and noise in the background region. For the FWHM calculation, we define the half maximum as half of the mean intensity from 173° to 187° (inclusive). Source uniformity is defined as the standard deviation of the reconstructed intensity from 173° to 187° and noise in the background region is defined as the standard deviation of the image from 0° to 120° and 240° to 360°. Smaller values of source uniformity and noise in the background region are preferable.

For the adaptive case, we use data from 13 off-center detector positions - the chosen detector positions are shown in red in Fig. 8.2. We chose detector positions that provide the best angular resolution for the center of the line source. The line source reconstructions use 21.7 minutes (1300 s) of data.

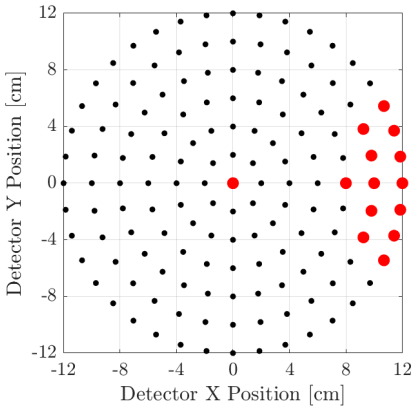

Figure 8.2: The red dots represent the detector positions that were used for the adaptive c-TEI reconstructions. 90s of data was used from all off-center detector positions and 130s of data from the center.

Since the adaptive case will utilize data from multiple detector positions, and thus have more unique measurements as opposed to better statistics, we expect the adaptive reconstructions to have better uniformity both for the source and the background. Additionally, given the better angular resolution of the system in the adaptive case, we expect the width estimates to be more accurate.

8.1.1 Gamma-Ray Reconstructions

Fig. 8.3 shows the gamma-ray spectrum from the line source experiment collected with the CLLBC detector. The dashed blue lines extending from 275 - 425 keV highlight the gamma-rays used in these reconstructions. Note that the peaks at ∼360 keV and ∼400 keV are not photopeaks but rather are the accumulation of many prominent emission lines from Pu-239 and Am-241.

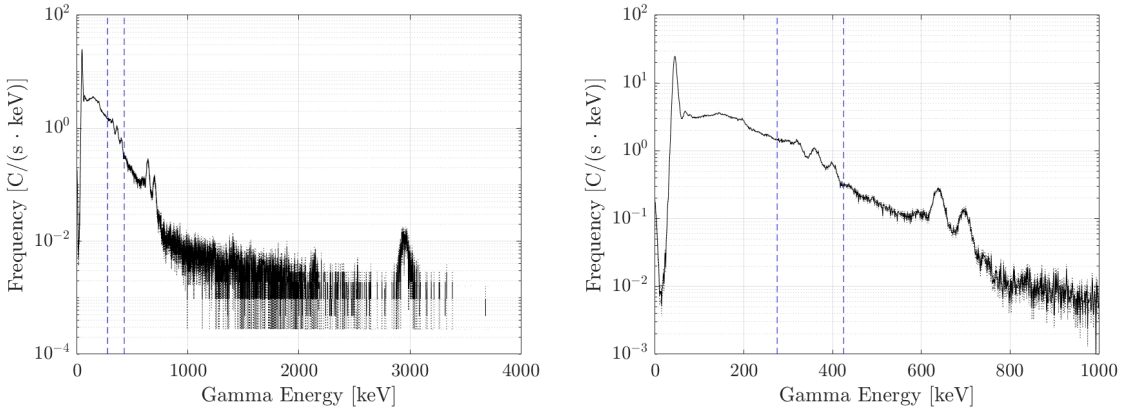

(a) Full energy range. (b) Magnified.

Figure 8.3: Gamma-ray energy spectrum collected using the CLLBC detector. Only pulses with energies between 275 and 425 keV are used in these reconstructions.

Fig. 8.4a is the low-iteration, gamma-ray reconstruction using the conventional, detector-centered setup and Fig. 8.4b is the adaptive case. The metrics are summarized in Table 8.1. Both the conventional and adaptive reconstructions show an extended source as expected. The FWHM from the adaptive reconstruction is closer to the truth but both estimates are smaller than expected. In terms of uniformity and background noise, the adaptive reconstruction is more uniform (uniformity metric is 37.5% smaller) and has 50% less noise in the background.

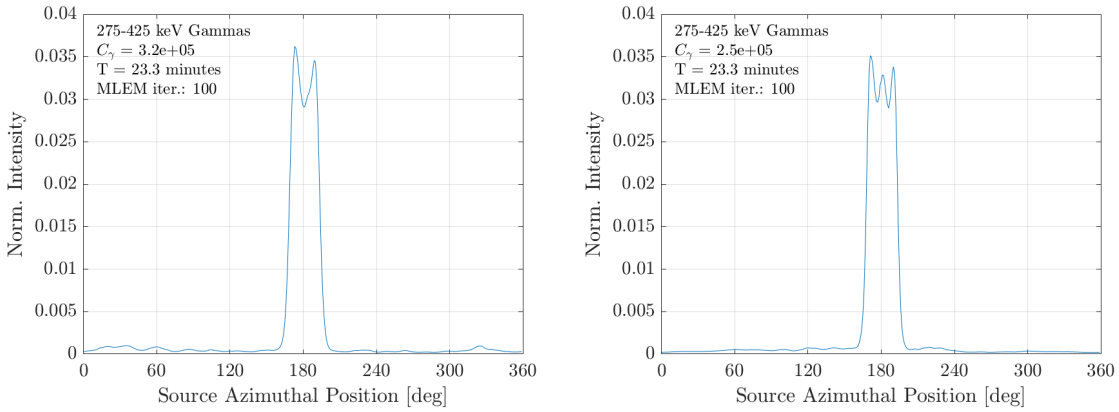

(a) Conventional, detector-centered setup.

(b) Adaptive setup.

Figure 8.4: Low-iteration, gamma-ray reconstruction of the line source.

Table 8.1: Line source FWHM, uniformity, and noise for low-iteration, gamma-ray reconstructions.

	Conventional	Adaptive
FWHM	25.8	26.5
Uniformity (10^{-3})	2.4	1.5
Noise (10^{-4})	2.2	1.1

Fig. 8.5a and 8.5b are reconstructions using the same data as Fig. 8.4a and 8.4b but MLEM was run for 1,000 iterations. The metrics are summarized in Table 8.2. Both the conventional and adaptive reconstructions show extended sources as expected. Compared to the low-iteration reconstructions, the FWHMs from both the conventional and adaptive high-iteration reconstructions are closer to the truth. The adaptive reconstruction only underestimates the width by 1.5°. Additionally, the adaptive reconstruction is significantly more uniform and has less noise in the background.

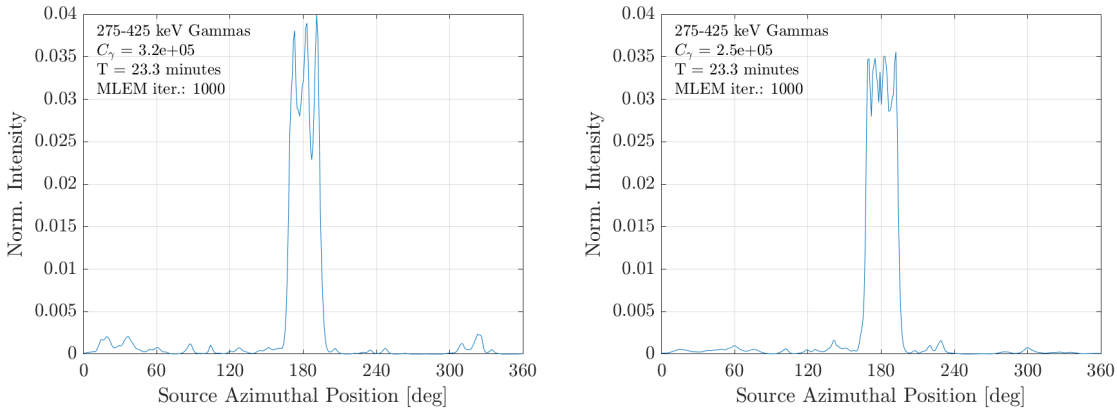

(a) Conventional, detector-centered setup.

(b) Adaptive setup.

Figure 8.5: High-iteration, gamma-ray reconstruction of the line source.

Table 8.2: Line source FWHM, uniformity, and noise for high-iteration, gamma-ray reconstructions.

	Conventional	Adaptive
FWHM	26.4	27.0
Uniformity (10^{-3})	4.9	2.3
Noise (10^{-4})	5.7	2.2

Based on the gamma-ray reconstructions, it is clear that combining data from multiple detector positions improves reconstructions for a line source. The line source intensity is 37.5% more uniform and the background noise is reduced by half for the low-interation reconstructions.

8.2 Split Line Source

The split line source is essentially the line source cut in half and separated by 20 cm. It is composed of two lines sources each made up of 3 stacks of 3 Pu-240 plates. To make each stack, the Pu-240 plates were placed one on top of the other with the 5.08 × 7.62 cm planes in contact. The 5.08 × 0.96 cm plane of each stack is in contact with the stacks next to it. From the perspective of MATADOR, each half of the split line source is 13.7° wide and the inside edges of the two halves are

separated by 12.7°. Fig. 8.6 is a picture of the setup. The split line source is centered at (90cm,180°).

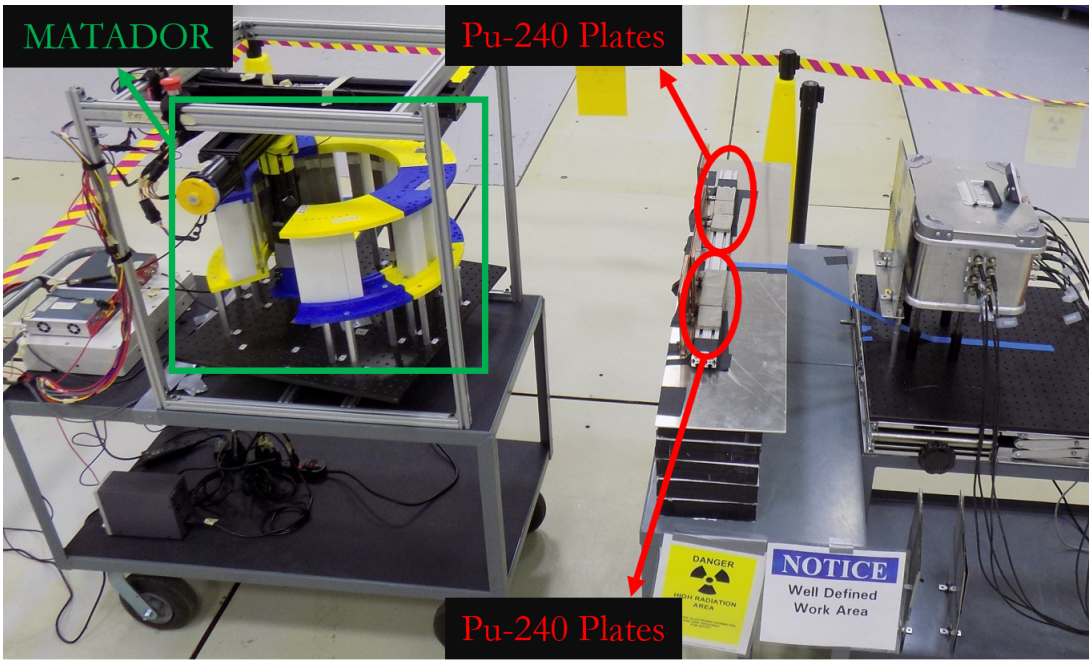

Figure 8.6: Picture of the split line source measurement at the ZPPR facility at INL.

Similar to the line source reconstructions, we use the offset detector model and show low-iteration MLEM reconstructions (terminated by the user based on the NRMSE) and high-iteration MLEM reconstructions (1,000 iterations).

Since there are two sources in the field-of-view (FOV), we refer to the line source at ∼168° and the line source at ∼194° as S_1 and S_2 respectively. We assess the reconstructions of each source in terms of the FWHM of the reconstruction, uniformity of the source, and noise in the background region. For the FWHM calculation, we define the half maximum for S_1 as half the mean source intensity from 165° to 173° and for S_2 as half the mean source intensity from 190° to 198°. Source uniformity is defined as the standard deviation of the reconstructed intensity over the ranges listed above. Noise in the background region is defined as the standard deviation of the image from 0° to 120° and 240° to 360°.

For the adaptive case, we use the same 13 off-center detector positions that were used for the line source. Fig. 8.7 shows the chosen detector positions in red. The measurement time is the same as well: 21.7 minutes (1300s).

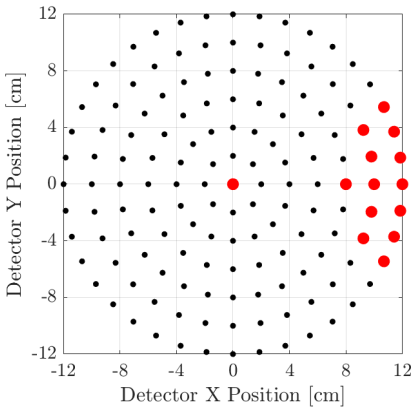

Figure 8.7: The red dots represent the detector positions that were used for the adaptive c-TEI reconstructions. 90s of data was used from all off-center detector positions and 130s of data from the center.

8.2.1 Gamma-Ray Reconstructions

Fig. 8.8a is the low-iteration, gamma-ray reconstruction using the conventional, detector-centered setup and Fig. 8.8b is the adaptive case. The metrics are summarized in Table 8.3.

Both the conventional and the adaptive reconstructions show two extended objects that are well separated. The FWHMs of S_1 and S_2 from both reconstructions are the same. For both S_1 and S_2, the adaptive reconstruction is more uniform than the conventional by $\sim$25%. The background noise is 37.5% lower for the adaptive reconstruction relative to the conventional.

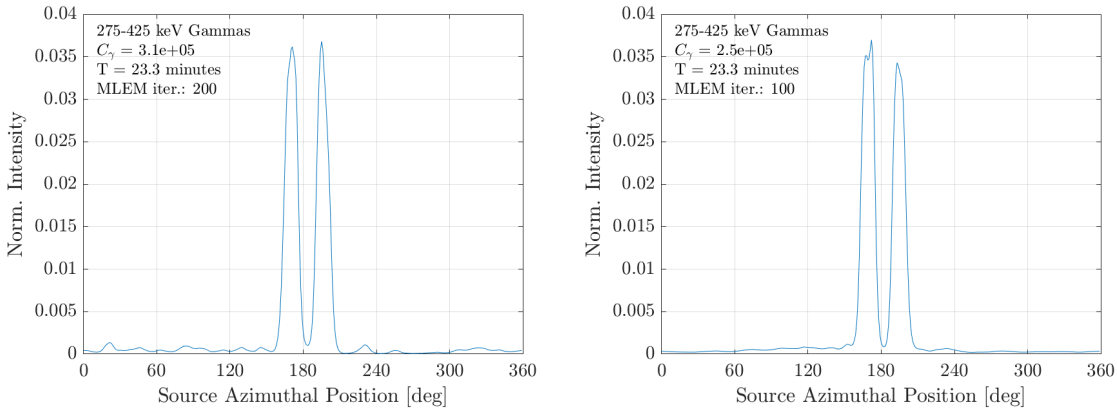

(a) Conventional, detector-centered setup.

(b) Adaptive setup.

Figure 8.8: Low-iteration, gamma-ray reconstruction of the split line source.

Table 8.3: Split line source FWHM, uniformity, and noise for low-iteration, gamma-ray reconstructions.

	Conventional	Adaptive
S_1 FWHM	12.5	12.5
S_2 FWHM	12.2	12.1
S_1 Uniformity (10^{-3})	2.5	1.9
S_2 Uniformity (10^{-3})	4.0	2.9
Noise (10^{-4})	2.4	1.5

Fig. 8.9a and 8.9b are reconstructions using the same data as Fig. 8.8a and 8.8b but MLEM was run for 1,000 iterations. The relevant metrics are summarized in Table 8.4.

In both reconstructions, it is clear that there are two extended sources present. For S_1, the uniformity of the conventional reconstruction is better whereas for S_2 the uniformity of the adaptive reconstruction is better. With respect to the noise in the background, the adaptive reconstruction has 50% less noise.

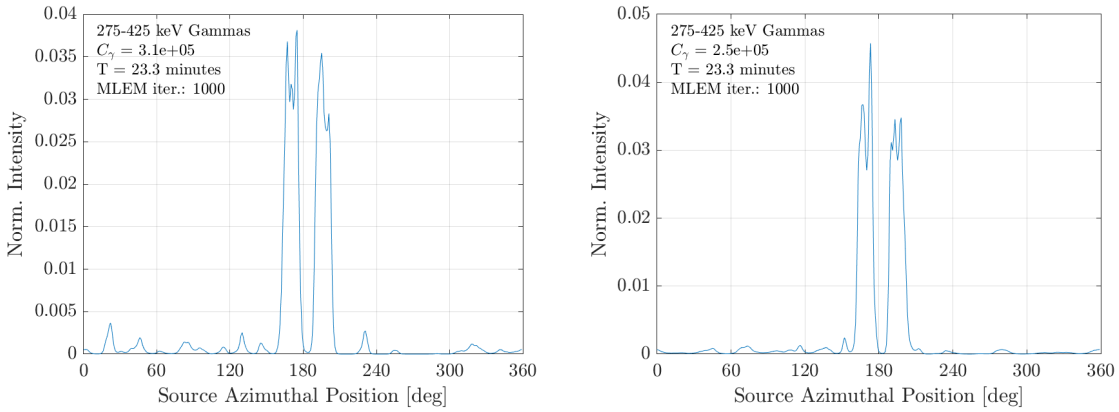

(a) Conventional, detector-centered setup.

(b) Adaptive setup.

Figure 8.9: High-iteration, gamma-ray reconstruction of the split line source.

Table 8.4: Split line source FWHM, uniformity, and noise for high-iteration, gamma-ray reconstructions.

	Conventional	Adaptive
S_1 FWHM	13.3	13.1
S_2 FWHM	13.6	13.2
S_1 Uniformity (10^{-3})	3.0	5.8
S_2 Uniformity (10^{-3})	3.6	2.7
Noise (10^{-4})	5.4	2.7

For gamma-ray reconstructions, utilizing data from multiple detector positions results in better source uniformity and lower background noise. Based on the low-iteration, gamma-ray reconstructions, the uniformity of the adaptive reconstructions is ∼25% better and the background noise is 37.5% lower.

8.3 Multiple Source

The multiple source experiments consists of multiple sources spread out in the FOV. A picture of the setup is in Fig. 8.10 and Fig. 8.11 shows the setup in $r - \theta$ space.

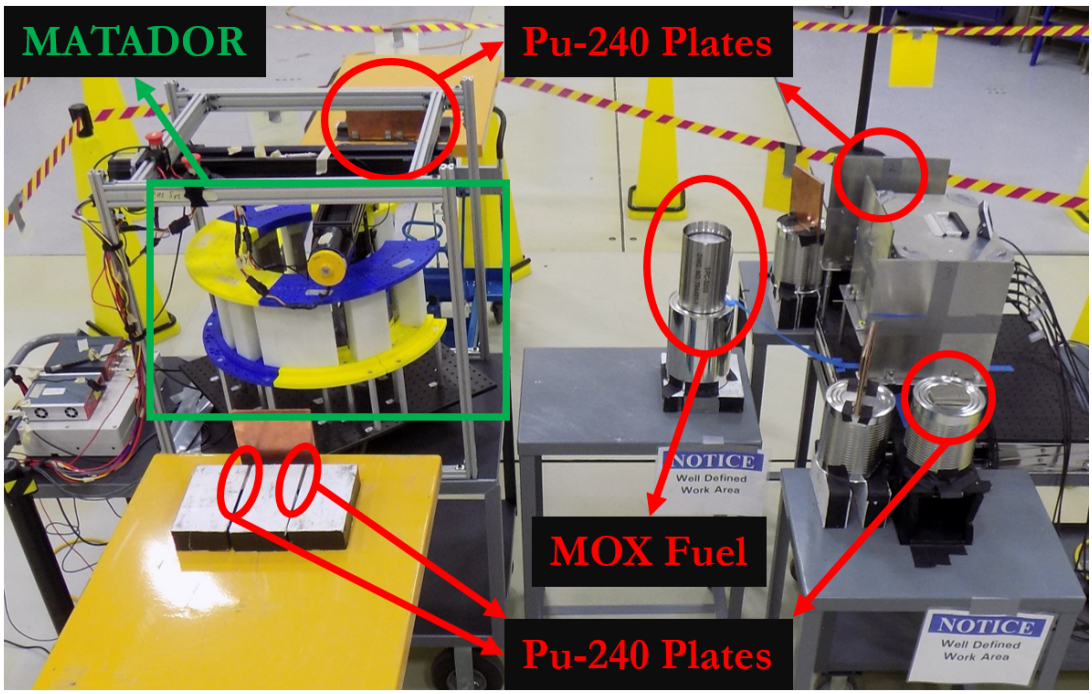

Figure 8.10: Picture of a multiple source measurement at the ZPPR facility at INL.

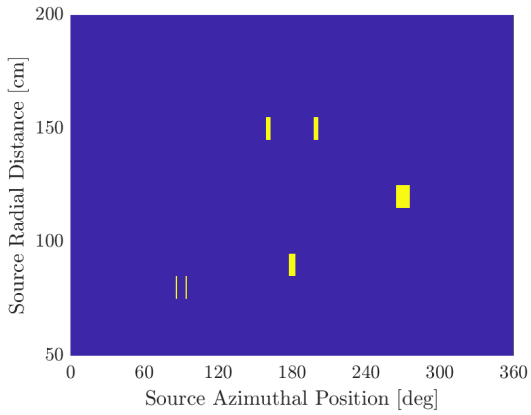

Figure 8.11: Experimental setup of the multiple source measurement.

There are five objects of interest in the multiple source setup:

1. MOX fuel canister: at $(90\text{cm}, 180°)$, there are 32 MOX fuel pins arranged in a lattice [161]. The fuel pins are inside of a 0.4 cm thick steel container. The MOX fuel canister is significantly hotter than any other object in the FOV.

2. Pu-240 stack #1: at $(150\text{cm}, 160°)$, there are 5 Pu-240 plates stacked one on top of the other. The 5.08×7.62 cm planes are in contact and the 0.32 cm edge is facing MATADOR. This object is shielded by 0.32 cm of tin and 0.64 cm of copper.

3. Pu-240 stack #2: at $(150\text{cm}, 200°)$, there are 5 Pu-240 plates stacked one on top of the other. The 5.08×7.62 cm planes are in contact and the 0.32 cm edge is facing MATADOR. This object is shielded by 0.32 cm of tin and 0.64 cm of copper.

4. Line source: centered at $(120\text{cm}, 270°)$, there are 4 Pu-240 plates placed in a line. The 7.62×0.32 cm long sides are in contact and the 5.08 cm edge of each plate is facing MATADOR. From the perspective of MATADOR, the source is 9.7° wide. This object is shielded by 0.32 cm of tin and 0.64 cm of copper.

5. Two source: centered at $(80\text{cm}, 90°)$, there are 2 stacks of 2 Pu-240 plates placed 10.2 cm apart. Within each stack, each plate is standing on its 7.62×0.32 cm edge and the 7.62×5.08 cm planes are in contact. The stacks are sandwiched between $20.32 \times 10.16 \times 5.08$ cm lead bricks. From the perspective of MATADOR, the two stacks of Pu-240 plates appear as two point sources separated by 8°. This object is shielded by 1.27 cm of copper.

This experimental setup contains

- multiple sources,
- sources with widely different intensities,
- sources with different emission spectra,

- sources at different radial distances from the system,
- extended sources, and
- sources that are close together,

thus it is an interesting but challenging source scene to image.

These reconstructions will demonstrate two concepts: collecting data with the detector at multiple positions in the mask

1. enables depth estimation, and
2. provides greater angular resolution even in complex scenarios.

To show 2D imaging ability, we focus on the MOX fuel as it is the most intense. 2D imaging is possible using the MATADOR system due to parallax as the detector moves. To maximize the parallax effect, data should be collected from detector positions that are far apart. Angular resolution of the imaging system also plays a role in 2D positioning, thus we utilize data from detector positions that provide both a large parallax and acceptable angular resolution for the MOX fuel.

To show improved angular resolution, we focus on the two source object at $(80\text{cm}, 90^\circ)$. Under the conventional c-TEI system, the two sources cannot be separated, but when we incorporate data from different positions, the sources are separated. Much of the allotted time is spent at detector positions that provide higher resolution data for the two source object.

For the adaptive case, the detector positions we selected are the red dots in Fig. 8.12. 90 seconds of data was used for the off-center detectors and 220 seconds of data when the detector is at the center. The following reconstructions use a total of 36.7 minutes (2200 s) of data.

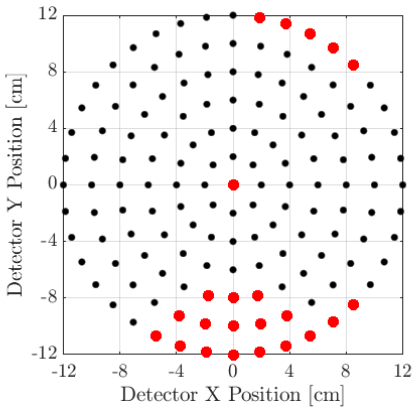

Figure 8.12: The red dots represent the detector positions that were used for the adaptive c-TEI reconstructions. 90s of data was used from all off-center detector positions and 220s of data from the center.

8.3.1 Gamma-Ray Reconstructions

Fig. 8.13 shows the gamma-ray spectrum from the CLLBC detector. Since the MOX fuel has less shielding than the other sources in the FOV, the lower energy gammas are predominantly from the MOX fuel. The dashed blue lines extending from 275-425 keV highlight the gamma rays used in these reconstructions.

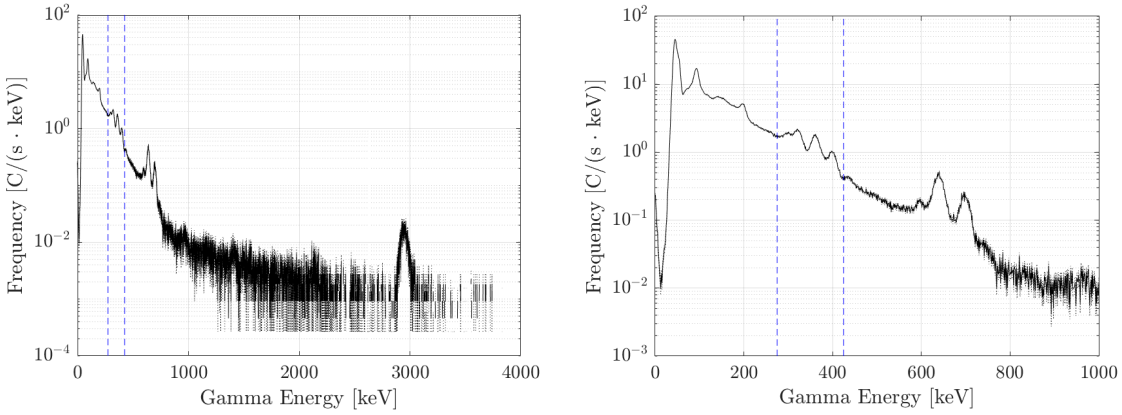

(a) Full energy range. (b) Magnified.

Figure 8.13: Gamma-ray energy spectrum collected using the CLLBC detector. Only pulses with energies between 275 and 425 keV are used in these reconstructions.

First, we show reconstructions from the conventional setup and then contrast those

against the adaptive setup. Fig. 8.14 is the 2D reconstruction from the conventional setup and Fig. 8.15 and 8.16 are slices from the 2D image - Fig. 8.15 is an azimuthal slice at 182° and Fig. 8.16 is a radial slice at 80 cm. These reconstructions are also shown in log scale.

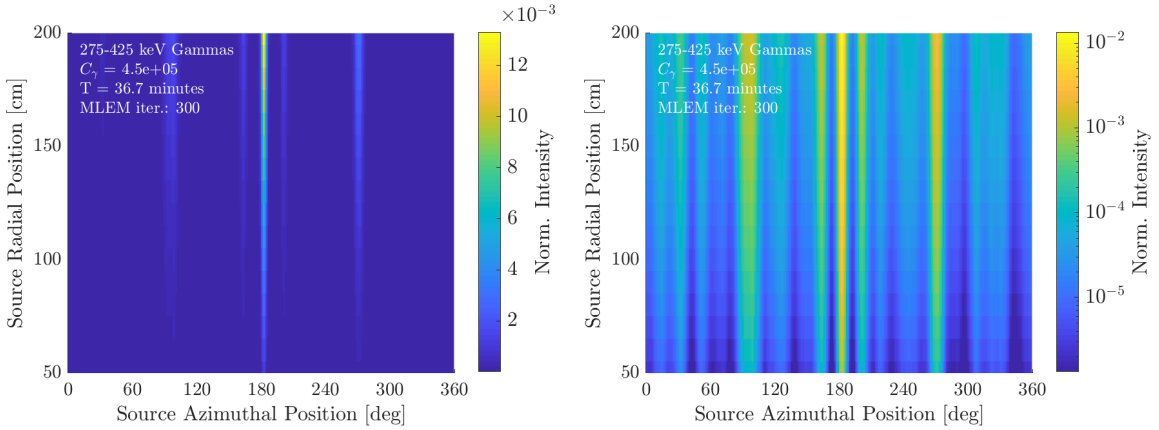

(a) Linear scale (b) Logarithmic scale.

Figure 8.14: 2D reconstruction made with the conventional c-TEI.

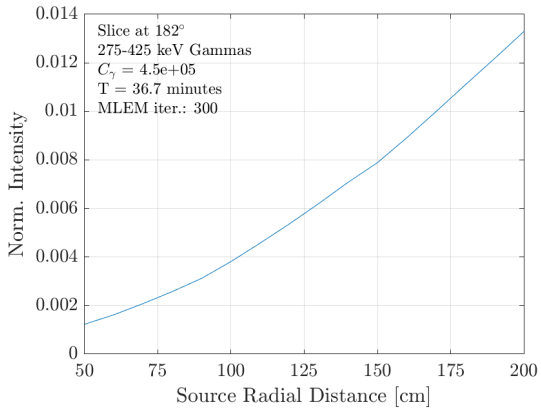

Figure 8.15: Azimuthal slice of the 2D reconstruction at 182°. Conventional c-TEI.

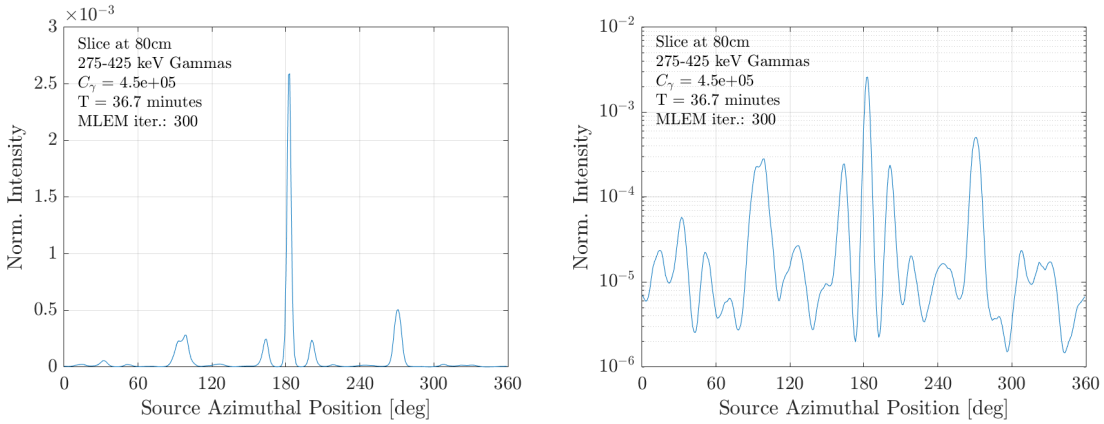

(a) Linear scale.

(b) Logarithmic scale.

Figure 8.16: Radial slice of the 2D reconstruction at 80 cm. Conventional c-TEI.

For the conventional case, we only use data when the detector is centered, thus the system cannot effectively create 2D images. Thus, in Fig. 8.14, the sources are not localized radially. Moreover, as shown in Fig. 8.15, source pixels that are further away from the system are reconstructed with higher intensity. This is a direct consequence of initializing MLEM with the inverse sensitivity of the system response. If instead one were to initialize MLEM with a constant value, the source pixels that are closer to the system would have higher intensity.

Fig. 8.16 shows the radial slice at 80 cm. The two source object is at 90°, thus we expect to see two separated sources, but the resolution of the system is not sufficient to separate the two sources. Instead, we see a slightly broadened peak.

Fig. 8.17 is the 2D reconstruction for adaptive c-TEI and Fig. 8.18 and 8.19 are slices from the 2D image - Fig. 8.18 is an azimuthal slice at 182° and Fig. 8.19 is a radial slice at 80 cm. These reconstructions are also shown in log scale.

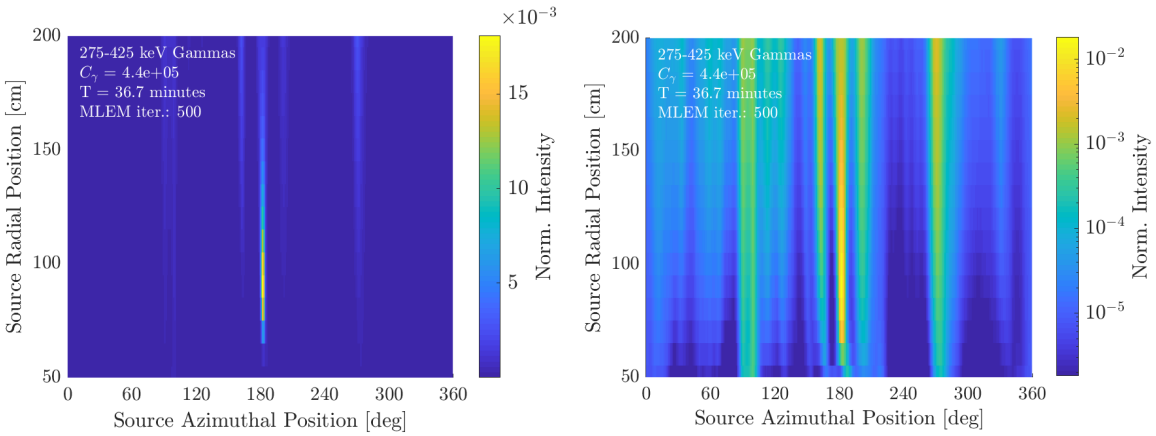

(a) Linear scale (b) Logarithmic scale.

Figure 8.17: 2D reconstruction made with the adaptive setup.

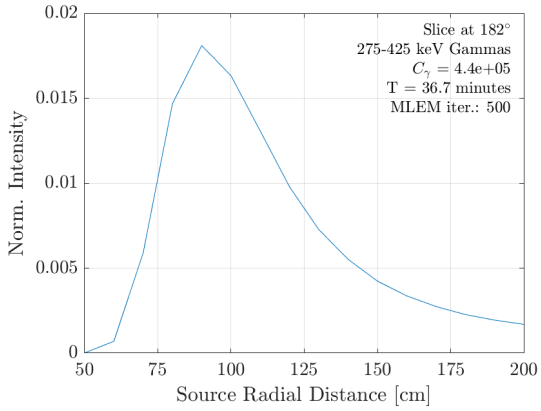

Figure 8.18: Azimuthal slice of the 2D reconstruction at 182°. Adaptive.

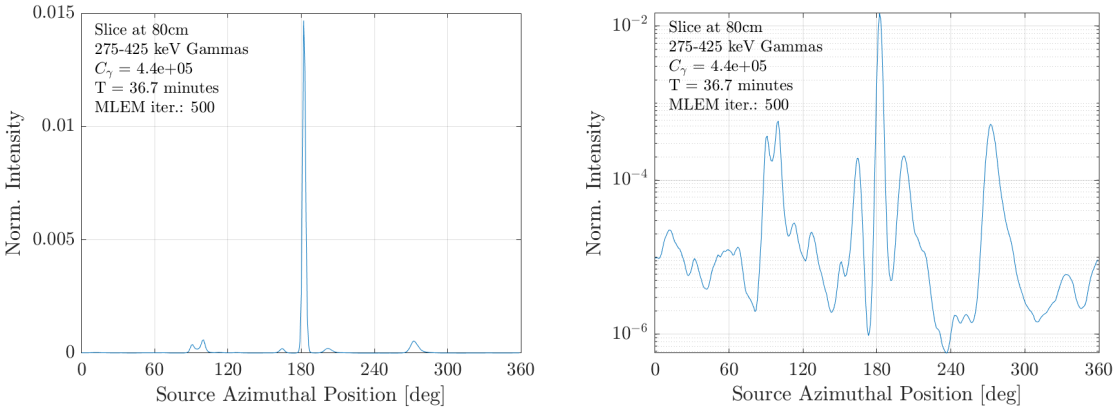

(a) Linear scale. (b) Logarithmic scale.

Figure 8.19: Radial slice of the 2D reconstruction at 80 cm. Adaptive.

As shown in both Fig. 8.17 and Fig. 8.18, the addition of off-center detector positions enables 2D imaging. The peak intensity in Fig. 8.18 is at 90 cm as expected and the half maximum occurs at 75 cm and 125 cm. Determining the radial position of sources is more challenging for sources that are further away from the the imaging system since the parallax effect is smaller. Thus, Fig. 8.18 is not symmetric. We do not have enough data to radially localize the weaker sources in the FOV using MLEM.

In the radial slice (Fig. 8.19), at 90°, we can see that there are two sources present. In the conventional case, these sources could not be separated, but by collecting data at higher resolution detector positions, the two sources can be separated. The ratio of the saddle to the peak is ∼0.5 indicating that two sources are clearly separated.

8.4 Conclusions

To demonstrate the benefit of collecting data at multiple detector positions, we measured special nuclear material in complex geometries including a line source, a split line source, and a multiple source setup at the ZPPR facility at INL. When reconstructing gamma-ray data, we find that combining data from multiple detector positions significantly improves image quality in all three experiments. For the line source reconstructions, the uniformity of the line source improved by 37.5% and the noise in the background region reduced by 50%. We find similar results for the split line source: uniformity improved by ∼25% and noise in the background region reduced by 37.5%. Additionally, in the multiple source experiment, we showed that collecting data at multiple detector positions enables 2D imaging and can increase the angular resolution of the system even when there are many sources in the field. These results indicate that adaptive imaging can be applied to real-world scenarios

and can significantly improve image quality.

CHAPTER IX

Summary and Future Work

This dissertation contributes to the growing research on cylindrical, time-encoded imaging (c-TEI) systems in three ways:

1. we verified three system response models and discussed the conditions under which each is valid and accurate,

2. utilized those models to explore the trade-offs between size, weight, angular resolution, and the contrast-to-noise ratio for various c-TEI designs,

3. explored the benefit of adaptive imaging in a c-TEI system with respect to generating higher resolution images, detecting sources, and reconstructing complex objects.

Below, we review each contribution in turn and highlight key findings. In Sec. 9.2, we discuss future research directions relating to this work.

9.1 Key Findings

Despite the growing use and interest in c-TEI systems, there is relatively little work on system response models for c-TEI systems and the design spaces where they are accurate. In Chap. III, we developed the large detector model and compared its

predictions to the small detector model for a range of different c-TEI designs. We mapped out the regions where the small detector assumption may be used without significant deviation from the large detector model and regions where using the small detector model would result in worse imaging performance. For example, we found that for a handheld system where the mask is close to the detector, the small detector model over predicts the total count rate by 12.7% and the normalized root mean squared error (NRMSE) between the small and large detector models is 14.5%. Using the small detector model for such a system would likely result in lower contrast-to-noise ratio (CNR) and artifacts in the reconstructed image. In contrast, for the MATADOR system, we found that the NRMSE between the small and large detector models is $\sim$1.4% and such a deviation does not lead to significantly different reconstructions.

In Chap. IV, we used the large detector model to explore the tradeoffs between size, weight, angular resolution, and the CNR. Based on those simulations, we designed the MATADOR system for use in nuclear non-proliferation and safeguards applications. Chap. IV also describes the construction and limitations of MATADOR.

In Chap V, we utilized the MATADOR system to experimentally verify the large and offset detector model. We found that both models accurately model the experimental data. In particular, the offset detector model can generate precise estimates of the source position and source intensity for the MATADOR system. Maximum likelihood estimates (MLEs) of the source position differ by less than 1° across different detector positions and the MLEs of the source intensity differ by less than 5%. Additionally, although the unmodulated intensity[1] impinging on the detector changes as a function of detector position, the source-to-background ratio

[1]The unmodulated intensity consists of natural background and source scatter from the environment, mask, and detector.

(S:B) ratio, defined as the count rate from a fully open region of the mask divided by the unmodulated intensity, is relatively constant. This enables one to use the source position, source intensity, and unmodulated intensity estimates from one system configuration to predict the response expected in a different system configuration thus paving the way for adaptive imaging.

Chap. VI to VIII focused on adaptive imaging with a c-TEI system. Adaptive imaging concepts can be implemented in a c-TEI system in two ways: adaptive detector movements and adaptive mask movements. In Chap. VI, we utilized adaptive detector movements to generate higher resolution images. Through a clairvoyant analysis, we investigated the impact of collecting data at any detector position inside the mask. Our results indicate that moving the detector inside the mask can dramatically improve the angular resolution of the system. For example, when imaging a point source, the angular resolution improved by 20%, and when imaging two equal intensity point sources that are 10° apart, the angular resolution improved by 50%. We experimentally verified these results both through MLE of the source positions and by comparing reconstructed images. For the point source case, the standard deviation in the maximum likelihood (ML) source position reduced by ∼17.7% and the full width at half maximum (FWHM) of the image reduced by ∼25.1%. For the two-sources case, the quadrature-sum of the standard deviations of the ML source positions reduced by ∼42%. Additionally, in the adaptive reconstructions, the two sources were clearly separated and resolved while in the conventional reconstruction, the sources could not be separated.

In Sec. 6.5.2, we extended this work and investigated the angular resolution gain for two point sources at various source separations and at various relative intensities. We found that the angular resolution gain varies significantly based on

the source separation and the relative intensity of the sources. In general, we found that regardless of the relative intensities of the sources, if the sources are less than 20° apart, the angular resolution gain is greater than 20%. Additionally, if there is a large difference in the relative intensities of the sources, then the gain is between 10% to 30%. We also found that the angular resolution gain decreases as the sources move further apart. This effect is more significant for equal intensity sources such that if two equal intensity sources are more than 90° apart, the angular resolution gain is less than 10%. Finally, for both the point source and two point source cases, we investigated the benefit of collecting data at two detector positions instead of only one detector position. We found that in most cases, there is no benefit to collecting data at two detector positions instead of one. Note that throughout Chap. VI, the radial position of the source is treated as a known parameter. The value of collecting data at multiple detector positions with respect to angular resolution may change if the radial position of the source is unknown.

In Chap. VII, we showed that adaptive mask movements can improve detection of a weak source in the presence of a strong source. Through a clairvoyant analysis, we found that the adaptive mask movements can achieve the same detection performance as the conventional case in 20% - 40% less time depending on the position of the weak source. This improvement in detection performance, however, comes at a cost. Since only a fraction of the total rotation of the mask is sampled, the system does not have enough information to uniquely localize the source.

Additionally, Sec. 7.4 presents an adaptive detection algorithm that captures some of the performance predicted by the clairvoyant analysis. For the case where the weak source is -90° from the strong source, we experimentally showed that the probability of detection for a false-alarm rate of 5% doubles under the adaptive detection algorithm

relative to the conventional. Note that unlike the clairvoyant analysis where the true values of the unknown parameters are known, the adaptive detection algorithm estimates all of the unknown parameters from the measured data.

Finally, in Chap. VIII, we demonstrated the benefit of collecting data at multiple detector positions when imaging complex source geometries made with special nuclear material. When reconstructing a line source, we found that utilizing data from multiple detector positions improves the uniformity of the reconstruction by 38% and reduces the noise in the background region by 50%. Similarly, for a split line source, we found that uniformity improved by 25% and noise reduced by 38%. In the multiple source experiment, we demonstrated 2D (azimuthal and radial) imaging with the MATADOR system and showed higher resolution images even when there are many sources in the field.

Overall, these results indicate that adaptive imaging can significantly improve performance of a c-TEI system when considering tasks such as generating high resolution images, detecting sources, and reconstructing complex source scenes.

9.2 Future Work

This dissertation is the first implementation of adaptive imaging in a c-TEI system and accordingly there are many opportunities to improve on this work. Below we highlight key opportunities and provide suggestions on how to proceed.

All of the analytical system responses used in this dissertation assume that scatter from the mask and scatter from the environment are uniform as a function of mask rotation angle. As evinced by Fig. 5.11, this assumption is not true when the detector is at the center of the mask. Moreover, when the detector is not at the center, we expect the scatter from the mask to be even more non-uniform. Thus, we suggest the

development of system response models that account for scatter from the mask, and if possible, scatter from the environment. Naturally, one solution for the non-uniform scatter problem is to use Monte Carlo simulations to model the scatter. We attempted this using both traditional MCNP and the adjoint method [162, 163]. We found that the MCNP method was too computationally expensive, and although we had reasonable success using the adjoint method, it was also not computationally feasible for 2D or 3D reconstructions. Thus, an alternative solution is needed.

This dissertation evaluated the potential for both adaptive detector movements to improve angular resolution and adaptive mask movements to improve source detection. The complement - adaptive mask movements to improve angular resolution and adaptive detector movements to improve source detection - still needs to be investigated. We expect that adaptive mask movements will also lead to better angular resolution since measurement time can be focused on edge detection of the source(s). Additionally, adaptive detector movements may improve detection. Moving the detector closer to the weak source can increase sensitivity and perhaps there exists a detector-mask position combination that results in well-separated mask transitions from both sources. The methods used in this dissertation should provide a starting point for this research.

We also suggest implementing adaptive imaging for different tasks. For example, the extended source reconstructions in Chap. VIII are preliminary, but a much more rigorous and thorough analysis is needed. Future work could focus on evaluating the benefit of collecting many unique measurements as opposed to higher angular resolution measurements. Additionally as we noted in the source detection discussion (Chap. VII), our approach to source detection meant that the source could not be uniquely localized. Thus, there is a joint detection-selectivity problem to solve.

Perhaps one can modify the objective function to include a measure of similarity between all of the columns of the system response matrix.

Finally, given the promising results in this dissertation, the next step could be real-time implementation. In this case, the planning step is by far the most expensive. All of the adaptive imaging related optimizations in this dissertation were done by brute force. From an exploratory standpoint, this is reasonable, but real-world, real-time applications need a faster approach. Constraining the optimization problem, implementing optimization algorithms, or using alternative definitions of the objective function could be a stating point for real-time implementation of these concepts.

APPENDICES

APPENDIX A

Additional Figures on Verification of the Offset Detector Model

This appendix contains additional results relating to Sec. 5.2. The source position, source intensity, and unmodulated intensity were estimated as a function of light output using ML. Additionally, the S:B ratio is shown as well.

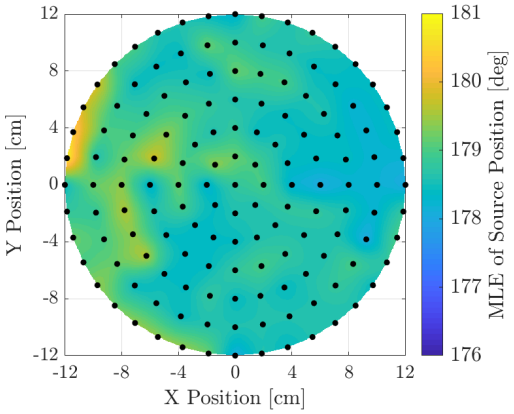

(a) Light output range: 50-150 keVee.

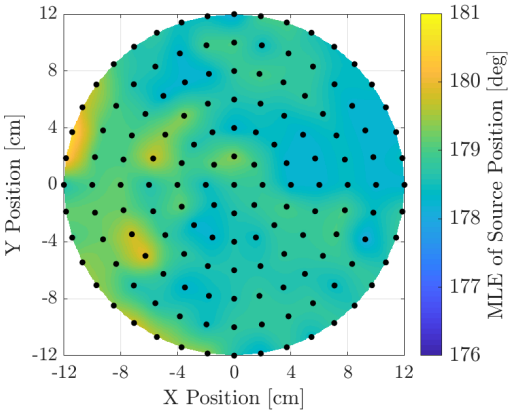

(b) Light output range: 150-250 keVee.

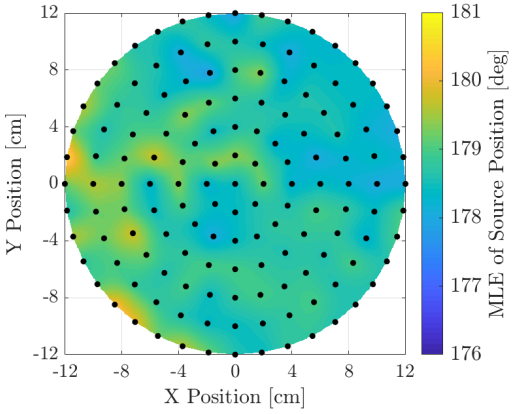

(c) Light output range: 250-350 keVee.

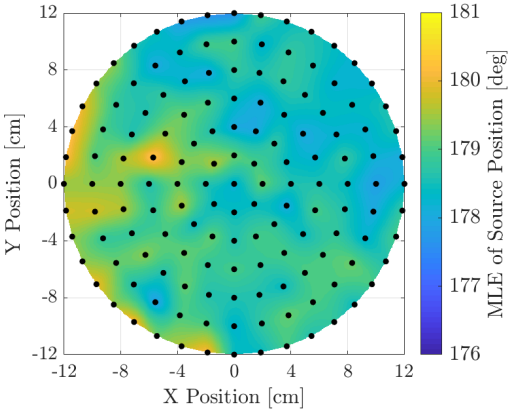

(d) Light output range: 350-450 keVee.

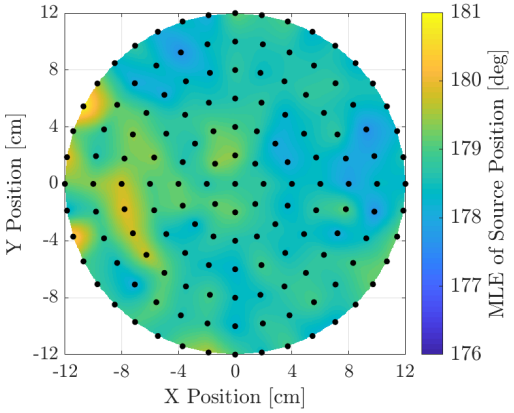

(e) Light output range: 450-550 keVee.

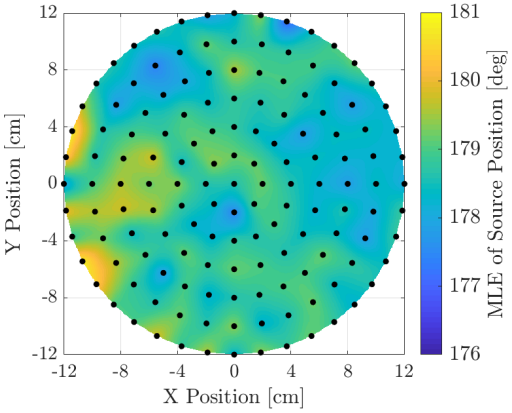

(f) Light output range: 550-650 keVee.

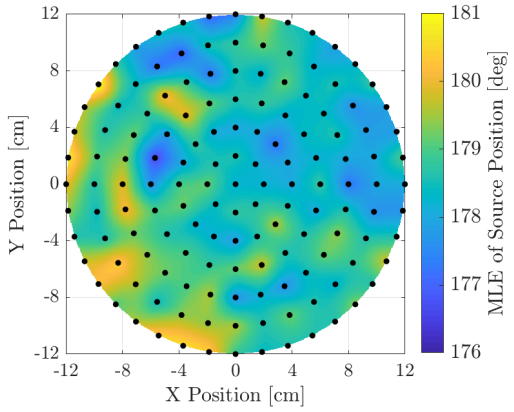

(g) Light output range: 650-750 keVee.

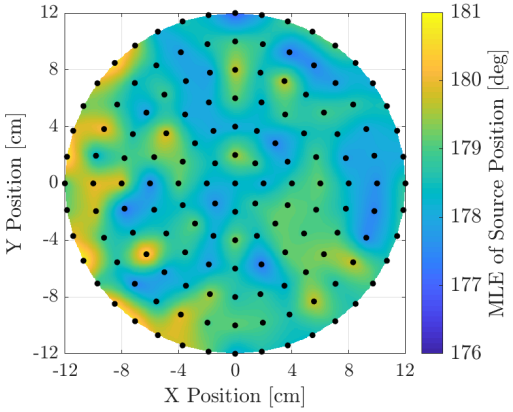

(h) Light output range: 750-850 keVee.

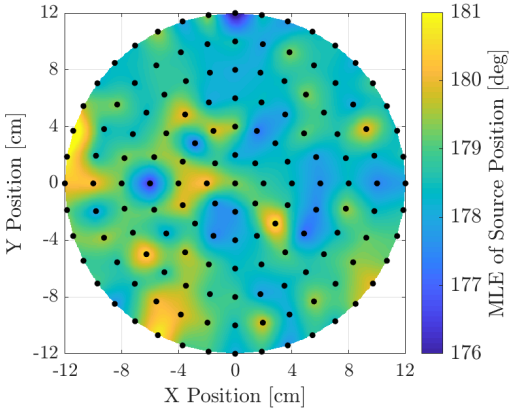

(i) Light output range: 850-950 keVee.

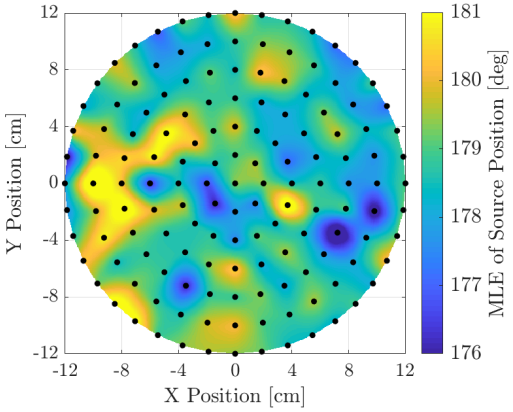

(j) Light output range: 950-1050 keVee.

Figure A.1: Source position MLEs as a function of light output range.

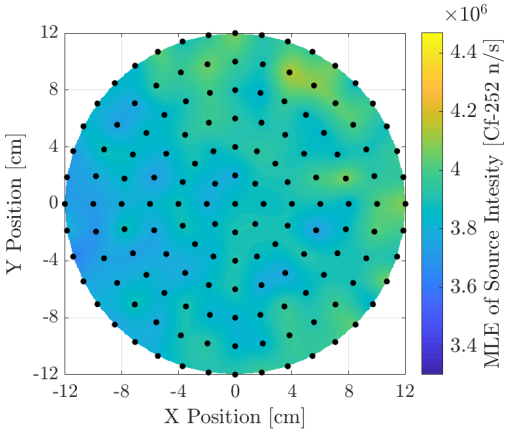

(a) Light output range: 50-150 keVee.

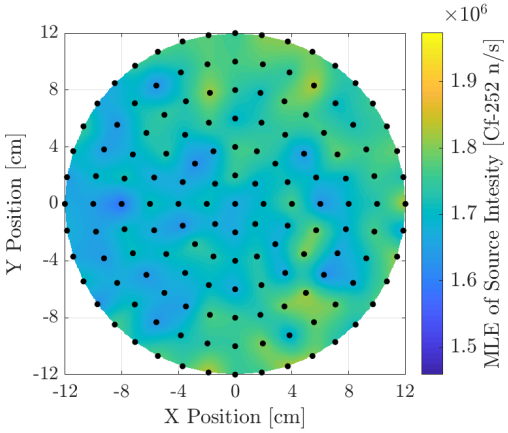

(b) Light output range: 150-250 keVee.

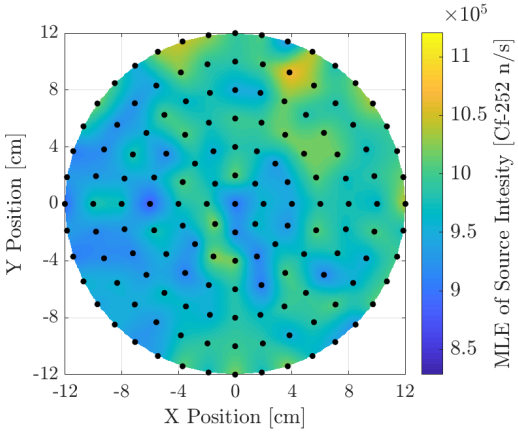

(c) Light output range: 250-350 keVee.

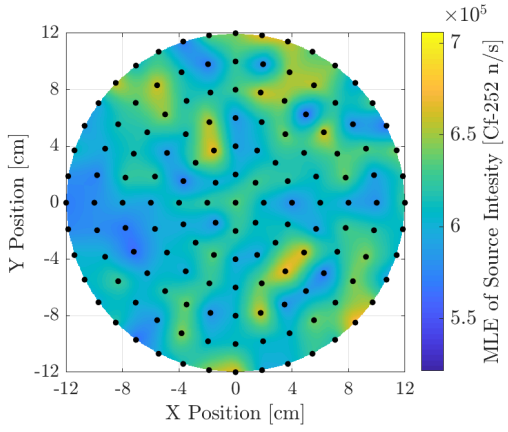

(d) Light output range: 350-450 keVee.

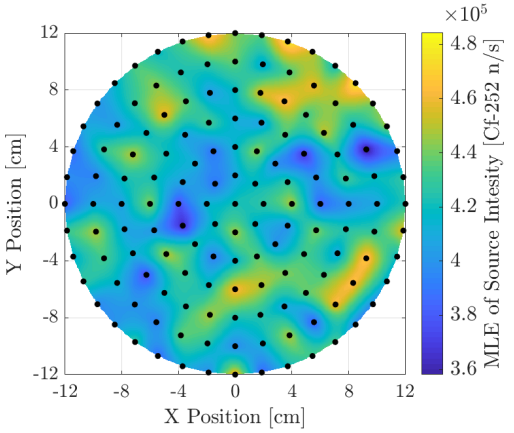

(e) Light output range: 450-550 keVee.

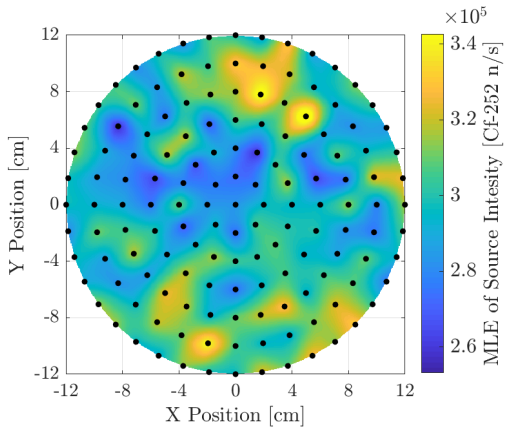

(f) Light output range: 550-650 keVee.

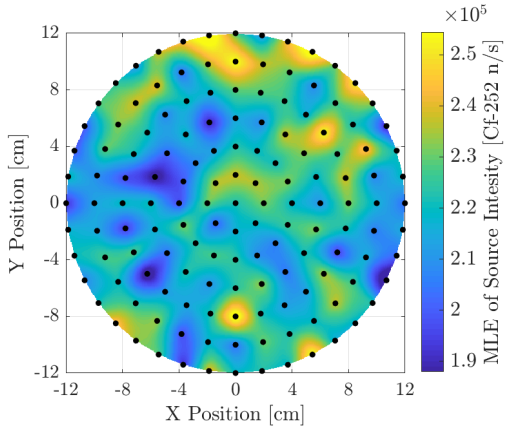

(g) Light output range: 650-750 keVee.

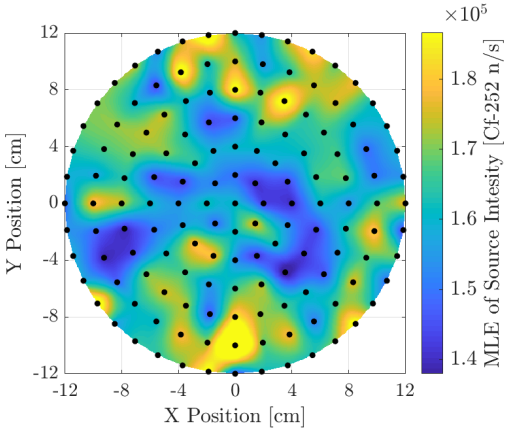

(h) Light output range: 750-850 keVee.

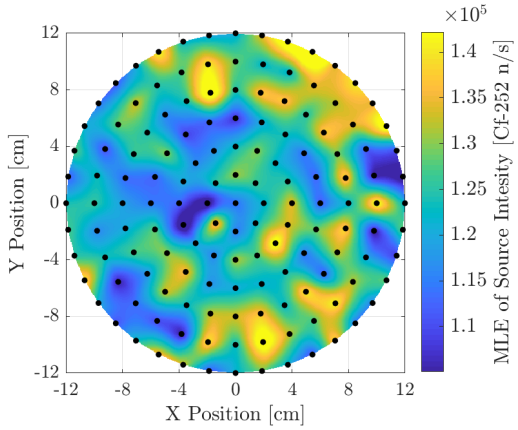

(i) Light output range: 850-950 keVee.

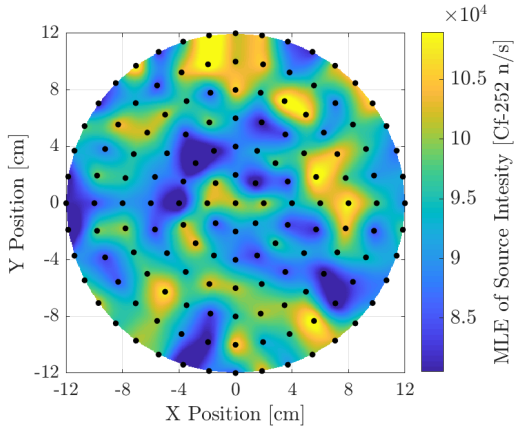

(j) Light output range: 950-1050 keVee.

Figure A.2: Source intensity MLEs as a function of light output range. Note that the color bar range extends from -15% to +15% of the median for all plots.

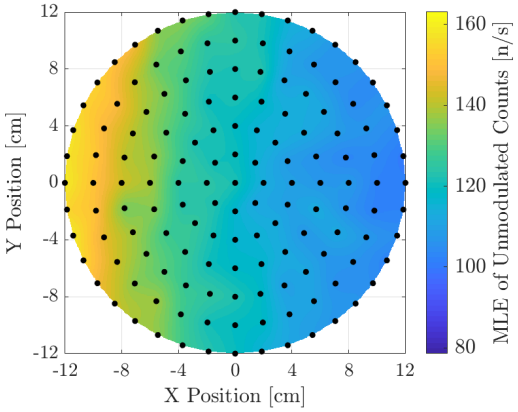

(a) Light output range: 50-150 keVee.

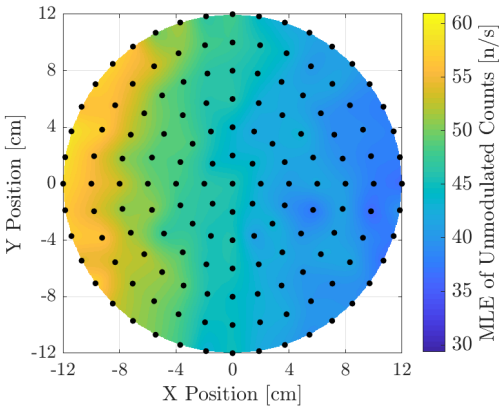

(b) Light output range: 150-250 keVee.

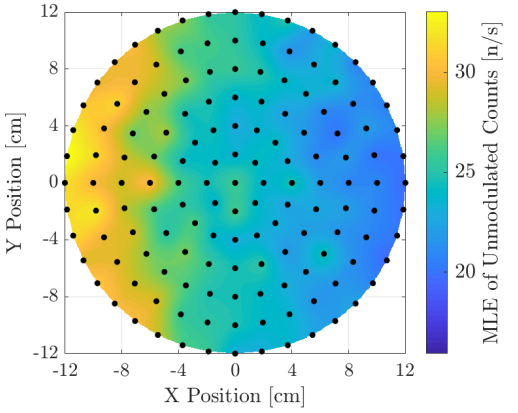

(c) Light output range: 250-350 keVee.

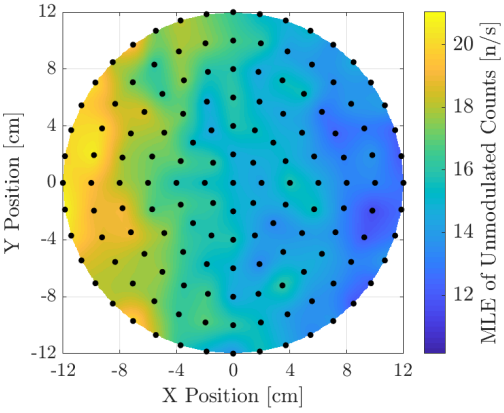

(d) Light output range: 350-450 keVee.

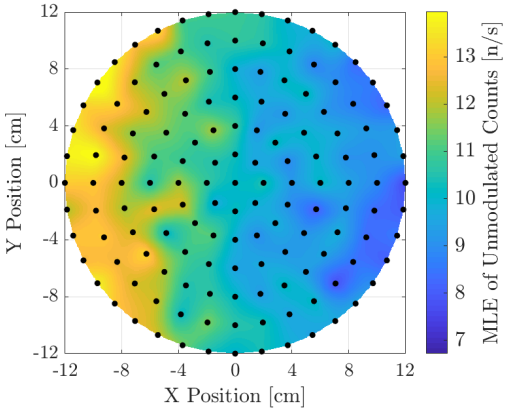

(e) Light output range: 450-550 keVee.

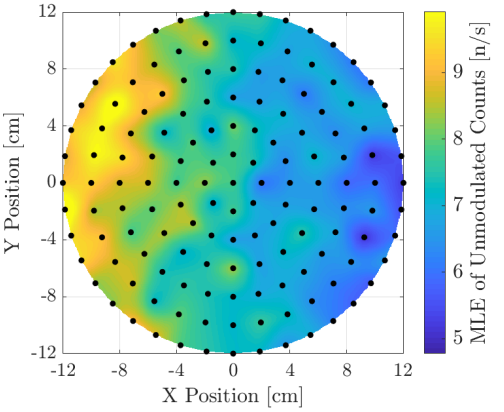

(f) Light output range: 550-650 keVee.

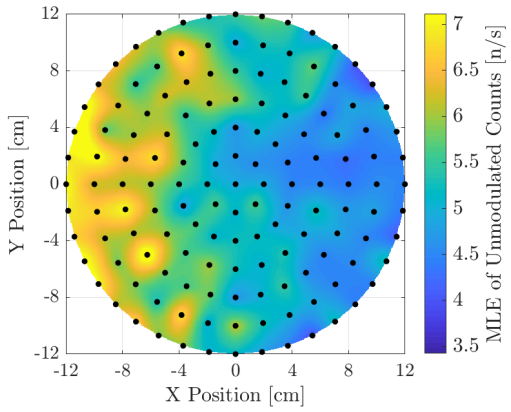

(g) Light output range: 650-750 keVee.

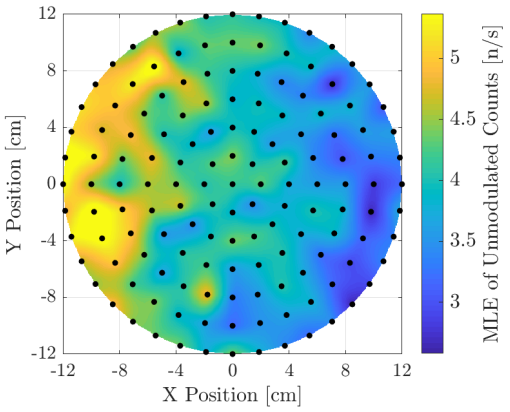

(h) Light output range: 750-850 keVee.

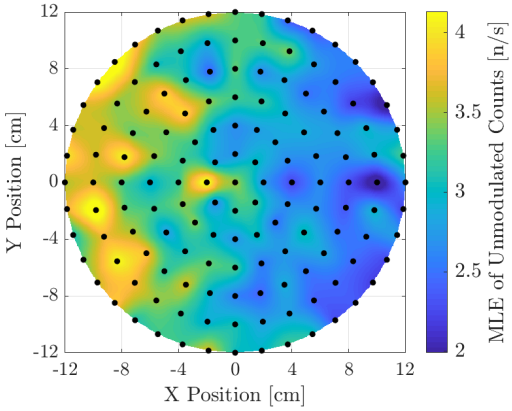

(i) Light output range: 850-950 keVee.

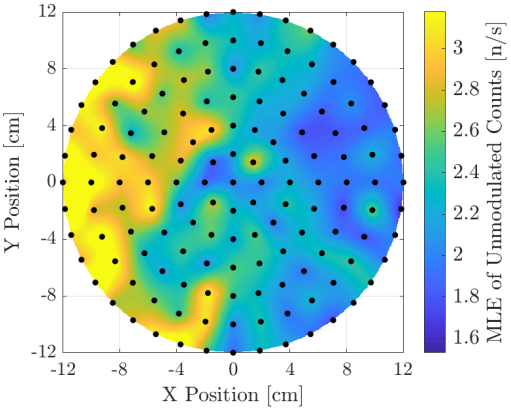

(j) Light output range: 950-1050 keVee.

Figure A.3: Unmodulated intensity MLEs as a function of detector position. Note that the color bar extends from -35% to +35% of the median for all plots.

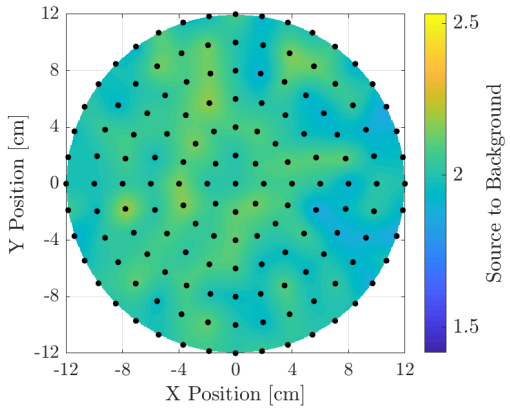

(a) Light output range: 50-150 keVee.

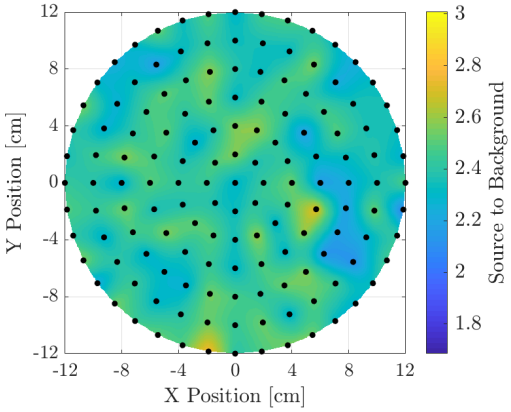

(b) Light output range: 150-250 keVee.

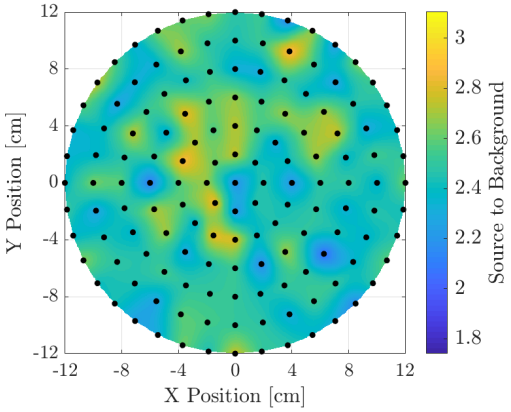

(c) Light output range: 250-350 keVee.

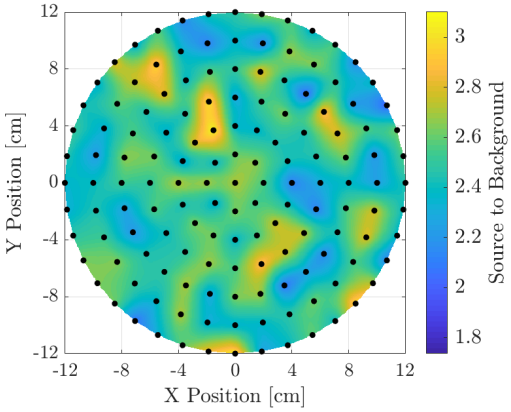

(d) Light output range: 350-450 keVee.

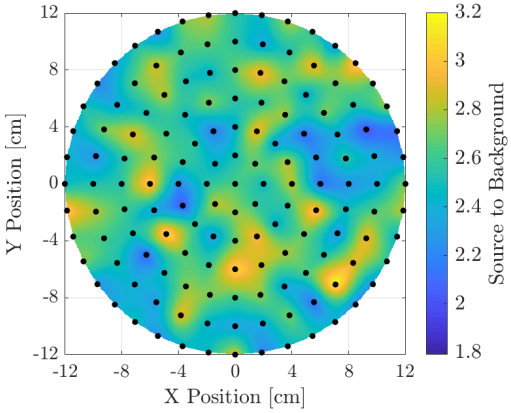

(e) Light output range: 450-550 keVee.

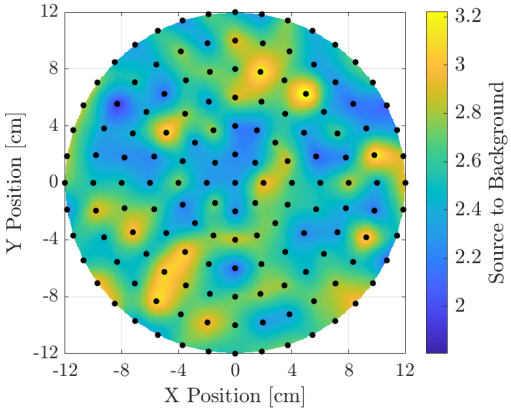

(f) Light output range: 550-650 keVee.

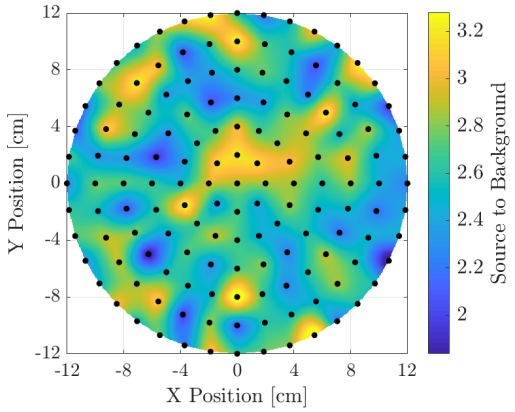

(g) Light output range: 650-750 keVee.

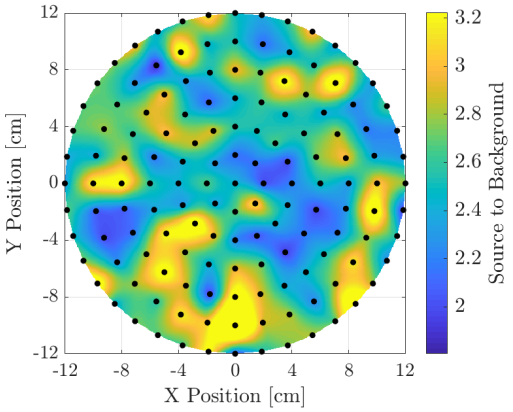

(h) Light output range: 750-850 keVee.

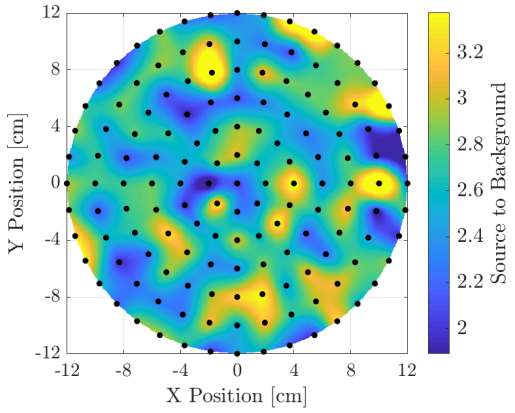

(i) Light output range: 850-950 keVee.

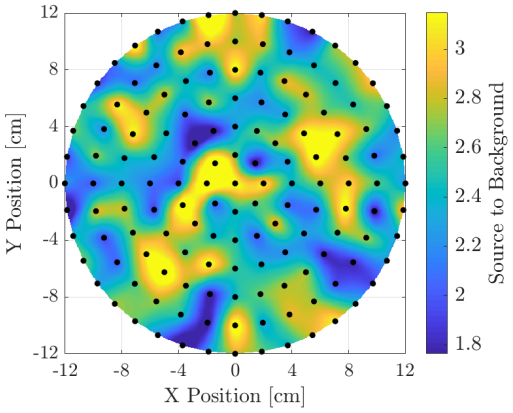

(j) Light output range: 950-1050 keVee.

Figure A.4: S:B ratio as a function of detector position. Note that the color bar extends from -25% to +25% of the median for all plots.

APPENDIX B

Fisher Information Matrix for a Poisson Distribution

Here, we calculate the FIM for a Poisson distributed process. We start with the definition of the FIM:

$$I(\boldsymbol{\theta}) = -\mathbb{E}\left[\nabla_{\boldsymbol{\theta}} \nabla_{\boldsymbol{\theta}}^T \ \ell(\boldsymbol{y} \mid \boldsymbol{\theta})\right] \tag{B.1}$$

For a Poisson distributed process, $\ell(\boldsymbol{y} \mid \boldsymbol{\theta})$ is

$$\ell(\boldsymbol{y} \mid \boldsymbol{\theta}) = \sum_{i=1}^{N_O} \left(y_i \ln\left(\overline{y}_i\right) - \overline{y}_i - \ln\left(y_i!\right)\right) \tag{B.2}$$

Plugging Eq. B.2 into B.1, applying the chain rule for differentiation, and taking the expectation we get

$$\begin{aligned}
-\mathbb{E}\left[\nabla_{\boldsymbol{\theta}} \nabla_{\boldsymbol{\theta}}^T \ \ell(\boldsymbol{y} \mid \boldsymbol{\theta})\right] &= -\mathbb{E}\left[\nabla_{\boldsymbol{\theta}} \nabla_{\boldsymbol{\theta}}^T \sum_{i=1}^{N_O} \left(y_i \ln\left(\overline{y}_i\right) - \overline{y}_i - \ln\left(y_i!\right)\right)\right] \\
&= -\mathbb{E}\left[\nabla_{\boldsymbol{\theta}} \sum_{i=1}^{N_O} \left(\frac{y_i \nabla_{\boldsymbol{\theta}}^T \ \overline{y}_i}{\overline{y}_i} - \nabla_{\boldsymbol{\theta}}^T \ \overline{y}_i\right)\right] \\
&= -\mathbb{E}\left[\sum_{i=1}^{N_O} \left(\frac{y_i \nabla_{\boldsymbol{\theta}} \nabla_{\boldsymbol{\theta}}^T \ \overline{y}_i}{\overline{y}_i} - \frac{y_i \nabla_{\boldsymbol{\theta}} \ \overline{y}_i \nabla_{\boldsymbol{\theta}}^T \ \overline{y}_i}{\overline{y}_i^2} - \nabla_{\boldsymbol{\theta}} \nabla_{\boldsymbol{\theta}}^T \ \overline{y}_i\right)\right] \\
&= \sum_{i=1}^{N_O} \left(\frac{\nabla_{\boldsymbol{\theta}} \ \overline{y}_i \nabla_{\boldsymbol{\theta}}^T \ \overline{y}_i}{\overline{y}_i}\right)
\end{aligned} \tag{B.3}$$

APPENDIX C

Likelihood Ratio of the GLRT for a Poisson Distribution

Here, we show the calculations to find the generalized likelihood ratio test (GLRT) for a Poisson distributed process.

The likelihood ratio in the GLRT is

$$2\ln(\Lambda_{\text{GLRT}}) = 2\ln\left(\frac{p(\boldsymbol{y} \mid \hat{\boldsymbol{\theta}}_{\text{ML},\mathcal{H}_A})}{p(\boldsymbol{y} \mid \hat{\boldsymbol{\theta}}_{\text{ML},\mathcal{H}_N})}\right) \tag{C.1}$$

For a Poisson distributed process:

$$2\ln(\Lambda_{\text{GLRT}}) = 2\ln\left(\frac{\prod_{i=1}^{N_O} \frac{\overline{y}_{i,A}^{y_i} e^{-\overline{y}_{i,A}}}{y_i!}}{\prod_{i=1}^{N_O} \frac{\overline{y}_{i,N}^{y_i} e^{-\overline{y}_{i,N}}}{y_i!}}\right) \tag{C.2}$$

Taking the natural log and expanding:

$$2\ln(\Lambda_{\text{GLRT}}) = 2\sum_{i=1}^{N_O}\left(\left(y_i \ln\left(\overline{y}_{i,A}\right) - \overline{y}_{i,A}\right) - \left(y_i \ln\left(\overline{y}_{i,N}\right) - \overline{y}_{i,N}\right)\right) \tag{C.3}$$

Rearranging and combining like terms:

$$2\ln(\Lambda_{\text{GLRT}}) = 2\sum_{i=1}^{N_O}\left(y_i \ln\left(\frac{\overline{y}_{i,A}}{\overline{y}_{i,N}}\right)\right) - \sum_{i=1}^{N_O}\left(\overline{y}_{i,A} - \overline{y}_{i,N}\right) \tag{C.4}$$

Thus, the GLRT is

$$\Lambda'_{\text{GLRT}} = 2\ln(\Lambda_{\text{GLRT}}) = 2\sum_{i=1}^{N_O}\left(y_i \ln\left(\frac{\overline{y}_{i,A}}{\overline{y}_{i,N}}\right)\right) - \sum_{i=1}^{N_O}\left(\overline{y}_{i,A} - \overline{y}_{i,N}\right) \underset{\mathcal{H}_N}{\overset{\mathcal{H}_A}{\gtrless}} \eta_{\text{crit}} \qquad \text{(C.5)}$$

APPENDIX D

On the Relative Change in Time Metric to Compare ROC Curves

Here, we derive an equation for $\tau_{2\to1}$ which is the relative change in time for receiver operator characteristic (ROC) curve 2 to match ROC curve 1 when using the asymptotic distribution for the likelihood ratio in the GLRT. Conceptually, $\tau_{2\to1}$ is

$$\tau_{2\to1} = \frac{T_2}{T_1} - 1 \tag{D.1}$$

where T_1 is the total measurement time for system configuration 1 and T_2 is the total measurement time required for system configuration 2 to match the detection performance of system configuration 1.

The ROC curves from the asymptotic GLRT are only dependent on the non-centrality parameter, λ, thus we need to find the measurement time such that

$$\lambda_2 = \lambda_1 \tag{D.2}$$

To aid in this process, the symbol $(\cdot)'$ will indicate that the variable has been divided by the total measurement time (T).

We use the following model to describe the measured data

$$\overline{y}_i = \left(\sum_{j=1}^{S} \left(\alpha_j A\left[i, j'(\phi_j)\right] \right) + b_D[i] \right) t[i]T \tag{D.3}$$

where T is the total measurement time and $t[i]$ is the relative time spent at observation bin i. $\sum_{i=1}^{N_O} t[i] = 1$. Let

$$\overline{y}'_i = \frac{\overline{y}_i}{T} \tag{D.4}$$

Then, the FIM is

$$\begin{aligned} I(\boldsymbol{\theta}) &= -\mathbb{E}\left[\nabla_{\boldsymbol{\theta}} \nabla_{\boldsymbol{\theta}}^T \, \ell(\boldsymbol{y} \mid \boldsymbol{\theta})\right] \\ &= \sum_{i=1}^{N_O} \left(\frac{\nabla_{\boldsymbol{\theta}} \, \overline{y}_i \nabla_{\boldsymbol{\theta}}^T \, \overline{y}_i}{\overline{y}_i} \right) \\ &= \sum_{i=1}^{N_O} \left(\frac{\nabla_{\boldsymbol{\theta}} \, \overline{y}'_i T \nabla_{\boldsymbol{\theta}}^T \, \overline{y}'_i T}{\overline{y}'_i T} \right) \\ &= T \sum_{i=1}^{N_O} \left(\frac{\nabla_{\boldsymbol{\theta}} \, \overline{y}'_i \nabla_{\boldsymbol{\theta}}^T \, \overline{y}'_i}{\overline{y}'_i} \right) \end{aligned} \tag{D.5}$$

Let

$$I'(\boldsymbol{\theta}) = \frac{I(\boldsymbol{\theta})}{T} \tag{D.6}$$

then

$$I'(\boldsymbol{\theta}) = \sum_{i=1}^{N_O} \left(\frac{\nabla_{\boldsymbol{\theta}} \, \overline{y}'_i \nabla_{\boldsymbol{\theta}}^T \, \overline{y}'_i}{\overline{y}'_i} \right) \tag{D.7}$$

The non-centrality parameter is

$$\begin{aligned} \lambda = (\boldsymbol{\theta}_{r,A} - \boldsymbol{\theta}_{r,N})^T \, [\, & I_{\boldsymbol{\theta}_r \boldsymbol{\theta}_r} (\boldsymbol{\theta}_{r,A}, \boldsymbol{\theta}_n) - \\ & I_{\boldsymbol{\theta}_r \boldsymbol{\theta}_n} (\boldsymbol{\theta}_{r,A}, \boldsymbol{\theta}_n) \, I^{-1}_{\boldsymbol{\theta}_n \boldsymbol{\theta}_n} (\boldsymbol{\theta}_{r,A}, \boldsymbol{\theta}_n) \, I_{\boldsymbol{\theta}_n \boldsymbol{\theta}_r} (\boldsymbol{\theta}_{r,A}, \boldsymbol{\theta}_n) \,] \, (\boldsymbol{\theta}_{r,A} - \boldsymbol{\theta}_{r,N}) \end{aligned} \tag{D.8}$$

For simplicity, we drop $\boldsymbol{\theta}$ in the subscripts for the partitions of the FIM:

$$\begin{aligned} \lambda = (\boldsymbol{\theta}_{r,A} - \boldsymbol{\theta}_{r,N})^T \, [\, & I_{rr} (\boldsymbol{\theta}_{r,A}, \boldsymbol{\theta}_n) - \\ & I_{rn} (\boldsymbol{\theta}_{r,A}, \boldsymbol{\theta}_n) \, I^{-1}_{nn} (\boldsymbol{\theta}_{r,A}, \boldsymbol{\theta}_n) \, I_{nr} (\boldsymbol{\theta}_{r,A}, \boldsymbol{\theta}_n) \,] \, (\boldsymbol{\theta}_{r,A} - \boldsymbol{\theta}_{r,N}) \end{aligned} \tag{D.9}$$

Plugging Eq. D.7 in Eq. D.9:

$$\begin{aligned} \lambda = (\boldsymbol{\theta}_{r,A} - \boldsymbol{\theta}_{r,N})^T \, [\, & I'_{rr} (\boldsymbol{\theta}_{r,A}, \boldsymbol{\theta}_n) \, T - \\ & I'_{rn} (\boldsymbol{\theta}_{r,A}, \boldsymbol{\theta}_n) \, T (I'_{nn} (\boldsymbol{\theta}_{r,A}, \boldsymbol{\theta}_n) \, T)^{-1} I'_{nr} (\boldsymbol{\theta}_{r,A}, \boldsymbol{\theta}_n) \, T \,] \, (\boldsymbol{\theta}_{r,A} - \boldsymbol{\theta}_{r,N}) \end{aligned} \tag{D.10}$$

Utilizing the property $(cA)^{-1} = c^{-1}A^{-1}$, we have

$$\lambda = \left(\boldsymbol{\theta}_{r,A} - \boldsymbol{\theta}_{r,N}\right)^T \left[I'_{rr}\left(\boldsymbol{\theta}_{r,A}, \boldsymbol{\theta}_n\right) T - I'_{rn}\left(\boldsymbol{\theta}_{r,A}, \boldsymbol{\theta}_n\right) T I'^{-1}_{nn}\left(\boldsymbol{\theta}_{r,A}, \boldsymbol{\theta}_n\right) T^{-1} I'_{nr}\left(\boldsymbol{\theta}_{r,A}, \boldsymbol{\theta}_n\right) T \right] \left(\boldsymbol{\theta}_{r,A} - \boldsymbol{\theta}_{r,N}\right) \tag{D.11}$$

Next, we simplify and pull out T:

$$\lambda = T\left(\boldsymbol{\theta}_{r,A} - \boldsymbol{\theta}_{r,N}\right)^T \left[I'_{rr}\left(\boldsymbol{\theta}_{r,A}, \boldsymbol{\theta}_n\right) - I'_{rn}\left(\boldsymbol{\theta}_{r,A}, \boldsymbol{\theta}_n\right) I'^{-1}_{nn}\left(\boldsymbol{\theta}_{r,A}, \boldsymbol{\theta}_n\right) I'_{nr}\left(\boldsymbol{\theta}_{r,A}, \boldsymbol{\theta}_n\right) \right] \left(\boldsymbol{\theta}_{r,A} - \boldsymbol{\theta}_{r,N}\right) \tag{D.12}$$

Let

$$\lambda' = \frac{\lambda}{T} \tag{D.13}$$

Thus, the non-centrality parameter scales linearly with the total measurement time and

$$\begin{aligned} \lambda_2 &= \lambda_1 \\ \lambda'_2 T_2 &= \lambda'_1 T_1 \\ \frac{T_2}{T_1} &= \frac{\lambda'_1}{\lambda'_2} \end{aligned} \tag{D.14}$$

Thus,

$$\tau_{2\to 1} = \frac{\lambda'_1}{\lambda'_2} - 1 \tag{D.15}$$

which is equivalent to

$$\tau_{2\to 1} = \frac{\lambda_1}{\lambda_2} - 1 \tag{D.16}$$

APPENDIX E

Demonstrations using Special Nuclear Material - Fast Neutron Reconstructions

Chap. VIII presented gamma-ray reconstructions from the three experiments conducted at the ZPPR facility at INL. Here, we show the fast-neutron results. Fast-neutron reconstructions are made using data from the 2" stilbene detector. All fast-neutrons depositing > 40 keVee are used. For brevity, we only include the results and some brief analysis. For a more detailed understanding of the experiments, see Chap. VIII.

E.1 Line Source

Fig. E.1 is a PSD plot from the 2" stilbene detector from the line source experiment. The fast neutrons are clearly separated from the gamma rays.

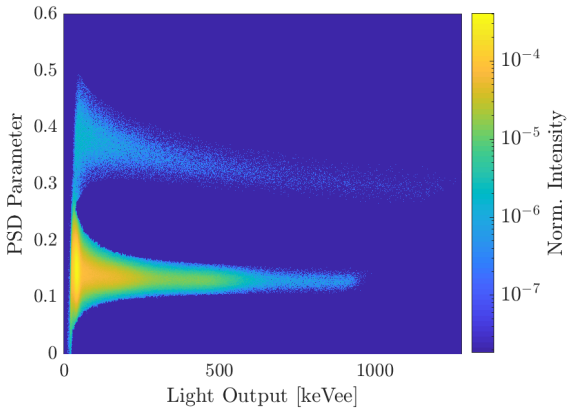

Figure E.1: PSD plot from the line source experiment showing good separated between fast-neutron and gamma-ray pulses.

Fig. E.2a is the fast-neutron reconstruction using the conventional, detector-centered setup and the Fig. E.2b is the adaptive case. The relevant metrics are summarized in Table E.1.

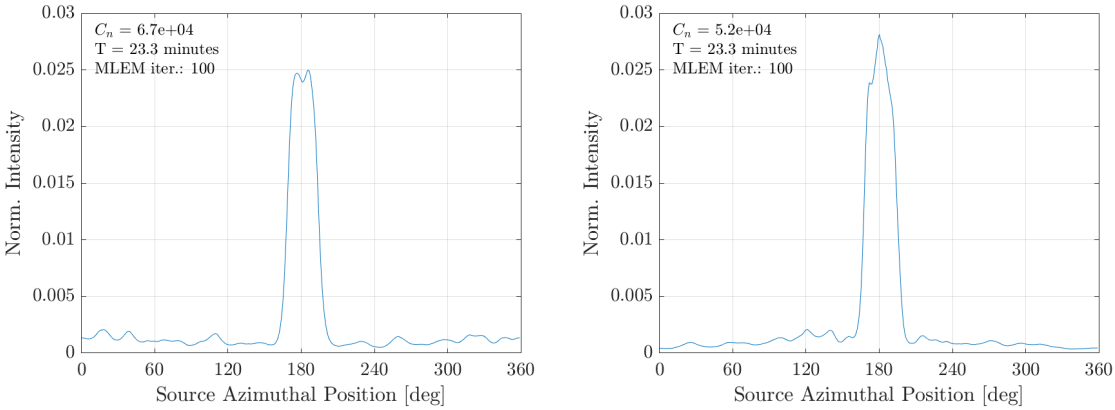

(a) Conventional, detector-centered setup.

(b) Adaptive setup.

Figure E.2: Fast-neutron reconstruction of the line source. 100 MLEM iterations.

Table E.1: Line source FWHM, uniformity, and noise for fast-neutron reconstructions.

	Conventional	Adaptive
FWHM	26.1	27.1
Uniformity (10^{-3})	0.4	1.5
Noise (10^{-4})	3.3	2.8

Although both the conventional and adaptive reconstructions show an extended

source, the conventional reconstruction has better uniformity of the source. Both the noise in the background and the FWHM from the two cases are relatively similar. The adaptive reconstruction has slightly lower noise in the background and the FWHM estimate is closer to the true FWHM.

Fig. E.3a and E.3b are reconstructions using the same data as Fig. E.2a and E.2b but maximum likelihood expectation maximization (MLEM) was run for 1,000 iterations. The relevant metrics are summarized in Table E.2. While both reconstructions suffer from high frequency noise, the conventional case is more uniform reconstruction. On the other hand, the noise in the background region is lower for the adaptive case than the conventional.

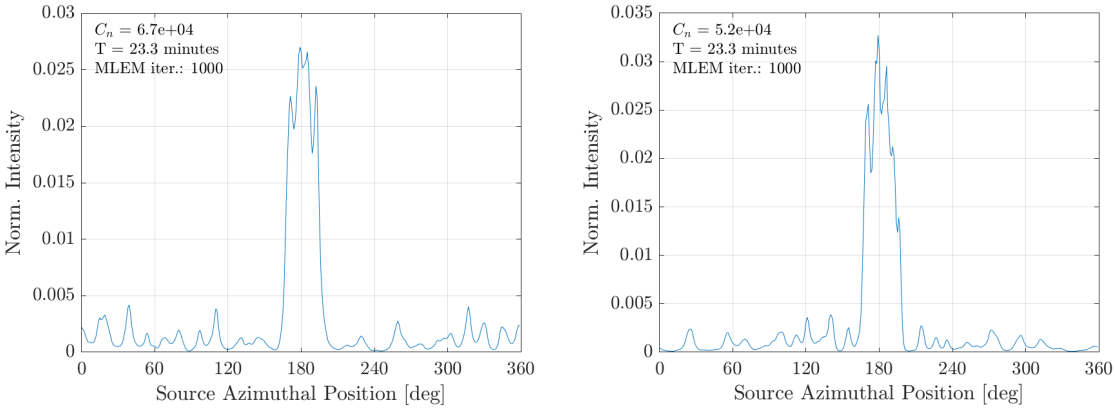

(a) Conventional, detector-centered setup.

(b) Adaptive setup.

Figure E.3: Fast-neutron reconstruction of the line source after running MLEM for many iterations. 1,000 MLEM iterations.

Table E.2: Line source FWHM, uniformity, and noise for high MLEM iteration fast-neutron reconstructions.

	Conventional	Adaptive
FWHM	27.5	28.0
Uniformity (10^{-3})	2.5	4.2
Noise (10^{-4})	8.8	5.7

In the case of fast-neutron reconstructions, collecting data at multiple detector

positions does not improve line source reconstructions. Although the noise in the background is slightly lower in the adaptive reconstructions, the source uniformity is worse. More work is necessary to understand why the adaptive reconstructions are worse than the conventional.

E.2 Split Line Source

Fig. E.4a is the fast-neutron reconstruction using the conventional, detector-centered setup and the Fig. E.4b is the adaptive case. The relevant metrics are summarized in Table E.3.

Both reconstructions show two extended sources although in the adaptive case, the reconstructions have more extent, particularly the source at 194°. Note that although the peak heights of the two line sources are quite different in the adaptive reconstruction, the total area is similar.

The adaptive reconstruction has lower noise in the background region, but there appears to be a slow roll off in intensity to the left and right of S_1 and S_2 respectively (at 150° and 210°).

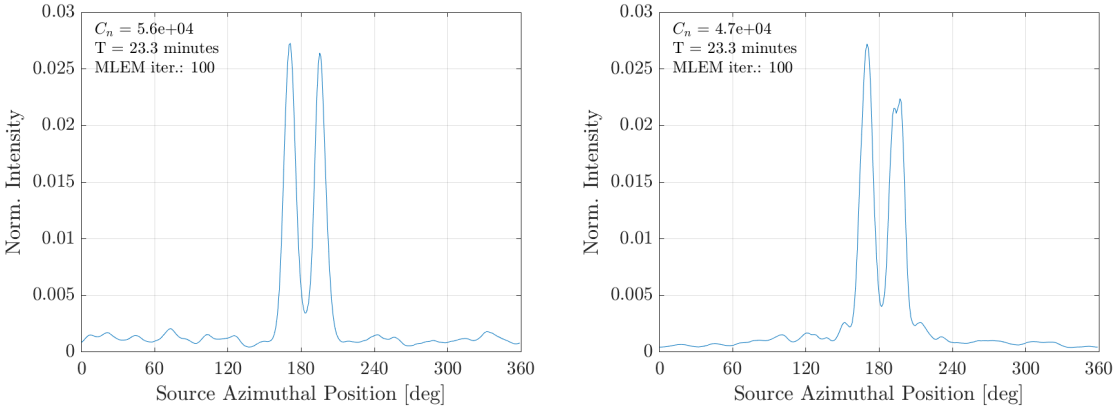

(a) Conventional, detector-centered setup. (b) Adaptive setup.

Figure E.4: Fast-neutron reconstruction of the split line source. 100 MLEM iterations.

Table E.3: Split line source FWHM, uniformity, and noise for fast-neutron reconstructions.

	Conventional	Adaptive
S_1 FWHM	12.4	13.3
S_2 FWHM	11.9	14.9
S_1 Uniformity (10^{-3})	3.3	2.8
S_2 Uniformity (10^{-3})	3.7	1.0
Noise (10^{-4})	3.1	2.6

Fig. E.5a and E.5b are reconstructions using the same data as Fig. E.4a and E.4b but MLEM was run for 1,000 iterations. The relevant metrics are summarized in Table E.4.

In terms of source uniformity, the line sources in the convention reconstruction are more uniform than those in the adaptive, but the background noise is lower in the adaptive case.

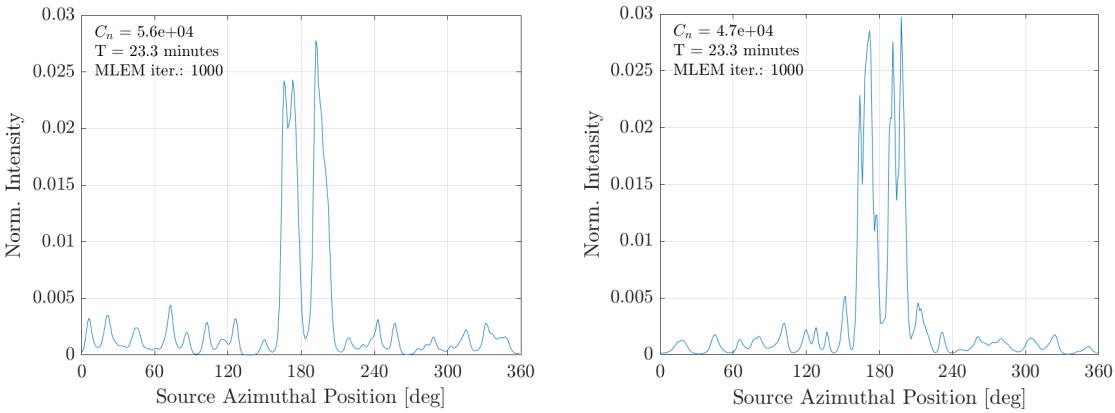

(a) Conventional, detector-centered setup.

(b) Adaptive setup.

Figure E.5: Fast-neutron reconstruction of the split line source after running MLEM for many iterations. 1,000 MLEM iterations.

Table E.4: Split line source FWHM, uniformity, and noise for high MLEM iteration fast-neutron reconstructions.

	Conventional	Adaptive
S_1 FWHM	14.8	14.7
S_2 FWHM	13.6	16.1
S_1 Uniformity (10^{-3})	1.5	4.8
S_2 Uniformity (10^{-3})	4.2	5.6
Noise (10^{-4})	8.7	5.3

Overall, for fast-neutron reconstructions, utilizing data from multiple detector positions did not result in significantly better reconstructions. The adaptive case suffers from artifacts to the left of S_1 and to the right of S_2. These results imply that there is some model mismatch that is negatively affecting the adaptive case reconstructions.

E.3 Multiple Source

Fig. E.6 is a PSD plot from the multiple source experiment. The fast neutrons are clearly separated from the gamma-rays.

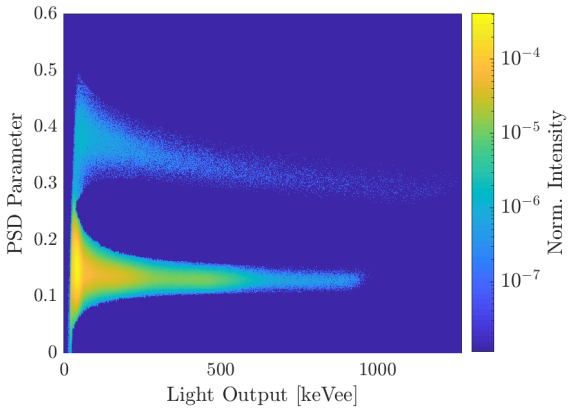

Figure E.6: PSD plot showing good separated between fast-neutron and gamma-ray pulses. Conventional, detector-centered.

First, we show reconstructions from the conventional setup and then contrast those against the adaptive setup. Fig. E.7 is the 2D reconstruction from the conventional

setup and Fig. E.8 and E.9 are slices from the 2D image - Fig. E.8 is an azimuthal slice at 182° and Fig. E.9 is a radial slice at 80cm. These reconstructions are also shown in log scale.

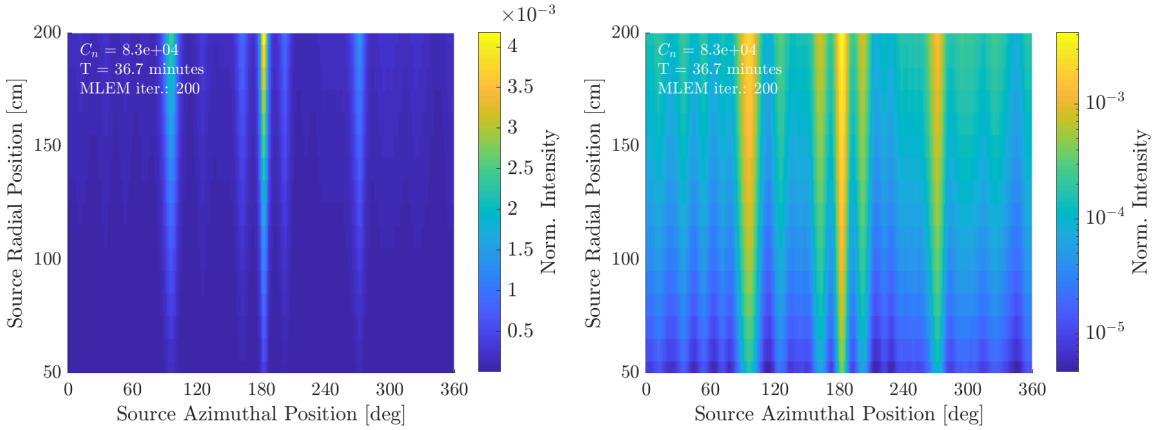

(a) Linear scale

(b) Logarithmic scale.

Figure E.7: 2D reconstruction made with the conventional c-TEI setup.

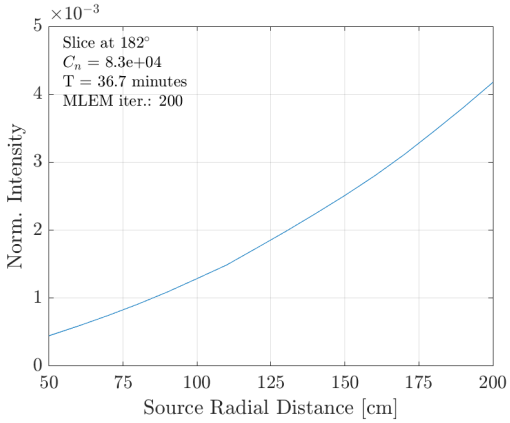

Figure E.8: Azimuthal slice of the 2D reconstruction at 182°. Conventional c-TEI.

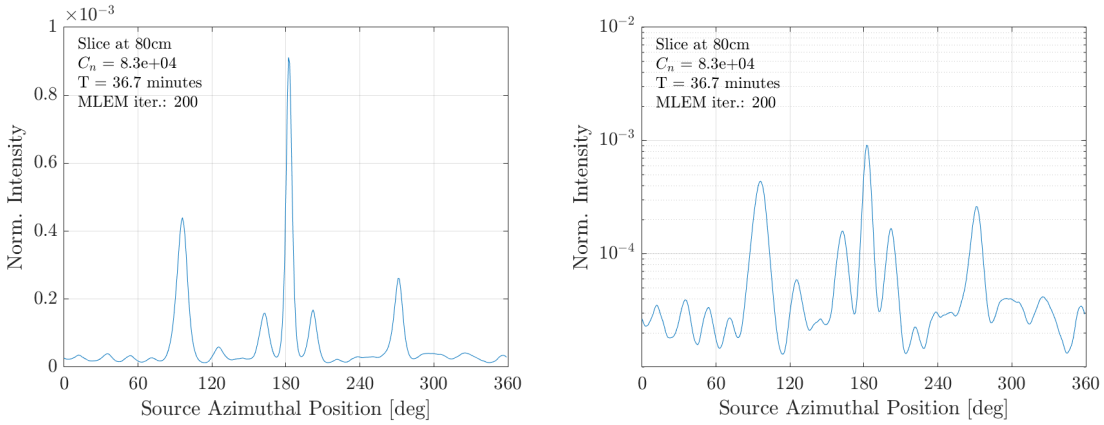

(a) Linear scale.

(b) Logarithmic scale.

Figure E.9: Radial slice of the 2D reconstruction at 80cm. Conventional c-TEI.

Since only data from the center detector was used, the system cannot effectively create 2D images. Thus in Fig. E.7, the sources are not radially localized. Moreover, as shown in Fig. E.8, source pixels that are further away from the system are reconstructed with higher intensity. This is a direct consequence of initializing MLEM with the inverse sensitivity of the system response. If instead one were to initialize MLEM with a constant value, the source pixels that are closer to the system would have higher intensity.

Fig. E.9 shows the radial slice at 80cm. The two source object is at 90°, thus we expect to see two separated sources, but the resolution of the system is not sufficient to separate the two sources. Instead, we see a slightly broadened peak.

Fig. E.10 is the 2D reconstruction for adaptive c-TEI and Fig. E.11 and E.12 are slices from the 2D image - Fig. E.11 is an azimuthal slice at 182° and Fig. E.12 is a radial slice at 80cm. These reconstructions are also shown in log scale.

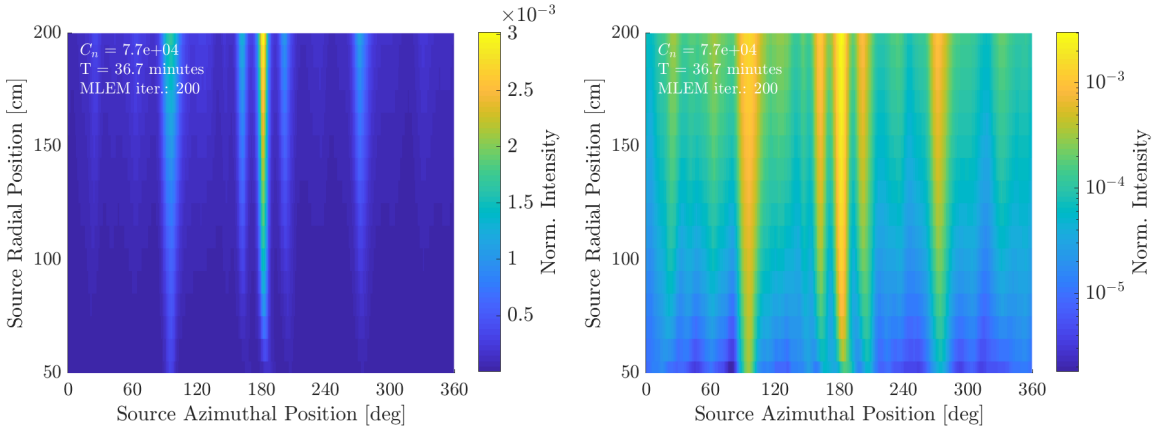

(a) Linear scale

(b) Logarithmic scale.

Figure E.10: 2D reconstruction made with the adaptive setup.

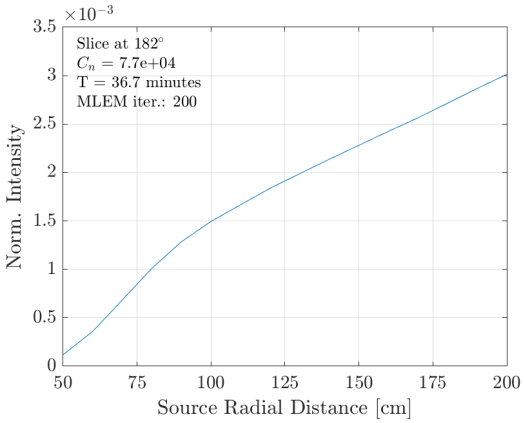

Figure E.11: Azimuthal slice of the 2D reconstruction at 182°. Adaptive.

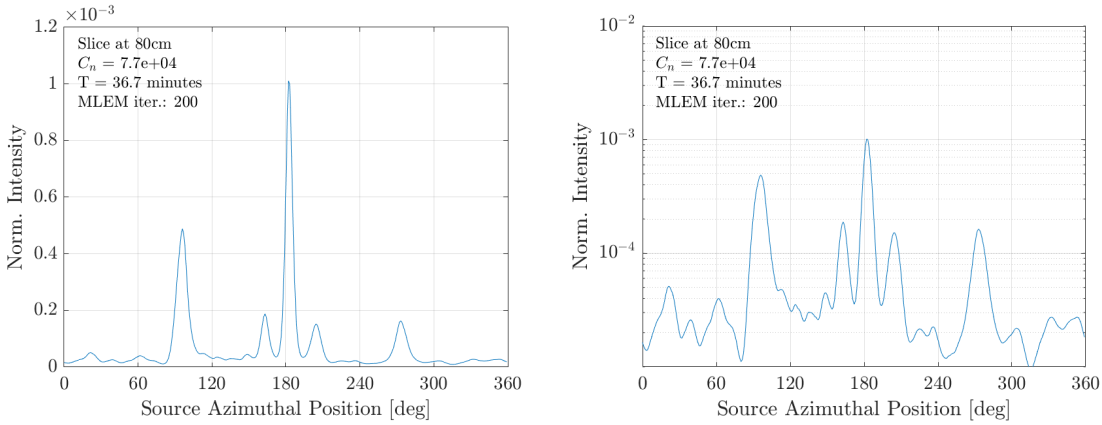

(a) Linear scale.

(b) Logarithmic scale.

Figure E.12: Radial slice of the 2D reconstruction at 80cm. Adaptive.

Although data was collected at multiple detector positions in the mask, the MOX fuel cannot be radially localized as evidenced by Fig. E.11. Additionally, the two source object cannot be separated into two sources in Fig. E.12. For fast-neutron data, adaptive detector movements have not significantly improved the reconstructed images in terms of radial localization and angular resolution.

E.4 Conclusions

Based on these reconstructions, it appears that there is some mismatch between the collected data and the system response although the exact reason is unknown.

BIBLIOGRAPHY

BIBLIOGRAPHY

[1] R. C. Runkle, "Neutron sensors and their role in nuclear nonproliferation," *Nuclear Instruments and Methods in Physics Research, Section A*, vol. 652, 2011.

[2] K. P. Ziock, "Principles and applications of gamma-ray imaging for arms control," *Nuclear Instruments and Methods in Physics Research, Section A*, vol. 878, 2018.

[3] H. A. Hamrashdi, S. D. Monk, and D. Cheneler, "Passive gamma-ray and neutron imaging systems for national security and nuclear non-proliferation in controlled and uncontrolled detection areas: Review of past and current status," *Sensors*, vol. 19, 2019.

[4] K. P. Ziock, C. J. Hailey, T. B. Gosnell, and J. H. Lupton, "A Gamma-Ray Imager for Arms Control," *IEEE Transactions on Nuclear Science*, vol. 39, 1992.

[5] P. Hausladen, M. A. Blackston, E. Brubaker, D. Chichester, P. Marleau, and R. J. Newby, "Fast neutron coded-aperture imaging of special nuclear material configurations," *53rd Annual Meeting of the INMM*, 2012.

[6] M. A. Blackston and P. A. Hausladen, "Fast-neutron elastic-scatter imaging for material characterization," *2015 IEEE Nuclear Science Symposium and Medical Imaging Conference, NSS/MIC 2015*, vol. 1, 2016.

[7] M. C. Hamel, J. K. Polack, M. L. Ruch, M. J. Marcath, S. D. Clarke, and S. A. Pozzi, "Active neutron and gamma-ray imaging of highly enriched uranium for treaty verification," *Scientific Reports*, vol. 7, no. 1, pp. 1–10, 2017.

[8] G. Phillips, "Applications of Compton imaging in nuclear waste characterization and treaty verification," tech. rep., U.S. Naval Research Laboratory, 2002.

[9] J. Mihalczo and J. Mullens, "Nuclear Material Identification System with Imaging and Gamma-Ray Spectrometry for Plutonium, Highly Enriched Uranium, High Explosives, and Other Materials," tech. rep., Oak Ridge National Laboratory, 2012.

[10] S. Mochizuki, J. Kataoka, L. Tagawa, Y. Iwamoto, H. Okochi, N. Katsumi, S. Kinno, M. Arimoto, T. Maruhashi, K. Fujieda, T. Kurihara, and S. Ohsuka, "First demonstration of aerial gamma-ray imaging using drone for prompt radiation survey in Fukushima," *Journal of Instrumentation*, vol. 12, 2017.

[11] Y. Sato, Y. Terasaka, W. Utsugi, H. Kikuchi, H. Kiyooka, and T. Torii, "Radiation imaging using a compact Compton camera mounted on a crawler robot inside reactor buildings of Fukushima Daiichi Nuclear Power Station," *Journal of Nuclear Science and Technology*, vol. 56, 2019.

[12] K. Vetter, R. Barnowski, J. W. Cates, A. Haefner, T. H. Joshi, R. Pavlovsky, and B. J. Quiter, "Advances in nuclear radiation sensing: Enabling 3-D gamma-ray vision," *Sensors*, vol. 19, 2019.

[13] V. Schönfelder, A. Hirner, and K. Schneider, "A telescope for soft gamma ray astronomy," *Nuclear Instruments and Methods*, vol. 107, 1973.

[14] T. Ida, S. Motomura, M. Ueda, Y. Watanabe, and S. Enomoto, "Accurate modeling of event-by-event backprojection for a germanium semiconductor Compton camera for system response evaluation in the LM-ML-EM image reconstruction method," *Japanese Journal of Applied Physics*, vol. 58, 2019.

[15] R. T. Grannan, R. Koga, W. A. Millard, A. M. Preszler, M. Simnett, and R. S. White, "A Large Area Detector for Neutrons Between 2 and 100 MeV," *Nuclear Instruments and Methods*, vol. 3, 1972.

[16] K. Weinfurther, J. Mattingly, E. Brubaker, and J. Steele, "Model-based design evaluation of a compact, high-efficiency neutron scatter camera," *Nuclear Instruments and Methods in Physics Research, Section A: Accelerators, Spectrometers, Detectors and Associated Equipment*, vol. 883, 2018.

[17] K. Vetter, D. Chivers, B. Plimley, A. Coffer, T. Aucott, and Q. Looker, "First demonstration of electron-tracking based Compton imaging in solid-state detectors," *Nuclear Instruments and Methods in Physics Research, Section A*, vol. 652, 2011.

[18] J. E. M. Goldsmith, M. D. Gerling, and J. S. Brennan, "A compact neutron scatter camera for field deployment," *Review of Scientific Instruments*, vol. 87, 2016.

[19] "https://h3dgamma.com/home.php," 2020.

[20] "http://phdsco.com/," 2020.

[21] R. H. Dicke, "Scatter-Hole Cameras for X-Rays and Gamma-Rays," *The Astrophysical Journal*, vol. I, 1968.

[22] J. G. Ables, "Fourier Transform Photography: A New Method for X-Ray Astronomy," *Publications of the Astronomical Society of Australia*, vol. 1, 1968.

[23] E. Caroli, J. B. Stephen, G. D. Cocco, L. Natalucci, and A. Spizzichino, "Coded Aperture Imaging in X- and Gamma-Ray Astronomy," *Space Science Reviews*, vol. 45, 1987.

[24] G. K. Skinner, "Sensitivity of coded mask telescopes," *Applied Optics*, vol. 47, 2008.

[25] M. J. Cieślak, K. A. A. Gamage, and R. Glover, "Coded-aperture imaging systems: Past, present and future development – A review," *Radiation Measurements*, vol. 92, 2016.

[26] H. Bradt, G. Garmire, M. Oda, G. Spada, B. V. Sreekantan, P. Gorenstein, and H. Gursky, "The modulation collimator in x-ray astronomy," *Space Science Reviews*, vol. 8, 1968.

[27] H. W. Schnopper, R. I. Thompson, and S. Watt, "Predicted Performance of a Rotating Modulation Collimator for Locationg Celestial X-Ray Sources," *Space Science Reviews*, vol. 8, 1968.

[28] G. J. Hurford, E. J. Schmahl, R. A. Schwartz, A. J. Conway, M. J. Aschwanden, A. Csillaghy, B. R. Dennis, C. Johns-Krull, S. Krucker, R. P. Lin, J. McTiernan, T. R. Metcalf, J. Sato, and D. M. Smith, "The RHESSI imaging concept," *Solar Physics*, vol. 210, no. 1-2, pp. 61–86, 2002.

[29] B. R. Kowash and D. K. Wehe, "A unified near- and far-field imaging model for rotating modulation collimators," *Nuclear Instruments and Methods in Physics Research, Section A*, vol. 637, 2011.

[30] P. Durouchoux, H. Hudson, G. Hurford, K. Hurley, J. Matteson, and E. Orsal, "Gamma-Ray Imaging with a Rotating Modulator," *Astronomy and Astrophysics*, vol. 120, 1983.

[31] S. Kronenberg, G. J. Brucker, E. Bechtel, and F. Gentner, "Directional detector of gamma ray sources," *Health Physics*, vol. 70, 1996.

[32] J. Brennan, E. Brubaker, M. Gerling, P. Marleau, M. Monterial, A. Nowack, P. Schuster, B. Sturm, and M. Sweany, "Source detection at 100 meter standoff with a time-encoded imaging system," *Nuclear Instruments and Methods in Physics Research A*, vol. 877, 2018.

[33] K. Fujimoto, "A simple gamma ray direction finder," *Health Physics*, vol. 91, 2006.

[34] J. G. M. FitzGerald, "A Rotating Scatter Mask for inexpensive gamma-ray imaging in orphan source search: Simulation results," *IEEE Transactions on Nuclear Science*, vol. 62, 2015.

[35] K. F. Koral, W. L. Rogers, and G. F. Knoll, "Digital Tomographic Imaging with Time Modulated Pseudorandom Coded Aperture and Anger Camera," *Journal of Nuclear Medicine*, vol. 16, 1974.

[36] S. T. Brown, D. Goodman, J. Chu, B. Williams, M. R. Williamson, and Z. He, "Time-Encoded Gamma-Ray Imaging Using a 3D-Position-Sensitive CdZnTe Detector Array," *IEEE Transactions on Nuclear Science*, vol. 67, 2019.

[37] J. Brennan, E. Brubaker, M. Gerling, P. Marleau, K. McMillan, A. Nowack, N. Renard-Le Galloudec, M. Sweany, N. R. L. Galloudec, and M. Sweany, "Demonstration of two-dimensional time-encoded imaging of fast neutrons," *Nuclear Instruments and Methods in Physics Research A*, vol. 802, 2015.

[38] S. T. Brown, *Time-Encoded Thermal Neutron Imaging Using Large-Volume Pixelated CdZnTe Detectors*. PhD thesis, University of Michigan, 2017.

[39] K. Byard, "Square Element Antisymmetric Coded Apertures," *Experimental Astronomy*, vol. 2, 1992.

[40] J. Braga, T. Villela, U. B. Jayanthi, F. D'Amico, and J. A. Neri, "A New Mask-AntiMask Coded-Aperture for Hard X-Ray Astronomy," *Experimental A*, 1991.

[41] R. Accorsi, *Design of Near Field Coded Aperture Cameras for High Resolution Medical and Industrial Gamma Ray Imaging*. PhD thesis, Massachusetts Institute of Technology, 2001.

[42] R. Accorsi and R. C. Lanza, "Near-field artifact reduction in planar coded aperture imaging," *Applied Optics*, vol. 40, 2001.

[43] S. R. Gottesman and E. E. Fenimore, "New family of binary arrays for coded aperture imaging.," *Applied Optics*, vol. 28, 1989.

[44] P. Marleau, J. Brennan, E. Brubaker, and J. Steele, "Results from the coded aperture neutron imaging system," *IEEE Nuclear Science Symposium Conference Record*, 2010.

[45] A. Busboom, H. Elders-Boll, and H. D. Schotten, "Uniformly redundant arrays," *Experimental Astronomy*, vol. 8, 1998.

[46] X. Liang, X. Pang, D. Cao, X. Hu, D. Li, Z. Zhang, S. Liu, T. Hu, Y. Zhang, X. Wang, F. Meng, J. Zhang, X. Han, Q. Liu, L. Liu, Z. Zhou, J. Zhang, L. Wei, and L. Shuai, "Self-supporting design of a time-encoded aperture, gamma-neutron imaging system," *Nuclear Instruments and Methods in Physics Research, Section A*, vol. 951, 2020.

[47] D. A. Boardman, M. C. Guenette, A. Sarbutt, A. Flynn, and D. Prokopovich, "Compressive Gamma-Ray Imaging," in *presented at IEEE Nuclear Science Symposium & Medical Imaging Conference*, 2017.

[48] H. W. Babcock, "The Possibility of Compensating Astronomical Seeing," *Publications of the Astronomical Society of the Pacific*, vol. 65, 1953.

[49] F. Rigaut and B. Neichel, "Multiconjugate Adaptive Optics for Astronomy," *Annual Review of Astronomy and Astrophysics*, vol. 56, no. 1, pp. 277–314, 2018.

[50] J. F. Synnevåg, A. Austeng, and S. Holm, "Adaptive beamforming applied to medical ultrasound imaging," *IEEE Transactions on Ultrasonics, Ferroelectrics, and Frequency Control*, vol. 54, no. 8, pp. 1606–1613, 2007.

[51] G. J. Gang, J. W. Stayman, T. Ehtiati, and J. H. Siewerdsen, "Task-driven image acquisition and reconstruction in cone-beam CT," *Physics in Medicine and Biology*, vol. 60, no. 8, pp. 3129–3150, 2015.

[52] L. P. Panych and F. A. Jolesz, "A dynamically adaptive imaging algorithm for wavelet-encoded MRI," *Magnetic Resonance in Medicine*, vol. 32, no. 6, pp. 738–748, 1994.

[53] J. Zhou and J. Qi, "Adaptive imaging for lesion detection using a zoom-in PET system," *IEEE Transactions on Medical Imaging*, vol. 30, no. 1, pp. 119–130, 2011.

[54] N. Li and L. J. Meng, "Adaptive angular sampling for SPECT imaging," *IEEE Transactions on Nuclear Science*, vol. 58, no. 5 PART 1, pp. 2205–2218, 2011.

[55] S. Poopalasingam, M. Rozler, K. Popovic, and W. Chang, "Adjustable resolution/sensitivity slit-slat collimator for task-specific clinical SPECT imaging," *2014 IEEE Nuclear Science Symposium and Medical Imaging Conference, NSS/MIC 2014*, pp. 1–6, 2016.

[56] C. Chaix, S. Kovalsky, M. Kosmider, H. H. Barrett, and L. R. Furenlid, "Integration of AdaptiSPECT: a small-animal adaptive SPECT imaging system," *Medical Applications of Radiation Detectors III*, vol. 8853, no. September 2013, p. 88530A, 2013.

[57] B. Ristic, M. Morelande, and A. Gunatilaka, "Information driven search for point sources of gamma radiation," *Signal Processing*, vol. 90, no. 4, pp. 1225–1239, 2010.

[58] J. Towler, B. Krawiec, and K. Kochersberger, "Terrain and Radiation Mapping in Post-Disaster Environments Using an Autonomous Helicopter," *Remote Sensing*, vol. 4, no. 7, pp. 1995–2015, 2012.

[59] A. A. Redwan Newaz, S. Jeong, H. Lee, H. Ryu, and N. Y. Chong, "UAV-based multiple source localization and contour mapping of radiation fields," *Robotics and Autonomous Systems*, vol. 85, pp. 12–25, 2016.

[60] M. S. Lee, D. Shy, W. R. Whittaker, and N. Michael, "Active Range and Bearing-based Radiation Source Localization," *IEEE International Conference on Intelligent Robots and Systems*, pp. 1389–1394, 2018.

[61] C. M. Kreucher, A. O. Hero, K. D. Kastella, and M. R. Morelande, "An information-based approach to sensor management in large dynamic networks," *Proceedings of the IEEE*, vol. 95, no. 5, pp. 978–999, 2007.

[62] A. V. Klimenko, W. C. Priedhorsky, N. W. Hengartner, and K. N. Borozdin, "Efficient strategies for low-statistics nuclear searches," *IEEE Transactions on Nuclear Science*, vol. 53, no. 3, pp. 1435–1442, 2006.

[63] D. T. Willcox, B. R. Kowash, and D. K. Wehe, "Adaptive Imaging Using a Rotating Modulation Collimator (RMC)," in *IEEE Nuclear Science Symposium Conference Record*, 2010.

[64] J. G. Fitzgerald, L. W. Burggraf, B. R. Kowash, and E. L. Hull, "A Modulating Liquid Collimator for Coded Aperture Adaptive Imaging of Gamma-Rays," *IEEE Transactions on Nuclear Science*, vol. 60, 2013.

[65] A. Lorenz, "Review of Neutron Detection Methods and Instruments," tech. rep., Lawrence Livermore Laboratory, 1973.

[66] A. J. Peurrung, "Recent developments in neutron detection," *Nuclear Instruments and Methods in Physics Research A*, vol. 443, 2000.

[67] R. T. Kouzes, J. H. Ely, L. E. Erikson, W. J. Kernan, A. T. Lintereur, E. R. Siciliano, D. L. Stephens, D. C. Stromswold, R. M. V. Ginhoven, and M. L. Woodring, "Neutron detection alternatives to 3 He for national security applications," *Nuclear Instruments and Methods in Physics Research A*, vol. 623, 2010.

[68] R. C. Runkle, A. Bernstein, and P. E. Vanier, "Securing special nuclear material : Recent advances in neutron detection and their role in nonproliferation," *Journal of Applied Physics*, vol. 108, 2010.

[69] D. Henzlova, R. Kouzes, R. McElroy, P. Peerani, M. Aspinall, K. Baird, A. Bakel, M. Borella, M. Bourne, L. Bourva, F. Cave, R. Chandra, D. Chernikova, S. Croft, G. Dermody, A. Dougan, J. Ely, E. Fanchini, P. Finocchiaro, V. Gavron, M. Kureta, K. D. Ianakiev, K. Ishiyama, T. Lee, C. Martin, K. McKinny, H. O. Menlove, C. Orton, A. Pappalardo, B. Pedersen, D. Peranteau, R. Plenteda, S. Pozzi, M. Schear, M. Seya, E. Siciliano, S. Stave, L. Sun, M. T. Swinhoe, H. Tagziria, S. Vaccaro, J. Takamine, A. L. Weber, T. Yamaguchi, and H. Zhu, "Current Status of Helium-3 Alternative Technologies for Nuclear Safeguards," tech. rep., Los Alamos National Laboratory, 2015.

[70] B. D. Milbrath, A. J. Peurrung, M. Bliss, and W. J. Weber, "Radiation detector materials: An overview," *Journal of Materials Research*, vol. 23, no. 10, pp. 2561–2581, 2008.

[71] G. F. Knoll, *Radiation Detection and Measurement*. New York, NY: Wiley, 4th ed., 2010.

[72] N. Zaitseva, A. Glenn, L. Carman, H. Paul Martinez, R. Hatarik, H. Klapper, and S. Payne, "Scintillation properties of solution-grown trans-stilbene single crystals," *Nuclear Instruments and Methods in Physics Research A*, vol. 789, 2015.

[73] M. M. Bourne, S. D. Clarke, N. Adamowicz, S. A. Pozzi, N. Zaitseva, and L. Carman, "Neutron detection in a high-gamma field using solution-grown stilbene," *Nuclear Instruments and Methods in Physics Research A'*, vol. 806, 2016.

[74] R. Hawrami, L. S. Pandian, E. Ariesanti, J. Glodo, J. Finkelstein, J. Tower, and K. Shah, "Cs2LiLa(Br, Cl)6 Crystals for Nuclear Security Applications," *IEEE Transactions on Nuclear Science*, vol. 63, 2016.

[75] Hamamatsu, "Photomultiplier Tubes Basics and Applications," tech. rep., Hamamatsu, 2017.

[76] J. BIRKS, *The Theory and Practice of Scintillation Counting*. Oxford: Pergamon Press, 1964.

[77] CAEN, "DT5730/DT5725 User Manual UM3148," tech. rep., CAEN, 2019.

[78] C. S. Sosa, *The Importance of Light Collection Efficiency in Radiation Detection Systems That Use Organic Scintillators*. PhD thesis, University of Michigan, 2018.

[79] P. Schuster, P. Feng, and E. Brubaker, "On the relationship between scintillation anisotropy and crystal structure in pure crystalline organic scintillator material," *IEEE Transactions on Nuclear Science*, vol. 65, 2018.

[80] M. A. Norsworthy, A. Poitrasson-Rivière, M. L. Ruch, S. D. Clarke, and S. A. Pozzi, "Evaluation of neutron light output response functions in EJ-309 organic scintillators," *Nuclear Instruments and Methods in Physics Research Section A*, vol. 842, 2017.

[81] W. M. Steinberger, M. L. Ruch, A. Di-Fulvio, S. D. Clarke, and S. A. Pozzi, "Timing performance of organic scintillators coupled to silicon photomultipliers," *Nuclear Instruments and Methods in Physics Research A*, vol. 922, 2019.

[82] G. Liu, M. J. Joyce, X. Ma, and M. D. Aspinall, "A digital method for the discrimination of neutrons and γ rays with organic scintillation detectors using frequency gradient analysis," *IEEE Transactions on Nuclear Science*, vol. 57, 2010.

[83] M. J. Balmer, K. A. Gamage, and G. C. Taylor, "Comparative analysis of pulse shape discrimination methods in a 6Li loaded plastic scintillator," *Nuclear Instruments and Methods in Physics Research A*, vol. 788, 2015.

[84] K. A. Gamage, M. J. Joyce, and N. P. Hawkes, "A comparison of four different digital algorithms for pulse-shape discrimination in fast scintillators," *Nuclear Instruments and Methods in Physics Research A*, vol. 642, 2011.

[85] G. Liu, M. D. Aspinall, X. Ma, and M. J. Joyce, "An investigation of the digital discrimination of neutrons and γ rays with organic scintillation detectors using an artificial neural network," *Nuclear Instruments and Methods in Physics Research A*, vol. 607, 2009.

[86] S. D. Jastaniah and P. J. Sellin, "Digital techniques for n/γ pulse shape discrimination and capture-gated neutron spectroscopy using liquid scintillators," *Nuclear Instruments and Methods in Physics Research A*, vol. 517, 2004.

[87] P. A. Söderström, J. Nyberg, and R. Wolters, "Digital pulse-shape discrimination of fast neutrons and γ rays," *Nuclear Instruments and Methods in Physics Research A*, vol. 594, 2008.

[88] M. Monterial, P. Marleau, S. Clarke, and S. Pozzi, "Application of Bayes' theorem for pulse shape discrimination," *Nuclear Instruments and Methods in Physics Research A*, vol. 795, 2015.

[89] P. Schuster and E. Brubaker, "Characterization of the scintillation anisotropy in crystalline stilbene scintillator detectors," *Nuclear Instruments and Methods in Physics Research 'A*, vol. 859, 2017.

[90] R. A. Weldon, J. M. Mueller, C. Lynch, P. Schuster, S. Hedges, C. Awe, L. Li, P. Barbeau, and J. Mattingly, "High-precision characterization of the neutron light output of stilbene along the directions of maximum and minimum response," *Nuclear Instruments and Methods in Physics Research A*, vol. 927, 2019.

[91] E. Brubaker and J. Steele, "Neutron imaging using the anisotropic response of crystalline organic scintillators," *IEEE Nuclear Science Symposium Conference Record*, 2010.

[92] U. Shirwadkar, R. Hawrami, J. Glodo, E. V. Van Loef, and K. S. Shah, "Novel scintillation material Cs2LiLaBr6-xCl x:Ce for gamma-ray and neutron spectroscopy," *IEEE Nuclear Science Symposium Conference Record*, 2012.

[93] P. P. Guss, T. G. Stampahar, S. Mukhopadhyay, A. Barzilov, and A. Guckes, "Scintillation properties of a Cs 2 LiLa(Br 6)90%(Cl 6)10%:Ce (CLLBC) crystal," *Radiation Detectors: Systems and Applications XV*, vol. 9215, 2014.

[94] N. D'Olympia, P. Chowdhury, C. J. Lister, J. Glodo, R. Hawrami, K. Shah, and U. Shirwadkar, "Pulse-shape analysis of CLYC for thermal neutrons, fast

neutrons, and gamma-rays," *Nuclear Instruments and Methods in Physics Research, Section A*, vol. 714, 2013.

[95] E. E. Fenimore and T. M. Cannon, "Coded aperture imaging with uniformly redundant arrays," *Applied optics*, vol. 17, 1978.

[96] E. E. Fenimore, "Coded aperture imaging: predicted performance of uniformly redundant arrays.," *Applied optics*, vol. 17, 1978.

[97] I. D. Jupp, K. Byard, and A. J. Dean, "An improved sampling configuration for a coded aperture telescope," *Nuclear Instruments and Methods in Physics Research A*, vol. 345, 1994.

[98] R. S. Woolf, B. F. Phlips, A. L. Hutcheson, and E. A. Wulf, "Fast-neutron, coded-aperture imager," *Nuclear Instruments and Methods in Physics Research A*, vol. 784, 2015.

[99] F. J. MacWilliams and N. J. A. Sloane, "Pseudo-Random Sequences and Arrays," *Proceedings of the IEEE*, vol. 64, 1976.

[100] G. K. Skinner, "Imaging with coded-aperture masks," *Nuclear Instruments and Methods In Physics Research*, vol. 221, 1984.

[101] A. Busboom, H. Elders-Boll, and H. D. Schotten, "Combinatorial design of near-optimum masks for coded aperture imaging," *1997 IEEE International Conference on Acoustics, Speech, and Signal Processing*, vol. 4, 1997.

[102] S. Sun, Z. Zhang, L. Shuai, D. Li, Y. Wang, Y. Liu, X. Huang, H. Tang, T. Li, P. Chai, X. Jiang, B. Ma, M. Zhu, X. Wang, Y. Zhang, W. Zhou, F. Zeng, J. Guo, L. Sun, M. Yang, Y. Zhang, C. Wei, C. Ma, and L. Wei, "Development of a panorama coded-aperture gamma camera for radiation detection," *Radiation Measurements*, vol. 77, 2015.

[103] A. P. Hammersley and G. K. Skinner, "Data Processing of Imperfectly Coded Images," *Nuclear Instruments and Methods in Physics Research*, vol. 221, 1984.

[104] K. Byard, "Fast decoding algorithms for coded aperture systems," *Nuclear Instruments and Methods in Physics Research A*, vol. 754, 2014.

[105] E. E. Fenimore, "Coded aperture imaging: the modulation transfer function for uniformly redundant arrays.," *Applied optics*, vol. 19, 1980.

[106] T. M. Cannon and E. E. Fenimore, "Coded Aperture Imaging: Many Holes Make Light Work," *Optical Engineering*, vol. 19, 1980.

[107] E. Brubaker, J. Brennan, P. Marleau, A. Nowack, J. Steele, M. Sweany, and D. Throckmorton, "Bubble masks for time-encoded imaging of fast neutrons," tech. rep., Sandia National Laboratory, 2013.

[108] D. E. Holland, J. E. Bevins, L. W. Burggraf, and B. E. O'Day, "Rotating scatter mask optimization for gamma source direction identification," *Nuclear Instruments and Methods in Physics Research A*, vol. 901, 2018.

[109] B. Kowash, *A Rotating Modulation Imager for the Orphan Source Search Problem*. PhD thesis, University of Michigan, 2008.

[110] T. Ogawa and H. Kanada, "Solution for Ill-Posed Inverse Kinematics of Robot Arm by Network Inversion," *Journal of Robotics*, 2010.

[111] K. M. Hanson, "Introduction to Bayesian Image Analysis," *Image Processing*, vol. 1898, 1993.

[112] B. J. Brewer, "Introduction to Bayesian statistics."

[113] C. Geyer, "Introduction to MCMC methods," in *Handbook of Markov Chain Monte Carlo* (S. Brooks, A. Gelman, G. L. Jones, and X.-L. Meng, eds.), Chapman and Hall/CRC, 2011.

[114] A. Andreyev, A. Sitek, and A. Celler, "Fast image reconstruction for Compton camera using stochastic origin ensemble approach," *Medical Physics*, 2011.

[115] M. C. Hamel, J. K. Polack, A. Poitrasson-Rivière, M. Flaska, S. D. Clarke, S. A. Pozzi, A. Tomanin, and P. Peerani, "Stochastic image reconstruction for a dual-particle imaging system," *Nuclear Instruments and Methods in Physics Research A*, vol. 810, 2016.

[116] H. Zhang, J. Wang, D. Zeng, X. Tao, and J. Ma, "Regularization strategies in statistical image reconstruction of low-dose x-ray CT: A review," *Medical Physics*, vol. 45, 2018.

[117] J. Qi and R. M. Leahy, "Iterative reconstruction techniques in emission computed tomography," *Physics in Medicine and Biology*, vol. 51, 2006.

[118] Q. Xu, H. Y. Yu, X. Q. Mou, L. Zhang, J. Hsieh, and G. Wang, "Low-dose X-ray CT reconstruction via dictionary learning," *IEEE Transactions on Medical Imaging*, vol. 31, 2012.

[119] D. Hellfeld, T. H. Joshi, M. S. Bandstra, R. J. Cooper, B. J. Quiter, and K. Vetter, "Gamma-Ray Point-Source Localization and Sparse Image Reconstruction Using Poisson Likelihood," *IEEE Transactions on Nuclear Science*, vol. 66, 2019.

[120] D. Wang, H. Hu, F. Zhang, and Q. Jia, "Source reconstruction for neutron coded-aperture imaging: A sparse method," *Review of Scientific Instruments*, vol. 88, 2017.

[121] D. J. Lingenfelter, J. A. Fessler, and Z. He, "Sparsity regularization for image reconstruction with Poisson data," *Computational Imaging VII*, vol. 7246, 2009.

[122] A. J. Reader and S. Ellis, "Bootstrap-Optimised Regularised Image Reconstruction for Emission Tomography," *IEEE Transactions on Medical Imaging*, 2020.

[123] M. Zhang, J. Zhou, X. Niu, E. Asma, W. Wang, and J. Qi, "Regularization parameter selection for penalized-likelihood list-mode image reconstruction in PET," *Physics in Medicine and Biology*, vol. 62, 2017.

[124] J. Fessler, "Emission ML Image Reconstruction," in *Image Reconstruction: Algorithms and Analysis*, ch. Chapter 16, Unpublished, 2015.

[125] J. A. Fessler, Class Lecture, Topic: "Majorize-minimize methods." Electrical Engineering and Computer Science, University of Michigan, 2020.

[126] J. Fessler, "Optimization Transfer Methods," in *Image Reconstruction: Algorithms and Analysis*, ch. Chapter 12, Unpublished, 2018.

[127] C. Wahl, *Imaging , Detection , and Identification Algorithms for Position - Sensitive Gamma - Ray Detectors*. PhD thesis, University of Michigan, 2011.

[128] J. Chu, *Advanced Imaging Algorithms with Position-Sensitive Gamma-Ray Detectors*. PhD thesis, University of Michigan, 2018.

[129] K. Lange, "Beginning Examples," in *MM Optimization Algorithms*, Philadelphia, PA: Society for Industrial and Applied Mathematics, 2016.

[130] K. Lange, "Majorization and Minorization," in *MM Optimization Algorithms*, ch. Chapter 4, Philadelphia, PA: Society for Industrial and Applied Mathematics, 2016.

[131] D. R. Hunter and K. Lange, "A Tutorial on MM Algorithms," *American Statistician*, vol. 58, 2004.

[132] L. A. Shepp and Y. Vardi, "Maximum Likelihood Reconstruction for Emission Tomography," *IEEE Transactions on Medical Imaging*, vol. 1, 1982.

[133] H. M. Hudson and R. S. Larkin, "Ordered Subsets of Projection Data," *IEEE transactions on medical imaging*, vol. 13, 1994.

[134] S. J. Wilderman, N. H. Clinthorne, J. A. Fessler, and W. L. Rogers, "List-Mode Maximum Likelihood Reconstruction of Compton Scatter Camera Images in Nuclear Medicine," *1998 IEEE Nuclear Science Symposium Conference Record*, 1998.

[135] F. Ben Bouallègue, J. F. Crouzet, and D. Mariano-Goulart, "A heuristic statistical stopping rule for iterative reconstruction in emission tomography," *Annals of Nuclear Medicine*, vol. 27, 2013.

[136] J. K. Polack, *A Maximum-Likelihood Approach for Localizing and Characterizing Special Nuclear Material with a Dual-Particle Imager*. PhD thesis, University of Michigan, 2016.

[137] T. J. Herbert, "Statistical stopping criteria for iterative maximum likelihood reconstruction of emission images," *Physics in Medicine and Biology*, vol. 35, 1990.

[138] E. Veklerov and J. Llacer, "Stopping Rule for the MLE Algorithm Based on Statistical Hypothesis Testing," *IEEE Transactions on Medical Imaging*, vol. 6, 1987.

[139] S. J. Reeves, "Generalized cross-validation as a stopping rule for the Richardson-Lucy algorithm," *International Journal of Imaging Systems and Technology*, vol. 6, 1995.

[140] K. J. Coakley, "Resampling scheme for improving maximum likelihood reconstructions of positron emission tomography images," *Medical Imaging 1994: Image Processing*, vol. 2167, 2005.

[141] K. J. Coakley, "A Cross-Validation Procedure for Stopping the EM Algorithm and Deconvolution of Neutron Depth Profiling Spectra," *IEEE Transactions on Nuclear Science*, vol. 38, 1991.

[142] J. S. Liow and S. C. Strother, "Practical Tradeoffs Between Noise, Quantitation, and Number of Iterations for Maximum Likelihood-Based Reconstructions," *IEEE Transactions on Medical Imaging*, vol. 10, 1991.

[143] E. Veklerov and J. Llacer, "The Feasibility of Images Reconstructed with the Method of Sieves," *IEEE Transactions on Nuclear Science*, vol. 37, 1990.

[144] D. L. Snyder and M. I. Miller, "The Use of Sieves to Stabilize Images Produced with the ME Algorithm for Emission Tomography," *IEEE Transactions on Nuclear Science*, vol. NS-32, 1985.

[145] R. M. Leahy and J. Qi, "Statistical approaches in quantitative positron emission tomography," *Statistics and Computing*, vol. 10, 2000.

[146] E. Tanaka, "A Fast Reconstruction Algorithm for Stationary Positron Emission Tomography Based on a Modified EM Algorithm," *IEEE Transactions on Medical Imaging*, vol. 6, 1987.

[147] J. A. Stamos, W. L. Rogers, N. H. Clinthorne, and K. F. Koral, "Object-Dependent Performance Comparsion of Two Iterative Reconstruction Algorithms," *IEEE Transactions on Nuclear Science*, vol. 35, 1988.

[148] L. Jeih and S. C. Strother, "The convergence of object dependent resolution in maximum likelihood based tomographic image reconstruction," *Physics in Medicine and Biology*, vol. 38, 1993.

[149] S. M. Kay, *Fundamentals of Statistical Signal Processing: Estimation Theory*. Upper Saddle River, NJ: Prentice Hall, 1993.

[150] M. R. Chernick, *Bootstrap Methods: A Guide for Practitioners and Researchers*. Newtown, PA: Wiley, second ed., 2008.

[151] Online Lecture, Topic: "Cross-validation, Bootstraps and Consensus." Department of Statistics, Pennsylvania State University, 2020.

[152] N. P. Shah, J. VanderZanden, and D. K. Wehe, "Design and Construction of a 1-D, Cylindrical, Dual-Particle, Time-Encoded Imaging System," *Nuclear Inst. and Methods in Physics Research, A*, 2019.

[153] M. M. Bourne, S. D. Clarke, M. Paff, A. DiFulvio, M. Norsworthy, and S. A. Pozzi, "Digital pile-up rejection for plutonium experiments with solution-grown stilbene," *Nuclear Instruments and Methods in Physics Research Section A: Accelerators, Spectrometers, Detectors and Associated Equipment*, vol. 842, 2017.

[154] J. M. Verbeke, C. Hagmann, and D. Wright, "Simulation of Neutron and Gamma Ray Emission from Fission," Tech. Rep. UCRL-AR-228518, Lawrence Livermore National Laboratory, 2010.

[155] Z. Liu and A. Nehorai, "Statistical angular resolution limit for point sources," *IEEE Transactions on Signal Processing*, vol. 55, no. 11, 2007.

[156] S. T. Smith, "Statistical resolution limits and the complexified Cramér-Rao bound," *IEEE Transactions on Signal Processing*, vol. 53, no. 5, 2005.

[157] Sture Holm, "A Simple Sequentially Rejective Multiple Test Procedure," *Scandinavian Journal of Statistics*, vol. 6, 1979.

[158] J. Bartroff and J. Song, "Sequneital Tests of Multiple Hypotheses Controlling Type I and II Familywise Error Rates," *Journal of Statistical Planning and Inference*, vol. 153, 2014.

[159] D. L. Chichester, "Properties of Nuclear Fuel Used in Tests with the LLNL Gamma-Ray Mirror in September 2014," Tech. Rep. INL/MIS-14-33068, Idaho National Laboratory, 2014.

[160] D. L. Chichester, S. A. Pozzi, J. L. Dolan, M. Flaska, J. T. Johnson, E. H. Seabury, and E. M. Gantz, "Neutron Emission Characteristics of Two Mixed-Oxide Fuels: Simulations and Initial Experiments," Tech. Rep. INL/EXT-09-16566, Idaho National Laboratory, 2009.

[161] D. L. Chichester, J. Sanders, J. A. Turnage, J. D. West, and M. A. Willmore, "The INL Nuclear and Radiological Activity Center," tech. rep., Idaho National Laboratory, 2013.

[162] J. T. Goorley, M. R. James, T. E. Booth, F. B. Brown, J. S. Bull, L. J. Cox, J. W. Durkee, J. S. Elson, M. L. Fensin, R. A. Forster, J. S. Hendricks, H. G. Hughes, R. C. Johns, B. C. Kiedrowski, S. G. Mashnik, G. W. McKinney, D. B. Pelowitz, R. E. Prael, J. E. Sweezy, L. S. Waters, T. A. Wilcox, and A. Zukaitis, "MCNP6 user's manual," tech. rep., 2013.

[163] J. C. Wagner, E. L. Redmond II, S. P. Palmtag, and J. S. Hendricks, "MCNP: Multigroup/Adjoint Capabilitiees," tech. rep., Los Alamos National Laboratory, 1994.